COSMOLOGY AND ASTROPHYSICS FROM SMALL SCALES

Shivam Pandey

A DISSERTATION

in

Physics and Astronomy

Presented to the Faculties of the University of Pennsylvania
in
Partial Fulfillment of the Requirements for the
Degree of Doctor of Philosophy

2022

Supervisor of Dissertation

_____

Dr. Bhuvnesh Jain, Walter H. and Leonore C. Annenberg Professor

Graduate Group Chairperson

_____

Dr. Ravi Sheth, Professor

Dissertation Committee:

Dr. Mark Devlin, Professor

Dr. Ravi Sheth, Professor

Dr. Elisabeth Krause, Professor

Dr. Jonathan Heckman, Professor

Acknowledgments

First and foremost, I would like to express my sincere gratitude to my advisor Bhuvnesh Jain for continuously supporting me throughout my Ph.D., both academically and as a friend. Bhuv has been a phenomenal mentor, and his constant flow of ideas, enduring patience, pedagogical insights, and encouragement made this thesis possible. He also helped me connect with all the other experts in cosmology inside and outside Penn, which helped me broaden my horizon.

I would also like to thank Mark Devlin for his immense support and guidance in approaching the problems tackled in this thesis, especially related to SZ cross-correlations. I am greatly indebted to Elisabeth Krause for taking frequent time out of her very busy schedule to guide multiple projects in this thesis, theoretical modeling and data analysis training, guiding the research when things got tough, and pushing and challenging me throughout the later part of the Ph.D.. I also owe a lot to my first-year advisor, Ravi Sheth, for training me in various topics of cosmology, particularly on the halo model approach. Finally, I also thank Jonathan Heckman for taking the time to be on my committee and giving

games, bike rides and all the fun and laughs we had over the years, I will miss you all. It would be unfinished to not emphasize that my *time* at Penn would have been probably dry if not for those infinite table-tennis and tennis games throughout the years with Guram, Carles, Lucas, Eric, Bhuv, Chip, and Andy; I will miss those a lot!

Finally, I owe many thanks to my parents, family, and friends back home for their support in countless ways. Lastly, thank you Monica, for always being there through thick and thin, for being so understanding, and for giving me some of my happiest and most cherished memories.

ABSTRACT

COSMOLOGY AND ASTROPHYSICS FROM SMALL SCALES

Shivam Pandey

Bhuvnesh Jain

Cross-correlations between tracers of large-scale structure (LSS), such as galaxies, weak lensing, and thermodynamics of hot gas, provide powerful tests of the cosmological model. In this Ph.D. thesis, we develop analytical models of these tracers and apply them to compare measurements to theoretical predictions of the standard model of cosmology. The complicated non-linear interactions between various components of the Universe present a significant challenge to constraining cosmological or astrophysical models. We aim to maximize the information gained from current and future cosmological datasets in the presence of astrophysical and observational sources of uncertainty. In the first half of the thesis, we describe and validate a hybrid galaxy biasing model (non-linear mapping between dark matter and galaxies) aimed at analyzing the correlations between galaxy positions and weak lensing. We then apply this model to recent data from the Dark Energy Survey, leading to a significant gain in cosmological constraints. In the second half of the thesis, we carry out high significance measurements of cross-correlations between the pressure of hot gas and weak lensing (shear-y) and galaxy positions (galaxy-y). We constrain the evolution of the average thermal pressure of the Universe and find evidence for reduced pressure in low mass halos. Our results point to the effects of increased baryonic feedback (the impact of supernovae or active galactic nuclei on LSS). These results will help in understanding how baryonic feedback impacts galaxy formation and using the non-linear regime for cosmological analysis with future survey data.

Contents

List of Tables

List of Figures

Chapter 1

Introduction

1.1 Physical Cosmology

Obtaining a coherent model of the Universe that can broadly describe all the aspects of the Universe is one of the holy grails of human endeavor. Through centuries of theoretical and experimental progress, we currently have narrowed down to two *standard models* of physics: Standard Model (SM) of particle physics and ΛCDM model of cosmological physics. While it is possible to perform lab experiments to test the laws of particle physics [1], we are only given one Universe to *observe* the laws at cosmological scales. The SM has been tested to exquisite precision through these experiments, with almost all the observations explained through the current understanding of quantum physics. On the other hand, while the ΛCDM model can also successfully explain virtually all the recent

---

[1]subject to energy constraints
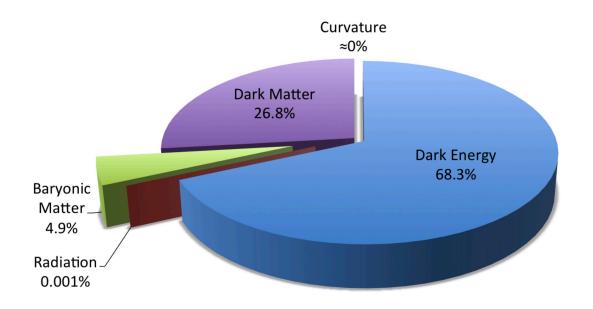
Figure 1.1: Distribution of the energy content of the Universe within ΛCDM model as constrained from current data. Credits: NASA

observations of the Universe from galactic to cosmological scales, it requires the existence of non-standard physics model components that we very poorly understand. According to this model, approximately 25% of the total energy density comprises of cold dark matter that drives the majority of structure formation by interacting using gravitational force [8,88]. The observed accelerating expansion of the Universe is driven by exotic dark energy which comprises of approximately 70% of the total energy budget (see Fig. 1.1) [233,257]. Both dark matter and dark energy most probably require beyond-SM physics that is an area of very active research.
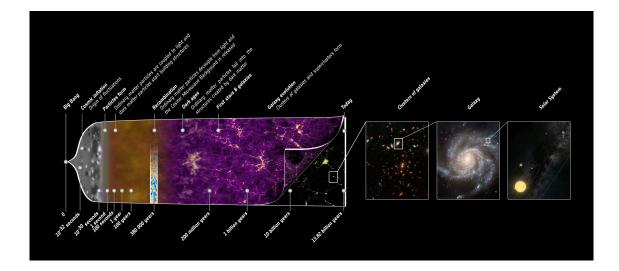
Figure 1.2: Timeline of the evolution of the Universe within ΛCDM model paradigm as constrained from current data. Credits: NASA

1.1.1 Cosmic timeline

Our best understanding of the evolution of the Universe is broadly described in Fig. 1.2 (see [251] for a review on which text of this sub-section is based). The Universe started with a singularity known as the big bang. A theory of quantum gravity, which represents the unification of the four fundamental forces, will be needed to describe what happened in the first 10^{-43}s of the Universe and is an area of active research. However, as this hot and small Universe started to expand, it started cooling. The temperature of the quark-gluon plasma dropped to the point where it underwent a phase transition, forming color-neutral baryons and mesons, a process known as the quantum chromodynamics phase transi-

tion. Processes appear to go out of the equilibrium in cosmic history because their cross-sections decrease as cosmic temperature decreases. This resulted in the decoupling of neutrinos and the freezing of the neutron-to-proton ratio, for example. Later, by nuclear fusion, these constituents began to generate the lightest elements. This occurred during the age of nucleosynthesis, and the projected element abundances match the latest measurements surprisingly well. Although the Universe was globally neutral, there were still free electrons and nucleons at this epoch. Recombination occurred 380,000 years after the big bang when unbound electrons and nucleons began to combine to create neutral atoms. The photons ceased interacting effectively with the electrons at this time, and the formerly opaque Universe became transparent to the radiation. While cooling to create the astoundingly homogeneous blackbody radiation field of temperature, T_{CMB} = 2.75K, the photons generated during recombination travel reasonably undisturbed until the present moment. This final scattering surface, or cosmic microwave background, is the furthest direct observation of the Universe that we can currently make. The cosmological standard model relies heavily on this relatively homogeneous final scattering surface, although there are modest temperature inhomogeneities in the temperature field, which are an imprint of the somewhat inhomogeneous matter distribution during recombination. These inhomogeneities increased as a result of gravitational evolution, and when they became large enough, gravitational collapse generated the first dark matter haloes.

These haloes eventually converged to produce larger and larger haloes. After re-combination, the baryonic gas followed the dark matter and accumulated in the dark matter potential wells. It might reach enough high concentrations there to cool efficiently, condense, and create the stars and galaxies we see today.

1.1.2 The expanding Universe

In this sub-section we describe the basics of an expanding Universe and the text in this sub-section is heavily inspired by [94]. General Relativity (GR) forms the backbone of the standard cosmological model (see [324] for a review). The Einstein field equations describing GR can be succinctly written as:

$$G_{\mu\nu} = 8\pi G T_{\mu\nu}, \tag{1.1.1}$$

where $G_{\mu\nu}$ describes the geometry of the spacetime and $T_{\mu\nu}$ describes all the sources of matter and energy in the spacetime. When additionally imposing the *cosmological principle*, which posits that the Universe is homogeneous and isotropic on large scales, the most general form of spacetime metric is known as the Friedmann-Lemaitre-Robertson-Walker (FLRW) metric:

$$ds^2 = dt^2 - a^2(t)\left[\frac{dr^2}{1 - Kr^2} + r^2(d\theta^2 + \sin^2(\theta)d\phi^2)\right], \tag{1.1.2}$$

where, r, θ and ϕ are the spherical coordinates of the position in space, t is time and K is the curvature describing global geometry of the Universe. This curvature term, K is strongly constrained to be zero, especially using the analysis

of the primary CMB anisotropies, and hence the baseline model is known as flat-ΛCDM model. We will use this condition of $K = 0$ everywhere in this thesis, unless specified otherwise.

Under this FLRW metric and assuming ΛCDM model, we can solve for the evolution of the scale of the Universe ($a(t)$), and these are described by the Friedmann equations:

$$H^2 \equiv \left(\frac{\dot{a}}{a}\right)^2 = \frac{8\pi G}{3}\rho + \frac{\Lambda}{3} \qquad (1.1.3)$$

$$\frac{\ddot{a}}{a} = -\frac{4\pi G}{3}\left(\rho + \frac{3p}{c^2}\right) + \frac{\Lambda}{3}, \qquad (1.1.4)$$

where, these equations describe how scale of the Universe depend upon the energy density (ρ) and pressure (p) of the contents of the Universe, and the cosmological constant (Λ). We can also encode the scale of the Universe using the parameter known as cosmological redshift which is defined as $z \equiv 1/a - 1$, hence we have cosmological scale factor of $a = 1$ at redshift $z = 0$.

The energy densities of the components of the Universe are also normalized relative to the characteristic critical density of the Universe, ρ_{critical} which is given by:

$$\rho_{\text{critical}} = \frac{3H^2(z)}{8\pi G}. \qquad (1.1.5)$$

The relative contribution to the total energy density of the Universe by the three major components, matter (Ω_{m}), radiation (Ω_{R}) and dark energy (Ω_Λ) at $z = 0$ is

then defined as:

$$\Omega_m \equiv \frac{\rho_m(z=0)}{\rho_{critical}(z=0)}, \Omega_R \equiv \frac{\rho_R(z=0)}{\rho_{critical}(z=0)}, \Omega_m \equiv \frac{\rho_\Lambda(z=0)}{\rho_{critical}(z=0)}, \quad (1.1.6)$$

where, ρ_m, ρ_R and ρ_Λ are the physical densities of matter, radiation and dark energy respectively. These three densities scale differently with the expansion of the Universe, due to different equation of state. With redshift, the matter density scales as $\rho_m \propto (1+z)^3$, radiation density scales as $\rho_m \propto (1+z)^4$ and the dark energy density, ρ_Λ remains constant. Observations show that at present time of $z = 0$ approximately, $\Omega_m \sim 0.3$, $\Omega_\Lambda \sim 0.7$ and $\Omega_R \sim 10^{-4}$. Therefore, radiation is sub-dominant contributor to the total energy density at present time and only becomes important at very high redshifts.

Lastly, we can use the above equations to define the distance measures in the expanding Universe. There are three measures of the distances that are generally used in cosmology, the comoving distance $\chi(z)$, luminosity distance $D_L(z)$ and the angular diameter distance $D_A(z)$. The comoving distance is given by:

$$\chi(z) = c \int_0^z \frac{dz'}{H(z')}. \quad (1.1.7)$$

The luminosity distance preserves the inverse square law for diminishing flux and is related to comoving distance as $D_L(z) = \chi(z) \times (1+z)$. The angular diameter distance is computed such that assuming a Eucledian geometry, the size (δL) and observed angular extent ($\delta\theta$) of a source is related as, $\delta L = D_A \delta\theta$. In a flat Universe, we get $D_A(z) = \chi(z)/(1+z)$.

1.2 Dynamics of matter: structure formation

In the standard model, dark energy does not cluster and only impacts the global geometric shape of the spacetime. Therefore, to understand the physics of structure formation, we aim to describe how the density of the matter component evolves.

1.2.1 Quasi-linear regime

In this sub-section, we describe the structure formation in quasi-linear regime, heavily based on [32]. Under the assumption that matter is a pressure less perfect fluid, its dynamics are fully governed by continuity equation, Euler equation and the Poisson equation. Transforming these equations fully to comoving coordinates, we get:

$$\text{Poisson}: \nabla^2 \phi = \frac{3}{2} \Omega_{\mathrm{m}} H_0^2 \frac{\delta}{a} \tag{1.2.1}$$

$$\text{Continuity}: \delta' + \nabla \cdot [\mathbf{v}(1+\delta)] = 0 \tag{1.2.2}$$

$$\text{Euler}: v_i' + \mathcal{H} v_i + \mathbf{v} \cdot \nabla v_i = -\nabla_i \phi, \tag{1.2.3}$$

where, ϕ is the peculiar gravitational potential and $\mathcal{H} = a(z)H(z)$ is the comoving Hubble constant. Note that the derivatives are with respect to co-moving time ($d\eta = dt/a$) and co-moving space coordinates.

1.2.1.1 Linearized equations

Firstly, neglecting all the terms beyond the linear order in the continuity and Euler equation and writing them in terms of velocity divergence ($\theta = \nabla \cdot v$) we get:

$$\delta' + \theta = 0 \tag{1.2.4}$$

$$\theta' + \mathcal{H}\theta = -\nabla^2\phi. \tag{1.2.5}$$

These two coupled equations (along with Poisson equation) can be easily combined as:

$$\delta'' + \mathcal{H}\delta' - \frac{3}{2}\Omega(z)\mathcal{H}^2\delta = 0. \tag{1.2.6}$$

This equation can have a growing and a decaying mode solution, and since only the growing mode solution can survive, it can easily be found to be:

$$D_+(z) = D_{+,0}H(z)\int_z^\infty \frac{dz'(1+z')}{H^3(z')}, \tag{1.2.7}$$

1.2.1.2 Perturbative solutions

Now, to solve the original set of equations, including all the terms, we write them down in Fourier space. The continuity equation becomes:

$$\delta'(\mathbf{k}) + \theta(\mathbf{k}) = -\int \frac{d^3\mathbf{q}}{(2\pi)^3}\frac{d^3\mathbf{q}'}{(2\pi)^3}\delta^D(\mathbf{k} - \mathbf{q} - \mathbf{q}')\alpha(\mathbf{q}, \mathbf{q}')\theta(\mathbf{q})\delta(\mathbf{q}'), \tag{1.2.8}$$

and Euler equation is written as:

$$\theta'(\mathbf{k}) + \mathcal{H}\theta(\mathbf{k}) + \frac{3}{2}\Omega_\mathrm{m}\mathcal{H}^2\delta(\mathbf{k}) = -\int \frac{d^3\mathbf{q}}{(2\pi)^3}\frac{d^3\mathbf{q}'}{(2\pi)^3}\delta^D(\mathbf{k} - \mathbf{q} - \mathbf{q}')\beta(\mathbf{q}, \mathbf{q}')\theta(\mathbf{q})\theta(\mathbf{q}')$$

$$\tag{1.2.9}$$

where the coupling kernels are:

$$\alpha(\mathbf{q}, \mathbf{q}') = \frac{\mathbf{q} \cdot (\mathbf{q} + \mathbf{q}')}{q^2} \tag{1.2.10}$$

$$\beta(\mathbf{q}, \mathbf{q}') = \frac{1}{2} \frac{\mathbf{q} \cdot \mathbf{q}'}{qq'} \left(\frac{q}{q'} + \frac{q'}{q} \right) + \frac{(\mathbf{q} \cdot \mathbf{q}')^2}{(qq')^2}. \tag{1.2.11}$$

These coupled equations can be solved perturbatively in the regime where $\delta \ll 1$ and $\theta \ll 1$. These solutions can be succinctly written as:

$$\delta(\mathbf{k}, z) = \sum_{i=1}^{\infty} a^i(z) \delta^{(i)}(\mathbf{k}) \tag{1.2.12}$$

$$\theta(\mathbf{k}, z) = -\mathcal{H}(z) \sum_{i=1}^{\infty} a^i(z) \theta^{(i)}(\mathbf{k}) \tag{1.2.13}$$

where,

$$\delta^{(i)}(\mathbf{k}) = \prod_{j=1}^{i} \left\{ \frac{d^3 q_j}{(2\pi)^3} \delta^{(1)}(\mathbf{q}_j) \right\} F_i(\mathbf{q}_1 \ldots \mathbf{q}_i) \delta^{(D)}\left(\mathbf{k} - \sum_{n=1}^{i} \mathbf{q}_n \right) \tag{1.2.14}$$

and

$$\theta^{(i)}(\mathbf{k}) = \prod_{j=1}^{i} \left\{ \frac{d^3 q_j}{(2\pi)^3} \delta^{(1)}(\mathbf{q}_j) \right\} G_i(\mathbf{q}_1 \ldots \mathbf{q}_i) \delta^{(D)}\left(\mathbf{k} - \sum_{n=1}^{i} \mathbf{q}_n \right). \tag{1.2.15}$$

Here, F_i and G_i are the coupling kernels, and for third-order perturbation theory, they are given as:

$$F_2(\mathbf{k}_1, \mathbf{k}_2) = \frac{5}{7} \alpha(\mathbf{k}_1, \mathbf{k}_2) + \frac{2}{7} \beta(\mathbf{k}_1, \mathbf{k}_2) \tag{1.2.16}$$

and

10

$$G_2(\mathbf{k}_1, \mathbf{k}_2) = \frac{3}{7}\alpha(\mathbf{k}_1, \mathbf{k}_2) + \frac{4}{7}\beta(\mathbf{k}_1, \mathbf{k}_2) \tag{1.2.17}$$

1.2.2   Non-linear regime

In this sub-section we describe the large scale structure in highly non-linear regime (we refer the reader to [67] which inspires the text of this sub-section). As the matter overdensity continues to evolve, simple perturbative treatment is not suitable to describe the structure formation. In the fully non-linear regime, a sufficiently large overdense patch is able to collapse on itself and relax into a virialized structure called a halo. This collapse is well approximated to first order by a spherical collapse model. In this model, we can calculate the cosmology-dependent overdensity threshold (δ_c) a region has to achieve to form a dark matter halo. Assuming a matter-dominated Universe ($\Omega_m = 1$), this threshold is approximately equal to $\delta_c = 1.69$. These collapsed structures have a density contrast (relative to the critical density, $\rho_{critical}$) that can be well approximated as (Δ_{vir}):

$$\Delta_{vir} = 18\pi^2 + 82(\Omega_m - 1) - 39(\Omega_m - 1)^2. \tag{1.2.18}$$

This density relation is then used to relate the M_{vir} and its corresponding R_{vir} of a halo.

The density distributions of virialized halos have been well studied using the simulations and result in a remarkable consistency in shape, showing very weak

dependence on the size, environment, and cosmology. This profile $(\rho_{\mathrm{m}}(r, M_{\mathrm{vir}}))$ of a halo with mass M_{vir} is in general proportional to :

$$\rho_{\mathrm{m}}(r, M) \propto \frac{1}{x(1+x)^2}, \tag{1.2.19}$$

where $x = r/r_{\mathrm{s}}$ and $r_{\mathrm{s}} = c_{M_{\mathrm{vir}}} R_{\mathrm{vir}}$ with $c_{M_{\mathrm{vir}}}$ being the concentration of the particular halo.

1.3 Large scale structure and its tracers

We don't observe all the components of the Universe but only the light emitted by the baryonic components. Therefore to constrain the properties of dark matter and dark energy, we have to observe their impact on the physics of baryonic matter. There are various tracers of this underlying matter field that are used to that end. In this thesis, we focus on the position of the galaxies, the weak lensing of the shape of the galaxies by the matter, and the pressure of the hot gas in the Universe.

1.3.1 Galaxies

The position of the galaxies naturally traces the total underlying matter field. The text in this sub-section is based on the review article [91]. Since the formation of galaxies occurred significantly later in the evolution of the Universe, the dark matter had already formed deep potential wells in the background. These

deep potential wells slowly collapse to form virialized structure, called halos. Moreover, they also provide a well for baryonic components to fall in and sequentially collapse to form stars, galaxies, etc. The probability of formation of the galaxies is related but is not directly proportional to the depth of the potential well of the background matter field. Galaxy formation happens preferentially at the locations where the density of the background matter field exceeds a certain threshold value. This leads to the phenomena of galaxy biasing.

The perturbation theory framework aims to describe the overdensity of a biased tracer of dark matter, such as galaxies, in terms of matter overdensity. This relationship is encoded in the bias parameters. In this analysis, we typically work on scales larger than the Lagrangian radius of the host halos of our galaxies (denoted by R_*), which is the radius in early Universe Lagrangian space from which the matter accretes inside the halo. On account of this, alongside the fact that the large-scale growth factor is scale-independent, we work under the approximation that the galaxy overdensity, δ_g, can be described as a function of matter density at the same redshift (see [91] for a detailed review).

At large scales and high redshift, the physics of overdensity perturbations is largely linear, and hence galaxy bias is well approximated by a linear relation:

$$\delta_g = b_1 \delta_m \qquad (1.3.1)$$

The gravitational evolution of the dark matter naturally results in non-linear and non-local effects, which become dominant at smaller scales and lower red-

shifts. Assuming homogeneity and isotropy, it can be shown that these non-linear and non-local terms can only be sourced by scalar quantities constructed out of gravitational evolution of matter density (δ_{m}), shear ($\nabla_i \nabla_j \phi$, where ϕ is gravitation potential), and velocity divergences ($\nabla_i v_j$, where v_j is the j-th component of the 3D particle velocity). As described in [60, 207], the expansion of the galaxy overdensity (δ_g) can be re-arranged into independent terms that contribute at different orders:

$$\delta_{\mathrm{g}} \sim f(\delta_{\mathrm{m}}, \nabla_i \nabla_j \Phi, \nabla_i v_j) \sim f^{(1)}(\delta_{\mathrm{m}}) + f^{(2)}(\delta_{\mathrm{m}}^2, s^2)$$

$$+ f^{(3)}(\delta_{\mathrm{m}}^3, \delta_{\mathrm{m}} s^2, \psi, st) + ... \quad (1.3.2)$$

where, f^i are functions that contribute to the total overdensity at i-th order only, and ψ, s and t are scalar quantities constructed out of shear and velocity divergences. Note that these terms are all spatially local, meaning that galaxy overdensity at any Eulerian position is expressed in terms of the matter density evaluated at the same position. Nevertheless, galaxy formation is a non-local process in which matter from nearby areas collapses. As described in [207], the lowest order contribution from this process is captured by the Laplacian of the matter overdensity, $\nabla^2 \delta_{\mathrm{m}}$. We incorporate this term in our theory model as well. The galaxy biasing model is further elucidated in § 1.4.2 and described in detail in Chapter 2 (see § 2.2).

1.3.2 Weak lensing

As the light travels from the background source galaxy towards the foreground lens galaxy, it gets distorted by the lensing effect of the intervening matter field. In this sub-section we describe this effect, drawing heavily on [95]. This lensing effect is broadly divided into three categories, "strong", "weak" and "micro" lensing. The strong lensing effect significantly alters the path of the photon by a large amount of lensing mass (e.g., a massive cluster), and micro-lensing occurs due to small lensing mass (e.g., stars and planets), which leads to a slight change in the brightness of background sources. While both of these types of lensing are relatively rare, weak lensing (WL) occurs for all the sources of the Universe by the total integrated matter in the foreground and hence provides an important tool in studying the distribution of the matter statistically. The weak gravitational lensing leads to small distortions in the shape of the background galaxies, and while this distortion in the shape of the galaxy is not observed at a significant level for any individual galaxy, it is a very powerful probe when analyzed at a statistical level using an ensemble of galaxies ($O(100)$million galaxies).

The WL convergence, κ at the sky location θ, is defined as projected surface mass density relative to the critical surface mass density:

$$\kappa(\theta) = \frac{\Sigma(\theta)}{\Sigma_{\text{critical}}},\tag{1.3.3}$$

where,

$$\Sigma(\theta) = \int \rho_l(D_l\theta, z)dz \tag{1.3.4}$$

$$\Sigma_{\text{critical}} = \frac{c^2}{4\pi G} \frac{D_s}{D_l D_{ls}}. \tag{1.3.5}$$

Here, D_l, D_s and D_{ls} are the distance to lens, source and between lens and source respectively. Moreover, ρ_l is the density of matter around the lens, c is the speed of light and G is the gravitational constant. In order to connect this convergence to gravitation potential, we can define lensing potential as:

$$\Psi(\theta) = \frac{2}{c^2} \frac{D_{ls}}{D_l D_s} \int \Phi(D_l\theta, z)dz, \tag{1.3.6}$$

where, Φ is the Newtonian potential of the lens. We can then describe the lensing convergence based on this potential:

$$\kappa = \frac{1}{2}(\partial_{11}\Psi + \partial_{22}\Psi), \tag{1.3.7}$$

where the partial derivatives are taken with respect to θ, the angular position in the sky. More generally, it is possible to express the full lensing physics using a Jacobian matrix, $\mathcal{A}$ that maps the light distribution in the source plane to the lensed light distribution, $\mathcal{A} = \partial\theta_{\text{source}}/\partial\theta_{\text{lens}}$. This matrix can be expressed as:

$$\mathcal{A} = \begin{pmatrix} 1 - \kappa - \gamma_1 & -\gamma_2 \\ -\gamma_2 & 1 - \kappa + \gamma_1 \end{pmatrix} \tag{1.3.8}$$

where, κ is defined above and the shear ($\gamma = \gamma_1 + i\gamma_2$) can be written in terms of the derivatives of the lensing potential as:

$$\gamma_1 = \frac{1}{2}(\partial_{11}\Psi - \partial_{22}\Psi), \ \gamma_2 = \partial_{12}\Psi. \tag{1.3.9}$$

Writing the convergence field for multiple sources with a redshift distribution of $n_s(z)$:

$$\kappa(\theta) = \int_0^\infty dz W(z) \delta_m(\chi(z)\theta, z) \qquad (1.3.10)$$

where, δ_m is the overdensity of matter, $\chi(z)$ is the comoving distance out to redshift z, and the lensing kernel $W(z)$ captures the strength of lensing due to matter at redshift z and for a flat ΛCDM cosmology can be written as:

$$W(z) = \frac{3}{2}\Omega_m H_0^2 \frac{1+z}{H(z)} \frac{\chi(z)}{c} \int_z^\infty dz_s n_s(z_s) \frac{\chi(z_s) - \chi(z)}{\chi(z_s)}, \qquad (1.3.11)$$

where, Ω_m is the density contrast at redshift $z = 0$, $H(z)$ is the Hubble parameter with H_0 being its present day value. Note that unlike galaxy positions, since κ directly traces the total underlying matter field density, it is an unbiased tracer of LSS.

1.3.3 Baryonic ionized gas

Other than stars, a vast majority of the baryonic component exists in the form of hot ionized gas that populates the dark matter halos discussed in § 1.2.2. In this sub-section, we briefly describe the thermodynamics of this hot gas, drawing heavily on the review article [55]. As mentioned in § 1.1.1, the baryonic component remains coupled to photons until 380,000 years after the big bang, which prevents it from falling into the dark matter wells that form during this period. After recombination, the neutral gas starts to collapse, and some of it turns into first stars, releasing strong electromagnetic radiation and re-ionizing most of the

baryons that exist in the Universe. Furthermore, as the gas falls into deep potential wells of dark matter halos, it gets gravitationally shock heated, becomes extremely energetic, and reaches temperatures in the range of $\sim 10^8 \mathrm{K}$. Therefore, these hot gas halos are powerful sources of X-ray emission.

Assuming that the dynamics of the gas are controlled by gravity (mostly true for massive halos), it is possible to derive the expected value of its thermodynamic properties, which can be compared with observations. Assuming that the gas reaches its thermal virial equilibrium, its average kinetic (E_{KE}) and potential energy (E_{PE}) are related as $-2\langle E_{\mathrm{KE}}\rangle = \langle E_{\mathrm{PE}}\rangle$. This can be written explicitly as:

$$\frac{3}{2}k_{\mathrm{B}}T_{\mathrm{vir}} = \frac{\mu m_p G M_{\mathrm{vir}}}{2R_{\mathrm{vir}}}, \tag{1.3.12}$$

where, k_{B} is the Boltzmann constant, T_{vir} is the average thermal temperature of the gas in a halo of mass M_{vir}, μ is the mean molecular weight per ion and m_p is the mass of proton. Assuming typical numbers we can get a characteristic electron thermal energy as:

$$\frac{3}{2}k_{\mathrm{B}}T_{\mathrm{vir}} = (0.73\mathrm{keV})\Delta_{\mathrm{virial}}^{1/3}\left(\frac{M_{\mathrm{vir}}}{10^{15}M_\odot}\right)\left(\frac{H(z)}{70}\right)^{2/3}. \tag{1.3.13}$$

Note that this can be changed to other definitions of halo masses as well, which is typically common in baryonic property studies.

We can now use this characteristic temperature to also define a characteristic electron pressure, $P_e = n_e k_{\mathrm{B}}T$, where n_e is the characteristic electron number density. We can assume for large systems that baryon fraction is largely same as

18

cosmic baryon fraction ($f_b \equiv \Omega_b/\Omega_m$, where $\Omega_b \sim 5 \times 10^{-2}$ is the fractional energy density in baryons). Hence we can write:

$$n_{e,\mathrm{vir}} = \frac{f_b \Delta_{\mathrm{vir}} \rho_{\mathrm{critical}}(z)}{\mu_e m_p}, \tag{1.3.14}$$

where, μ_e is the mean molecular weight per free electron. After using approximate values of the constants, we can then write the characteristic pressure of gas in halos as:

$$P_{e,\mathrm{vir}} = \frac{f_b}{8\pi} \frac{\mu}{\mu_e} \frac{\Delta_{\mathrm{vir}}^{4/3} H^{8/3}(z)}{(2G)^{1/3}} M_{\mathrm{vir}}^{2/3} \tag{1.3.15}$$

$$= (3.4 \times 10^{-6}\,\mathrm{keV\,cm^{-3}}) \Delta_{\mathrm{vir}}^{4/3} \left(\frac{M_{\mathrm{vir}}}{10^{15} M_\odot}\right)^{2/3} \left(\frac{H(z)}{70}\right)^{8/3}. \tag{1.3.16}$$

Remarkably these characteristic relations agree well with both observations and full hydrodynamical simulations for systems with large masses. However, for small mass systems, the assumptions made in the above calculations, particularly related to the domination of gravity, are violated.

As the galaxies form, several high-energy phenomena occur that can impact the thermodynamics of gas out to large distances. Of particular importance to this thesis are the energetic feedback associated with star formation (supernovae explosions) and accretion of gas onto supermassive black holes, called active galactic nuclei (AGN) feedback. These feedback processes (referred to as baryonic feedback) can provide reheating or redistribution of the hot gas, which can impact the observations of gas thermodynamics. Particularly, the small mass halo systems provide an ideal laboratory to study these feedback processes as

gravitational potentials are less energetically dominant.

A novel way of studying the pressure profile of low-mass halos is via the Sunyaev-Zel'dovich (SZ) effect. As the photons from CMB travel from the surface of the last scattering to us, they can get inverse Compton-scattered. When this scattering happens from the random thermal motion of the hot ionized gas in halos, it is known as the thermal SZ (tSZ) effect. This effect changes the spectral energy distribution of the CMB in a very characteristic way and is observable using multi-frequency observation of the sky in microwave frequencies. The amplitude of this effect is parameterized through the Compton-y parameter:

$$\frac{\Delta I_\nu}{I_{\nu,\text{CMB}}} = y g(\nu), \tag{1.3.17}$$

where, the CMB spectral intensity at any particular frequency ν is changed by ΔI_ν and $g(\nu)$ is the spectral distortion function that can be theoretically calculated. Assuming a non-relativistic population of electrons we have:

$$g(x \equiv h\nu/k_\text{B}T_\text{CMB}) = \frac{x^4 e^x}{(e^x - 1)^2}\left(x\frac{e^x + 1}{e^x - 1} - 4\right). \tag{1.3.18}$$

The Compton-y parameter is related to the integrated pressure along the line-of-sight:

$$y = \frac{\sigma_\text{T}}{m_e c^2}\int P_e dl, \tag{1.3.19}$$

where σ_T is the Thompson scattering cross-section, and m_e is the mass of the electron. Note that the Compton-y parameter is independent of any redshift, and hence its intensity does not decrease with distance. Therefore, tSZ is a uniquely

powerful probe of the distance Universe.

1.4 Multiprobe cosmological analysis

Jointly analyzing all the three probes mentioned above presents an opportunity to test the cosmological and astrophysical model in a range of environmental conditions and time. This is of paramount importance to have a concordance model of astrophysics and cosmology.

1.4.1 2-point correlations

The correlation in the configuration space between overdensities of field A and field B at positions $\mathbf{r}_1$ and $\mathbf{r}_2$ respectively is called 2-point correlation function ($\langle \delta_A(\mathbf{r}_1)\delta_B(\mathbf{r}_2)\rangle$) and under the assumptions of homogeneity and isotropy can be written as $\langle \delta_A(\mathbf{r}_1)\delta_B(\mathbf{r}_2)\rangle = \xi_{AB}(r = |\mathbf{r}_1 - \mathbf{r}_2|)$. In the Fourier space we have $\langle \delta_A(\mathbf{k}_1)\delta_B(\mathbf{k}_2)\rangle = (2\pi)^3 P_{AB}(k)\delta_D(\mathbf{k}_1 + \mathbf{k}_2)$, where $P_{AB}(k)$ is the power spectra between the two fields A and B. We refer the reader to [94] for a detailed description of 2-point statistics which inspires the text in this sub-section.

According to our current best understanding, the initial perturbations were seeded by stochastic quantum fluctuations, which expanded to larger scales via the process of inflation. Since there is no characteristic length in these random fluctuations, the power spectrum of density perturbations is well described by a power-law, $P(k) \propto k^{n_s}$, wherein the model of slow-roll inflation, we expect $n_s \leq 1$.

These initial perturbations go through radiation dominated phase before entering the matter-dominated phase. This radiation-dominated phase imparts additional shape-dependent correction to the initial seed power spectrum as the modes that enter the horizon evolve differently compared to the modes that remain larger than the horizon size. Assuming this effect is captured by a transfer function ($T(k)$), the power spectrum at the beginning of the matter-dominated phase can be written as $P(k) \propto k^{n_s} T^2(k)$. In order to account for the growth of modes with time in the linear theory, we solve the linearized continuity and Euler equation and obtain the growth function (see § 1.2.1.1):

$$D_+(z) = D_{+,0} H(z) \int_z^\infty \frac{dz'(1+z')}{H^3(z')},$$

(1.4.1)

$D_{+,0}$ is a normalization factor to ensure $D_+(z) = 1$ at $z = 0$. Therefore the linear matter power spectrum at is given by $P_{\mathrm{lin}}(k,z) \propto D_+^2(z) k^{n_s} T^2(k)$.

In the linear regime, the correlation between any two tracers is directly proportional to the linear matter power spectrum:

$$P_{AB}(k,z) = b_A b_B P_{\mathrm{lin}}(k,z),$$

(1.4.2)

where b_A and b_B are the effective bias of the tracers A and B. However, this biasing is only valid on very large scales. There are primarily two ways of modeling the small scale correlations, a perturbation theory approach, and a halo model-based approach.

1.4.2 Perturbation theory

An explicit expansion of Eq. 1.3.2 in terms of matter over-density δ_{m} introduces a set of "bare-bias" parameters that are unobservable and can not necessarily be attributed to a physical interpretation. At the power spectrum level, a re-normalization of these "bare-bias" parameters can be performed by combining terms with similar kernels (see [207] for a detailed calculation). After re-normalizing, we can write the tracer-matter cross-spectrum (P_{gm}) and the tracer auto power spectrum (P_{gg}) as:

$$P_{\mathrm{gm}}(k) = b_1 P_{\mathrm{mm}}(k) + \frac{1}{2}b_2 P_{\mathrm{b_1 b_2}}(k) + \frac{1}{2}b_{\mathrm{s}} P_{\mathrm{b_1 s^2}}(k) +$$
$$\frac{1}{2}b_{\mathrm{3nl}} P_{\mathrm{b_1 b_{3nl}}}(k) + b_k k^2 P_{\mathrm{mm}}(k) \quad (1.4.3)$$

$$P_{\mathrm{gg}}(k) = b_1^2 P_{\mathrm{mm}}(k) + b_1 b_2 P_{\mathrm{b_1 b_2}}(k) + b_1 b_{\mathrm{s}} P_{\mathrm{b_1 s^2}}(k) +$$
$$b_1 b_{\mathrm{3nl}} P_{\mathrm{b_1 b_{3nl}}}(k) + \frac{1}{4}b_2^2 P_{\mathrm{b_2 b_2}}(k) + \frac{1}{2}b_2 b_{\mathrm{s}} P_{\mathrm{b_2 s^2}}(k) +$$
$$\frac{1}{4}b_{\mathrm{s}}^2 P_{\mathrm{s^2 s^2}}(k) + 2b_1 b_k k^2 P_{\mathrm{mm}}(k) \quad (1.4.4)$$

where $b_1, b_2, b_{\mathrm{s}}, b_{\mathrm{3nl}}$ and b_{k} are the re-normalized bias parameters.

This five parameter 1-loop perturbation theory model is complete up to third order in its dependence on the matter overdensity and includes the higher-order bias contribution arising from non-local galaxy formation. The power spectrum

$P_{b_1 b_2}(k)$ is generated from the ensemble average of $\langle \delta_m \delta_m^2 \rangle$, $P_{b_1 s^2}(k)$ is generated from $\langle \delta_m s^2 \rangle$ and the kernel $P_{b_1 b_{3nl}}$ is generated from a combination of the ensemble average between δ_m and arguments of $f^{(3)}$ (see Eq. **??**) that contribute at 1-loop level [263]. These terms involve convolution of the linear matter power spectrum with various kernels and we refer the reader to Appendix A of [263] for the form of these kernels. The sum of the higher-order bias terms that are not directly coupled to $P_{mm}(k)$ gives the 1-loop corrections $P_{gg}^{1-loop}(k)$ and $P_{gm}^{1-loop}(k)$. The scale-dependent term including $k^2 P_{mm}(k)$ originates from higher derivative bias. This model is further detailed in Chapter 2 and Chapter 3.

1.4.3 Halo model

The halo model posits that all the matter in the Universe resides inside the virialized structure called halos, as briefly described in § 1.2.2. Then the tracers are supposed to occupy these halos depending upon the halo properties and with a profile constrained by simulations and observations. Then the total correlations between any two fields can be broken down into an intra-halo term (1-halo) and an inter-halo term (2-halo). Therefore, correlating the two tracers A and B in the Fourier space, the total correlation P_{AB} is a sum of 1-halo ($P_{A,B}^{1h}$) and 2-halo ($P_{A,B}^{2h}$) terms:

$$P_{AB} = P_{AB}^{1h} + P_{AB}^{2h}. \tag{1.4.5}$$

The 1-halo term is given by:

$$P_{AB}^{1h}(k,z) = \int_{M_{\min}}^{M_{\max}} dM \frac{dn}{dM} \bar{u}_A(k,M,z)\, \bar{u}_B(k,M,z), \qquad (1.4.6)$$

where dn/dM is the halo mass function, and $\bar{u}^A(k,M,z)$ and $\bar{u}^B(k,M,z)$ are the Fourier-space profiles of observables A and B occupying the halo of mass M at redshift z. The two-halo term is given by

$$P_{AB}^{2h} = b_A(k,z)\, b_B(k,z)\, P_{\rm lin}(k,z), \qquad (1.4.7)$$

where b_A and b_B are effective linear bias parameters describing the clustering of tracers A and B respectively, $P_{\rm lin}(k,z)$ is the linear matter power spectrum. This model will be detailed and extensively used in Chapter 5.

1.5   Outline of thesis

This chapter introduced the broad scope of observational cosmology and major sources of theoretical uncertainties that limit our ability to constrain cosmological and astrophysical models. The rest of the thesis aims at addressing two sources of uncertainties, non-linear galaxy biasing and baryonic feedback:

- In Chapter 2 we detail the galaxy biasing framework using perturbation theory and validate a non-linear model aiming to describe the galaxy and matter correlations in photometric surveys.

- In Chapter 3, we apply this model to the latest date from the DES, obtaining better cosmological constraints.

- In Chapter 4, we describe the correlations between galaxies and the pressure of hot gas in dark matter halos and how that can be used to constrain the average thermal energy of the Universe and its evolution with time.

- Finally, in Chapter 5, we describe the correlations between weak lensing and pressure of hot gas and use them to constrain baryonic feedback.

Chapter 2

Non-linear galaxy biasing:

Validation with simulations

The text in this chapter is based on the published manuscript [231]:

Abstract

We describe perturbation theory (PT) models of galaxy bias for applications to photometric galaxy surveys. We model the galaxy-galaxy and galaxy-matter correlation functions in configuration space and validate against measurements from mock catalogs designed for the Dark Energy Survey (DES). We find that an effective PT model with five galaxy bias parameters provides a good description of the 3D correlation functions above scales of 4 Mpc/h and $z < 1$. Our tests show that at the projected precision of the DES-Year 3 analysis, two of the non-linear bias parameters can be fixed to their co-evolution values, and a third (the k^2 term for higher derivative bias) set to zero. The agreement is typically at the 2 percent level over scales of interest, which is the statistical uncertainty of our simulation measurements. To achieve this level of agreement, our *fiducial* model requires using the full non-linear matter power spectrum (rather than the 1-loop PT one). We also measure the relationship between the non-linear and linear bias parameters and compare them to their expected co-evolution values. We use these tests to motivate the galaxy bias model and scale cuts for the cosmological analysis of the Dark Energy Survey; our conclusions are generally applicable to all photometric surveys.

2.1 Introduction

The structure in the universe at low redshift was seeded by small perturbations in the early universe. Although the evolution of these tiny perturbations is well

described in the linear regime, their non-linear evolution on small scales is an active area of research.

There is a well-formulated framework of non-linear perturbative expansions of these early fluctuations in both Eulerian and Lagrangian space (see [32] and [91] for a review). Major approaches include Standard Perturbation Theory (SPT, [130, 161]), Lagrangian Perturbation Theory (LPT, [43, 203]), Renormalized Perturbation Theory ([76]), Effective Field Theory (EFT, [56, 232, 316]). Although these theories analytically describe the relation between dark matter non-linear density perturbations and linear density perturbations, direct observations exist only for some biased tracers of the underlying dark matter field. These theories have therefore been extended to describe biased tracers like galaxies [53, 65, 122, 139, 203, 204, 207, 269] and applied to data [33, 36, 77, 128, 132, 160, 201, 295].

Another analytical approach for biased tracers is the halo model framework (see [67] for a review). The halo model assumes that all matter is bound in virialized objects (halos) and relates clustering statistics to halos. This framework can be extended to include the observed tracers, for example, via the Halo Occupation Distribution (HOD) ([31, 330]). However, unlike the perturbation theory, the parameterization of the HOD is tracer dependent and cannot be easily generalized [64, 329]. Moreover, the HOD only describes the distribution of galaxies inside halos (known as the 1-halo term). To correctly describe the clustering of galaxies on weakly non-linear scales, between the non-linear 1-halo regime and

the large scale linear regime, would require a combination with perturbative models.

Several studies have tested the perturbation theory (PT) of biased tracers in Fourier space (mostly focused on redshift surveys) [15, 79, 98, 263, 320]. This study focuses on PT in configuration space using Standard Perturbation Theory (SPT) and Effective Field Theory (EFT). We use the 3D correlation functions, ξ_{gg} and ξ_{gm}, constructed from galaxy and matter catalogs built from simulations. One of the key results of our analysis is the minimum length scale for which the correlation functions can be modeled with PT.

The mock catalogs used in this analysis are designed for the Dark Energy Survey (DES). As described in Section 2.3, our focus is on Year 3 (Y3) DES data sets, for which we use the mocks to validate our PT models. This data set constitutes the largest current imaging survey of galaxies, and thus careful testing and validation that matches its statistical power are essential for extracting information in the non-linear regime. We also project the 3D correlations from mocks to the angular correlations (as measured by photometric surveys), but since projection results in loss of information, our 3D tests are more stringent. Since the PT formalism is not tied to any particular tracer, and the scales of interest are well above the 1-halo regime (where differences in galaxy assignment schemes matter), we expect that our conclusions will have broad validity for the lensing and galaxy clustering analyses from imaging surveys.

We also aim to test the accuracy of different variants of perturbation theory for cosmological applications with DES. Although this analysis is at fixed cosmology, we implement fast evaluations of the projected correlations so that they can feasibly be used for cosmological parameter analysis. Finally, we explore the possibility of placing well-motivated priors on some of the PT bias parameters.

This paper is organized as follows. In Sec. 2.2, we review the existing perturbation theory literature and the models used in this study. Sec. 2.3 describes the simulations used for the measurements and Sec. 2.4 the analysis choices. The results are presented in Sec. 2.5, and we conclude in Sec. 2.6.

2.2 Formalism

We summarize in this section the perturbation theory formalism used in our study and the projected two-point statistics relevant for surveys like DES. We are interested in modeling both the matter and galaxy distribution. Different perturbation theory approaches describe the evolved galaxy density fluctuations $\delta_g(\mathbf{x})$ of a biased tracer, g, in terms of the linear matter density fluctuations $\delta_L(\mathbf{x})$. Although formally the relationship between $\delta_g(\mathbf{x})$ and $\delta_L(\mathbf{x})$ is on the full past Lagrangian path of a particle at Eulerian position $\mathbf{x}$, in this analysis we use the approximation that this relationship is instantaneous, meaning $\delta_g(\mathbf{x}, z)$ is related only to $\delta_L(\mathbf{x}, z)$ at any redshift z.

2.2.1   Standard Perturbation Theory

Standard perturbation theory expands the evolved dark matter density field, $\delta_{\mathrm{m}}(\mathbf{x})$ in terms of the extrapolated linear density field, shear field, the divergence of the velocity field and rotational invariants constructed using the gravitational potential. In Fourier space, this expansion can be written as [32]

$$\delta_{\mathrm{m}}(\mathbf{k}) = \sum \frac{1}{n!} \int \frac{d^3 k_1}{(2\pi)^3} \ldots \frac{d^3 k_n}{(2\pi)^3} (2\pi)^3 \delta_{\mathrm{D}}(\mathbf{k}_{1..n} - \mathbf{k})$$

$$F_n(\mathbf{k}_1, .., \mathbf{k}_n) \delta_{\mathrm{L}}(\mathbf{k}_1) \ldots \delta_{\mathrm{L}}(\mathbf{k}_n). \quad (2.2.1)$$

Here $F_n(\mathbf{k}_1, .., \mathbf{k}_n)$ are the mode coupling kernels constructed out of correlations between the scalar quantities mentioned above and δ_{D} is the Dirac delta function. The form of the F_n kernels can be derived by solving the perturbative fluid equations. For example under the assumptions of the spatially flat, cold dark matter model of cosmology, F_2 is well approximated by

$$F_2(\mathbf{k}, \mathbf{k}') = \left[(1 + \alpha) + \mu \left(\frac{k}{k'} + \frac{k'}{k} \right) + (1 - \alpha)\mu^2 \right]. \quad (2.2.2)$$

For $\Omega_{\mathrm{m}} < 1$, $\alpha = \frac{3}{7}(\Omega_{\mathrm{m}})^{-2/63}$ and $\mu = \frac{\mathbf{k} \cdot \mathbf{k}'}{k \cdot k'}$. In this analysis, we use the Einstein de-Sitter limit and assume $\alpha = \frac{3}{7}$.

2.2.1.1 Biased tracers

The overdensity of biased tracers is modeled as the sum of a deterministic function of the dark matter density ($f[\delta_m(\mathbf{x})]$) and a stochastic component ($\varepsilon(\mathbf{x})$) [81, 202, 298]

$$\delta_g(\mathbf{x}) = f[\delta_m(\mathbf{x})] + \varepsilon(\mathbf{x}). \tag{2.2.3}$$

Given the galaxy sample and scales of our interest (which are greater than the lagrangian radius of the host halos of our galaxy sample) in this analysis, we ignore the stochastic contribution and focus on the deterministic relation between the dark matter field and the biased tracer. Assuming a local biasing scheme, this expansion is given as ([130])

$$\delta_g^{\text{local}}(\mathbf{x}) = \sum_{n=1}^{\infty} \frac{b_n}{n!} \delta_m^n(\mathbf{x}). \tag{2.2.4}$$

However, as is well known ([122, 269]), on small scales this local biasing in Eulerian space rapidly breaks down. Assuming isotropy and homogeneity, the bias parameters have to be scalar and hence the density of a tracer can only depend on scalar quantities ([207]). Therefore, non-local terms can only be sourced by scalar quantities constructed out of gravitational evolution of matter density (δ_m), shear ($\nabla_i \nabla_j \Phi$) and velocity divergences ($\nabla_i v_j$). Following the procedure in [60, 99, 207], these contributions can be re-arranged into independent terms

that contribute to the overdensity of galaxies (δ_g) at different orders

$$\delta_g \sim f(\delta_m, \nabla_i \nabla_j \Phi, \nabla_i v_j) \sim f^{(1)}(\delta_m) + f^{(2)}(\delta_m^2, s^2)$$
$$+ f^{(3)}(\delta_m^3, \delta_m s^2, \psi, st) + ... \quad (2.2.5)$$

Here f^i are the functions that contribute to the total overdensity at i-th order only and ψ, s and t are the scalar quantities constructed out of shear and velocity divergences. When expanding the form of these function f^i up to third order, we introduce un-normalized bias factors as given in Eq 9 and Eq 12 of [207]. In Fourier space, the equivalent equation is Eq. (A14) of [263].

2.2.2   Higher derivative bias

In the above section, the non-local terms included in the expansion of galaxy overdensity comes only from shear and velocity divergences. However, those terms are still local in the spatial sense, meaning that the formation of biased tracers only depends on the scalar quantities discussed above at the same position as the tracer. A short-range non-locality due to non-linear effects in halo and galaxy formation within some some scale R, will change Eq. 2.2.3 to: ([207])

$$\delta_g(\mathbf{x}) = f\left[\delta_m(\mathbf{x}')\right], \quad (2.2.6)$$

where, generally $|\mathbf{x} - \mathbf{x}'| < R$ and R is usually of the order of halo radius. Taylor expanding this function we can see that lowest order gradient-type term that can contribute to δ_g is proportional to $\nabla^2 \delta_m$. Hence, we can further generalize our

Eq. 2.2.5 to include this gradient-type term as

$$\delta_g \sim f(\delta_m, \nabla_i \nabla_j \Phi, \nabla_i v_j) \sim f^{(1)}(\delta_m) + f^{(2)}(\delta_m^2, s^2)$$

$$+ f^{(3)}(\delta_m^3, \delta_m s^2, \psi, st) + f^{\text{grad}}(\nabla^2 \delta_m) + \dots \quad (2.2.7)$$

Note that in Fourier space, this term would scale as $k^2 \delta_m(k)$.

2.2.3 Effective Field Theory

Moreover, as discussed in [56], it is theoretically inconsistent to use small scale modes in the integration over Fourier space. So we use effective integrated ultra-violet (UV) terms in the final expansion for the power spectrum. This effective term also enters as a k^2 contribution in the large-scale limit. For example, if we expand the non-linear matter power spectrum in terms of the linear power spectrum ($P_L(k)$) using the PT framework, we have to include this k^2 piece usually written as $c_s^2 k^2 P_L(k)$, where c_s is the effective adiabatic sound speed.

2.2.4 Regularized PT power spectra

Note that the bias parameters that will appear in the expansion of δ_g in Eq. 2.2.7 will be un-observable "bare bias" parameters and need not have the physical meaning usually attributed to the large scale tracer bias (for example, the measurable responses of galaxy statistics to a given fluctuation). We refer the reader to [207] for the details on the renormalization of these "bare bias" parameters by

combining all the parameters with similar power spectrum kernels. After renormalizing, we can write the tracer-matter cross spectrum (P_{gm}) and auto power spectrum of the tracer (P_{gg}) as:

$$P_{\mathrm{gm}}(k) = b_1 P_{\mathrm{mm}}(k) + \frac{1}{2}b_2 P_{\mathrm{b_1 b_2}}(k) + \frac{1}{2}b_{\mathrm{s}} P_{\mathrm{b_1 s^2}}(k) +$$
$$\frac{1}{2}b_{\mathrm{3nl}} P_{\mathrm{b_1 b_{3nl}}}(k) + (b_{\nabla^2 \delta}^{\mathrm{hd}} + c_{\mathrm{s}}^2)k^2 P_{\mathrm{mm}}^{\mathrm{grad}}(k). \quad (2.2.8)$$

$$P_{\mathrm{gg}}(k) = b_1^2 P_{\mathrm{mm}}(k) + b_1 b_2 P_{\mathrm{b_1 b_2}}(k) + b_1 b_{\mathrm{s}} P_{\mathrm{b_1 s^2}}(k) +$$
$$b_1 b_{\mathrm{3nl}} P_{\mathrm{b_1 b_{3nl}}}(k) + \frac{1}{4}b_2^2 P_{\mathrm{b_2 b_2}}(k) + \frac{1}{2}b_2 b_{\mathrm{s}} P_{\mathrm{b_2 s^2}}(k) +$$
$$\frac{1}{4}b_{\mathrm{s}}^2 P_{\mathrm{s^2 s^2}}(k) + b_1 (2b_{\nabla^2 \delta}^{\mathrm{hd}} + c_{\mathrm{s}}^2)k^2 P_{\mathrm{mm}}^{\mathrm{grad}}(k). \quad (2.2.9)$$

Here the bias parameters like b_1, b_2, b_{s} and b_{3nl} are the renormalized bias parameters which are physically observable. The bias parameter $b_{\nabla^2 \delta}^{\mathrm{hd}}$ is the higher-derivative bias parameter and c_{s}^2 is the sound speed term as described by EFT (§2.2.3). As for the kernels, $P_{\mathrm{b_1 b_2}}(k)$ is generated from ensemble average of $\langle \delta_{\mathrm{m}} \delta_{\mathrm{m}}^2 \rangle$, $P_{\mathrm{b_1 s^2}}(k)$ is generated from $\langle \delta_{\mathrm{m}} s^2 \rangle$ and $P_{\mathrm{b_1 b_{3nl}}}$ is generated from a combination of ensemble average between δ_{m} and arguments of $f^{(3)}$ (see Eq. 2.2.7) that contribute at 1-loop level [263]. For the exact form of above kernels, see the Appendix A of [263].

Instead of expanding the Eulerian galaxy overdensity field directly as we have done above, we can also predict the galaxy overdensity by evolving the

Lagrangian galaxy overdensity (see [204] for detailed calculations). These two approaches should evaluate to the same galaxy overdensity at a given loop order [19, 60, 121, 204, 263]. By equating the two approaches and neglecting shear-like terms in the Lagrangian overdensity as they are small for bias values of our interest (see §2.5 and [213]), we get the prediction of the co-evolution value of the renormalized bias parameters: $b_s = (-4/7) \times (b_1 - 1)$ and $b_{3nl} = (b_1 - 1)^1$ [204, 263]. This co-evolution picture naturally describes how gravitational evolution generates the non-local biasing even from the local biased tracers in high redshift Lagrangian frame.

We use different choices of P_{mm} and P_{mm}^{grad} in our analysis. These choices will be detailed in the §2.4.1.

2.2.5 3D statistics to projected statistics

We are interested in the cosmological applications of imaging surveys via projected correlation functions. Projections of the 3D correlation functions ξ_{gg} and ξ_{gm}, to angular coordinates in finite redshift bins give the projected correlations known as $w_{gg}(\theta)$ and $\gamma_t(\theta)$ respectively. We estimate the covariance of these projected statistics for the DES-Y3 like survey. This allows us to estimate the angular scales for which our perturbation theory model is a good description for DES-Y3 like sensitivity.

---

[1]note that our co-evolution value of b_{3nl} differs from [263] as we include their prefactor of 32/315 in our definition of P_{b1b3nl}

2.2.5.1 Galaxy-Galaxy clustering

The angular correlation function $w_{\mathrm{gg}}(\theta)$ is given by the Limber integral

$$w_{\mathrm{gg}}(\theta) = \int_0^\infty d\chi \; \chi^4 \; \phi^2(\chi) \int_{-\infty}^\infty dr_\parallel \; \xi_{\mathrm{gg}}\left(\sqrt{r_\parallel^2 + \chi^2\theta^2}\right), \tag{2.2.10}$$

where χ is the comoving distance and $\phi(\chi)$ is the normalized radial selection function of the lens galaxies, related to the normalized redshift distribution of lens galaxies $(n_{\mathrm{g}}(z))$ as $\phi(\chi) = (1/\chi^2)(dz/d\chi)n_{\mathrm{g}}(z)$.

To simplify the above equation and ones that follow, the inner integral will be denoted by $w_{\mathrm{gg}}^p = \int_{-\infty}^\infty dr_\parallel \; \xi_{\mathrm{gg}}\left(\sqrt{r_\parallel^2 + \chi^2\theta^2}\right)$. A similar equation applies for the galaxy-matter correlation as well. The integral limits for this projection integral are from $-\infty$ to ∞. Though our analysis of survey data is over a finite projection length, as described below in §2.3, our thinnest tomographic bin spans redshift $0.3 < z < 0.45$ – a distance of over 500 Mpc/h. Moreover, as our analysis uses true galaxy redshifts, there is no peculiar velocity effect on projected integrals [311]. Therefore ignoring the finite bin size introduces negligible errors in our correlation function predictions.

Substituting the radial selection function in terms of the galaxy redshift distribution and using the above definition of w^p, the projected galaxy clustering, $w_{\mathrm{gg}}(\theta)$, can be expressed as

$$w_{\mathrm{gg}}(\theta) = \int_0^\infty dz \; \frac{dz}{d\chi} \; n_{\mathrm{g}}^2(z) \; w_{\mathrm{gg}}^p(\chi\theta). \tag{2.2.11}$$

38

2.2.5.2 Galaxy-galaxy lensing

The galaxy-galaxy lensing signal (γ_t) is related to the excess surface mass density ($\Delta\Sigma$) around lens galaxies by

$$\gamma_t(\theta, z_l, z_s) = \frac{\Delta\Sigma(\theta, z_l)}{\Sigma_{crit}(z_l, z_s)}, \tag{2.2.12}$$

where Σ_{crit} is the critical surface mass density given by

$$\Sigma_{crit}(z_l, z_s) = \frac{c^2}{4\pi G} \frac{D_A(z_s)}{D_A(z_l)D_A(z_l, z_s)}. \tag{2.2.13}$$

Here D_A is the angular diameter distance, z_l is the redshift of the lens and z_s is the redshift of the source.

The surface mass density at the projected distance $r_p = \chi\theta$ can be related to the projected galaxy-matter correlation function by

$$\Sigma(r_p, z) = \langle\Sigma\rangle + \rho_m(z)\, w_{gm}^p(r_p, z), \tag{2.2.14}$$

where $\langle\Sigma\rangle$ is the mean surface density

$$\langle\Sigma\rangle = \int_{z_{min}}^{z_{max}} dz\, \frac{d\chi}{dz}\, \rho_m(z), \tag{2.2.15}$$

and $\rho_m(z) = \Omega_{m,0}(1+z)^3 \rho_{crit,0}$ is the mean density of the universe.

Therefore, the excess surface density is

$$\Delta\Sigma(r_p, z) = \rho_m(z)(\bar{w}_{gm}^p(r_p, z) - w_{gm}^p(r_p, z)) \tag{2.2.16}$$

$$= \rho_m(z)\Delta w_{gm}^p(r_p, z) \tag{2.2.17}$$

where, $\bar{w}^p_{\text{gm}}(r_p, z)$ is given as:

$$\bar{w}^p_{\text{gm}}(\chi\theta, z) = \frac{2}{(\chi\theta)^2}\left[\int_0^{\chi\theta} dr_p\ r_p\ w^p_{\text{gm}}(r_p, z)\right]. \qquad (2.2.18)$$

Now combining all the above equations, the galaxy-galaxy lensing signal for lenses at redshift z_l and sources at redshift z_s is

$$\gamma_t(\theta, z_l, z_s) = \frac{\Delta w^p_{\text{gm}}(\chi\theta, z_l)\ \rho_m(z_l)}{\Sigma_{\text{crit}}(z_l, z_s)}. \qquad (2.2.19)$$

Averaging this signal with the redshift distribution of sources $(n_s(z_s))$ would give

$$\gamma_t(\theta, z_l) = \Delta w^p_{\text{gm}}(\chi\theta)\ \rho_m(z)\int_0^\infty dz_s\ n_s(z_s)\ \frac{1}{\Sigma_{\text{crit}}(z_l, z_s)}. \qquad (2.2.20)$$

Finally, averaging this signal with the redshift distribution of lens galaxies $(n_g(z_l))$ gives

$$\gamma_t(\theta) = \int_0^\infty dz_l\ \rho_m(z_l)\ n_g(z_l)\ \Delta w^p_{\text{gm}}(\chi\theta)$$
$$\times \int_0^\infty dz_s\ n_s(z_s)\ \frac{1}{\Sigma_{\text{crit}}(z_l, z_s)}. \qquad (2.2.21)$$

The tangential shear $\gamma_t(\theta)$ is nonlocal and depends on the correlation function at all scales smaller than the transverse distance $\chi\theta$ (Eq. 2.2.18, see [20, 193] for a detailed analysis). Perturbation theory is not adequate for modeling these small scales. We therefore add to γ_t a term representing a point mass contribution: B/θ^2, where B is the average point-mass for a sample of lens and source galaxies and is treated as a free parameter. Any spherically symmetric mass distribution within the minimum scale used is captured by the point mass term,

thus removing our sensitivity to these scales. Our final expression for the galaxy-galaxy lensing signal is

$$\gamma_{\mathrm{t}}(\theta) = \gamma_{\mathrm{t}}^{\text{theory}}(\theta) + \frac{B}{\theta^2},$$

(2.2.22)

with $\gamma_{\mathrm{t}}^{\text{theory}}$ given by Eq. 2.2.21.

2.3 Simulations and mock catalogs

The full DES survey was completed in 2019 and covered ~ 5000 square degrees of the South Galactic Cap. Mounted on the Cerro Tololo Inter-American Observatory (CTIO) 4 m Blanco telescope in Chile, the 570-megapixel Dark Energy Camera [110] images the field in $grizY$ filters. The raw images are processed by the DES Data Management (DESDM) team [215, 276]. The Year 3 (Y3) catalogs of interest for this study span the full footprint of the survey but with fewer exposures (and depth) than the complete survey. About 100 million galaxies have shear and photometric redshift measurements that enable their use for cosmology. For the full details of the data and the galaxy and lensing shear catalogs, we refer the readers to [277] and [280].

We use DES-like mock galaxy catalogs from the MICE simulation suite in this analysis. The MICE Grand Challenge simulation (MICE-GC) is an N-body simulation run in a cube with side-length 3 Gpc/h with 4096^3 particles using the Gadget-2 code [287] with mass resolution of $2.93 \times 10^{10} M_\odot/h$. Halos are identified using a Friend-of-Friends algorithm with linking length 0.2. For further

details about this simulation, see [113]. These halos are then populated with galaxies using a hybrid sub-halo abundance matching plus halo occupation distribution (HOD) approach, as detailed in [57]. These methods are designed to match the joint distributions of luminosity, $g - r$ color, and clustering amplitude observed in SDSS [329]. The construction of the halo and galaxy catalogs is described in [74]. MICE assumes a flat ΛCDM cosmological model with $h = 0.7$, $\Omega_m = 0.25$, $\Omega_b = 0.044$ and $\sigma_8 = 0.8$.

We use two galaxy samples generated from the full MICE galaxy catalog. A DES-like lightcone catalog of redMaGiC galaxies [261] with average photometric errors matching DES Y1 data is generated. We also use another galaxy sample (Maglim hereafter) based on cuts on galaxy magnitude only. This sample is created by imposing a cut on the simulated DES i-band like magnitudes (mag-i) of MICE galaxies [246]. The galaxies in this Maglim sample follow the conditions: mag-i> 17.5 and mag-i< $4z + 18$ where z is the true redshift of the galaxy. This definition results from a sample optimization process when deriving cosmological information from a combined clustering and lensing analysis [246]. Both simulated galaxy samples populate one octant of the sky (ca. 5156 sq. degrees), which is slightly larger than the sky area of DES Y3 data (approximately 4500 sq. degrees, [280]). From these simulations, we measure the non-linear bias parameters at fixed cosmology, which we use as fiducial values for the DES galaxy sample(s).

As detailed in later sections, we divide our galaxy samples into four tomographic bins with edges $[0.3, 0.45, 0.6, 0.75, 0.9]$. These bins are the same as the last four of the five tomographic bins used in the DES Y1 analysis [89, 194]. We do not fit to the first tomographic bin of DES Y1 analysis (which is $0.15 < z < 0.3$) because we are limited by the jackknife covariance estimate (see §2.4.4 and Appendix A.1). These tomographic bins cover a similar redshift range as planned for the DES Y3 analysis. Note that we bin our galaxies used in this analysis using their true spectroscopic redshift. Therefore there is no overlap in the redshift distribution of galaxies between two different bins. After all color, magnitude, and redshift cuts, there are 2.1 million `redMaGiC` galaxies and 2.0 million `MagLim` galaxies (downsampled to have approximately the same number density as `redMaGiC`) used in this analysis. The normalized number densities of two catalogs are shown in Fig. 2.1.

We note that although both the mock catalogs used in this analysis are calibrated with DES Y1 data, we do not expect our tests and conclusions to change with Y3 mock catalog. Since our tests are based on the true redshifts of the galaxies, we are not sensitive to photometric redshift uncertainties, exact tomography choices, and color selection of the galaxies.
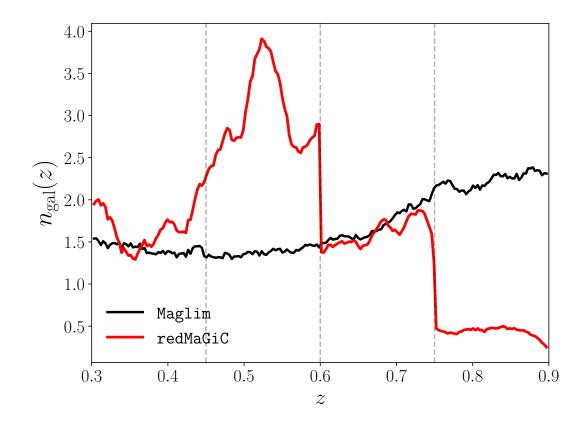
Figure 2.1: Comparison of normalized number density of galaxies corresponding to redMaGiC and Maglim samples. The dashed vertical lines denote the tomographic bin edges.

2.4 Analysis

2.4.1 Data Vector and Models

Our main analysis involves the auto and cross-correlations functions for galaxies and matter: ξ_{mm}, ξ_{gm} and ξ_{gg}. Our focus is on galaxy bias, so we would like to minimize artifacts that are specific to the clustering of matter, in particular sampling effects due to the finite volume of the simulations (see Appendix A.1). Therefore, we fit our theory models to the ratios: $\xi_{\mathrm{gg}}/\xi_{\mathrm{mm}}$ and $\xi_{\mathrm{gm}}/\xi_{\mathrm{mm}}$ so that the galaxy two-point functions are analyzed relative to the matter-matter correlation (see Appendix A.2 and Fig. A.3 for an analysis on correlation functions ξ_{gm} and ξ_{gg} directly). We consider three models to describe these measured ratios:

$$
\begin{aligned}
\mathrm{A} : & \quad \frac{\xi_{\mathrm{gm}}}{\xi_{\mathrm{mm}}} = b_1 \\[2ex]
\mathrm{B} : & \quad \frac{\xi_{\mathrm{gm}}}{\xi_{\mathrm{mm}}} = \frac{\mathcal{F}\left[b_1 P_{\mathrm{mm}}^{1-\mathrm{loop}}(k) + P_{\mathrm{gm}}^{1-\mathrm{Loop}}(k) + k^2 b_{\nabla^2 \delta} P_{\mathrm{lin}}(k)\right]}{\mathcal{F}\left[P_{\mathrm{mm}}^{\mathrm{HF}}(k)\right]} \\[2ex]
\mathrm{C} : & \quad \frac{\xi_{\mathrm{gm}}}{\xi_{\mathrm{mm}}} = \frac{\mathcal{F}\left[b_1 P_{\mathrm{mm}}^{\mathrm{HF}}(k) + P_{\mathrm{gm}}^{1-\mathrm{Loop}}(k) + k^2 b_{\nabla^2 \delta} P_{\mathrm{mm}}^{\mathrm{HF}}(k)\right]}{\mathcal{F}\left[P_{\mathrm{mm}}^{\mathrm{HF}}(k)\right]},
\end{aligned}
\tag{2.4.1}
$$

where, $\mathcal{F}$ denotes the Fourier transform and $P_{\mathrm{gm}}^{1-\mathrm{Loop}}(k)$ is the effective sum of all the terms dependent on b_2, b_{s} and $b_{3\mathrm{nl}}$ in Eq. 2.2.8. An analogous form of this expansion can be derived for $P_{\mathrm{gg}}(k)$. The term $P_{\mathrm{mm}}^{1-\mathrm{Loop}}(k)$ is the 1-Loop PT estimate of the matter-matter correlation function. Model A is the linear bias model and

the numerator in Model B is similar to the model considered by previous analyses using the EFT description of clustering [25, 63, 77, 129, 160, 232, 275]. In this study, we also analyze Model C, which differs from Model B in the use of the full nonlinear matter power spectrum using *halofit* (as opposed to 1-loop PT in Model B) in the numerator. This model is motivated by completely re-summing the matter-matter auto-correlation term to all orders as it uses the fully non-linear fits to simulations such as *halofit* [296]: $P_{\mathrm{mm}}^{\mathrm{NL}} = P_{\mathrm{mm}}^{\mathrm{HF}}$. We make similar a choice for $P_{\mathrm{mm}}^{\mathrm{grad}}(k)$ [18]. The bias term, $b_{\nabla^2\delta}$ is the sum of both the higher-derivative bias term ($b_{\nabla^2\delta}^{\mathrm{hd}}$) and the sound speed term (c_{s}^2) for $P_{\mathrm{gm}}(k)$. The sound speed term is zero in Model C as the fully non-linear matter power spectra include any correction from the UV divergent integrals. Hence in Model C, $b_{\nabla^2\delta} = b_{\nabla^2\delta}^{\mathrm{hd}}$. Unlike Model C, in Model B the sound speed term is not zero, so there we denote $b_{\nabla^2\delta} = b_{\nabla^2\delta}^{\mathrm{hd}} + c_{\mathrm{s}}^2$.

The choice of different power spectra for the three models are given in Table 2.1.

Note that the denominator of Models B and C implicitly assumes that *halofit* is a good description of the matter-matter correlation on the scales we are interested in. We check this assumption using the matter density field from the MICE simulations. The residuals of the matter-matter correlation functions for both *halofit* and EFT are shown in Fig. 2.2. The EFT theory curve is predicted by fitting the measured ξ_{mm} on scales larger than 4 Mpc/h with the model:

Models	P_{mm}	$P_{\mathrm{mm}}^{\mathrm{grad}}$	Remarks
Model A	$P_{\mathrm{mm}}^{\mathrm{HF}}$	0	Linear bias model
Model B	$P_{\mathrm{mm}}^{1-\mathrm{loop}}$	P_{L}	1-Loop EFT model
Model C	$P_{\mathrm{mm}}^{\mathrm{HF}}$	$P_{\mathrm{mm}}^{\mathrm{HF}}$	*Fiducial* model

Table 2.1: Variations in the choice of power spectra elements in the three models considered here. Based on the analysis of the three models, we will used Model C as our *fiducial* model (see §2.5)

$\xi_{\mathrm{mm}} = \mathcal{F}(P_{\mathrm{mm}}^{1-\mathrm{Loop}}(k) + c_{\mathrm{s}}^2 k^2 P_{\mathrm{lin}}(k))$. We can see that EFT shows deviations at the 5% level while *halofit* is a good description of ξ_{mm} over all scales and redshifts – typically within 2% for the bins with percent level error bars on the measurement.

2.4.2 Goodness of fit

To assess the goodness of fit of the models, we use the reduced χ^2. For a good fit to n_{d} number of data-points, using a model with n_{v} free parameters, we expect the χ^2/d.o.f to have a mean of 1 and standard deviation of $\sqrt{2/\mathrm{d.o.f}}$, where d.o.f $= n_{\mathrm{d}} - n_{\mathrm{v}}$ is the total number of degrees of freedom.
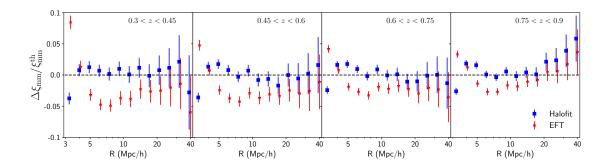
Figure 2.2: Residuals of the matter-matter correlation function for the four tomographic bins (from left to right) when using *halofit* and EFT as the theoretical model. The difference between the model and measurements from the MICE simulations is plotted. *Halofit* performs significantly better on small scales. The reduced χ^2 for *halofit* using the data points above 4Mpc/h (outside of the gray shaded regions) are $0.36, 0.53, 0.49$ and 0.55 for the four tomographic bins respectively. The red and blue points are staggered for clarity.

2.4.3 FAST-PT

The mode coupling kernels that appear in perturbative terms, such as the higher-order bias contributions in Eq. 2.2.8, in Fourier space take the form of convolution integrals. For example in Standard Perturbation Theory, we expand the evolved over-density field of tracers in terms of the linear overdensity, up to third order. This results in terms in the power spectrum that are proportional to $P_{22}(k)$ (given by the ensemble average $\langle \delta^{(2)}\delta^{(2)}\rangle$) and $P_{13}(k)$ (given by $\langle \delta^{(1)}\delta^{(3)}\rangle$). These kernels can be efficiently evaluated using fast Fourier transform techniques pre-

sented in [105, 208, 271], if one transforms these convolution integrals to the prescribed general form. We use the publicly available Python code FAST-PT as detailed in [208] to evaluate all the PT kernels, which is also tested against a C version of the code CFASTPT[2].

2.4.4 Covariance Estimation

We estimate a covariance for the data vector by applying the jackknife method [250, 309] to the simulation split into N_{jk} number of patches. We use the k-means clustering algorithm to get the patches, which roughly divides the octant of sky occupied by our galaxy samples into N_{jk} equal-area patches. We use these same patches for covariance calculation in each of our tomographic bins. The accuracy of the estimated covariance increases with increasing N_{jk} and for scales much smaller than the size of an individual patch [119, 222]. As the total area of the mock catalogs is fixed, changing the number of jackknife patches changes each patch's size.

In order to provide constraints on both non-linear and linear bias parameters, the analysis requires a covariance estimate that correctly captures the auto and cross-correlations between radial bins over both small and large scales to provide constraints on both non-linear and linear bias parameters. We find that we need to limit the analysis to $z > 0.3$ to achieve stable covariance estimates. For this

---

[2]FAST-PT is available at `https://github.com/JoeMcEwen/FAST-PT`, and CFASTPT is available at `https://github.com/xfangcosmo/cfastpt`

reason, we do not analyze the MICE catalog over the first tomographic bin used in the DES-Y1 analysis ($0.15 < z < 0.3$).

We estimate the jackknife covariance using $N_{\text{jk}} = 300$ patches. For the lowest redshift bin ($0.3 < z < 0.45$), this results in an individual jackknife patch with a side length of approximately $100 \text{Mpc}/h$. We determine the maximum scale included in our analysis by varying the number of patches and comparing the estimated errors at different scales. We find the covariance estimate to be stable below $40 \text{ Mpc}/h$ and use this as our maximum scale cut. These tests are detailed in Appendix. A.1.

We explicitly remove the cross-covariance between tomographic bins as there is negligible overlap in the galaxy samples of two different redshift bins, and as length scales of interest are much smaller than the radial extent of the tomographic bins. We correct for biases in the inverse covariance (when calculating the reduced χ^2) due to the finite number of jackknife patches using the procedure described in [136].

Note that Fig. A.2 shows the signal to noise for these 3D statistics for each radial bin for our *fiducial* covariance.

2.5   Results

2.5.1   Measurements

We split the galaxy sample into four tomographic bins, following the DES Year-1 analysis [89]. The redshift ranges for the four bins are: $0.3 < z < 0.45$, $0.45 < z < 0.6$, $0.6 < z < 0.75$ and $0.75 < z < 0.9$.

The auto and cross-correlations measured with the galaxy and matter catalogs in the `MICE` simulations are shown in Fig. 2.3. We use the Landy-Szalay estimator [178] to estimate the correlation functions ξ_{gg}, ξ_{gm} and ξ_{mm} for all the N_{jk} jackknife patches (see §2.4.4). We create a random catalog with 10 times the number of galaxies in each tomographic bin and with number densities corresponding to smoothed galaxy number density. We then use the ratios ξ_{gg}/ξ_{mm} and ξ_{gm}/ξ_{mm} to create our datavector and jackknife covariance. We use the public code Treecorr [162] to measure the cross correlations. We jointly fit these ratios ξ_{gg}/ξ_{mm} and ξ_{gm}/ξ_{mm} with PT models mentioned in §2.4.1, as described next.

2.5.2   Results on fitting the 3D correlation functions

As a first analysis step, we fit the correlation function ratios measured from the simulation with the three models, Model A, B and C (Eq. 2.4.1) described in §2.4.1. Model A only has one free parameter, linear bias b_1, while Model B and
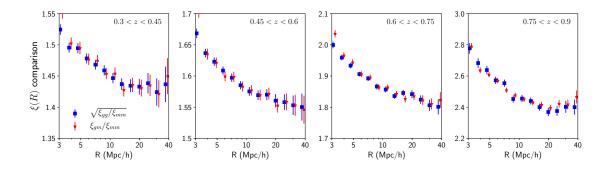
Figure 2.3: Measurements of ratio of the 3D galaxy-matter correlation functions (ξ_{gg}) and the matter-matter auto correlation (ξ_{mm}) for the four tomographic bins of the redMaGiC galaxy sample in MICE simulations. The errorbars are estimated from jackknife covariances. We fit PT models to the ratios ξ_{gg}/ξ_{mm} and ξ_{gm}/ξ_{mm} as shown in subsequent figures.

C in principle have b_1, b_2, b_s, b_{3nl} and $b_{\nabla^2 \delta}$ as free parameters. Here $b_{\nabla^2 \delta}$ is the higher-derivative bias parameter. Among these parameters, by using the equivalence of Lagrangian and Standard Eulerian perturbation theory (see §2.2.4), we can write b_s and b_{3nl} in terms of b_1 as their co-evolution value. Therefore, the simplest complete 1Loop model has b_1, b_2 and $b_{\nabla^2 \delta}$ as free parameters. We fit our measurements while varying the number of free parameters in both Model B and Model C, to find the minimum number of parameters needed to describe the measured correlation function for different scale cuts.

We analyze the MICE data-vector with two different minimum scale cuts: $8\text{Mpc}/h$ and $4\text{Mpc}/h$. In Fig. 2.4, we compare the marginalized constraints on $b_{\nabla^2 \delta}$ for Model B and C for each redshift bin. The marginalized constraints on $b_{\nabla^2 \delta}$ are consistent with zero for Model C, for all redshift bins, and both scale cuts. In contrast, Model B shows significant detection of the $b_{\nabla^2 \delta}$ term. It appears that the EFT term mostly captures the departure of the matter correlation function model from the truth.

Figure 2.5 compares the goodness of fit of different models by showing the reduced χ^2 estimated from the best-fit of various model choices (as given in the x-axis). We find that using Model C with only b_1 and b_2 as free parameters gives a reduced χ^2 consistent with 1 for all redshift bins (with b_s & b_{3nl} fixed to their co-evolution value and $b_{\nabla^2 \delta} = 0$). Hence, we conclude that adding these as free parameters is not needed to model the measurements on the scales considered

here. In what follows, we consider this model choice of using 1Loop PT with free b_1 and b_2 as our *fiducial* model. We also compare our fits to Model A, with free linear bias parameter b_1. The residuals of the observables, i.e., the ratios ξ_{gg}/ξ_{mm} and ξ_{gm}/ξ_{mm}, are shown in Fig. 2.6 for a scale cut of 8Mpc/h, and in Fig. 2.7 for a scale cut of 4Mpc/h. Note that *halofit* describes the matter-matter autocorrelation above scales of 4Mpc/h at about the 2% level (see Fig. 2.2). In these and following figures, we refer to $\xi_{gg}^{\text{model}} = \xi_{gg}/\xi_{mm}$ and $\xi_{gm}^{\text{model}} = \xi_{gm}/\xi_{mm}$. Our *fiducial* model fits the simulations on scales above 4Mpc/h and $z < 1$ within 2%, while the linear bias model performs significantly worse.

We also show the residuals of our fits to the Maglim sample in Fig. 2.7. We find that similar to the redMaGiC sample results, the *fiducial* model describes the measurements within about 2% above scales of 4Mpc/h.

2.5.3 Relations between bias parameters

In this section we revisit the approximation that the non-linear bias parameters b_s and b_{3nl} follow the co-evolution relation. The equivalence of the local Lagrangian and non-local Eulerian description predicts $b_s = -4/7(b_1 - 1)$ and $b_{3nl} = (b_1 - 1)$ (see §2.2.4). We test this assumption by freeing up these parameters in addition to b_1 and b_2 and re-fitting the measurements with these extended models. Figure 2.8 shows the relation between the non-linear bias parameters and b_1 at the two scale cuts and for both redMaGiC and Maglim galaxy samples.
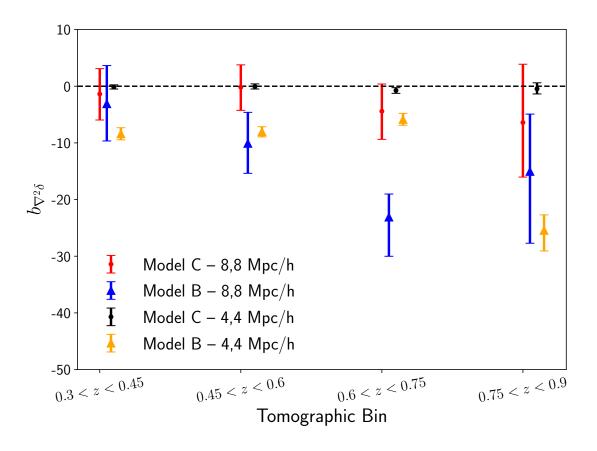
Figure 2.4: The effective field theory parameter ($b_{\nabla^2\delta}$) estimated from two different models, described in Eq. 2.4.1, at two different scale cuts and using the redMaGiC galaxy sample. For example, the red points are the result of a joint analysis of ratios ξ_{gg}/ξ_{mm} and ξ_{gm}/ξ_{mm} (see Fig. 2.3) above 8Mpc/h using Model C with free b_1, b_2 and $b_{\nabla^2\delta}$ parameters for each tomographic bin. We see that when the matter-matter correlation function is described by non-linear *halofit* (Model C), the marginalized EFT terms are consistent with zero for all redshifts and both scale cuts.
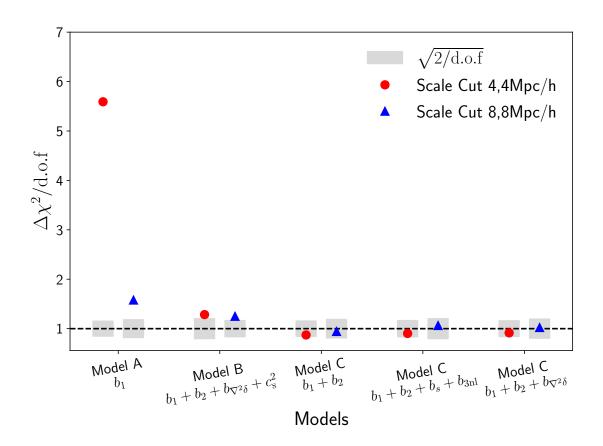
Figure 2.5: The reduced χ^2 for various choices of free parameters in the models described in Eq. 2.4.1, when fitting the 3D measurements of the `redMaGiC` galaxy sample at scale cuts of 8Mpc/h and 4Mpc/h. The gray band denotes the expected error in the reduced χ^2 for a given number of degrees of freedom. We use Model C with two free parameters, b_1 and b_2 as our *fiducial* model (with b_{s} & b_{3nl} fixed to their co-evolution value and $b_{\nabla^2\delta} = 0$).
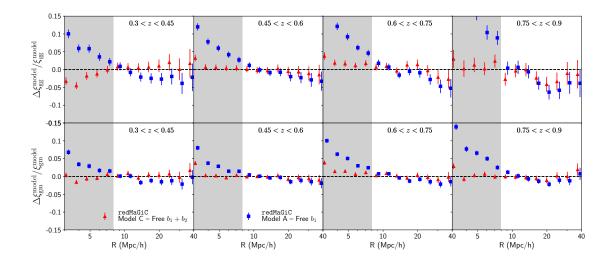
Figure 2.6: Residuals ((data - best-fit)/best-fit) after doing a joint fit to the measurements of 3D statistics in the `redMaGiC` galaxy sample in four tomographic bins shown in Fig.2.3 with Model A (*linear bias model*) and our *fiducial* model, Model C (*1Loop PT* model, with free b_1 & b_2 bias parameter for each bin, b_s & b_{3nl} fixed to the co-evolution value, $b_{\nabla^2\delta} = 0$) and using *halofit* for matter-matter auto-correlation. Panels in the upper row show the residuals for the galaxy-galaxy correlation function, and panels in the lower row show the residuals for galaxy-matter correlation function. Note that we refer to $\xi_{gg}^{model} = \xi_{gg}/\xi_{mm}$ and $\xi_{gm}^{model} = \xi_{gm}/\xi_{mm}$. Model C is an adequate description of the simulation measurements. We use a scale cut of 8Mpc/h here and only fit the data-points outside the grey region.
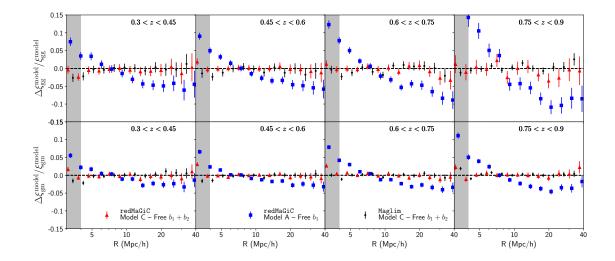
Figure 2.7: Same as Fig.2.6 but analyzed with scale cut of 4Mpc/h. Here we also show the residuals for the Maglim galaxy sample. Model C fits the simulation measurements with these smaller scale cuts for both redMaGiC and Maglim samples.
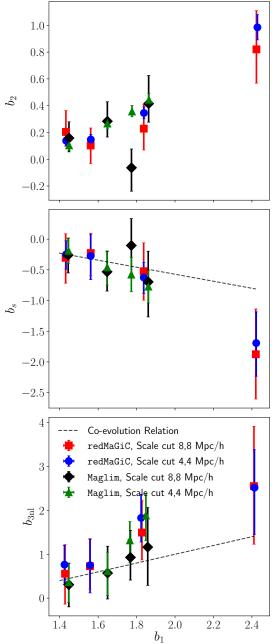
Figure 2.8: The relation between the best-fit non-linear bias parameters and the linear bias parameter b_1 for the four tomographic bin at two different scale cuts. We show the results for both `red-MaGiC` and `Maglim` galaxy samples. The top panel shows second order bias parameter b_2 with b_s and b_{3nl} fixed to their co-evolution Lagrangian values. The middle panel shows b_s (with b_{3nl} fixed to the coevolution Lagrangian value). The bottom panel shows b_{3nl} (with b_s fixed to the coevolution Lagrangian value).

The points in each panel for each scale cut corresponds to the four tomographic bins. The top panel shows the relation between b_1 and b_2 (when the parameters b_s and b_{3nl} are fixed to their co-evolution value), the middle panel shows the relation between b_1 and b_s (when b_{3nl} is fixed to its co-evolution value) and the bottom panel shows the relation between b_1 and b_{3nl} when (b_s is fixed to its co-evolution value). The fits obtained when all the parameters are free have bigger uncertainty but are consistent with the other approaches: the relation between the parameters $b_s - b_1$ and $b_{3nl} - b_1$ are consistent with the expected co-evolution value. We also note that the recovered relation with b_1 is consistent for the two scale cuts, which is a further test that the 1Loop PT is a sufficient and complete model for the scales of interest in this analysis.

It is possible to predict the relation between b_2 and b_1 for our galaxy samples (the measurements are shown in the top panel of Fig. 2.8). However, unlike the $b_s - b_1$ and $b_{3nl} - b1$ relation, predicting $b_2 - b_1$ relation requires knowledge of the HOD of galaxy samples. Since an accurate HOD of the galaxy sample in data is challenging and not yet available for DES, we have treated b_2 as a free parameter. Therefore, only the measurements of the $b_2 - b_1$ relation from simulations are shown in Fig. 2.8.

2.5.4 Inferences for the projected statistics

As described in §2.2.5, we can convert our measurements and fits for the 3D correlation functions to the projected statistics typically used by the imaging surveys. We show such a conversion in Fig. 2.9 for galaxy number densities in MICE simulations corresponding to the redMaGiC galaxies satisfying $0.3 < z_l < 0.45$ and fourth source tomographic bin as used in the DES Y1 analysis. Note that Fig. 2.9 does not show direct measurements of $w(\theta)$ and γ_t, but a transformation of the measured and best-fit datavector to angular statistics. Since our analysis is based on the ratios ξ_{gg}/ξ_{mm} and ξ_{gm}/ξ_{mm}, we first convert our measured datavector and best-fit theory curves to ξ_{gg} and ξ_{gm} and then apply Eq. 2.2.11 and Eq. 2.2.22 to estimate angular correlation functions. We use *halofit* prediction of ξ_{mm}, which is a good fit to the matter-matter autocorrelation for our scales of interest (see Fig. 2.2) to convert the ratios to ξ_{gg} and ξ_{gm}.

The error bars in Fig. 2.9 are calculated from Gaussian covariance[3] as we do not expect significant non-gaussian contribution to the covariance of the angular statistics (see [173]). The covariance is estimated using all the galaxies satisfying the redshift criteria mentioned above in the MICE simulation. Explicitly, we generate this covariance with lens and source galaxies covering 5156.6 square degrees with number densities (per square arc-minutes) of lens galaxies in four

---

[3]We use the COSMOSIS package [334] https://bitbucket.org/joezuntz/cosmosis/wiki/Home

tomographic bins corresponding to 0.039, 0.058, 0.045 and 0.028 respectively. The number density and shape noise of source galaxies is assumed to be the same as DES Y3 [120]. Due to a similar area and number densities, this covariance is comparable to the expected DES Year-3 covariance [120]. Note that the shaded region corresponds to scales below 4Mpc/h, which are not used in the 3D fits. The top panel shows the projected galaxy correlation function, $w(\theta)$ and bottom panel shows galaxy-galaxy lensing signal, $\gamma_t(\theta)$. Note that to estimate γ_t, we fit for the point-mass term as described in §2.2.5. This best-fit value of the point-mass term is obtained by fitting for the coefficient B in Eq. 2.2.22.

Figure 2.9 demonstrates that our model describes the projected angular correlation functions well above scales of 4Mpc/h. The error bars in that figure provide a DES Y3 like benchmark for such an agreement. Note that the fractional statistical uncertainties for projected statistics are much larger than their 3D counterparts. Hence the 3D tests presented in §2.5.2 are substantially more stringent than the projected statistics require.

The analysis of measured $w(\theta)$ and $\gamma_t(\theta)$ is detailed in Appendix A.3.

2.5.5 Comparison with other studies in literature

There have been multiple studies in the literature probing the validity of PT models using simulations [15,79,98,263,320]. Most of these studies have focused on Fourier space rather than configuration space. One reason for this choice
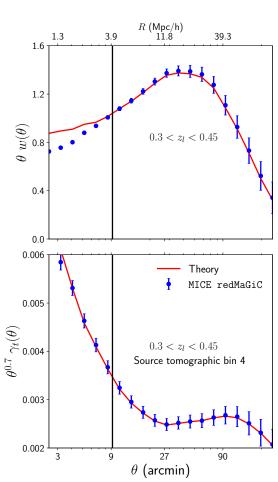
Figure 2.9: The blue error-bars show the projected statistics $w(\theta)$ and $\gamma_t(\theta)$ transformed from 3D measurements of MICE redMaGiC sample (using Eq. 2.2.11 and Eq. 2.2.22). The red theory curve is also estimated similarly from the best-fit to the 3D statistics on scales above 4Mpc/h (see Fig. 2.7). These transformations use the $n(z)$ corresponding to our first lens tomographic bin ($0.3 < z_l < 0.45$) (of the redMaGiC sample) and fourth source redshift bin (see [194]) in the MICE simulation. The shaded region shows the scale cut of 4Mpc/h. The errorbars are estimated using the Gaussian halo model covariance for the best-fit bias values. The theory curve for γ_t includes the contribution from point-mass (See Eq. 2.2.22).

is that non-linear and linear scales are better separated in Fourier space while in configuration space, even large scales receive a contribution from non-linear Fourier modes. However, many cosmic surveys perform their cosmological parameter analysis in configuration space as it is easier to take into account a non-contiguous mask and depth variations. Hence an understanding of the validity of PT models is required in real space to get unbiased cosmology constraints.

The Fourier space studies conducted by [263] and [15] focus only on dark-matter halos and do not aim to reduce the number of free parameters required to explain the auto and cross-correlations between dark matter halos and dark matter particles. [79] and [320] probe this question on the minimum number of bias parameters but again focus on dark matter halos as the biased tracers. Recently [98] have conducted a study similar to ours in Fourier space using three different galaxy samples (mock SDSS and BOSS catalogs) and four halo samples. For a most general case, they find that a four-parameter model (linear, quadratic, cubic non-local bias, and constant shot noise with fixed quadratic tidal bias) can describe correlations between galaxies and matter catalogs, with the inclusion of scale-dependent noise from halo exclusion being particularly beneficial for the combination of auto and cross spectra. They also explore the restriction to a two-parameter model by imposing co-evolution relations, as done in this paper, and find that in general, this reduces the highest Fourier mode for which the model is robust, but it can result in higher constraining power compared to the five

parameter model. However, this particular scenario is not general across samples and requires careful validation with simulations, as done here. The main differences in our study are: we work in configuration space with two different galaxy samples that have a higher number density, cover a wider redshift range, and probe smaller host halo masses. Our galaxy samples also have a significantly larger satellite fraction (for example, the first two `redMaGiC` bins have a $\sim 50\%$ satellite fraction) compared to SDSS and BOSS catalogs.

These crucial differences make our study complementary to the above studies. Ours is especially relevant for imaging surveys as it is tailored to DES. The consistency of our conclusions with [98] suggests that a two-parameter model may have wide applicability, particularly for surveys with different galaxy selections. This would be an extremely useful result and is worth investigating in detail for the next generation of surveys.

2.6 Conclusion

We have presented an analysis of galaxy bias comparing perturbation theory and 3D correlation functions measured from N-body simulation-based mock catalogs. We used an effective PT model to analyze the galaxy-galaxy and galaxy-matter correlations jointly.

Our *fiducial* model successfully describes the measurements from simulations above a scale of 4 Mpc/h, which is significantly lower than the scale cut used in

the DES Year 1 analysis (where a linear bias model was used). In addition to the linear bias parameter b_1, we include four bias parameters in our model: b_2, b_s, b_{3nl} and $b_{\nabla^2\delta}$. We find that treating only the first and second-order bias parameters b_1 and b_2 as free parameters is sufficient to describe the correlation functions over the scales of interest. We find that the constraints on the higher-derivative bias parameter $b_{\nabla^2\delta}$ are consistent with zero in Model C, and we thus fix it to zero in our *fiducial* model. We demonstrate that fixing the parameters b_s and b_{3nl} to their co-evolution value maintains the accuracy of our model. The agreement of our model with measurements from simulations is typically at the 2 percent level over scales of interest. This is within the statistical uncertainty of our simulation measurements and below the requirements of the DES Year 3 analysis.

We show the relationship between the non-linear and linear bias parameters at different redshifts and scale cuts. We find that the relationship between $b_s - b_1$ and $b_{3nl} - b_1$ is consistent with the expectations from the co-evolution relationship. Moreover, we find the relationship between $b_2 - b_1$ is consistent at different scale cuts, which is a useful validation of our model.

We have validated our model with two lens galaxy samples having different and broad host halo mass distribution – the redMaGiC and Maglim samples – that could be used in DES Y3 cosmological analyses, which combine the projected galaxy clustering signal, $w(\theta)$ and the galaxy-galaxy lensing signal, γ_t. Note that these projected statistics have significantly higher (fractional) cosmic variance

66

than their 3D counterparts ξ_{gg} and ξ_{gm}, due to the smaller number of independent modes. Furthermore, the statistical uncertainty of γ_t includes weak lensing shape noise, which is not included in the error budget of its 3D counterpart (ξ_{gm}). Hence, we analyze 3D correlation functions as the measurements from simulations are more precise and provide a percent-level test of our model.

The scales of interest (above $4\,\mathrm{Mpc}/h$) are well above the 1-halo regime, where differences in HOD implementations are greatest. So we expect that our conclusions about bias modeling with PT will have broad validity for the lensing and galaxy clustering analysis from imaging surveys. Nevertheless, at the percent level of accuracy, tests with a variety of schemes for assigning galaxies will be valuable. Moreover, pushing the analysis to higher redshift, or a completely different galaxy selection requires additional testing. We leave these studies for future work.

Chapter 3

Cosmological and galaxy bias constraints with DES Year-3 data

The text in this chapter is based on the submitted manuscript [229]:

S. Pandey, E. Krause, J. DeRose, N. MacCrann, B. Jain, M. Crocce, J. Blazek, A. Choi, H. Huang, C. To, X. Fang, J. Elvin-Poole, J. Prat, A. Porredon, L. F. Secco, M. Rodriguez-Monroy, N. Weaverdyck, Y. Park, M. Raveri, E. Rozo, E. S. Rykoff, G. M. Bernstein, C. Sãnchez, M. Jarvis, M. A. Troxel, G. Zacharegkas, C. Chang, et al. 2021, Submitted to PRD,

Abstract

We constrain cosmological and galaxy-bias parameters using the combination of galaxy clustering and galaxy-galaxy lensing measurements from the Dark Energy Survey Year-3 data. We describe our modeling framework, and choice of scales analyzed, validating their robustness to theoretical uncertainties in small-scale clustering by analyzing simulated data. Using a linear galaxy bias model and redMaGiC galaxy sample, we obtain constraints on the matter density to be $\Omega_m = 0.325^{+0.033}_{-0.034}$. We also implement a non-linear galaxy bias model to probe smaller scales that includes parameterization based on hybrid perturbation theory and find that it leads to a 17% gain in cosmological constraining power. We perform robustness tests of our methodology pipeline and demonstrate the stability of the constraints to changes in the theoretical model. Using the redMaGiC galaxy sample as foreground lens galaxies, we find the galaxy clustering and galaxy-galaxy lensing measurements to exhibit significant signals akin to de-correlation between galaxies and mass on large scales, which is not expected in any current models. This likely systematic measurement error biases our constraints on galaxy bias and the S_8 parameter. We find that a scale-, redshift- and sky-area-independent phenomenological de-correlation parameter can effectively capture the impact of this systematic error. We trace the source of this de-correlation to a color-dependent photometric issue and minimize its impact on our result by changing the selection criteria of redMaGiC galaxies. Using this new sample, our constraints on the S_8 parameter are consistent with previous studies, and we find a small shift in the Ω_m constraints compared to the fidu-

cial `redMaGiC` sample. We constrain the mean host halo mass of the `redMaGiC` galaxies in this new sample to be approximately $1.6 \times 10^{13} M_\odot/h$.

3.1   Introduction

Wide-area imaging surveys of galaxies provide cosmological information through measurements of galaxy clustering and weak gravitational lensing. Galaxies are useful tracers of the full matter distribution, and their spatial clustering is used to infer the matter power spectrum. The shapes of distant galaxies are lensed by the intervening matter, providing a second way to probe the mass distribution. With wide-area galaxy surveys, these two probes of the late time universe have provided information on both the geometry and growth of structure in the universe. In recent years, the combination of two-point correlations— galaxy-galaxy lensing (the cross-correlation of lens galaxy positions with background source galaxy shear) and the angular auto-correlation of the lens galaxy positions—have been developed in a theoretical framework [20, 50, 51, 312, 322] and used to constrain cosmological parameters [52, 72, 96, 177, 199, 214, 284, 323]. In practice, two galaxy samples are used: *lens* galaxies tracing the foreground large scale structure, and background *source* galaxies whose shapes are used to infer the lensing shear and this combination of galaxy-galaxy lensing and galaxy clustering is refereed to as "2×2pt" datavector. This is generally complemented with the two-point of cosmic shear (the lensing shear auto-correlation, referred to as

1×2pt). The Dark Energy Survey (DES) presented cosmological constraints from their Year 1 (Y1) data set from cosmic shear [307] and a joint analysis of all three two-point correlations (henceforth called the "3×2pt" datavector) [2].

This paper is part of a series describing the methodology and results of DES Year 3 (Y3) 3×2pt analysis. The cosmological constraints are presented for cosmic shear [14, 273], the combination of galaxy clustering and galaxy-galaxy lensing using two different lens galaxy samples [?, this paper;]]y3-2x2ptaltlensresults,y3-2x2ptmagnification, as well as the 3×2pt analysis [88]. These cosmological results are enabled by extensive methodology developments at all stages of the analysis from pixels to cosmology, which are referenced throughout. This paper presents the modeling methodology and cosmology inference from DES Y3 galaxy clustering [258] and galaxy-galaxy lensing [247] measurements. We focus on the redMaGiC [261] galaxy sample, described further below. A parallel analysis using a different galaxy sample, the MagLim sample [245], is presented in a separate paper [244].

Incomplete theoretical understanding of the relationship of galaxies to the mass distribution, called galaxy bias, has been a limiting factor in interpreting the lens galaxy auto-correlation function (denoted $w(\theta)$) and galaxy-galaxy lensing (and denoted $\gamma_\mathrm{t}(\theta)$). At large scales, galaxy bias can be described by a single number, the linear bias b_1. On smaller scales, bias is non-local and non-linear, and its description is complicated [122, 269]. Perturbation theory (PT)

approaches have been developed for quasi-linear scales ~ 10 Mpc, though the precise range of scales of its validity is a subtle question that depends on the galaxy population, the theoretical model, and the statistical power of the survey.

With a model for galaxy bias, $w(\theta)$ and γ_t measurements, together called the "$2 \times 2\text{pt}$" datavector, can probe the underlying matter power spectrum. They are also sensitive to the distance-redshift relation over the redshift range of the lens and source galaxy distributions. These two datavectors constitute a useful subset of the full $3 \times 2\text{pt}$ datavector, since bias and cosmological parameters can both be constrained (though the uncertainty in galaxy bias would limit either $w(\theta)$ or $\gamma_t(\theta)$ individually).

A major part of the modeling and validation involves PT models of galaxy bias and tests using mock catalogs based on N-body simulations with various schemes of populating galaxies. Approaches based on the halo occupation distribution (HOD) have been widely developed and are used for the DES galaxy samples. For the Year 3 (Y3) dataset of DES, two independent sets of mock catalogs have been developed, based on the Buzzard [86] and MICE simulations [73, 114, 116].

An interesting recent development in cosmology is a possible disagreement between the inference of the expansion rate and the amplitude of mass fluctuations (denoted σ_8) and direct measurements or the inference of these quantities in the late-time universe. The predictions are anchored via measurements of

the cosmic microwave background (CMB) and use general relativity and a cosmological model of the universe to extrapolate to late times. This cosmological model, denoted by ΛCDM, relies on two ingredients in the energy budget of the universe that have yet to be directly detected: cold dark matter (CDM) and dark energy in the form of a cosmological constant denoted as Λ. The experiments that infer the cosmological constraints using the lensing of source galaxies, particularly using the cosmic-shear 2pt correlation are unable to generally break the degeneracy between Ω_m and σ_8. A derived parameter, $S_8 = \sigma_8 (\Omega_m/0.3)^{0.5}$, is well constrained as it approximately controls the amplitude of the cosmic shear correlation function. The value of S_8 or σ_8 inferred from measurements of cosmic shear and the 3×2pt datavector [2, 14, 88, 141–143, 273, 307], from galaxy clusters [4, 306] and the redshift-space power spectrum [234] tends to be lower than the CMB prediction. The significance of this tension is a work in progress and crucial to the viability of ΛCDM. The Hubble tension refers to the measured expansion rate being higher than predicted by the CMB. The resolution of the two tensions, and their possible relationship, is an active area of research in cosmology and provides additional context for the analysis presented here.

Figure 3.1, based on simulated data, shows the expected constraints on S_8 and Ω_m from the 2×2pt datavector and cosmic shear (1×2pt). It is evident that the two have some complementarity, which enables the breaking of degeneracies in both ΛCDM and wCDM cosmological models (where w is the dark energy equa-

tion of state parameter and $w \neq -1$ points towards the departure from standard ΛCDM model). Particularly noteworthy are the significantly better constraints compared to 1×2pt on the parameter w and Ω_{m} using 2×2pt in the wCDM and ΛCDM models respectively. Note that unlike in 1×2pt, where all the matter in front of source galaxy contributes to its signal, 2×2pt receives contribution only from galaxies within the narrow lens redshift bins. Therefore, we attribute better constraints on these cosmological parameters from 2×2pt to significantly more precise redshifts of the lens galaxy sample. This allows for precise tomographic measurements of 2×2pt datavector which constrains the background geometric parameters like w and Ω_{m}. With data, these somewhat independent avenues to cosmology provide a valuable cross-check, as the leading sources of systematics are largely different.

The formalism used to compute the 2×2pt datavector is presented in §3.2. The description of the lens and source galaxy samples, their redshift distributions and measurement methodology of our datavector and its covariance estimation are presented in §3.3. In §3.4 we validate our methodology using N-body simulations and determine the scale cuts for our analysis. Note that in this paper we focus on validation of analysis when using the `redMaGiC` lens galaxy sample and we refer the reader to [244] for validation of analysis choices for the `Maglim` sample. The results on data are presented in §3.5, and we conclude in §3.6.
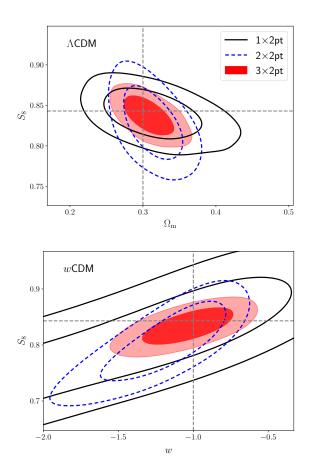
Figure 3.1: Comparison of *simulated* constraints on cosmological parameters Ω_m and S_8 from cosmic shear alone (1×2pt), galaxy clustering + galaxy-galaxy lensing (2×2pt) and including all three probes (3×2pt). This plot uses a *simulated noise-less baseline datavector* (see §3.4.2) and shows that 2×2pt adds complementary information to cosmic shear constraints, particularly, providing stronger constraints on Ω_m and w.

3.2 Theoretical model

3.2.1 Two-point correlations

Here we describe the hybrid perturbation theory (PT) model used to make theoretical predictions for the two-point statistics $w(\theta)$ and $\gamma_t(\theta)$.

3.2.1.1 Power spectrum

To compute the two-point projected statistics $w(\theta)$ and $\gamma_t(\theta)$, we first describe our methodology of predicting galaxy-galaxy and galaxy-matter power spectra (P_{gg} and P_{gm} respectively). PT provides a framework to describe the distribution of biased tracers of the underlying dark matter field in quasi-linear and linear scales. This framework allows for an order-by-order controlled expansion of the overdensity of biased tracer (here galaxies) in terms of the overdensity of the dark matter field where successively higher-order non-linearities dominate only in successively smaller-scale modes. We will analyze two PT models in this analysis, an hybrid linear bias model (that is complete only at first order) and an hybrid one–loop PT model (that is complete up to third order).

For the linear bias model, we can write the galaxy-matter cross spectrum as $P_{gm}(k) = b_1 P_{mm}$ and auto-power spectrum of the galaxies as $P_{gg}(k) = b_1^2 P_{mm}(k)$. Here b_1 is the linear bias parameter and $P_{mm}(k)$ is the *non-linear* power spectrum of the matter field. We use the non-linear matter power spectrum prediction

from [296] to model $P_{\mathrm{mm}}(k)$ (referred to as HALOFIT hereafter). We use the [35] prescription to model the impact of massive neutrinos in this HALOFIT fitting formula. We refer the reader to [175] for robustness of our results despite the limitations of these modeling choices (c.f. [210] for an alternative modeling scheme).

In the hybrid one–loop PT model used here, P_{gm} and P_{gg} can be expressed as:

$$P_{\mathrm{gm}}(k,z) = b_1 P_{\mathrm{mm}}(k,z) + \frac{1}{2} b_2 P_{b_1 b_2}(k,z) + \frac{1}{2} b_s P_{b_1 s^2}(k,z)$$

$$+ \frac{1}{2} b_{3\mathrm{nl}} P_{b_1 b_{3\mathrm{nl}}}(k,z) + b_k k^2 P_{\mathrm{mm}}(k,z) \tag{3.2.1}$$

$$P_{\mathrm{gg}}(k,z) = b_1^2 P_{\mathrm{mm}}(k,z) + b_1 b_2 P_{b_1 b_2}(k,z) + b_1 b_s P_{b_1 s^2}(k,z) + b_1 b_{3\mathrm{nl}} P_{b_1 b_{3\mathrm{nl}}}(k,z)$$

$$+ \frac{1}{4} b_2^2 P_{b_2 b_2}(k,z) + \frac{1}{2} b_2 b_s P_{b_2 s^2}(k,z) + \frac{1}{4} b_s^2 P_{s^2 s^2}(k,z) + 2 b_1 b_k k^2 P_{\mathrm{mm}}(k,z).$$

$$\tag{3.2.2}$$

Here the parameters b_1, b_2, b_s, $b_{3\mathrm{nl}}$ and b_k are the renormalized bias parameters [207]. The kernels $P_{b_1 b_2}$, $P_{b_1 s^2}$, $P_{b_1 b_{3\mathrm{nl}}}$, $P_{b_2 b_2}$, $P_{b_2 s^2}$ and $P_{s^2 s^2}$ are described in [263] and are calculable from the linear matter power spectrum. We validated this model in [231] using 3D correlation functions, ξ_{gg} and ξ_{gm}, of redMaGiC galaxies measured in DES-like MICE simulations [73, 114, 116]. These configuration space statistics are the Fourier transforms of the power spectra mentioned above. We found this model to describe the high signal-to-noise 3D measurements on the simulations above scales of 4 Mpc/h and redshift $z < 1$ with a reduced χ^2 consistent with one. Our tests also showed that at the projected precision of this analysis, two of the nonlinear bias parameters (b_s and $b_{3\mathrm{nl}}$) can be

fixed to their co-evolution values given by $b_s = (-4/7)(b_1 - 1)$ and $b_{3nl} = (b_1 - 1)$; while b_k can be fixed to zero. We will use this result as our *fiducial* modeling choice for the one–loop PT model.

3.2.1.2 Angular correlations

In order to calculate our observables $w(\theta)$ and $\gamma_t(\theta)$, we project the 3D power spectra described above to angular space. The projected galaxy clustering and galaxy-galaxy lensing angular power spectra of tomography bins i, j are given by:

$$C_{AB}^{ij}(\ell) = \frac{2}{\pi} \int d\chi_1 W_A^i(\chi_1) \int d\chi_2 W_B^j(\chi_2)$$

$$\int dk \, k^2 \, P_{AB}[k, z(\chi_1), z(\chi_2)] j_\ell(k\chi_1) j_\ell(k\chi_2), \tag{3.2.3}$$

where, $AB = gg$ models galaxy clustering and $AB = g\kappa$, where κ denotes the convergence field, models galaxy-galaxy lensing. Here $W_g^i(\chi) = n_g^i(z(\chi)) dz/d\chi$ is the normalized radial selection function of lens galaxies for tomographic bin i, and W_κ^i is the tomographic lensing efficiency of the source sample

$$W_\kappa^i(\chi) = \frac{3\Omega_m H_0^2}{2} \int_\chi^\infty d\chi' n_s'[z(\chi')] \frac{\chi}{a(\chi)} \frac{\chi' - \chi}{\chi'}, \tag{3.2.4}$$

with $n_{g/s}^i(z)$ the normalized redshift distribution of the lens/source galaxies in tomography bin i. For the galaxy-galaxy lensing observable, we use the Limber approximation [188, 190] which simplifies the Eq. 3.2.3 to

$$C_{g\kappa}^{ij}(\ell) = \int d\chi \frac{W_g^i(\chi) W_\kappa^j(\chi)}{\chi^2} P_{g\kappa}\left[k = \frac{l + 1/2}{\chi}, z(\chi)\right]. \tag{3.2.5}$$

In the absence of other modeling ingredients that are described in the next section, we have $C_{g\kappa}^{ij}(\ell) \equiv C_{gm}^{ij}(\ell)$ (similarly $P_{g\kappa} \equiv P_{gm}$). As described in [108], even at the accuracy beyond this analysis, it is sufficient to use the Limber approximation for the galaxy-galaxy lensing observable, while for galaxy clustering this may cause significant cosmological parameter biases.

To evaluate galaxy clustering statistics using Eq. 3.2.3, we split the predictions into small and large scales. The non-Limber correction is only significant on large scales where non-linear contributions to the matter power spectra as well as galaxy biasing are sub-dominant. Therefore we use the Limber approximation for the small-scale non-linear corrections and use non-Limber corrections strictly on large scales using linear theory. Schematically, i.e., ignoring contributions from redshift-space distortions and lens magnification [175], the galaxy clustering angular power spectrum between tomographic bins i and j is given by:

$$
C_{gg}^{ij}(\ell)
$$

$$
= \int d\chi \, \frac{W_g^i(\chi) W_g^j(\chi)}{\chi^2} \left[P_{gg}\left(\frac{\ell + 0.5}{\chi}, \chi\right) - b_1^i b_1^j P_{lin}\left(\frac{\ell + 0.5}{\chi}, \chi\right) \right]
$$

$$
+ \frac{2}{\pi} \int d\chi_1 \, b_1^i W_g^i(\chi_1) D[z(\chi_1)] \int d\chi_2 \, b_1^j W_g^j(\chi_2) D[z(\chi_2)] \int \frac{dk}{k} k^3 P_{lin}(k, 0) j_\ell(k\chi_1) j_\ell(k\chi_2),
$$

$$(3.2.6)$$

where $D(z(\chi))$ is the growth factor, and P_{lin} is the linear matter power spectrum. The full model of galaxy clustering, including the contributions from other modeling ingredients like redshift-space distortions and lens magnification that we

describe below, is detailed in [108] and [175].

The real-space projected statistics of interest can be obtained from these angular correlations via:

$$w^{ij}(\theta) = \sum \frac{2\ell+1}{4\pi} \overline{P_\ell}[\cos(\theta)] \, C_{gg}^{ij}(\ell) \tag{3.2.7}$$

$$\gamma_t^{ij}(\theta) = \sum \frac{2\ell+1}{4\pi\ell(\ell+1)} \overline{P_\ell^2}[\cos(\theta)] \, C_{g\kappa}^{ij}(\ell) \tag{3.2.8}$$

where $\overline{P_\ell}$ and $\overline{P_\ell^2}$ are bin-averaged Legendre Polynomials (see [118] for exact expressions).

3.2.2 The rest of the model

To describe the statistics measured from data, we have to model various other physical phenomena that contribute to the signal to obtain unbiased inferences. In this section, we describe the leading sources of these modeling systematics. We have also validated in [175] that higher-order corrections do not bias our results.

3.2.2.1 Intrinsic Alignment

Galaxy-galaxy lensing aims to isolate the percent-level coherent shape distortions, or shear, of background source galaxies due to the gravitational potential of foreground lens galaxies. The local environment, however, including the gravitational tidal field, can also impact the intrinsic shapes of source galaxies and contribute to the measured shear signal. This interaction between the source

galaxies and their local environment, generally known as "intrinsic alignments" (IA) is non-random. When there is a non-zero overlap between the source and lens redshift distributions, IA can have a non-zero contribution to the galaxy-galaxy lensing signal. To account for this effect, we model IAs using the "tidal alignment and tidal torquing" (TATT) model [38]. Ignoring higher-order effects, such as lens magnification (see [101, 247]), IA contributes to the galaxy-shear angular power spectra through the correlation of lens density and the E-mode component of intrinsic source shapes: $C_{g\kappa}^{ij}(\ell) \to C_{g\kappa}^{ij}(\ell) + C_{gI_E}^{ij}(\ell)$. The $C_{gI_E}^{ij}(\ell)$ term is detailed in [175], [273], [247], and [38]. Within our implementation of the TATT framework, $C_{gI_E}^{ij}(\ell)$ for all tomographic bin combinations i and j can be expressed using five IA parameters — a_1 and a_2 (normalization of linear and quadratic alignments); α_1 and α_2 (their respective redshift evolution); and b_{ta} (normalization of a density-weighting term) — and the linear lens galaxy bias. Therefore this model captures higher order contributions to the intrinsic alignment of source galaxies as compared to the simpler non-linear linear alignment (NLA) model that was used in the DES Y1 analysis [2, 44, 151, 174]. In principle, there are also contributions at one-loop order in PT involving the non-linear galaxy bias and non-linear IA terms. However, in this analysis, we neglect these terms as we expect them to be subdominant, and they can be largely captured through the free b_{ta} parameter (see [37] for further discussion of these terms).

3.2.2.2 Magnification

All the matter between the observed galaxy and the observer acts as a gravitational lens. Hence, the galaxies get magnified, increasing the size of galaxy images (parameterized by the magnification factor, μ) and increasing their total flux. The galaxy magnification decreases the observed number density due to stretching of the local sky, whereas increasing the total flux results in an increase in number density (as intrinsically fainter galaxies, which are more numerous, can be observed). This changes the galaxy-galaxy angular power spectrum to: $C_{gg}^{ij}(\ell) \rightarrow C_{gg}^{ij}(\ell) + 2C_{\mu g}^{ij}(\ell) + C_{\mu\mu}^{ij}(\ell)$ and the galaxy-shear angular power spectrum to $C_{g\kappa}^{ij}(\ell) \rightarrow C_{g\kappa}^{ij}(\ell) + C_{\mu I_E}^{ij}(\ell) + C_{\mu\kappa}^{ij}(\ell)$. The auto and cross-power spectra with magnification are again given by Eq. 3.2.3. For example, $C_{\mu g}^{ij}(\ell) = 2(\mu^i - 1)C_{g\kappa}^{ij}(\ell)$, where, as described below, we fix μ^i for the five tomographic bins to $[1.31, -0.52, 0.34, 2.25, 1.97]$. We refer the reader to [175] for the detailed description of the equations for each of the power spectra.

The magnification coefficients are computed with the Balrog image simulations [102, 290] in a process described in [101]. Galaxy profiles are drawn from the DES deep fields [137] and injected into real DES images [216]. The full photometry pipeline [278] and redMaGiC sample selection are applied to the new images to produce a simulated redMaGiC sample with the same selection effects as the real data. To compute the impact of magnification, the process is repeated, this time applying a constant magnification to each injected galaxy. The mag-

nification coefficients are then derived from the fractional increase in number density when magnification is applied. This method captures both the impact of magnification on the galaxy magnitudes and the galaxy sizes, including all numerous sample selection effects. A similar procedure is repeated to estimate the magnification coefficients for the `Maglim` sample. We refer the reader to [101] for further details about the impact of magnification on our observable and their constraints from data.

3.2.2.3 Non-locality of galaxy-galaxy lensing

The configuration-space estimate of the galaxy-galaxy lensing signal is a non-local statistic. The galaxy-galaxy lensing signal of source galaxy at redshift z_s by the matter around galaxy at redshift z_l at transverse distance R is related to the mass density of matter around lens galaxy by:

$$\gamma_t(R; z_g, z_s) = \frac{\Delta\Sigma(R; z_g)}{\Sigma_{\text{crit}}(z_g, z_s)}, \tag{3.2.9}$$

where, Σ_{crit} is the critical surface mass density given by :

$$\Sigma_{\text{crit}}(z_g, z_s) = \frac{c^2}{4\pi G} \frac{D_A(z_s)}{D_A(z_g) D_A(z_g, z_s)}. \tag{3.2.10}$$

Here D_A is the angular diameter distance, z_l is the redshift of the lens and z_s is the redshift of the source. In Eq. 3.2.9, $\Delta\Sigma(R; z_g) = \bar{\Sigma}(0, R; z_g) - \Sigma(R; z_g)$ and $\Sigma(R; z_g)$ is the surface mass density at a transverse separation R from the lens and $\bar{\Sigma}(0, R)$ is the average surface mass density within a separation R from that lens.

Through the $\bar{\Sigma}(0, R)$ term, γ_t at any scale R is dependent on the mass distribution at all scales less than R. This makes γ_t highly non-local, and any model that is valid only on large scales above some r_{min} will break down more rapidly than for a more local statistic like $w(\theta)$. However, as the dependence on small scales is through the *mean* surface mass density, the impact of the mass distribution inside r_{min} on $\gamma_t(\theta)$ can be written as:

$$\gamma_t(R; z_g, z_s) = \frac{1}{\Sigma_{crit}(z_g, z_s)} \left[\Delta\Sigma_{model}(z_g) + \frac{B(z_g)}{R^2} \right], \qquad (3.2.11)$$

where $\Delta\Sigma^{model}$ is the prediction from a model (which is given by PT here) that is valid on scales above r_{min} (also see [20]). Here, B is the effective total residual mass below r_{min} and is known as the point mass (PM) parameter. In this analysis we use the thin redshift bin approximation (see Appendix B.1 for details of this validation) and hence the average γ_t signal between lens bin i and source bin j can be written as:

$$\gamma_t^{ij} = \gamma_{t,model}^{ij} + G^{ij}/\theta^2, \qquad (3.2.12)$$

where,

$$G^{ij} = B^i \int dz_g \, dz_s \, n_g^i \, n_s^j \, \Sigma_{crit}^{-1}(z_g, z_s) \, \chi^{-2}(z_g) \equiv B^i \, \beta^{ij}. \qquad (3.2.13)$$

Here B^i is the PM for lens bin i, n_g^i is the redshift distribution of lens galaxies for tomographic bin i, n_s^j is the redshift distribution of source galaxies for tomographic bin j.

However, instead of directly sampling over the parameters B^i for each tomographic bin, we implement an analytic marginalization scheme as described in [193]. We modify our inverse-covariance when calculating the likelihood as described in §3.3.4.2.

3.3 Data description

3.3.1 DES Y3

The full DES survey was completed in 2019 using the Cerro Tololo Inter-American Observatory (CTIO) 4-m Blanco telescope in Chile and covered approximately 5000 square degrees of the South Galactic Cap. This 570-megapixel Dark Energy Camera [110] images the field in five broadband filters, *grizY*, which span the wavelength range from approximately 400nm to 1060nm. The raw images are processed by the DES Data Management team [215, 276] and after a detailed object selection criteria on the first three years of imaging data (detailed in [2]), the Y3 GOLD data set containing 400 million sources is constructed (single-epoch and coadd images are available[1] as Data Release 1). We further process this GOLD data set to obtain the lens and source catalogs described in the following subsections.

---

[1]https://des.ncsa.illinois.edu/releases/dr1

3.3.1.1 `redMaGiC` lens galaxy sample

The principal lens sample used in this analysis is selected with the `redMaGiC` algorithm [261] run on DES Year 3 data. `redMaGiC` selects Luminous Red Galaxies (LRGs) according to the magnitude-color-redshift relation of red-sequence galaxies, calibrated using an overlapping spectroscopic sample. This procedure is based on selecting galaxies above a threshold luminosity that fit (using χ^2_{RM} as goodness-of-fit criteria) this `redMaGiC` template of magnitude-color-redshift relation to a threshold better than $\chi^2_{\mathrm{RM}} < \chi^2_{\mathrm{max}}$. The value of χ^2_{max} is chosen such that the sample has a constant co-moving space density and is typically less than 3. The full `redMaGiC` algorithm is described in [261], and after application of this algorithm to DES Y3 data, we have approximately 2.6 million galaxies.

[258] found that the `redMaGiC` number density fluctuates with several observational properties of the survey, which imprints a non-cosmological bias into the galaxy clustering. To account for this we assign a weight to each galaxy, which corresponds to the inverse of the angular selection function at that galaxy's location. The computation and validation of these weights are described in [258].

3.3.1.2 `Maglim` lens galaxy sample

DES cosmological constraints are also derived using a second lens sample, `Maglim`, selected by applying the criterion $i < 4z + 18$ to the `GOLD` catalog, where z is the photometric redshift estimate given by the Directional Neighbourhood Fitting

(DNF) algorithm [80]. This selection is shown by [245] to be optimal in terms of its 2×2pt cosmological constraints. We additionally apply a lower magnitude cut, $i > 17.5$, to remove contamination from bright objects. The resulting sample has about 10.7 million galaxies.

Similarly to redMaGiC, we correct the impact of observational systematics on the Maglim galaxy clustering by assigning a weight to each galaxy, as described and validated in [258]. This sample is then used in [244] to obtain cosmological constraints from the combination of galaxy clustering and galaxy-galaxy lensing from DES Y3 data. We refer to [244] for a detailed description of the sample and its validation.

3.3.1.3   Source galaxy shape catalog

To estimate the weak lensing shear of the observed source galaxies, we use the METACALIBRATION algorithm [157, 279]. This method estimates the response of a shear estimator to artificially sheared galaxy images and incorporates improvements like better PSF estimation [164], better astrometric methods [278] and inclusion of inverse variance weighting. The details of the method applied to our galaxy sample are presented in [125]. This methodology does not capture the object-blending effects and shear-dependent detection biases and we use image simulations to calibrate this bias as detailed in [195]. The galaxies that pass the selection cuts designed to reduce systematic biases (as detailed in [125]) are

used to make our source sample shape catalog. This catalog consists of approximately 100 million galaxies with effective number density of $n_{\mathrm{eff}} = 5.6$ galaxies per arcmin^2 and an effective shape noise of $\sigma_{\mathrm{e}} = 0.26$.

3.3.2 Buzzard Simulations

The Buzzard simulations are N-body lightcone simulations that have been populated with galaxies using the Addgals algorithm [319], endowing each galaxy with positions, velocities, spectral energy distributions, broad-band photometry, half-light radii and ellipticities. In order to build a lightcone that spans the entire redshift range covered by DES Y3 galaxies, we combine three lightcones constructed from simulations with box sizes of 1.05, 2.6 and $4.0 \, (h^{-3} \, \mathrm{Gpc}^3)$, mass resolutions of 3.3×10^{10}, 1.6×10^{11}, $5.9 \times 10^{11} \, h^{-1} M_{\odot}$, spanning redshift ranges $0.0 < z \leq 0.32$, $0.32 < z \leq 0.84$ and $0.84 < z \leq 2.35$ respectively. Together these produce $10,000$ square degrees of unique lightcone. The lightcones are run with the L-Gadget2 N-body code, a memory optimized version of Gadget2 [288], with initial conditions generated using 2LPTIC at $z = 50$ [75]. From each $10,000$ square degree catalog, we can create two DES Y3 footprints.

The Addgals model uses the relationship, $P(\delta_R | M_r)$, between a local density proxy, δ_R, and absolute magnitude M_r measured from a high-resolution subhalo abundance matching (SHAM) model in order to populate galaxies into these lightcone simulations. The Addgals model reproduces the absolute–magnitude–

dependent clustering of the SHAM. Additionally, we employ a conditional abundance matching (CAM) model, assigning redder SEDs to galaxies that are closer to massive dark matter halos, in a manner that allows us to reproduce the color-dependent clustering measured in the Sloan Digital Sky Survey Main Galaxy Sample (SDSS MGS) [84, 319].

These simulations are ray-traced using the spherical-harmonic transform (SHT) configuration of CALCLENS, where the SHTs are performed on an $N_{side} = 8192$ HEALPIX grid [27]. The lensing distortion tensor is computed at each galaxy position and is used to deflect the galaxy angular positions, apply shear to galaxy intrinsic ellipticities, including effects of reduced shear, and magnify galaxy shapes and photometry. We have conducted convergence tests of this algorithm and found that resolution effects are negligible on the scales used for this analysis [86].

Once the simulations have been ray-traced, we apply DES Y3-specific masking and photometric errors. To mask the simulations, we employ the Y3 footprint mask but do not apply the bad region mask [278], resulting in a footprint with an area of 4143.17 square degrees. Each set of three N-body simulations yields two Y3 footprints that contain 520 square degrees of overlap. In total, we use 18 Buzzard realizations in this analysis.

We apply a photometric error model to simulate wide-field photometric errors in our simulations. To select a lens galaxy sample, we run the redMaGiC

galaxy selection on our simulations using the same configuration as used in the Y3 data, as described in [258]. A weak lensing source selection is applied to the simulations using PSF-convolved sizes and i-band SNR to match the non-tomographic source number density, 5.9 arcmin^{-2}, from the Metacalibration source catalog. This matching was performed using a slightly preliminary version of the Metacalibration catalog, so this number density is slightly different from the final Metacalibration catalog that is used in our DES Y3 analyses. We employ the *fiducial* redshift estimation framework (see §3.3.3.3) to our simulations in order to place galaxies into four source redshift bins with number densities of 1.46 arcmin^{-2} each. Once binned, we match the shape noise of the simulations to that measured in the Metacalibration catalog per tomographic bin, yielding shape noise values of $\sigma_e = [0.247, 0.266, 0.263, 0.314]$.

Two-point functions are measured in the Buzzard simulations using the same pipeline used for the DES Y3 data, where we set Metacalibration responses and inverse variance weights equal to 1 for all galaxies, as these are not assigned in our simulation framework. We have opted to make measurements without shape noise in order to reduce the variance in the simulated analyses using these measurements. Lens galaxy weights are produced in a manner similar to that done in the data and applied to measure our clustering and lensing signals. The clustering and galaxy-galaxy lensing predictions match the DES redMaGiC measurements to $10 - 20\%$ accuracy over most scales and tomographic bins, except

for the first lens bin, which disagrees by 50% in $w(\theta)$. We refer the reader to Fig. 4 in [85] for a more detailed comparison.

3.3.3 Tomography and measurements

In this section we detail the estimation of the photometric redshift distribution of our source galaxy sample and two lens galaxy samples. These three samples are qualitatively different and have different redshift attributes, requiring different redshift calibration methods detailed below.

3.3.3.1 redMaGiC redshift methodology

We split the redMaGiC sample into $N_{z,g} = 5$ tomographic bins, selected on the redMaGiC redshift point estimate quantity ZREDMAGIC. The bin edges used are $z = 0.15, 0.35, 0.50, 0.65, 0.80, 0.90$. The first three bins use a luminosity threshold of $L_{\min} > 0.5 L_*$ and are known as the high-density sample. The last two redshift bins use a luminosity threshold of $L_{\min} > 1.0 L_*$ and are known as the high-luminosity sample. The galaxy number densities (in the units of arcmin^{-2}) for the five tomographic bins are $\langle n_g \rangle = 0.022, 0.038, 0.059, 0.03, 0.025$.

The redshift distributions are computed by stacking four samples from the PDF of each redMaGiC galaxy, allowing for non-Gaussianity of the PDF. We find an average individual redshift uncertainty of $\sigma_z/(1+z) < 0.0126$ in the redshift range used from the variance of these samples. We refer the reader to [261]

for more details on the algorithm of redshift assignment for redMaGiC galaxies and to [59] for more details on the calibration of redshift distribution of the Y3 redMaGiC sample.

3.3.3.2 Maglim redshift methodology

We use DNF [80] for splitting the Maglim sample into tomographic bins and estimating the redshift distributions. DNF uses a training set from a spectroscopic database as reference, and then provides an estimate of the redshift of the object through a nearest-neighbors fit in a hyperplane in color and magnitude space.

We split the Maglim sample into $N_{z,g} = 6$ tomographic bins from $z = 0.2$ and $z = 1.05$, selected using the DNF photometric redshift estimate. The bin edges are $[0.20, 0.40, 0.55, 0.70, 0.85, 0.95, 1.05]$. The galaxy number densities (in the units of arcmin^{-2}) for the six tomographic bins of this sample are $\langle n_g \rangle = 0.15, 0.107, 0.109, 0.146, 0.106, 0.1$. The redshift distributions in each bin are then computed by stacking the DNF PDF estimates of each Maglim galaxy. See [244] for a more comprehensive description and validation of this methodology and [127] for estimation of redshift distributions of this sample using the same methodology as used for source galaxies that is described below.

3.3.3.3 Source redshift methodology

The description of the tomographic bins of source samples and the methodology for calibrating their photometric redshift distributions are summarized in [219].

Overall, the redshift calibration methodology involves the use of self-organizing maps [219], clustering redshifts [124] and shear-ratio [267] information. The Self-Organizing Map Photometric Redshift (SOMPZ) methodology leverages additional photometric bands in the DES deep-field observations [137] and the BALROG simulation software [103] to characterize a mapping between color space and redshifts. This mapping is then used to provide redshift distribution samples in the wide field, after including the uncertainties from sample variance and galaxy flux measurements in a way that is not subject to selection biases. The clustering redshift methodology performs the calibration by analyzing cross-correlations between redMaGiC and spectroscopic data from Baryon Acoustic Oscillation Survey (BOSS) and its extension (eBOSS). Candidate $n_s(z)$ distributions are drawn from the posterior distribution defined by the combination of SOMPZ and clustering-redshift likelihoods. These two approaches provide us the mean redshift distribution of source galaxies and uncertainty in this distribution. The shear-ratio calibration uses the ratios of small-scale galaxy-galaxy lensing data, which are largely independent of the cosmological parameters but help calibrate the uncertainties in the redshift distributions. We include it downstream in our analysis pipeline as an external likelihood, as briefly described in §3.3.3.5 and detailed in [267].

Finally, we split the source catalog into $N_{z,s} = 4$ tomographic bins. The mean redshift distribution of redMaGiC lens galaxies and source galaxies are compared
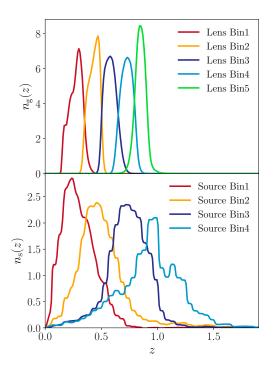
Figure 3.2: Comparison of the normalized redshift distributions of various to-
mographic bins of the source galaxies and `redMaGiC` lens galaxies in the data.

in Fig. 3.2. We refer the reader to [244] for `MagLim` sample redshift distribution.

3.3.3.4   2pt measurements

For galaxy clustering, we use the Landy-Szalay estimator [179] given as:

$$w(\theta) = \frac{DD - 2DR + RR}{RR} \qquad (3.3.1)$$

where DD, DR and RR are normalized weighted number counts of galaxy-galaxy,
galaxy-random and random-random pairs within angular and tomographic bins.
For lens tomographic bins, we measure the auto-correlations in $N_\theta = 20$ log-
spaced angular bins ranging from 2.5 arcmin to 250 arcmin. Each lens galaxy

94

in the catalog (g_i) is weighted with its systematic weight w_{g_i}. This systematic weight aims to remove the large-scale fluctuations due to changing observing conditions at the telescope and Galactic foregrounds. Our catalog of randoms is 40 times larger than the galaxy catalog. The validation of this estimator and systematic weights of the lens galaxies is presented in [258]. In total we have $N_{w(\theta)} = N_{z,g} \times N_\theta = 100$ measured $w(\theta)$ datapoints.

The galaxy-galaxy lensing estimator used in this analysis is given by:

$$\gamma_t(\theta) = \frac{\sum_k w_{r_k}}{\sum_i w_{g_i}} \frac{\sum_{ij} w_{g_i} w_{s_j} e_{t,ij}^{LS}}{\sum_{kj} w_{r_k} w_{s_j}} - \frac{\sum_{kj} w_{r_k} w_{s_j} e_{t,kj}^{RS}}{\sum_{kj} w_{r_k} w_{s_j}} \qquad (3.3.2)$$

where $e_{t,ij}^{LS}$ and $e_{t,kj}^{RS}$ is the measured tangential ellipticity of source galaxy j around lens galaxy i and random point k respectively. The weight w_{g_i} is the systematic weight of lens galaxy as described above, w_{r_k} is the weight of random point that we fix to 1 and w_{s_j} is the weight of the source galaxy that is computed from inverse variance of the shear response weighted ellipticity of the galaxy (see [125] for details). This estimator has been detailed and validated in [285] and [247]. We measure this signal for each pair of lens and source tomographic bins and hence in total we have $N_{\gamma_t(\theta)} = N_{z,g} \times N_{z,s} \times N_\theta = 400$ measured $\gamma_t(\theta)$ datapoints.

We analyze both of these measured statistics jointly and hence we have in total $N_{\text{data}} = N_{w(\theta)} + N_{\gamma_t(\theta)} = 500$ datapoints. Our measured signal to noise (SNR)^2, using `redMaGiC` lens sample, of $w(\theta)$ is 171 [258], of $\gamma_t(\theta)$ is 121 [247]; giving

---

[2] The SNR is calculated as $\sqrt{(\vec{\mathcal{D}} \mathcal{C}^{-1} \vec{\mathcal{D}})}$, where $\vec{\mathcal{D}}$ is the data under consideration and $\mathcal{C}$ is its covariance.

total joint total SNR of 196. In the §3.4, we describe and validate different sets of scale cuts for the linear bias model (angular scales corresponding to (8,6)Mpc/h for $w(\theta), \gamma_t(\theta)$ respectively) and the non-linear bias model ((4,4)Mpc/h). After applying these scale cuts, we obtain the joint SNR, that we analyze for cosmological constraints, as 81 for the linear bias model and 106 for the non-linear bias model.[3]

3.3.3.5 Shear ratios

As will be detailed in §3.4.1.3, in this analysis, we remove the small scales' non-linear information from the 2pt measurements that are presented in the above sub-section. However, as presented in [267], the ratio of $\gamma_t(\theta)$ measurements for the same lens bin but different source bins is well described by our model (see §3.2) even on small scales. Therefore we include these ratios (referred to as shear-ratio henceforth) as an additional independent dataset in our likelihood. In this shear-ratio datavector, we use the angular scales above 2Mpc/h and less than our *fiducial* scale cuts for 2pt measurements described in §3.4.1.3 (we also leave two datapoints between 2pt scale cuts and shear-ratio scale cuts to remove any potential correlations between the two). The details of the analysis choices for shear-ratio measurements and the corresponding covariance matrix are detailed

---

[3]Using a more optimal SNR estimator, SNR=$\frac{(\vec{\mathcal{D}}^{\text{data}}\,\mathcal{C}^{-1}\,\vec{\mathcal{D}}^{\text{model}})}{\sqrt{(\vec{\mathcal{D}}^{\text{model}}\,\mathcal{C}^{-1}\,\vec{\mathcal{D}}^{\text{model}})}}$, where $\vec{\mathcal{D}}^{\text{data}}$ is the measured data and $\vec{\mathcal{D}}^{\text{model}}$ is the bestfit model, we get SNR=79.5 for the linear bias model scale cuts of (8,6)Mpc/h.

in [267] and [88].

3.3.4 Covariance

In this analysis, the covariance between the statistic $w(\theta)$ and $\gamma_t(\theta)$ ($\mathcal{C}$) is modeled as the sum of a Gaussian term ($\mathcal{C}_G$), trispectrum term ($\mathcal{C}_{NG}$) and supersample covariance term ($\mathcal{C}_{SSC}$). The analytic model used to describe ($\mathcal{C}_G$) is described in [118]. The terms $\mathcal{C}_{NG}$ and $\mathcal{C}_{SSC}$ are modeled using a halo model framework as detailed in [171] and [174]. The covariance calculation has been performed using the CosmoCov package [106], and the robustness of this covariance matrix has been tested and detailed in [118]. We also account for two additional sources of uncertainties that are not included in our *fiducial* model using the methodology of analytical marginalization [46] as detailed below.

3.3.4.1 Accounting for LSS systematics

As described in [258], we modify the $w(\theta)$ covariance to analytically marginalize over two sources of uncertainty in the correction of survey systematics: the choice of correction method, and the bias of the *fiducial* method as measured on simulations.

These systematics are modelled as

$$w'(\theta) = w(\theta) + A_1 \Delta w_{\text{method}}(\theta) + A_2 w_{\text{r.s.bias}}(\theta), \qquad (3.3.3)$$

where $\Delta w_{\text{method}}(\theta)$ is the difference between two systematics correction meth-

ods: Iterative Systematic Decontamination (ISD) and Elastic Net (ENET), and $w_{\rm r.\,s.\,bias}(\theta)$ is the residual systematic bias measured on Log-normal mocks. Both terms are presented in detail in [258]. Also note that here A_1 and A_2 are arbitrary amplitudes.

We analytically marginalise over these terms assuming a unit Gaussian as the prior on the amplitudes A_1 and A_2. The measured difference is a 1σ deviation from the prior center. The final additional covariance term to be added to the *fiducial* covariance is:

$$\Delta\mathcal{C} = \Delta\mathbf{w}_{\rm method}\Delta\mathbf{w}_{\rm method}{}^T + \mathbf{w}_{\rm r.\,s.\,bias}\mathbf{w}_{\rm r.\,s.\,bias}{}^T. \tag{3.3.4}$$

The systematic contribution to each tomographic bin is treated as independent so the covariance between lens bins is not modified.

3.3.4.2 Point mass analytic marginalization

As mentioned in §3.2.2.3, we modify the inverse covariance to perform analytic marginalization over the PM parameters. As detailed in [193], using the generalization of the Sherman-Morrison formula, this procedure changes our *fiducial* inverse-covariance $\mathcal{C}^{-1}$ to $\mathcal{C}^{-1}_{\rm wPM}$ as follows:

$$\mathcal{C}^{-1}_{\rm wPM} = \mathcal{C}^{-1} - \mathcal{C}^{-1}\mathcal{U}(\mathcal{I} + \mathcal{U}^{\rm T}\mathcal{C}^{-1}\mathcal{U})^{-1}\mathcal{U}^{\rm T}\mathcal{C}^{-1}. \tag{3.3.5}$$

Here $\mathcal{C}^{-1}$ is the inverse of the halo-model covariance as described above, $\mathcal{I}$ is the identity matrix and $\mathcal{U}$ is a $N_{\rm data} \times N_{\rm z,g}$ matrix where the i-th column is given

by $\sigma_{B^i} \vec{t^i}$. Here σ_{B^i} is the standard deviation of the Gaussian prior on point mass parameter B^i and $\vec{t^i}$ is given as:

$$
\left(\vec{t^i}\right)_a = \begin{cases} 0 & \text{if } a\text{-th element does not correspond to } \gamma_t(\theta) \text{ and if lens-redshift of } a\text{-th element} \neq i \\ \\ \\ \beta^{ij}\theta_a^{-2} & \text{otherwise} \end{cases} \tag{3.3.6}
$$

where the expression for β^{ij} is shown in Eq.3.2.13. We evaluate that term at fixed *fiducial* cosmology as given in Table 3.1. In our analysis we put a wide prior on PM parameters B^i by choosing $\sigma_{B^i} = 10000$ which translates to the effective mass residual prior of $10^{17} M_\odot/h$ (see Eq. B.1.1).

3.3.5 Blinding and unblinding procedure

We shield our results from observer bias by randomly shifting our results and datavector at various phases of the analysis [217]. This procedure prevents us from knowing the impact of any particular analysis choice on the inferred cosmological constraints from our data until all analysis choices have been made. This procedure, as well as the decision tree used to unblind, is detailed in [88], which is also employed here. Therefore, all of our cosmology results acquired with fiducial galaxy samples described in this section are achieved using analysis choices that were validated prior to unblinding (see § 3.4). The results ob-

tained by changing analysis choices (and with a different galaxy sample), after unblinding, are confined to § 3.5.7 and § 3.5.8 of the main article, and in the Appendix B.3.

Model	Parameter	Prior	Fiducial
	Cosmology		
	Ω_m	$\mathcal{U}[0.1, 0.9]$	0.3
	$A_s \times 10^{-9}$	$\mathcal{U}[0.5, 5]$	2.19
	Ω_b	$\mathcal{U}[0.03, 0.07]$	0.048
	n_s	$\mathcal{U}[0.87, 1.06]$	0.97
	h	$\mathcal{U}[0.55, 0.91]$	0.69
	$\Omega_\nu h^2 \times 10^{-4}$	$\mathcal{U}[6.0, 64.4]$	8.3
	Intrinsic Alignment		
	a_1	$\mathcal{U}[-5.0, 5.0]$	0.7
	a_2	$\mathcal{U}[-5.0, 5.0]$	-1.36
	α_1	$\mathcal{U}[-5.0, 5.0]$	-1.7
	α_2	$\mathcal{U}[-5.0, 5.0]$	-2.5
Common Parameters	b_ta	$\mathcal{U}[0.0, 2.0]$	1.0
	Lens photo-z		
	Δz_g^1	$\mathcal{G}[0.006, 0.004]$	0.0
	Δz_g^2	$\mathcal{G}[0.001, 0.003]$	0.0
	Δz_g^3	$\mathcal{G}[0.004, 0.003]$	0.0
	Δz_g^4	$\mathcal{G}[-0.002, 0.005]$	0.0
	Δz_g^5	$\mathcal{G}[-0.007, 0.01]$	0.0
	σz_g^5	$\mathcal{G}[1.23, 0.054]$	1.0

	Shear Calibration		
	m^1	$\mathcal{G}[-0.0063, 0.0091]$	0.0
	m^2	$\mathcal{G}[-0.0198, 0.0078]$	0.0
	m^3	$\mathcal{G}[-0.0241, 0.0076]$	0.0
	m^4	$\mathcal{G}[-0.0369, 0.0076]$	0.0
	Source photo-z		
	Δz_s^1	$\mathcal{G}[0.0, 0.018]$	0.0
	Δz_s^2	$\mathcal{G}[0.0, 0.015]$	0.0
	Δz_s^3	$\mathcal{G}[0.0, 0.011]$	0.0
	Δz_s^4	$\mathcal{G}[0.0, 0.017]$	0.0
	Point Mass		
	B_i $i \in [1, 5]$	$\mathcal{G}[0.0, 10^4]$	0.0
	Cosmology		
wCDM	w	$\mathcal{U}[-2, -0.33]$	-1.0
	Galaxy Bias		
Linear Bias	b_1^i $i \in [1, 3]$	$\mathcal{U}[0.8, 3.0]$	1.7
	b_1^i $i \in [4, 5]$	$\mathcal{U}[0.8, 3.0]$	2.0
	Non-Linear Galaxy Bias		
	$b_1^i \sigma_8$ $i \in [1, 3]$	$\mathcal{U}[0.67, 2.52]$	1.42
	$b_1^i \sigma_8$ $i \in [4, 5]$	$\mathcal{U}[0.67, 2.52]$	1.68

$b_2^i \sigma_8^2$ $i \in [1, 3]$	$\mathcal{U}[-3.5, 3.5]$	0.16
$b_2^i \sigma_8^2$ $i \in [4, 5]$	$\mathcal{U}[-3.5, 3.5]$	0.35

Table 3.1: The parameters varied in different models, their prior range used ($\mathcal{U}[X, Y] \equiv$ Uniform prior between X and Y; $\mathcal{G}[\mu, \sigma] \equiv$ Gaussian prior with mean μ and standard-deviation σ) in this analysis and the *fiducial* values used for simulated likelihood tests.

3.4 Validation of parameter inference

We assume the likelihood to be a multivariate Gaussian

$$\ln \mathcal{L}(\vec{\mathcal{D}}|\Theta) = -\frac{1}{2}[\vec{\mathcal{D}} - \vec{\mathcal{T}}(\Theta)]^{\mathrm{T}} \mathcal{C}_{\mathrm{wPM}}^{-1} [\vec{\mathcal{D}} - \vec{\mathcal{T}}(\Theta)]. \tag{3.4.1}$$

Here $\vec{\mathcal{D}}$ is the measured $\gamma_t(\theta)$ and $w(\theta)$ datavector of length N_{data} (if we use all the angular and tomograhic bins), $\vec{\mathcal{T}}$ is the theoretical prediction for these statistics for the parameter values given by Θ, and $\mathcal{C}_{\mathrm{wPM}}^{-1}$ is the inverse covariance matrix of shape $N_{\mathrm{data}} \times N_{\mathrm{data}}$ (including modifications from the PM marginalization term).

For our analysis we use the Polychord sampler with the settings described

in [187]. The samplers probe the posterior ($\mathcal{P}(\Theta|\vec{\mathcal{D}})$) which is given by:

$$\mathcal{P}(\Theta|\vec{\mathcal{D}}) = \frac{\mathcal{L}(\vec{\mathcal{D}}|\Theta)P(\Theta)}{P(\vec{\mathcal{D}})} \qquad (3.4.2)$$

where $P(\Theta)$ are the priors on the parameters of our model, described in §3.4.1.4, and $P(\vec{\mathcal{D}})$ is the evidence of data.

To estimate the constraints on the cosmological parameters, we have to marginalize the posterior over all the rest of the multi-dimensional parameter space. We quote the mean and 1σ variance of the marginalized posteriors when quoting the constraints. However, note that these marginalized constraints can be biased if the posterior has significant non-Gaussianities, particularly in the case of broad priors assigned to poorly constrained parameters. The maximum-a-posteriori (MAP) point is not affected by such "projection effects"; therefore, we also show the MAP value in our plots. However, we note that in high-dimensional parameter space with a non-trivial structure, it is difficult to converge on a global maximum of the whole posterior (also see [165] and citations therein).

3.4.1 Analysis choices

In this subsection, we detail the galaxy bias models that we use, describe the free parameters of our models, and choose priors on those parameters.

3.4.1.1 PT Models

In this analysis, we test two different galaxy bias models:

1. *Linear bias* model: The simplest model to describe the overdensity of galaxies, valid at large scales, assumes it to be linearly biased with respect to the dark matter overdensity (see §3.2.1.1). In this model, for each lens tomographic bin j, the average bias of galaxies is given by a constant free parameter b_1^j.

2. *Non-linear bias* model: To describe the clustering of galaxies at smaller scales robustly, we also implement a one–loop PT model. As described in §3.2.1.1, in general, this model has five free bias parameters for each lens tomographic bin. For each tomographic bin j, we fix two of the non-linear parameters to their co-evolution value given by: $b_s^j = (-4/7)(b_1^j - 1)$ and $b_{3nl}^j = b_1^j - 1$ [207, 263], while set $b_k^j = 0$ [231]. Therefore, in our implementation, we have two free parameters for each tomographic bin: linear bias b_1^j and non-linear bias b_2^j. This allows us to probe smaller scales with minimal extra degrees of freedom, obtaining tighter constraints on the cosmological parameters while keeping the biases due to projection effects, as described below, in control.

As we describe below, in order to test the robustness of our model, we analyze the bias in the marginalized constraints on cosmological parameters. However, given asymmetric non-Gaussian degeneracies between the parameters of the model (particularly between cosmological parameters and poorly constrained non-linear bias parameters b_2^j and intrinsic alignment

parameters), the marginalized constraints show projection effects. We find that imposing priors on the non-linear bias model parameters in combination with σ_8, as $b_1^j \sigma_8$ and $b_2^j \sigma_8^2$ removes much of the posterior projection effect. As detailed later, these parameters are sampled with flat priors. We emphasize that the flat priors imposed on these non-linear combinations of parameters are non-informative, and our final constraints on b_1^j and b_2^j are significantly tighter than the projection of priors on these parameters.

3.4.1.2 Cosmological Models

We report the constraints on two choices of the cosmological model:

1. Flat ΛCDM : We free six cosmological parameters the total matter density Ω_m, the baryonic density Ω_b, the spectral index n_s, the Hubble parameter h, the amplitude of scalar perturbations A_s and $\Omega_\nu h^2$ (where Ω_ν is the massive neutrino density). We assume a a flat cosmological model, and hence the dark energy density, Ω_Λ, is fixed to be $\Omega_\Lambda = 1 - \Omega_m$.

2. Flat wCDM: In addition to the six parameters listed above, we also free the dark energy equation of state parameter w. Note that this parameter is constant in time and $w = -1$ corresponds to ΛCDM cosmological model.

3.4.1.3 Scale cuts

The complex astrophysics of galaxy formation, evolution, and baryonic processes like feedback from active galactic nuclei (AGN), supernova explosions, and cooling make higher-order non-linear contributions that we do not include in our model. The contribution from these poorly understood effects can exceed our statistical uncertainty on the smallest scales; hence we apply scale cuts chosen so that our PT models give unbiased cosmological constraints.

As mentioned earlier, marginalizing over a multi-dimensional parameter space can lead to biased 2D parameter constraints due to projection effects. To calibrate this effect for each of our models, we first perform an analysis using a *baseline* datavector constructed from the *fiducial* values of that model. We then run our MCMC chain on the *contaminated* datavector that includes higher-order non-linearities, and we measure the bias between the peak of the marginalized *baseline* contours and the peak of the marginalized *contaminated* contours.

From a joint analysis of 3D galaxy-galaxy and galaxy-matter correlation functions at fixed cosmology in simulations [231], we find that the *linear bias* model is a good description above 8Mpc/h while the two-parameter *non-linear bias* model describes the correlations above 4Mpc/h. We convert these physical co-moving distances to angular scale cuts for each tomographic bin and treat them as starting guesses. Then for each model, we iterate over scale cuts until we find the minimum scales at which the bias between marginalized *baseline* and *contami-*

nated contours is less than 0.3σ. For the ΛCDM model, we impose this criterion on the $\Omega_{\mathrm{m}} - S_8$ projected plane, and for the wCDM model, we impose this criterion on all three 2D plane combinations constructed out of Ω_{m}, S_8 and w. Further validation of these cuts is performed using simulations in 3.4.3 and [85].

3.4.1.4 Priors and Fiducial values

We use locally non-informative priors on the cosmological parameters to ensure statistically independent constraints on them. Although our constraints on cosmological parameters like the Hubble constant h, spectral index n_{s} and baryon fraction Ω_{b} are modest compared to surveys like *Planck*, we have verified that our choice of wide priors does not bias the inference on our cosmological parameters of interest, Ω_{m} and S_8.

When analyzing the *linear bias* model, we use a wide uniform prior on these linear bias parameters, given by $0.5 < b_1^j < 3$. For the *non-linear bias* model, as mentioned above, we sample the parameters $b_1^j \sigma_8$ and $b_2^j \sigma_8^2$. We use uninformative uniform priors on these parameters for each tomographic bin j given by $0.67 < b_1^j \sigma_8 < 3.0$ and $-4.2 < b_2^j \sigma_8^2 < 4.2$. At each point in the parameter space, we calculate σ_8 and retrieve the bias parameters b_1^j and b_2^j from the sampled parameters to get the prediction from the theory model. The *fiducial* values of the linear bias parameters b_1^j used in our simulated likelihood tests are motivated by the recovered bias values in N-body simulations and are summarized in Table 3.1.

For the non-linear bias parameters, the *fiducial* values of b_2^j are obtained from the interpolated $b_1 - b_2$ relation extracted from 3D tests in MICE simulations (see Fig. 8 of [231]) for the *fiducial* b_1^j for each tomographic bin.

For the intrinsic alignment parameters, we again choose uniform and uninformative priors. As the IA parameters are directly dependent on the source galaxy population, it is challenging to motivate a reasonable choice of prior from other studies. The *fiducial* values of these parameters required for the simulated test are motivated by the Y1 analysis as detailed in [264].

We impose an informative prior for our measurement systematics parameters, lens photo-z shift errors (Δz_g^j), lens photo-z width errors (σz_g^j), source photo-z shift errors (Δz_s^j) and shear calibration biases (m^j) for various tomographic bins i. The photo-z shift parameter changes the redshift distributions for lenses (g) or sources (s) for any tomographic bin j, used in the theory predictions (see §3.2) as $n_{g/s}^j(z) \longrightarrow n_{g/s}^j(z - \Delta z_{g/s}^j)$, while the photo-$z$ width results in $n_g^j(z) \longrightarrow n_g^j(\sigma z_g^j[z - \langle z \rangle^j] + \langle z \rangle^j)$, where $\langle z \rangle^j$ is the mean redshift of the tomographic bin j. Lastly, the shear calibration uncertainity modifies the galaxy-galaxy lensing signal prediction between lens bin i and source bin j as $\gamma_t^{ij} \longrightarrow (1 + m^j)\gamma_t^{ij}$.

For the source photo-z, we refer the reader to [219] for the characterization of source redshift distribution, [124] for reducing the uncertainity in these redshift distribution using cross-correlations with spectroscopic galaxies and [70] for a validation of the shift parameterization using a more complete method based on

sampling the discrete distribution realizations. For the shear calibration biases, we refer the reader to [195] which tests the shape measurement pipeline and determine the shear calibration uncertainity while accounting for effects like blending using state-of-art image simulation suite. For the priors on the lens photo-z shift and lens photo-z width errors, we refer the reader to [59], which cross-correlated the DES lens samples with spectroscopic galaxy samples from Sloan Digital Sky Survey to calibrate the photometric redshifts of lenses (also see [244] and [127] for further details on `Maglim` redshift calibration).

In this paper we fix the magnification coefficients to the best-fit values described in [101, 175], but we refer the reader to [101] for details on the impact of varying the magnification coefficients on the cosmological constraints. Note that in our tests to obtain scale cuts for cosmological analysis using simulated datavectors (described below), we remain conservative and fix the shear systematics to their *fiducial* parameter values and analyze the datavectors at the mean source redshift distribution $n_s(z)$, as shown in Fig. 3.2. This procedure, after fixing the systematic parameters, results in tighter constraints and ensures that the impact of baryons and non-linear bias on the cosmological inference is overestimated. Therefore, we expect our recovered scale cuts to be conservative.
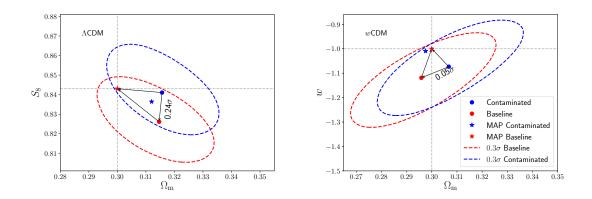
Figure 3.3: Simulated datavector parameter constraints from a datavector contaminated with non-linear bias + baryons but analyzed with a linear bias + HALOFIT model. Dashed grey lines mark the truth values for the simulated datavector. The left panel shows contours for ΛCDM, and the right panel shows wCDM. The scale cuts are (8,6) Mpc/h for $w(\theta)$ and γ_t respectively. In both panels, we compare the peak of the marginalized constraints in the 2D parameter plane for the contaminated datavector (blue circle) and the baseline datavector (red square). The peaks of the marginalized baseline contours are within 0.3σ of the peaks of the marginalized contaminated contours, which is our criterion for acceptable scale cuts. We also show the corresponding maximum posterior value obtained for all the contours (with a star symbol), obtained using the methodology described in the main text.

111

3.4.2 Simulated Likelihood tests

We perform simulated likelihood tests to validate our choices of scale cuts, galaxy bias model and the cosmological model (including priors and external datasets when relevant). In this analysis we focus on determining and validating the scale cuts using `redMaGiC` lens galaxy sample and we refer the reader to [244] for validation using the `Maglim` lens galaxy sample. We require that the choices adopted return unbiased cosmological parameters. This first step based on the tests on noiseless datavectors in the validation is followed by tests on cosmological simulations.

3.4.2.1 Scale cuts for the linear bias model

Our baseline case assumes linear galaxy bias and no baryonic impact on the matter-matter power spectrum. We use the linear bias values for the five lens bins (in order of increasing redshift) $b_1 = 1.7, 1.7, 1.7, 2.0,$ and 2.0. We compare the cosmology constraints from the baseline datavector with a simulated datavector contaminated with contributions from non-linear bias and baryonic physics. For baryons, the non-linear matter power spectra ($P_{\mathrm{mm}}^{\mathrm{cont}}$) used in generating the contaminated datavector is estimated using following prescription:

$$P_{\mathrm{mm}}^{\mathrm{cont}} = \left(\frac{P_{\mathrm{mm}}^{\mathrm{hydro-sim}}}{P_{\mathrm{mm}}^{\mathrm{DM-only}}} \right) P_{\mathrm{mm}}^{\mathrm{HALOFIT}}, \tag{3.4.3}$$

where, $P_{\mathrm{mm}}^{\mathrm{hydro-sim}}$ and $P_{\mathrm{mm}}^{\mathrm{DM-only}}$ are the matter power spectra measured from a full hydrodynamical simulation and dark matter only simulation respectively.
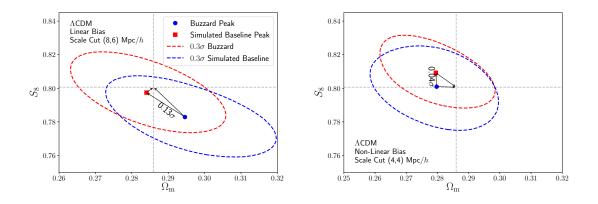
Figure 3.4: The blue contours show constraints from Buzzard simulations (blue contours) compared with Buzzard -like theory datavector (red contours) in the ΛCDM cosmological model. The left (right) panel shows the constraints for linear (non-linear) bias models with the scale cuts given in the legend. The linear and non-linear bias values are extracted from fits to the 3D correlation functions (ξ_{gg} and ξ_{gm}). We see that both the scale-cut choices satisfy our validation criterion.

We use the measurements from the OWLS-AGN simulations, which is based on hydrodynamical simulations that include the effects of supernovae and AGN feedback, metal-dependent radiative cooling, stellar evolution, and kinematic stellar feedback [182] To capture the effect of non-linear bias, we use the *fiducial* b_2^j values as described in the previous section and fix the bias parameters b_s^j and b_{3nl}^j to their co-evolution values.

Fig. 3.3 shows the 0.3σ contours when implementing the angular cuts corre-
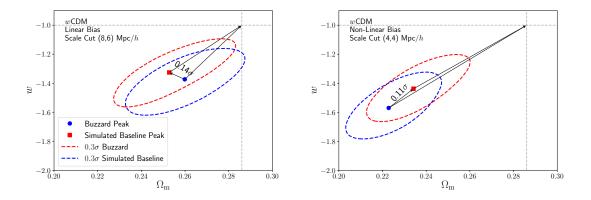
Figure 3.5: Same as Fig. 3.4 but for wCDM cosmology.

sponding to (8,6) Mpc/h for $w(\theta)$ and γ_t. The left panel is for ΛCDM, and the

right panel for wCDM (only the $w - \Omega_m$ plane is shown, but we also verified that

the criterion is satisfied in the $\Omega_m - S_8$ and $S_8 - w$ planes). The figure shows the

peaks of marginalized contaminated and baseline posteriors in 2D planes with

blue and red markers respectively. We find that a 0.24σ marginalized contam-

inated contour intersects the peak of baseline marginalized posterior in ΛCDM

model, while same is true for a 0.05σ contour in wCDM model. We find that for

the linear bias model, (8,6) Mpc/h scale cuts pass the above-mentioned criteria

that the distance between the peaks of baseline and contaminated contours is

less than 0.3σ. In Fig. 3.3, we also show the MAP parameter values for each run

using a star symbol. In order to obtain the MAP value, we use the Nelder-Mead

algorithm [221] to minimize the posterior value after starting the optimization

from the highest posterior point of the converged parameter inference chain. We

find that the MAP point also lies within 0.3σ of the true cosmology, further validating the inferred scale cuts (although, note the caveats about MAP mentioned in §3.4).

3.4.3 Buzzard simulation tests

Finally, we validate our model with mock catalogs from cosmological simulations for analysis choice combinations that pass the simulated likelihood tests. These tests, and tests of cosmic shear and 3×2-point analyses, are presented in full in [85], and we summarize the details relevant for 2×2-point analyses here. We use the suite of Y3 Buzzard simulations described above. We again require that our analysis choices return unbiased cosmological parameters. In order to reduce the sample variance, we analyze the mean datavector constructed from 18 Buzzard realizations.

3.4.3.1 Validation of linear bias model

We have run simulated 2×2-point analyses on the mean of the measurements from all 18 Buzzard simulations. We compare our model for $w(\theta)$ and $\gamma_{\rm t}(\theta)$ to our measurements at the true Buzzard cosmology, leaving only linear bias and lens magnification coefficients free. In this case, we have ten free parameters in total, and we find a chi-squared value of 13.6 for 285 data points using our *fiducial* scale cuts and assuming the covariance of a single simulation, as appropriate

for application to the data. This analysis assumes true source redshift distributions, and we fix the source redshift uncertainties to zero as a conservative choice. This results in cosmological constraints where the mean two-dimensional parameter biases are 0.23σ in the $S_8 - \Omega_{\mathrm{m}}$ plane and 0.18σ in the $w - \Omega_{\mathrm{m}}$ plane. These biases are consistent with noise, as they have an approximately $1/\sqrt{18}\sigma$ error associated with them (assuming 1σ error from a single realization). We perform a similar analysis using calibrated photometric redshift distributions where we use redMaGiC lens redshift distributions, and use the SOMPZ redshift distribution estimates of source galaxies. These are weighted by the likelihood of those samples given the cross-correlation of our source galaxies with redMaGiC and spectroscopic galaxies (we refer the reader to Appendix F of [85] for detailed procedure). This procedure results in the mean two-dimensional parameter biases of 0.07σ in the $S_8 - \Omega_{\mathrm{m}}$ plane and 0.05σ in the $w - \Omega_{\mathrm{m}}$ plane.

The left panels of Fig. 3.4 and Fig. 3.5 show the 0.3σ constraints obtained from analyzing linear galaxy bias models in ΛCDM and wCDM cosmologies on the Buzzard datavector in blue colored contours. Since we expect the marginalized posteriors to be affected by the projection effects, we compare these contours to a simulated noiseless baseline datavector obtained at the input cosmology of Buzzard (denoted by gray dashed lines in Fig. 3.4 and Fig. 3.5, also see [86]). We find that similar to results obtained with simulated datavectors in previous section, our parameter biases are less than the threshold of 0.3σ for the fiducial scale

116

cuts. For a more detailed discussion how these shift compare with probability to exceed (PTE) values of exceeding a 0.3σ bias, see Section V of [85].

Also note that as changing the input truth values of the parameters impacts the shape of the multi-dimensional posterior, we find that the effective magnitude and direction of the projection effects of the baseline contours (comparison of red contours in Fig. 3.3 with Fig. 3.4 and Fig. 3.5) are different.

3.4.3.2   Scale cuts for non-linear bias model

Likewise, we have run simulated 2×2-point analyses including our non-linear bias model on the mean of the measurements from all 18 simulations. Similar to the procedure used to determine the linear bias scale cuts in §3.4.2.1, we iterate over scale cuts for each tomographic bin defined from varying physical scale cuts.

We compare our model for $w(\theta)$ and $\gamma_t(\theta)$ to our measurements at the true BUZZARD cosmology, leaving our bias model parameters and magnification coefficients free, which adds 15 free parameters. We find a χ^2 value of 15.6 for 340 data points using our non-linear bias scale cuts and assuming the covariance of a single simulation. Simulated analyses using true redshift distributions result in cosmological constraints where the associated mean two-dimensional parameter biases for these analyses are 0.04σ in the $S_8 - \Omega_m$ plane and 0.11σ in the $w - \Omega_m$ plane. This is again consistent with noise due to finite number of realizations.

In the right panel of Fig. 3.4 we show the constraints on Ω_m and S_8 from the mean Buzzard 2×2pt measurements for ΛCDM cosmological model. The results for non-linear bias models are shown, where we find, the criterion for unbiased cosmology is satisfied for the choice of scale cuts of (4,4)Mpc/h for $(w(\theta), \gamma_t(\theta))$ respectively. Again for a more detailed discussion how these shift compare with PTE values of exceeding a 0.3σ bias, see [85]. The Figure 3.5 shows the same analysis for wCDM cosmological model in the Ω_m and w plane, where we find similar results. We therefore use (4,4)Mpc/h as our validated scale cuts when analyzing data with non-linear bias model.

3.5   Results

In this section we present the 2×2pt cosmology results using the DES Y3 red-MaGiC lens galaxy sample and study the implications of our constraints on galaxy bias.

3.5.1   redMaGiC **cosmology constraints**

In Fig. 3.6, we compare the constraints on the cosmological parameters obtained from jointly analyzing $w(\theta)$ and $\gamma_t(\theta)$ with both linear and non-linear bias models. We find $\Omega_m = 0.325^{+0.033}_{-0.034}$ from the linear bias model (a 10% constraint) at the *fiducial* scale cuts of (8,6) Mpc/h (for $(w(\theta), \gamma_t(\theta))$ respectively), while using the non-linear bias model at same scale cuts gives completely consistent constraints.
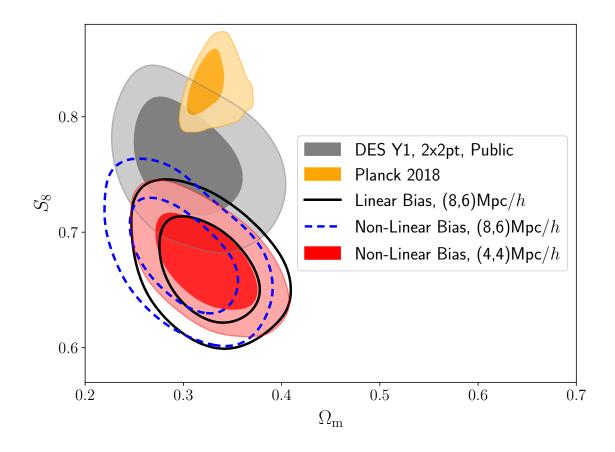
Figure 3.6: Comparison of the $2 \times 2\text{pt}$ ΛCDM constraints, using `redMaGiC` lens galaxy sample, for both linear bias and non-linear bias models at their respectively defined scale cuts given in the legend. We find a preference for a low value of S_8, compared to DES Y1 $2 \times 2\text{pt}$ public result [2] and Planck 2018 public result [8], with both models of galaxy bias which we investigate in §3.5.3. We also show that analyzing smaller scales using the non-linear galaxy bias model leads to 17% better constraints in the $\Omega_\text{m} - S_8$ plane.

We also show the results for the scale cuts of (4,4) Mpc/h using the non-linear bias model where we find $\Omega_\mathrm{m} = 0.323^{+0.034}_{-0.035}$. These marginalized constraints on Ω_m are completely consistent with the public DES-Y1 2×2pt results [2] and *Planck* results (including all three correlations between temperature and E-mode polarization, see [8] for details).

With the analysis of linear bias model with (8,6) Mpc/h scale cuts (referred to as *fiducial* model in following text), we find $S_8 = 0.668^{+0.026}_{-0.033}$. As is evident from the contour plot in Fig. 3.6, our constraints prefer lower S_8 compared to previous analyses. We use the Monte-Carlo parameter difference distribution methodology (as detailed in [186]) to assess the tension between our *fiducial* constraints and *Planck* results. Using this criterion, we find a tension of 4.1σ, largely driven by the differences in the S_8 parameter. We find similar constraints on S_8 from the non-linear bias as well for both the scale cuts. We investigate the cause of this low S_8 value in the following sub-sections.

Note that the non-linear bias model at (4,4) Mpc/h scale cuts results in tighter constraints in the $\Omega_\mathrm{m} - S_8$ plane. We estimate the total constraining power in this $\Omega_\mathrm{m} - S_8$ plane by estimating 2D figure-of-merit (FoM), which is defined as $\mathrm{FoM}_{p_1, p_2} = 1/\sqrt{[\det \mathrm{Cov}(p_1, p_2)]}$, for any two parameters p_1 and p_2 [159,318]. This statistic here is proportional to the inverse of the confidence region area in the 2D parameter plane of $\Omega_\mathrm{m} - S_8$. We find that the non-linear bias model at (4,4) Mpc/h results in a 17% increase in constraining power compared to the linear

bias model at (8,6) Mpc/h.

3.5.2 Comparison with `Maglim` results

In Fig. 3.7, we show the comparison of the cosmology constraints obtained from 2×2pt analysis using the `Maglim` sample (see [244]) with the results obtained here with the `redMaGiC` lens galaxy sample. The top panel compares the $\Omega_m - S_8$ contours assuming ΛCDM cosmology while the bottom panel compares the $\Omega_m - w$ contours assuming wCDM cosmology. We compare both the linear bias and the non-linear bias model at the (8,6) Mpc/h and (4,4) Mpc/h scale cuts respectively. We again find that the S_8 constraints obtained with the `redMaGiC` sample are low compared to the `Maglim` sample for both linear and non-linear bias models. As the source galaxy sample, the measurement pipeline and the modeling methodology used are the same for the two 2×2pt analysis, this suggests that the preference for low S_8 in our *fiducial* results is driven by the Y3 `redMaGiC` lens galaxy sample, which we investigate in the following sub-sections.

In the bottom panel showing the wCDM cosmology constraints, we also show the maximum a posteriori (MAP) estimate in the $\Omega_m - w$ plane, in order to estimate the projection effects arising from marginalizing over the large multi-dimensional space to these two dimensional contours (see Fig. 3.3 and Fig. 3.5). We find that the non-linear bias model suffers from mild projection effects (although note the caveats about the MAP estimator mentioned in §3.4). We also
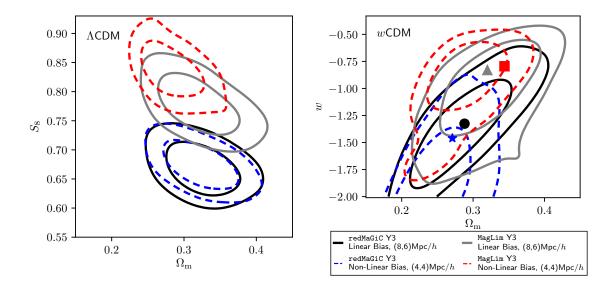
Figure 3.7: Comparing the constraints from 2×2pt between the redMaGiC and Maglim samples. The black dot and blue star denote the MAP point estimate for redMaGiC linear and non-linear bias model respectively, while the gray triangle and red square show the same for the Maglim sample.

emphasize that using the non-linear galaxy bias model with smaller scale cuts gives similar improvement in the figure-of-merit of the cosmology contours shown in Fig. 3.7, using both redMaGiC and Maglim lens galaxy samples.

3.5.3 Internal consistency of the redMaGiC results

To investigate the low S_8 constraints in the *fiducial* analysis of the redMaGiC galaxy sample, we first check various aspects of the modeling pipeline. In Fig. 3.8, we show the constraints on Ω_m, S_8 and galaxy bias for the third tomographic bin
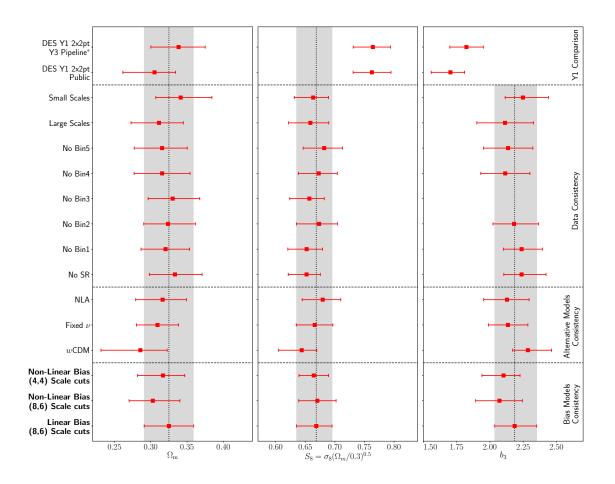
Figure 3.8: The consistency of the redMaGiC 2×2pt cosmology and galaxy bias constraints when changing the analysis choices (see §3.5.3 for details). We also compare our constraints to the DES Y1 public 2×2pt results as well as its reanalysis with the current analysis pipeline (∗ – we fix the point mass parameters when re-analyzing the DES Y1 data due to the large degeneracy between point mass parameters and cosmology at the scale cuts described and validated in [2]).

b_3, for various robustness tests. We choose to show the third tomographic bin for the galaxy bias constraints as this bin has the highest signal-to-noise ratio. We divide the figure into three parts, separated by horizontal black lines. The bottom panel shows the marginalized constraints from the results described in the previous subsection (see Fig. 3.6). As mentioned previously, we obtain completely consistent constraints from both linear and non-linear bias models. To check the robustness and keep the interpretation simple, we use the linear bias model using the scale cuts of (8,6) Mpc/h in the following variations.

In the next part of the Figure, moving upwards from the bottom, we test the robustness of the model. In particular, we check the robustness of the *fiducial* intrinsic alignment model by using the NLA model. We also run the analysis by fixing the neutrino masses to $\Omega_\nu h^2 = 0.00083$. This choice of $\Omega_\nu h^2$ parameter corresponds to the sum of neutrino masses, $\sum m_\nu = 0.06$eV at the *fiducial* cosmology described in Table 3.1 (which is the baseline value used in the *Planck* 2018 cosmology results as well [8]). Lastly, we test the impact of varying the dark energy parameter using the wCDM model. We find entirely consistent constraints for all of the above variations.

In the next part of the figure, we test the internal consistency of the datavector. Firstly we remove the contribution of shear-ratio information to the total likelihood, resulting in entirely consistent constraints. Also, note that the size of constraints on the cosmological parameters do not change in this case com-

pared to the *fiducial* results. This demonstrates that the majority of constraints on the cosmological and bias parameters are obtained from the $w(\theta)$ and $\gamma_t(\theta)$ themselves. We also test the impact of removing one tomographic bin at a time from the datavector. We find consistent constraints in all five cases. Lastly, we also split the datavector into large and small scales. The small-scales run uses the datavector between angular scales corresponding to (8,6) Mpc/h and (30,30) Mpc/h. The large-scales run uses the datavector between angular scales corresponding to (30,30) Mpc/h and 250 arcmins. When analyzing the large scales, we fix the point-mass parameters to their *fiducial* values (see Table 3.1), because of the large degradation of constraining power at these larger-scale cuts due to the degeneracy between point-mass parameters, galaxy bias and cosmological parameter σ_8 (see Appendix B.1 and [193]). In both of these cases, we find similar constraints on all parameters, demonstrating that the low S_8 does not originate from either large or small scales.

As an additional test of the robustness of the modeling pipeline, we analyze the $w(\theta)$ and $\gamma_t(\theta)$ measurements as measured from DES Y1 data [2]. Note that in this analysis, we keep the same scale cuts as described and validated in [2], which are 8 Mpc/h for $w(\theta)$ and 12 Mpc/h for $\gamma_t(\theta)$. To analyze this datavector, while we use the model described in this paper, we fix the point-mass parameters again to zero due to similar reasons as described above in the analysis of large scales. The constraints we obtain are consistent with the public results described

125

in [2]. We attribute an approximately 1σ shift in the marginalized Ω_m posterior to the improvements made in the current model, compared to the model used for the public Y1 results [174]. In particular, we use the full non-limber calculation, including the effects of redshift-space distortions, for galaxy clustering (also see [108]).

Lastly, to assess the impact of projection effects on the S_8 parameter, we compare the profile posterior to the marginalized posterior. The profile posterior in Fig. 3.9 is obtained by dividing the samples into 20 bins of S_8 values and calculating the maximum posterior value for each bin. Therefore, unlike the marginalized posterior, the profile posterior does not involve the projection of a high dimensional posterior to a single S_8 parameter. Hence the histogram of the profile posterior is not impacted by projection effects. We compare the marginalized posterior and profile posterior in Fig. 3.9, showing that projection effects have a sub-dominant impact on the marginalized S_8 constraints. This demonstrates that projection effects do not explain the preference for low S_8 with the redMaGiC sample.

In summary, the results presented in this sub-section demonstrate that our modeling methodology is entirely robust, and hence we believe our data are driving the low S_8 constraints with the redMaGiC sample. Moreover, as described above, no individual part of the data drives a low value of S_8; therefore, we perform global checks of the datavector in the following sub-sections.

126

3.5.4 Galaxy bias from individual probes

In this sub-section, we test the compatibility of the $w(\theta)$ and $\gamma_t(\theta)$ parts of the datavector. As we will lose the power of complementarity when analyzing them individually, we fix the cosmological parameters to the maximum posterior obtained from the DES Y1 3×2pt analysis [2]. We find that the best-fit bias values from the $w(\theta)$ part of the datavector are systematically higher than $\gamma_t(\theta)$ for each tomographic bin. We parameterize this difference in bias values with a phenomenological parameter X for each tomographic bin i as:

$$X^i_{\text{lens}} = b^i_{\gamma_t(\theta)}/b^i_{w(\theta)} \tag{3.5.1}$$

We refer to X as a "de-correlation parameter" because its effect on the data is very similar to assuming that the mass and galaxy density functions have less than 100% correlation. A value of $X = 1$ is expected from local biasing models. The constraints on the parameter X^i_{lens} are shown in Fig. 3.10. We also compare the constraints of these X^i_{lens} parameters obtained from Y1 redMaGiC 2×2pt (see [2] and [248] for details) and the 2×2pt datavector using Y3 Maglim lens galaxy sample. For the Y1 redMaGiC datavector, we fix the scale cuts and priors on the calibration of photometric redshifts of lens and source galaxies as described in the [2] and for analysis of Y3 Maglim datavector we follow the analysis choices detailed in [244]. In this analysis of all the datavectors, we use the linear bias galaxy bias model while keeping the rest of the model the same as described in §3.2.2. We find that the Y1 redMaGiC as well as Y3 Maglim 2×2pt data are

consistent with $X^i_{\text{lens}} = 1$ for all the tomographic bins, while redMaGiC Y3 2 × 2pt data have a persistent preference for $X^i_{\text{lens}} < 1$ for all the tomographic bins.

Noticeably, we find that for the DES Y1 best-fit cosmological parameters, the Y3 redMaGiC datavector prefers a value of $X^i_{\text{lens}} \sim 0.9$ for each tomographic bin. Therefore, in order to keep the interpretation simple, we use a single parameter X_{lens} to describe the ratio of galaxy bias $b^i_{\gamma_t(\theta)}/b^i_{w(\theta)}$ for all tomographic bins $i \in [1,5]$. We constrain this single redshift-independent parameter to be $X_{\text{lens}} = 0.9^{+0.03}_{-0.03}$ for Y3 redMaGiC, a 3.5σ deviation from $X_{\text{lens}} = 1$. Within general relativity, even when including the impact of non-linear astrophysics, we do not expect a de-correlation between galaxy clustering and galaxy-galaxy lensing to be present at more than a few percent level [91]. We comment on the impact of this de-correlation on the redMaGiC cosmology constraints in §3.5.6.

Note that the inferred value of X_{lens} depends on the cosmological parameters, because the large-scale amplitudes of galaxy clustering and galaxy-galaxy lensing involve different combinations of galaxy bias, σ_8 and Ω_{m}. Therefore, a self-consistent inference of X_{lens} requires the full 3 × 2pt datavector and is presented in [88]. However, the DES Y1 3 × 2pt best-fit cosmological parameters are fairly close to the DES Y3 3 × 2pt best-fit parameters, therefore we expect the results presented here to be good approximations to those obtained with the Y3 3 × 2pt datavector.
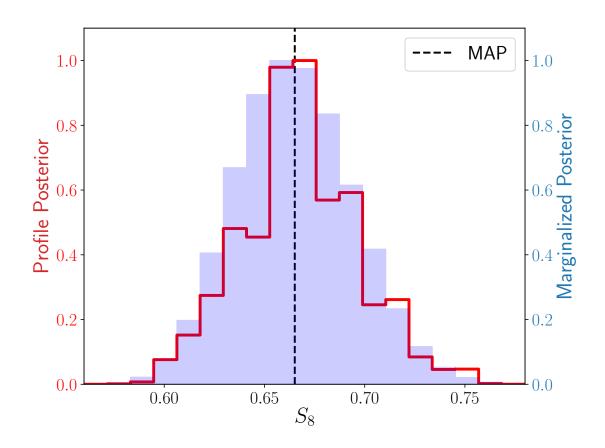
Figure 3.9: Comparison of the profile posterior and marginalized posterior on the S_8 parameter from the 2×2pt redMaGiC LCDM chain.
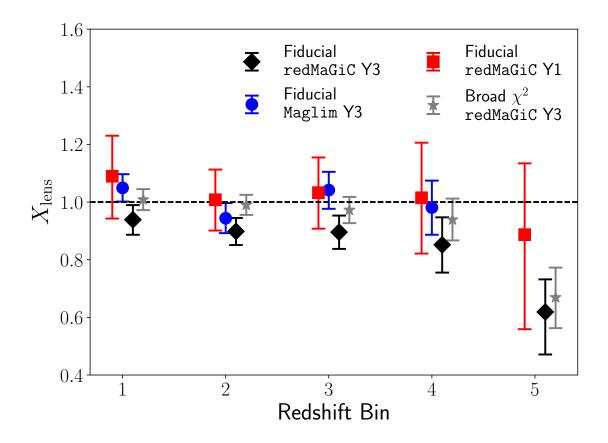
Figure 3.10: Constraints on the phenomenological de-correlation parameter, X_{lens}, for each tomographic bin obtained from $2 \times 2\text{pt}$ analysis using Y1 red-MaGiC , Y3 fiducial redMaGiC sample, Y3 broad-χ^2 redMaGiC sample (see § 3.5.7) and Y3 Maglim as the lens galaxies (the cosmological parameters are fixed to the DES Y1 best-fit values [2]).

3.5.5 Area split of the de-correlation parameter

In order to further study the properties of this de-correlation parameter X_{lens}, we estimate it independently in 10 approximately equal area patches of the DES Y3 footprint. We measure the datavectors, $w(\theta)$ and $\gamma_{\text{t}}(\theta)$ in each of these 10 patches, using the same methodology presented in §3.3.3.4. In order to obtain the covariance for each patch, we rescale the *fiducial* covariance (see §3.3.4) of the full footprint to the area of each patch. We then estimate X_{lens} from each patch while keeping all the other analysis choices the same.

In Fig. 3.11 we show the DES footprint split into 10 regions. In this figure, each region is colored in proportion to the mean value of the X_{lens} parameter we obtain using `redMaGiC` as the lens galaxy sample. We run a similar analysis when using `Maglim` as the lens sample.

In Fig. 3.12 we show a scatter plot between the value of X_{lens} recovered from each of 10 regions using `redMaGiC` and `Maglim` as lens samples. We find a tight correlation between the value of X_{lens} from the two lens samples, as would be expected if they share noise from sample variance and fluctuations in the source galaxy population. Note that the scatter in the inferred X_{lens} for both the `Maglim` and the `redMaGiC` samples corresponding to each sky patch (red points) around the mean of full sample (the blue point), is consistent with the expectation. This shows that, compared with `Maglim` , the `redMaGiC` lens sample has a preference for $X_{\text{lens}} < 1$ in the whole DES footprint. This correlation and area independence

of the ratio $X_{\mathrm{Redmagic}}/X_{\mathrm{Maglim}}$ is remarkable and suggests that the potential systematic in the redMaGiC sample has a more global origin.

3.5.6   Impact of de-correlation on 2×2pt cosmology

To summarize, assuming a standard cosmological model, we have identified that the galaxy-clustering and galaxy-galaxy lensing signal measured using the Y3 redMaGiC lens galaxy sample are incompatible with each other (at the set of cosmological parameters preferred by previous studies). We have further identified that this incompatibility is well-captured by a redshift-, scale- and area-independent phenomenological parameter X_{lens}. Using Y3 redMaGiC lens sample, we detect $X_{\mathrm{lens}} \sim 0.9$, at the 3.5σ confidence level away from the expected value of $X_{\mathrm{lens}} = 1$. This 2×2pt analysis is done when the cosmological parameters are fixed to their DES Y1 best-fit values; a self-consistent X_{lens} inference analysis with free cosmological parameters requires the full 3×2pt datavector. This is presented in [88], where the inferred constraints on this de-correlation parameter are $X_{\mathrm{lens}} = 0.87^{+0.02}_{-0.02}$.

In Fig. 3.13, we fix $X_{\mathrm{lens}} = 0.87$ in our model and re-run the Y3 redMaGiC 2×2pt analysis. We find, as expected, that this has a significant impact on the marginalized S_8 values and results in the marginalized constraints $S_8 = 0.76^{+0.034}_{-0.037}$, completely consistent with 2×2pt Y1 redMaGiC public results as well as Y3 Maglim results. Also note that the marginalized constraints on Ω_{m} for $X_{\mathrm{lens}} =$

Figure 3.11: The DES footprint is split into 10 regions. The color of each area corresponds to the mean value of the constraints on X_lens from that particular area, inferred at fixed DES-Y1 cosmology and using the redMaGiC lens sample. This plot shows that no special region in the sky (for example, near the galactic plane) drives the preference for low X_lens. While a variation over the sky in the inferred X_lens is expected from analyzing only the 2×2pt data due to the variations in the photometric redshift distribution of source galaxies, we find that the preferred mean value of X_lens from the redMaGiC sample is significantly lower than the expected value of 1 (see Fig. 3.12).
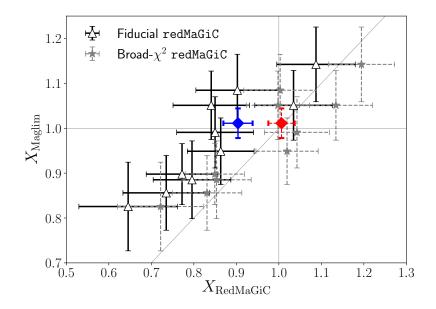
Figure 3.12: Each errorbar corresponds to the 68% credible interval constraints on X_{lens} from one of the 10 regions (see Fig. 3.11), using either the redMaGiC sample or the Maglim lens galaxy sample. The blue errorbar corresponds to the constraints on X_{lens} from the entire Y3 area using the Maglim sample and the fiducial redMaGiC sample, whereas the red errorbar uses the broad-χ^2 galaxy sample (see § 3.5.7). We find a tight correlation between X_{Redmagic} and X_{Maglim}, due to common sources of statistical noise (e.g., photometric redshifts of the source galaxies). We find that, while the inferred X_{lens} from 10 regions using the Maglim and the broad-χ^2 redMaGiC sample fluctuates around its mean value that is close to 1, the inference from the fiducial redMaGiC sample fluctuates around a mean value that is significantly lower than 1. This figure shows that the fiducial redMaGiC sample prefers X_{lens} to be lower than 1, independent of the sky-area.
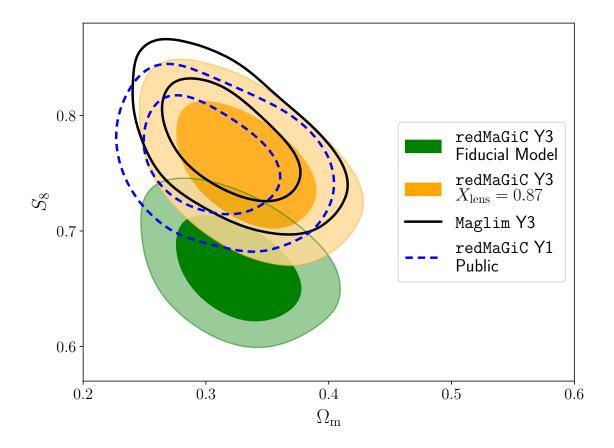
Figure 3.13: Comparison of the constraints from 2×2pt analysis when using the mean value of X_{lens} parameter for `redMaGiC` lens sample analysis, as estimated and described in [88]. We find a shift in S_8 parameter compared to our *fiducial* results in §3.5.1, but Ω_{m} constraints are fully consistent.

0.87 model are $\Omega_{\rm m} = 0.331^{+0.037}_{-0.037}$, which remains consistent with the *fiducial* result.

3.5.7   Broad-χ^2 `redMaGiC` sample

In order to further investigate the source of the de-correlation, we modify the $\chi^2_{\rm RM}$ threshold for a galaxy to be classified as a `redMaGiC` galaxy when fitting to the `redMaGiC` template using the procedure as described in [261]. As described in § 3.3.1.1, the fiducial `redMaGiC` catalog is generated by implementing the $\chi^2_{\rm RM}$ threshold of 3. This low-$\chi^2_{\rm RM}$ threshold only selects the galaxies that closely match the template. In case there are any residual variations in the `redMaGiC` catalog number densities caused by variations in the colors that are not already corrected using the fiducial weighting scheme (as described in [258]), it would contribute a spurious galaxy clustering signal. This would contribute towards $X_{\rm lens} < 1$, as we found above. In order to test this hypothesis, we increase the threshold criteria and generate another catalog with $\chi^2_{\rm RM} = 8$ and denote this new sample as the "broad-χ^2" sample.

We show the result for $X^i_{\rm lens}$ for all the five tomographic bins in Fig. 3.10. We find that with the broad-χ^2 sample, $X^i_{\rm lens}$ is consistent with 1 for the first four tomographic bins. While we still find that for the fifth tomographic bin, $X^5_{\rm lens} < 1$, this bin has low constraining power. We also show the inferred $X_{\rm lens}$ from 10 independent regions over the DES footprint in the Fig. 3.11. We find that with

136
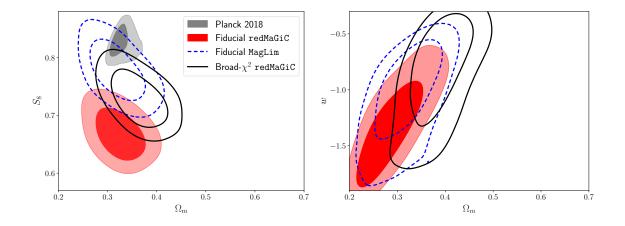
Figure 3.14: Constraints on the cosmological parameters using the linear bias model with the broad-χ^2 redMaGiC sample. The top figure corresponds to the ΛCDM cosmological model and the bottom figure corresponds to the wCDM cosmological model. We also compare the constraints from the fiducial redMaGiC and the fiducial MagLim lens galaxy samples.

the new sample, the scatter in the inferred X_{lens} is consistent with expected value of 1. Moreover, as shown with a red symbol in the Fig. 3.11, we find the redshift and area independent X_{lens} to be entirely consistent with 1 using the broad-χ^2 sample. This validates our hypothesis and points towards an uncorrected systematic that might be related to a color-dependent photometric issue in the DES data. Since the shear catalog, as well as the `Maglim` galaxy catalog, do not select galaxies based on a red-galaxy template, we do not expect this systematic to have an effect on those catalogs.

In Appendix B.3, we further describe details of this new sample and compare it with our fiducial `redMaGiC` sample. With this new sample, we use conservative analysis choices and implement the following approximations:

- We downsample the broad-χ^2 catalog to roughly match the number densities of the fiducial `redMaGiC` sample. This ensures that the validations of analysis choices performed for the redmagic sample, including the covariance, scale cuts, and methodology, remain true for the broad-χ^2 sample as well.

- We use a two-parameter model (shift and stretch parameterization) to account for the uncertainty in the lens redshift distribution for each tomographic bin [59]. We implement this model to reduce the impact of the outliers in the assigned galaxy redshifts for this new sample. The Gaussian priors on the shift and stretch parameters are tabulated in Table B.1.

We show the cosmological constraints from the broad-χ^2 sample in Fig. 3.14 and find that they are consistent with the results from Maglim sample in both ΛCDM and wCDM cosmological models. Using the ΛCDM model, we constrain $\Omega_{\rm m} = 0.363^{+0.0375}_{-0.0388}$ and $S_8 = 0.73^{+0.035}_{-0.029}$, and using the wCDM model, we constrain $w = -0.821^{+0.1908}_{-0.4341}$.

We note that this analysis is showing the constraints on the cosmological parameters under the approximation that we neglect the contribution to the LSS covariance systematic term. We use the ISD method to get the weights for this sample. Moreover, we assume that the same scale cuts work with this sample as we obtained for the fiducial redMaGiC sample. Lastly, we have used the same value of lens magnification as for the fiducial redMaGiC sample. We do not expect these choices to have any major effects on the cosmological constraints described above. However, we leave a detailed study optimizing the $\chi^2_{\rm RM}$ value, validating the analysis choices, and obtaining final constraints with redMaGiC sample to [90].

3.5.8 redMaGiC host halo mass inference

In the halo model framework (see [68] for a review), the value of the linear bias of a tracer of dark matter can be related to the host halo mass of that tracer. The standard halo occupation distribution (HOD) approach parameterizes the distribution of galaxies inside halos, and hence the observed number density as
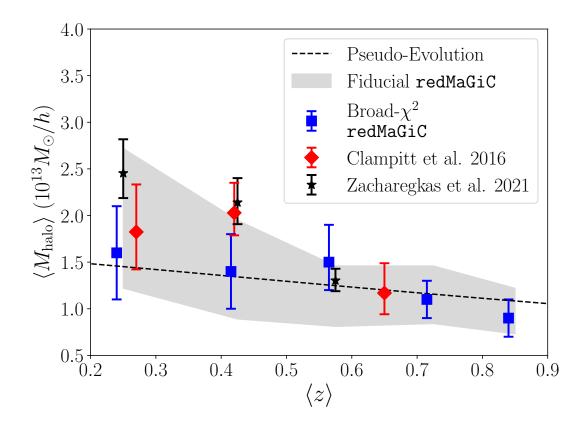
Figure 3.15: This figure shows the inferred constraints on mean host halo masses of redMaGiC galaxies for five tomographic bins. We use the HOD framework to make this inference as detailed in the Appendix B.4 and use the linear bias constraints obtained using the broad-χ^2 redMaGiC sample. We infer the mean host halo masses from the linear bias constraints for all the five tomographic bins. We compare our results to [64] and [327], and also show the expected pseudo-evolution of a halo having $M_{\mathrm{halo}} = 1.6 \times 10^{13} M_\odot/h$ at $z = 0$.

well as the large scale bias values of any galaxy sample can be expressed in terms of its HOD parameters [30,328,331]. The same HOD parameters can also be used to infer the mean host halo mass of the galaxy sample. We use the constraints on linear galaxy bias parameters and the co-moving number density to infer the mean host halo mass of the broad-χ^2 redMaGiC galaxy sample by marginalizing over HOD parameters.

The details of the halo model framework used here are given in Appendix B.4. Note that we have neglected the effects of assembly bias and the correlation between number density and bias constraints in this analysis. With these caveats in mind, in Fig. 3.15 we show approximately 25% constraints on mean host halo mass of broad-χ^2 redMaGiC galaxies and the constraints for different tomographic bins show its evolution with redshift. This redshift evolution trend is broadly consistent with the pseudo-evolution of halo masses due to changing background reference density with redshift (see [93] for more details). Therefore we find that the broad-χ^2 redMaGiC sample lives in halos of mass of approximately $1.6 \times 10^{13} M_\odot / h$, which remains broadly constant with redshift.

We also bracket the uncertainty in the host-halo masses of the fiducial red-MaGiC sample with a gray band in Fig. 3.15. In order to estimate the band, we use the linear bias constraints from the 2×2pt analysis with fiducial redMaGiC sample, after fixing $X_{\text{lens}} = 0.87$. This de-correlation parameter results in $w(\theta)$ and γ_{t} preferring different linear bias parameters, related by $b^i[w(\theta)]/b^i[\gamma_{\text{t}}(\theta)] =$

$X_{\mathrm{lens}} = 0.87$, for all tomographic bins i. Therefore, we infer the host halo masses using both linear bias parameter values. The band is estimated by using the lower limit of masses inferred by $b^i[\gamma_{\mathrm{t}}(\theta)]$ and upper limit of masses inferred by $b^i[w(\theta)]$ for all tomographic bins i. We find that the broad-χ^2 sample has a slight preference for lower halo masses, but it is consistent with constraints for the fiducial sample.

We find that our results are also broadly consistent with the analysis of [64], which used the redMaGiC galaxies of DES Science-Verification dataset and estimated the mean halo masses by studying galaxy-galaxy lensing signal in a broad range of scales (including high signal-to-noise small scales that we remove here) using HOD model.[4] We also find broad agreement with a similar study presented in [327], analyzing DES Y3 using the galaxy-galaxy lensing data estimated from the fiducial redMaGiC sample and on a wide range of scales with an improved halo model.

---

[4]Note that we use M_{200c} as our halo mass definition, which denotes the total mass within a sphere enclosing a mean density which is 200 times the *critical* density of the universe. [64] work with M_{200m} as their mass definition, denoting the total mass within a sphere enclosing a mean density which is 200 times the *mean* density of the universe, therefore we convert their constraints to M_{200c} in the above figure.

3.6 Conclusions

This paper has presented the cosmological analysis of the 2×2pt datavector of the DES Year 3 dataset using `redMaGiC` lens sample. We refer the reader to [244] for similar results using `MagLim` lens sample and [101] for details on the impact of lens magnification on the 2×2pt datavector. The 2×2pt datavector comprises the 2-point correlations of galaxy clustering and galaxy lensing using five redshift bins for the lens galaxies and four bins for source galaxies. It provides independent constraints on two primary parameters of interest, the mass density Ω_{m} and amplitude of fluctuations S_8. As shown in Fig. 3.1, these constraints are complementary to those from cosmic shear. The combination of 2×2pt with cosmic shear is thus better able to constrain Ω_{m}, S_8 as well as the dark energy equation of state parameter w. Perhaps more importantly, this provides a robustness check on the results from either approach.

The estimation and marginalization of galaxy bias parameters is one of the central tasks in extracting cosmology from the 2×2pt datavector. We have developed and validated the methodology for this based on perturbation theory. We use a five-parameter description of galaxy bias per redshift bin, with three of the parameters fixed based on theoretical considerations. We validated these choices using mock catalogs built on N-body simulations as detailed in our earlier study [231] and Section §3.4.3. We carry out two analyses: the first using linear bias with more conservative scale cuts, and the second using the full PT bias

model going down to smaller scales. Other elements of our model include intrinsic alignments, magnification and "point mass marginalization" (see §3.2.2). The validation of the analysis choice and scale cuts with simulated datavectors (both idealized and from mock catalogs) are presented in §3.4.1.

Our cosmological results are presented in Figs. 3.6, 3.7 and 3.8, which show preference for low value of S_8 parameter when compared with previous results. We refer the reader to [88], where, after unblinding the cosmological parameter constraints, we find similar inconsistency in the S_8 parameter constraints between Y3 2×2pt redMaGiC analysis and Y3 cosmic shear analysis, as well as a high χ^2 using the ΛCDM model. As detailed in [88], we discovered that the reason for the high χ^2 of the 3×2pt analysis with the *fiducial* model was due to inconsistencies in the galaxy-galaxy lensing and galaxy clustering signals. The source of this inconsistency is still undetermined, however we found that a single parameter X_{lens}, representing the ratio of the bias inferred from $w(\theta)$ and γ_{t}, substantially improves the goodness of fit. This ratio is cosmology-dependent and can only be inferred consistently (along with the other model parameters) when using the full 3×2pt analysis, presented in [88].

This ratio is expected to be unity in the absence of galaxy stochasticity, an effect that is expected to be only at the percent level on scales above ~ 10 Mpc [91]. Several previous analyses with similar datasets have also found this ratio to be consistent with unity [50, 199, 248]. However, we detect a value of $X_{\mathrm{lens}} = 0.87$,

below 1 at the 5-σ level. This purely phenomenological model assumes no scale or redshift dependence, and we found consistent values of X_{lens} when fitting to different scales (see Fig. 3.8) and when fitting separate values for each *lens* redshift bin (see Fig. 3.10). Since no known cosmological effect can produce such a large and coherent deviation in clustering and galaxy lensing, we pursued possible systematic errors that could lead to this unusual result. Note that this kind of behavior can arise with potential systematics, for example unaccounted-for impact of photometric uncertainty or background subtraction for large or faint objects on the galaxy selection. This can introduce extra fluctuation of the number density of the lens galaxies across the footprint which will not be captured by the set of survey property maps used in the LSS weights estimation pipeline.

Fig. 3.13 shows the 2×2pt redMaGiC cosmology constraints after fixing $X_{\text{lens}} = 0.87$, the best fit value from [88]. There is a significant shift in S_8, while Ω_{m} remains stable. Interestingly the resulting contours are fully consistent with the Y1 analysis as well as the 2×2pt analysis using the Maglim lens galaxy sample [244]. We track down the source of this de-correlation to an aggressive threshold on the colors of galaxies to match the red-galaxy template. We find that using a sample with a relaxed threshold, which we call the broad-χ^2 sample, results in cosmological constraints that are consistent with the expectations from Maglim sample. This points towards the existence of a potential color-dependent systematic in the galaxy catalog, and we leave a detailed exploration and mitigation

of this systematic to a future study [90].

We note that although recent analyses using BOSS galaxies have found similar inconsistencies in the galaxy clustering and galaxy-galaxy lensing (see [180, 185] and references there-in); there are some important differences. In this analysis as well as in [88], unlike in [185], we do not use any small scale information for galaxy clustering and galaxy-galaxy lensing measurements. Therefore, we are significantly less prone to the impacts of poorly understood small scale non-linear physics, like baryon feedback and galaxy assembly biases [13, 326, 332]. Moreover, in [88], by leveraging all the three two-point functions used in 3×2pt, the analysis of the consistency between galaxy-lensing and galaxy-clustering can be carried out while freeing the relevant cosmological parameters. The analysis in this paper fixes the cosmological parameters close to the best-fit cosmology from [88], hence our results are a good approximation to the analysis using the full 3×2pt datavector. Similarly, a few recent studies jointly analyzing galaxy clustering auto-correlations and galaxy-CMB lensing cross-correlations have also reported preference for lower galaxy bias value for the cross-correlation compared to the auto correlations [135, 168]. However similar to above analysis with BOSS galaxies, these studies also fix their cosmological parameters to the best-fit cosmology from *Planck* results [8], which is different from this study (see [176] for related discussion).

To access the information in the measurements on smaller scales, we use

higher-order perturbation theory. We use a hybrid 1-loop perturbation theory model for galaxy bias, capturing the non-linear contributions to the overdensity field till third order. We have tested and validated our model using 3-dimensional correlation functions from DES-mock catalogs in [231] as well as with projected statistics in [85]; in this study, we validate the bias model with mocks for the 2×2pt redMaGiC datavector at scales above 4Mpc$/h$. This validation presented here, along with results in [231], are then also directly used to validate non-linear bias model for Maglim datavector. We apply it to the data and find that the non-linear bias model results in a gain in constraining power of approximately 17% in the $\Omega_{\rm m} - S_8$ parameter plane.

A different approach, the halo occupation distribution in the halo model, enables a connection between the masses of halos in which galaxies live and their large-scale bias. We use our constraints on linear bias parameters (along with the galaxy number density) and estimate the host halo masses of redMaGiC galaxies. We marginalize over the halo occupation distribution parameters and obtain 25% constraints on the mean mass of host halos. We show these constraints, including its evolution with redshift in Fig. 3.15, finding halo mass of approximately $1.5 \times 10^{13} M_{\odot}/h$ and its evolution with redshift consistent with the expected pseudo-evolution due to changing background density.

The 2×2pt combination of probes plays a crucial role in extracting the most cosmological information from LSS surveys, especially in constraining the mat-

ter content of universe (Ω_{m}) and the dark energy equation of state (w). In this analysis we measure the combination of galaxy clustering and galaxy-galaxy lensing at approximately 200σ; this significance is expected to dramatically increase with imminent large scale surveys like the Euclid Space Telescope,[5] the Dark Energy Spectroscopic Instrument,[6] the Nancy G. Roman Space Telescope,[7] and the Vera C. Rubin Observatory Legacy Survey of Space and Time.[8] In order to optimally analyze these high precision measurements, especially at non-linear small scales, we need better models and ensure their proper validation before applying them to measurements. We have shown that the hybrid perturbation theory galaxy bias model can be validated with simulations to sufficient accuracy for the present analysis. By relaxing the priors on all five parameters (per redshift bin), the model's accuracy can be improved though the increase in model complexity poses other challenges in parameter estimation. Finally, and perhaps most importantly, we have highlighted how understanding potential sources of systematic uncertainty is of paramount importance for extracting unbiased cosmological information in this era of precision cosmology.

---

[5]https://www.euclid-ec.org

[6]https://www.desi.lbl.gov

[7]https://roman.gsfc.nasa.gov

[8]https://www.lsst.org

Chapter 4

Baryonic feedback constraints using galaxy & tSZ correlations

Abstract

An understanding of astrophysical feedback is important for constraining models of galaxy formation and for extracting cosmological information from current and future weak lensing surveys. The thermal Sunyaev-Zel'dovich effect, quantified via the Compton-y parameter, is a powerful tool for studying feedback, because it directly probes the pressure of the hot, ionized gas residing in dark matter halos. Cross-correlations between galaxies and maps of Compton-y obtained from cosmic microwave background surveys are sensitive to the redshift evolution of the gas pressure, and its dependence on halo mass. In this work, we use galaxies identified in year one data from the Dark Energy Survey and Compton-y maps constructed from *Planck* observations. We find highly significant (roughly 12σ) detections of galaxy-y cross-correlation in multiple redshift bins. By jointly fitting these measurements as well as measurements of galaxy clustering, we constrain the halo bias-weighted, gas pressure of the Universe as a function of redshift between $0.15 \lesssim z \lesssim 0.75$. We compare these measurements to predictions from hydrodynamical simulations, allowing us to constrain the amount of thermal energy in the halo gas relative to that resulting from gravitational collapse.

4.1   Introduction

The nonlinear collapse of structure at late times leads to the formation of gravitationally bound dark matter halos. These massive objects are reservoirs of hot

150

gas, with virial temperatures as high as $T \sim 10^8$ K. This gas can be studied via its thermal emission, which is typically peaked in x-ray bands [40]. Another way to study the gas in halos is via the thermal Sunyaev-Zel'dovich (tSZ) effect [292], caused by inverse Compton scattering of CMB photons with the hot gas. This scattering process leads to a spectral distortion which is observable at millimeter wavelengths [55].

The amplitude of the tSZ effect in some direction on the sky is characterized by the Compton-y parameter, which is related to an integral along the line of sight of the ionized gas pressure. By measuring contributions to y as a function of redshift, we effectively probe the evolution of the gas pressure over cosmic time. For the most massive halos, the evolution of the gas pressure is expected to be dominated by gravitational physics. Gas falling into these halos is shock heated to the virial temperature during infall into the cluster potential [104]. For lower mass halos, on the other hand, other mechanisms may deposit energy and/or momentum into the gas; these mechanisms are generically referred to as "feedback."

An understanding of baryonic feedback is important for constraining models of galaxy formation [?, for a recent review, see]]Naab:2017. Furthermore, since feedback can redistribute mass around halos (e.g. via gas outflows), an understanding of these processes is necessary for extracting cosmological constraints from small-scale measurements of the matter power spectrum with e.g. weak

lensing surveys [262, 310].

Because y is sensitive to the line-of-sight *integrated* gas pressure, measurements of y alone (such as the y power spectrum) cannot be used to to directly determine the redshift evolution of the gas pressure. However, given some tracer of the matter density field which can be restricted to narrow redshift intervals, cross-correlations of this tracer with y can be used to isolate contributions to y from different redshifts. We take the cross-correlation approach in this analysis.

By cross-correlating a sample of galaxies identified in data from the Dark Energy Survey (DES) [109] with y maps generated from *Planck* data [10], we measure the evolution of the gas pressure as a function of redshift. As we discuss in §4.2, our cross-correlation measurements are sensitive to a combination of the gas pressure and the amplitude of galaxy clustering. To break this degeneracy, we perform a joint fit to measurements of the galaxy-y cross-correlation and to galaxy-galaxy clustering to constrain both the redshift evolution of the galaxy bias, and the redshift evolution of a term depending on the average gas pressure in dark matter halos.

Our analysis relies on the so-called redMaGiC galaxy selection from DES. The redMaGiC algorithm yields a sample of galaxies whose photometric redshifts are well constrained [260]. We note that we do not attempt to model the halo-galaxy connection for the redMaGiC galaxies. Rather, we use these galaxies only as tracers of the density field for the purposes of isolating contributions to y from dif-

ferent redshifts. Consequently, we will restrict our measurements to the *two-halo* regime, for which the galaxy-y cross-correlation can be modeled without dependence on the precise way that `redMaGiC` galaxies populate halos [69].

Several previous analyses have also considered the cross-correlation between galaxy catalogs and Compton-y maps from *Planck* [145, 197, 297, 314]. [314] (hereafter [314]) correlated *Planck y* maps with a sample of galaxy groups identified from Sloan Digital Sky Survey (SDSS) data by [325]. Our analysis differs from that of [314] in several important respects. First, the galaxy sample used in this analysis is derived from DES data, and extends to significantly higher redshift ($z \sim 0.7$) than considered by [314] ($z \lesssim 0.2$). Additionally, while [314] divided their correlation measurements into bins of halo mass, we divide our measurements into bins of halo redshift. The measurements presented here can be considered complementary to those of [314] with regard to constraining feedback models.

[145] used measurements and modeling similar to [314] in order to extract constraints on the halo Y-M relation, finding hints of departure from the predictions of self-similar models at low halo masses. Our approach is similar to that of [145], although we only fit measurements in the two-halo regime.

[238] correlated galaxies identified in SDSS data with *Planck y* maps. The galaxy catalog used by [238] was restricted to "isolated" galaxies in order to probe the pressure profiles of individual small mass halos (although note the

issues with this approach pointed out by [181], [131] and [145]). Several authors have also investigated related correlations between Compton-y and weak lensing [147, 313] .

Recently, [297] measured the correlation of luminous red galaxies (LRGs) with the *Planck y* maps in order to study astrophysical feedback. Our analysis differs from that of [297] in two crucial aspects. First, we are only interested in the galaxy-y cross-correlations in the two-halo regime, whereas [297] analyzed the full y profile around LRGs, including in the one-halo regime. Second, and more importantly, the quantity of interest in the present work, namely the bias weighted pressure of the universe, is not sensitive to the connection between the galaxies used for cross-correlations and the parent halo, nor to the properties of the galaxies. The analysis of [297] exhibits strong dependence on the connection between stellar mass and halo mass for their LRG sample.

The structure of the paper is as follows. In §4.2 we present our model for the galaxy-y and galaxy-galaxy cross-correlation measurements; in §4.3 we describe the DES, *Planck* and simulation data sets used in our analysis; in §4.4 we describe our measurement and fitting procedure, and validate this procedure by applying it to simulations; in §4.5 we present the results of our analysis applied to the data. We conclude in §4.6.

4.2 Formalism

We are interested in modeling both the galaxy-y and galaxy-galaxy correlation functions to extract constraints on the redshift evolution of the gas pressure. Our analysis will focus on the large-scale, two-halo regime in which the details of the galaxy-halo connection can be ignored. The primary motivation for this choice is that in the two-halo regime, the galaxy-y cross-correlation function is insensitive to the details of the galaxy-halo connection, significantly simplifying the analysis.

We will assume a fixed ΛCDM cosmological model throughout, and will therefore suppress dependence on cosmological parameters. When analyzing the data, we adopt a ΛCDM model with $h = 0.7$, $\Omega_{\rm m} = 0.28$, $\Omega_b = 0.044$, $n_s = 0.965$ and $\sigma_8 = 0.8$. Given the uncertainties on our measurement of the galaxy-y cross-correlation, adopting instead the best-fit cosmology from e.g. [243] has a negligible impact on our main constraints.

4.2.1 Model for galaxy-y cross-correlation

The observed temperature signal on the sky in the direction $\hat{n}$ and at frequency ν due to the tSZ effect can be written as

$$\Delta T(\hat{n}, \nu) = T_{\rm CMB} y(\hat{n}) f(\nu), \qquad (4.2.1)$$

155

where $T_{\mathrm{CMB}} = 2.73\,\mathrm{K}$ is the mean temperature of the CMB, and $y(\hat{n})$ is the Compton-y parameter. In the non-relativistic limit, we have [291]:

$$f(x = h\nu/k_B T_{\mathrm{CMB}}) = x\frac{e^x + 1}{e^x - 1} - 4, \tag{4.2.2}$$

where h is Planck's constant, and k_B is the Boltzmann constant.

The Compton-y parameter is in turn given by (suppressing the directional dependence):

$$y = \frac{\sigma_T}{m_e c^2} \int_0^\infty dl\, P_e(l), \tag{4.2.3}$$

where $P_e(l)$ is the electron gas pressure (which dominates the inverse Compton scattering process that gives rise to the tSZ effect) at line of sight distance l, σ_T is the Thomson cross section, m_e is the electron mass and c is the speed of light. For a fully ionized gas consisting of hydrogen and helium, the electron pressure, P_e, is related to the total thermal pressure, P_{th}, by:

$$P_e = \left[\frac{4 - 2Y}{8 - 5Y}\right] P_{th}, \tag{4.2.4}$$

where Y is the primordial helium mass fraction. We adopt $Y = 0.24$.

We denote the galaxy-y cross-correlation with $\xi_{yg}(R)$. This quantity represents the expectation value of y at transverse comoving separation R from the galaxies in excess of the cosmic mean. We work in comoving coordinates because this choice preserves the size of a halo of constant mass as measured by a spherical overdensity radius as a function of redshift. We will use r to denote the 3D comoving separation between the halo center and a given point.

The halo-y cross-correlation function for galaxies at redshift z can be written as

$$\xi_{yg}(R,z) = \frac{\sigma_T}{m_e c^2} \frac{1}{1+z} \int_0^\infty d\chi\, \xi_{Pg}\left(\sqrt{\chi^2 + R^2}, z\right), \qquad (4.2.5)$$

where χ is the comoving distance along the line of sight, and $\xi_{Pg}(r,z)$ is the 3D correlation function between the electron pressure and the galaxy sample of interest [314].

As functions of cluster-centric distance, halo mass, and halo redshift, we write the halo electron pressure profile and total density profile as $P_e(r,M,z)$ and $\rho(r,M,z)$. It is convenient to work with Fourier transformed quantities, rather than the real space ones, which we represent with $u_P(k,M,z)$ and $u_m(k,M,z)$, respectively. For u_P, for instance, we have

$$u_P(k,M,z) \equiv \int_0^\infty dr\, 4\pi r^2 \frac{\sin(kr)}{kr} P_e(r,M,z). \qquad (4.2.6)$$

An analogous equation holds for u_M.

The galaxy-pressure cross-correlation function can be related to the galaxy-pressure cross-power spectrum via

$$\xi_{Pg}(r,z) = \int_0^\infty \frac{dk}{2\pi^2} k^2 \frac{\sin(kr)}{kr} P_{Pg}(k,z), \qquad (4.2.7)$$

where k is the wavenumber, and $P_{Pg}(k,z)$ is the galaxy-pressure cross-power spectrum. This power spectrum can be decomposed into contributions from the halo in which the galaxy resides (i.e. one-halo) and contributions from other halos

(i.e. two-halo):

$$P_{Pg}(k,z) = P_{Pg}^{\text{one}-\text{halo}}(k,z) + P_{Pg}^{\text{two}-\text{halo}}(k,z). \qquad (4.2.8)$$

The one-halo part is given by:

$$P_{Pg}^{\text{one}-\text{halo}}(k,z) \qquad = \qquad \int dM \, \frac{dn}{dM} \frac{N(M,z)}{\bar{n}(z)} u_m(k,M,z) u_P(k,M,z), \quad (4.2.9)$$

where $u_m(k,M,z)$ and $u_P(k,M,z)$ are the Fourier transforms of the halo mass and pressure profiles for halos of mass M at redshift z. Here we have assumed that galaxies are distributed according to the dark matter profile. The average number of galaxies in a halo of mass M at a redshift z is given by $N(M,z)$ and the average number density of galaxies (across all masses) is given by $\bar{n}(z)$. The quantity dn/dM is the halo mass function, specifying the number density of halos (per comoving volume) and per mass interval.

The two-halo term is then:

$$P_{Pg}^{\text{two}-\text{halo}}(k,M,z) = \left[\frac{N(M,z)}{\bar{n}(z)} u_m(k,M,z) \right] \times$$
$$(1+z)^3 \left[\int dM' \left(\frac{dn}{dM'} \right) u_P(k,M',z) P_{hh}(k,M,M') \right], \quad (4.2.10)$$

where P_{hh} is the halo-halo power spectrum. In the two-halo limit, we can assume linear bias, i.e. $P_{hh}(k,M,M') = b(M)b(M')P_{\text{lin}}(k)$. Note that the $(1+z)^3$ factor comes from converting between physical coordinates and comoving coordinates.

As stated above, we are interested here in the large scale, two-halo regime. In

this limit (i.e. $k \to 0$),

$$u_P(k \to 0, M, z) = \int_0^\infty dr\, 4\pi r^2 P_e(r, M, z) \equiv E_T(M, z), \tag{4.2.11}$$

where we have defined E_T as the total thermal energy in a halo of mass M at redshift z. Similarly, we have

$$u_m(k \to 0, M) = \int_0^\infty dr\, 4\pi r^2 \frac{\rho(r, M)}{M} = \left\langle \frac{\rho}{M} \right\rangle. \tag{4.2.12}$$

Consequently, in this limit,

$$P_{Pg}(k, z) = \left(\int_0^\infty b_g(M, z) \frac{dn}{dM} dM \right)$$
$$\left((1+z)^3 \int_0^\infty dM' \frac{dn}{dM'} b(M', z) E_T(M', z) \right) P_{\text{lin}}(k, z). \tag{4.2.13}$$

We define the integral of b_g over halos as the linear bias of our galaxy sample, i.e.

$$b_g(z) = \int_0^\infty \frac{N(M, z)}{\bar{n}(z)} \left\langle \frac{\rho}{M} \right\rangle b(M, z) \frac{dn}{dM} dM. \tag{4.2.14}$$

Eq. 4.2.13 can then be simplified further by defining:

$$\langle bP_e \rangle(z) \equiv (1+z)^3 \int_0^\infty \frac{dn}{dM} b(M, z) E_T(M, z) dM. \tag{4.2.15}$$

This quantity represents the bias weighted thermal energy of all halos, and is the primary quantity of interest in this analysis. In order to estimate the $\langle bP_e \rangle$ from above equation, we use fitting formulae of halo mass function as described in [300] and large scale halo bias as descirbed in [303]. We plot cumulative of
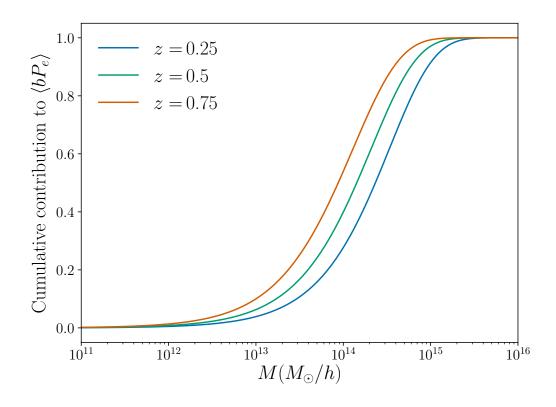
Figure 4.1: Cumulative contribution to the $\langle bP_e \rangle$ integral from theoretical esti-mates (using AGN feedback pressure profile described in §4.2.2) of Eq. 4.2.15 as a function of halo mass. Most contribution to the integral comes from halos in the range 10^{13} to $10^{15}\,M_\odot/h$. There is significant contribution to $\langle bP_e \rangle$ from halos with $M < 10^{14}\,M_\odot/h$; for current data, correlation analyses of the type considered here are the only way to probe this halo mass range.

the integrand of Eq. 4.2.15 at several redshifts in Fig. 4.1. The dominant contribution to $\langle bP_e \rangle$ comes from halos with masses in the range of about $3 \times 10^{12} \lesssim M/(M_\odot/h) \lesssim 10^{15}$.

In the two-halo limit, the galaxy-pressure cross-power spectrum then simplifies to:

$$P_{Pg}^{\text{two−halo}}(k,z) = b_g(z)\langle bP_e(z)\rangle P_{\text{lin}}(k,z). \tag{4.2.16}$$

Substituting back into Eq. 4.2.5, the two-halo contribution to the galaxy-y cross-correlation function becomes

$$\xi_{yg}^{\text{two−halo}}(R,z) = \frac{\sigma_T}{m_e c^2} b_g(z)\langle bP_e(z)\rangle$$
$$\frac{1}{1+z}\int_{-\infty}^{\infty} d\chi \, \xi_{\text{lin}}\left(\sqrt{\chi^2 + R^2}, z\right). \tag{4.2.17}$$

The integral in the above equation is the projected linear correlation function, $w_{p,lin}(R)$. So, succinctly, our model for the cross-correlation function becomes:

$$\xi_{yg}^{\text{two−halo}}(R,z) = \frac{\sigma_T}{m_e c^2} b_g(z)\langle bP_e(z)\rangle \frac{w_{p,\text{lin}}(R,z)}{1+z}. \tag{4.2.18}$$

A CMB experiment like *Planck* observes the sky convolved with a beam, which we must account for. To do this, we first transform the above equation to angular space. Since R denotes the comoving size of a halo, we have $\theta = R/\chi(z)$, where $\chi(z)$ is the comoving distance to redshift z. In Fourier space, the halo-y cross-power spectrum is:

$$C_{yg}^{\ell} = \frac{\sigma_T}{m_e c^2} b_g(z)\langle bP_e\rangle \int d\theta \, 2\pi\theta J_0(\ell\theta) \frac{w_{p,\text{lin}}(\chi(z)\theta)}{1+z}, \tag{4.2.19}$$

161

where J_0 is the Bessel function of the first kind.

Multiplying this power spectrum by the beam function, $B(\ell)$, and then inverse Fourier transforming, we obtain:

$$\xi_{yg}^{s,\text{two−halo}}(\chi\theta, z) = \int \frac{d\ell\,\ell}{2\pi} J_0(\ell\theta) C_{yg}(\ell) B(\ell). \qquad (4.2.20)$$

We thus obtain in the two-halo limit (see also [314]):

$$\xi_{yg}^{s,\text{two−halo}}(R, z) \approx \frac{\sigma_T}{m_e c^2} b_g(z) \langle bP_e(z) \rangle \frac{w_{\text{lin}}^S(R, z)}{1 + z}, \qquad (4.2.21)$$

where $w_{\text{lin}}^S(R, z)$ is the projected linear correlation function, smoothed by the beam as shown above.

Eq. 4.2.21 describes the cross-correlation between galaxies and y at a fixed redshift. The redMaGiC galaxies, however, are distributed over a broad redshift range, so we must average Eq. 4.2.21 over the normalized redshift distribution, $\omega^i(z)$, of the ith redMaGiC galaxy bin. Since the bias and bias-weighted pressure are expected to evolve slowly with redshift, and since the individual redshift bins of the redMaGiC galaxies are only $\Delta z \sim 0.15$, we can define effective parameters over the whole bin, b_g and $\langle bP_e \rangle$. The projected correlation function is also averaged across the redshift bins in this way. Our final model for the galaxy-y cross-correlation is given by:

$$\xi_{yg}^{s,i}(R >> r_{\text{vir}}, \bar{z}) \approx \frac{\sigma_T}{m_e c^2} b_g^i \langle bP_e \rangle^i \int_0^\infty \frac{w_{\text{lin}}^S(R, z)\omega^i(z)}{1 + z} dz. \qquad (4.2.22)$$

Given a cosmological model, $w_{\text{lin}}^S(R)$ is fixed. Consequently, specifying b_g and $\langle bP_e \rangle$ is sufficient to specify the galaxy-y cross-correlation function. As we will

show below, we can determine b_g using fits to the galaxy-galaxy correlation function, allowing us to use the galaxy-y measurements to solve for $\langle bP_e \rangle$.

4.2.2 Pressure profile model

Until now, we have been agnostic about the form of the halo pressure profile, $P_e(r, M, z)$. [22] (hereafter [22]) measured the pressure profiles of halos in hydrodynamical simulations, and we will use fitting functions from those measurements in our analysis below. The [22] fits use spherical overdensity definitions of the halo mass and radius, M_Δ and R_Δ, respectively. These are defined such that the mean density within R_Δ is Δ times critical density, $\rho_{\rm crit}(z)$, i.e.:

$$M_\Delta = \Delta \frac{4}{3} \pi R_\Delta^3 \, \rho_{\rm crit}(z). \tag{4.2.23}$$

We will use both $\Delta = 200$ and $\Delta = 500$ definitions below where convenient. The [22] pressure profile fitting function is then a generalized NFW model:

$$P(x = r/R_\Delta, M_\Delta, z) = P_\Delta P_0 (x/x_c)^\gamma \left[1 + (x/x_c)^\alpha \right]^{-\beta}, \tag{4.2.24}$$

where γ, α, β and x_c are redshift and mass dependent parameters of the model and the pressure normalization, P_Δ, is given by:

$$P_\Delta = \Delta \, \rho_{\rm crit}(z) \frac{\Omega_b}{\Omega_m} \frac{GM_\Delta}{2R_\Delta}, \tag{4.2.25}$$

where Ω_b and Ω_m are the baryon and matter fractions, respectively, at redshift $z = 0$. Because of significant degeneracy between the parameters, [22] set $\alpha = 1.0$ and $\gamma = -0.3$.

The free parameters of the [22] fits are then P_0, x_c and β. [22] additionally modelled the mass and redshift dependence of these parameters using fits of the form

$$A = A_0 \left(\frac{M_{200}}{10^{14} M_\odot} \right)^{\alpha_m} (1 + z)^{\alpha_z}, \qquad (4.2.26)$$

where A represents P_0, x_c or β. The best fit parameters are given in Table 1 of [22].

[22] considered different models for gas heating, described in more detail in [23] (hereafter [23]). In our analysis of the data we primarily rely on the 'shock heating' model from [23]. In this model, gas is shock heated during infall into the cluster potential; no additional energy sources or cooling models are included. Below, we will extend this model to include the possibility of additional energy sources, which we will use the data to constrain. For the purposes of generating simulated y maps, we will also employ the AGN feedback model from [23], which includes a prescription for radiative cooling, star formation, and supernovae feedback, in addition to AGN.

The quantity $\langle bP_e \rangle$ depends on the full pressure profile of the halos, and is therefore sensitive to its behavior at large r. At distances $r \gtrsim 2R_{200}$, [22] found that the pressure profile fits could depart from the mean profile in simulations by more than 5%. In our analysis, when computing $\langle bP_e \rangle$, we will truncate the model pressure profiles at $r = 3R_{500}$. We will consider the impact of varying this choice in §4.5.2. Additionally, the $\langle bP_e \rangle$ integral receives some contribution from $M \sim 10^{13} M_\odot / h$ halos, below the halo mass limit of the [23] simulations.

Consequently, when we model $\langle bP_e \rangle$ we will effectively be extrapolating the [23] fits to a regime just below where they were calibrated.

4.2.3   Model for additional energy sources

The main purpose of our analysis is to constrain the amount of energy in the halo gas relative to that expected from gravitational collapse. The energetics of the halo gas could be changed relative to the gravitational expectation by processes such as AGN feedback and cooling. As described above, the observable quantity $\langle bP_e \rangle$ is sensitive to the total thermal energy in halos in the mass range from about 10^{13} to $10^{15} M_\odot$. To constrain departures from the purely gravitational energy input to the gas, we adopt the model

$$E_T(M) = E_T^{\mathrm{sh}}(M)(1 + \alpha(M)), \qquad (4.2.27)$$

where $E_T^{\mathrm{sh}}(M)$ is the thermal energy computed as in Eq. 4.2.11 using the shock heating model for the pressure profile from [22] (i.e. gravitational energy input only, and no cooling). We adopt a simple phenomenological model for $\alpha(M)$:

$$\alpha(M) = \begin{cases} \alpha & \text{if } M < M_{\mathrm{th}} \\ 0 & \text{if } M > M_{\mathrm{th}} \end{cases}, \qquad (4.2.28)$$

where α is a constant. The motivation for introducing M_{th} is that for very massive halos, we expect the gravitational energy to dominate over all other energy sources. Below, we will set $M_{\mathrm{th}} = 10^{14} M_\odot$, although we will also consider the impact of taking $M_{\mathrm{th}} \to \infty$.

We emphasize that $\langle bP_e \rangle$ is sensitive to the *total* thermal energy in halos. Any process which changes the pressure profile, but does not change the total thermal energy content should not change $\langle bP_e \rangle$. Such process might include, for instance, bulk motions of gas. An additional point worth emphasizing is that the $\langle bP_e \rangle$ measurements for a particular redshift bin constrain the total thermal energy in the halos at that redshift. This thermal energy could be impacted by heating or cooling at *higher* redshift. For instance, AGN feedback at $z > 1$ could impact the measured $\langle bP_e \rangle$, provided that gas has not had sufficient time to cool by the redshift of observation.

4.2.4 Model for galaxy-galaxy clustering

At fixed cosmology, Eq. 4.2.21 shows that the galaxy-y cross-correlation in the two-halo regime is completely determined once $\langle bP_e \rangle$ and b_g are specified. We can break the degeneracy between the two quantities using information from galaxy clustering, which is sensitive to b_g, but not $\langle bP_e \rangle$. By performing a joint fit to the galaxy-y and galaxy-galaxy correlation functions, we can therefore constrain $\langle bP_e \rangle$ as a function of z.

To constrain b_g we rely on measurements of galaxy-galaxy clustering. We now develop a model for this observable in the two-halo regime. The power spectrum

166

of the galaxies in the two-halo regime is given by:

$$P_{gg}^{\text{two-halo}}(k,z) =$$

$$\left[\int dM \frac{dn}{dM} \frac{N(M,z)}{\bar{n}(z)} u_m(k,M,z) b(M,z) \right]^2 P_{\text{lin}}(k,z). \quad (4.2.29)$$

In the two-halo regime, we can take the low-k limit for the dark matter halo

profile $u_m(k,M,z)$, yielding:

$$P_{gg}^{\text{two-halo}}(k,z) =$$

$$\left[\int dM \frac{dn}{dM} \frac{N(M,z)}{\bar{n}(z)} \left\langle \frac{\rho}{M} \right\rangle b(M,z) \right]^2 P_{\text{lin}}(k,z). \quad (4.2.30)$$

Using the same definition of b_g as in Eq. 4.2.14, we find the galaxy-galaxy

power spectrum to be:

$$P_{gg}^{\text{two-halo}}(k,z) = b_g(z)^2 P_{\text{lin}}(k,z). \quad (4.2.31)$$

The Limber approximation [189, 191] can then be used to relate the 3D power

spectrum to the harmonic-space power spectrum on the sky:

$$C_{gg}(\ell) = \int d\chi \frac{q_g^2(z)}{\chi^2} P_{\text{lin}} \left(\frac{\ell + 1/2}{\chi}, \chi \right), \quad (4.2.32)$$

where q is the weight function given by:

$$q_g(z) = b_g \omega(z) \frac{dz}{d\chi}. \quad (4.2.33)$$

The angular correlation functions can then be related to the harmonic cross-

spectra for any given redshift bin i via:

$$w^{ii}(\theta) = \sum_\ell \frac{2\ell + 1}{4\pi} P_\ell (\cos(\theta)) C_{gg}^{ii}(\ell) \quad (4.2.34)$$

where $P_\ell(\cos(\theta))$ is the Legendre polynomial of the ℓ-th order. We note that this model is equivalent to that employed in the [89] analysis, which uses the same galaxy clustering measurements as employed here.

4.3   Data

4.3.1   DES `redMaGiC` catalog

The primary goal of this analysis is to constrain the redshift evolution of the pressure of the Universe by measuring the correlation between galaxies and maps of the Compton-y parameter. To this end, we require a sample of galaxies that have well measured redshifts, and which can be detected out to large redshift. An ideal catalog for this purpose is the `redMaGiC` catalog [89] derived from first year (Y1) DES observations.

The Dark Energy Survey is a 5.5 year survey of 5000 sq. deg. of the southern sky in five optical bands (g, r, i, z, and Y) to a depth of $r > 24$. In this analysis, we use first Y1 data from DES covering approximately 1321 sq. deg. to roughly $r \sim 23$ [78, 109].

`redMaGiC` galaxies are identified in DES data based on a fit to a red sequence template using the methods described in [260]. The photometric accuracy of the selection is high: $\sigma_{\text{rmg}} = 0.0167(1 + z)$. For details of the validation of the `redMaGiC` redshift estimates, see [260] and [58].

168

Throughout this analysis, we use the same selection of galaxies and redshift binning as used in the analysis of [89]. Using the same selection as in [89] is advantageous since systematic errors in the redshift estimates for this sample have been thoroughly studied in [58], and the impact of observational systematics on redMaGiC galaxy detection have been studied in [100].

The Y1 redMaGiC sample was divided into five redshift bins from $z = 0.15$ to $z = 0.9$. The first three redshift bins use a luminosity cut of $L/L_* > 0.5$, while the fourth and fifth redshift bins use cuts of $L/L_* > 1.0$ and $L/L_* > 1.5$, respectively, where L_* is computed using a Bruzual and Charlot model [48], as described in [260]. Given the small number of galaxies in the fifth bin and the potential for higher contamination of the galaxy-y cross-correlation measurements in that bin (see below), we restrict our analysis to the first four redshift bins.

Galaxies are placed into redshift bins based on their photometric redshift as estimated by the redMaGiC algorithm [260]. redMaGiC assigns a redshift estimate, z_{rmg}, to each galaxy. The estimated $\omega(z)$ for each bin is then computed as a sum of Gaussian probability distribution functions centered at z^i_{rmg}, with standard deviation σ_{rmg}. The corresponding redshift distributions are shown in Fig. 4.2.
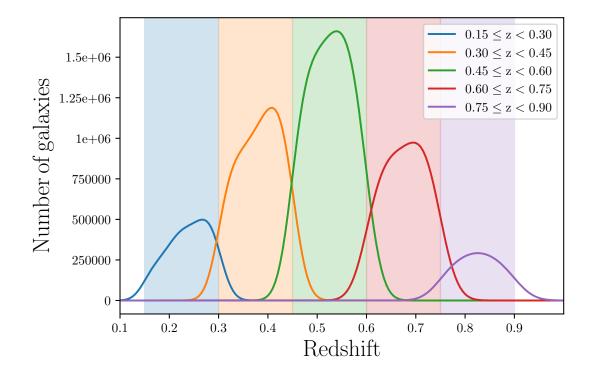
Figure 4.2: Redshift distributions of Y1 redMaGiC galaxies used in this analysis. The galaxy sample is divided into five redshift bins, which are identical to the ones used in [89]. We only use the first four of these bins in the present analysis, as described in §4.3.1. The integral of each curve over dz is equal to the number of galaxies in the bin. In total, the sample contains approximately 600,000 galaxies.

4.3.2 *Planck* **maps**

We correlate the `redMaGiC` galaxies with maps of the Compton-y parameter derived from *Planck* data. *Planck* observed the sky in nine frequency bands from 30 GHz to 857 GHz from 2009 to 2013 [239, 299]. The resolution of the *Planck* experiment is band dependent, varying from roughly 30 arcminutes at the lowest frequencies to 5 arcminutes at the highest.

We use the publicly available 2015 *Planck* High Frequency Instrument (HFI) and Low Frequency Instrument (LFI) maps in this analysis [235, 241] and construct Compton-y maps using the Needlet Internal Linear Combination (NILC) algorithm that is described in [83] and [133]. For comparison, we will also make use of the publicly available *Planck* estimates of y described in [10] which uses the same set of temperature maps.

While constructing various versions of Compton-y map (see below), we use the same galactic mask as used in [10] which blocks 2% of the sky area (mostly in the galactic center). We also use the point source mask which is the union of the individual frequency point-source masks discussed in [236].

4.3.3 **Simulated sky maps**

One of the primary concerns for the present analysis is possible contamination of the estimated y maps by astrophysical foregrounds. The most significant potential contaminant is the cosmic infrared background (CIB), which is predomi-

nantly sourced by thermal emission from galaxies throughout the Universe. CIB emission comes from a broad range of redshifts, roughly $z \sim 0.1$ to 4.0, with the bulk of emission coming from $z \gtrsim 1$ [270]. The majority of CIB emission is therefore beyond the redshift range of the galaxies considered in this analysis, and will therefore be uncorrelated with the redMaGiC galaxies. Such emission could constitute an additional noise source, but will not in general lead to a bias in the estimated galaxy-y cross-correlation functions.

However, some CIB emission is sourced from $z \lesssim 0.7$, which overlaps with the redshift range of the redMaGiC galaxies. Since the CIB is traces the large-scale structure, it will be correlated with the redMaGiC galaxies. Consequently, any leakage of CIB into the estimated y maps over this redshift range could result in a bias to the estimated galaxy-y cross-correlation functions.

Another possible source of contamination is bright radio sources. Although the brightest sources are detected and masked, there will also be radio point sources that are not individually detected. For instance, in a recent study by [282], it was found that radio sources can bias the tSZ-lensing correlation when using *Planck* data. Lastly, we may also have to worry about the potential biases and loss of signal-to-noise that may arise due to galactic dust contamination. We assess the effects of all the above mentioned biases using simulated sky maps as described below.

We rely on both the *Websky* mocks[1] and the [274] simulations. These two sets of simulations are useful in this analysis because they have produced correlated CIB maps and partially cover the frequency range used by *Planck*.

The *Websky* mocks are full sky simulations of the extragalactic microwave sky generated using the mass-Peak Patch approach, which is a fully predictive initial-space algorithm, and a fast alternative to a full N-body simulation. As described in [289], the mass-Peak Patch method finds an overcomplete set of just-collapsed structures through coarse-grained ellipsoidal dynamics and then resolves those structures further. These maps are provided for frequencies 143, 217, 353, 545, and 857 GHz which are very similar to the *Planck* HFI channels.

The [274] simulations are another set of full sky simulations which provide maps for the cosmic microwave background, tSZ, kinetic SZ, populations of dusty star forming galaxies, populations of galaxies that emit strongly at radio wavelengths, and dust from the Milky Way galaxy. Maps are provided at six different frequencies: 30, 90, 148, 219, 277, and 350 GHz which are very similar to the *Planck* LFI channels and some of the HFI channels. These sets of maps allow us to directly test the effects of bright radio sources and galactic dust on the Compton-y and its cross-correlation with halos that populate redMaGiC -like galaxies.

We generate simulated sky maps in Healpix[2]format by combining the var-

---

[1] mocks.cita.utoronto.ca

[2] healpix.jpl.nasa.gov

ious component maps from the simulations described above. For the *Websky* mocks, we combine Compton-y, lensed CMB and CIB; for the Sehgal simulations, we combine Compton-y, lensed CMB, CIB, radio galaxies and Milky Way galactic dust emission. The "true" sky maps are then convolved with Gaussian beams with frequency-dependent full width half maxima (FWHM) corresponding to the *Planck* data. Finally, we add *Planck*-like white noise to each channel at the levels given in Table 6 of [237].

4.3.4 MICE and Buzzard N-body simulations

In addition to the estimation of y from the *Planck* maps, the other major step in our analysis is the inference of $\langle bP_e \rangle$ from the measured correlation functions. In order to test the methodology and assumptions involved in this step of the analysis, we rely on simulated redMaGiC galaxy catalogs and y maps. The simulations used for this purpose are the MICE [57,115,117] and Buzzard [87] N-body simulations. Both simulations have been populated with galaxy samples approximating redMaGiC .

MICE Grand Challenge simulation (MICE-GC) is an N-body simulation run on a 3 Gpc/h box with 4096^3 particles produced using the Gadget-2 code [287]. The mass resolution of this simulation is $2.93 \times 10^{10} M_\odot/h$ across the full redshift range that we analyze here ($z < 0.75$), and halos are identified using a FoF algorithm using a linking length of 0.2. These halos are then populated with galaxies

using a hybrid sub-halo abundance matching and a halo occupation distribution (HOD) approach, as detailed in [57]. These methods are designed to match the joint distributions of luminosity, $g-r$ color, and clustering amplitude observed in SDSS [329]. The construction of the halo and galaxy catalogs is described in [74]. A DES Y1-like catalog of galaxies with the spatial depth variations matching the real DES Y1 data is generated as described in [194]. MICE assumes a flat ΛCDM cosmological model with $h = 0.7$, $\Omega_m = 0.25$, $\Omega_b = 0.044$ and $\sigma_8 = 0.8$.

Buzzard is a suite of simulated DES Y1-like galaxy catalogs constructed from dark matter-only N-body lightcones and including galaxies with DES $griz$ magnitudes with photometric errors, shape noise, and redshift uncertainties appropriate for the DES Y1 data [87]. This simulation is run using the code L-Gadget2 which is a proprietary version of the Gadget-2 code and the galaxy catalogs are built from the lightcone simulations using the ADDGALS algorithm [87, 194, 321]. Spherical-overdensity masses are assigned to all halos in Buzzard . Buzzard assumes a flat ΛCDM cosmological model with $h = 0.7$, $\Omega_m = 0.286$, $\Omega_b = 0.047$ and $\sigma_8 = 0.82$.

We generate mock Compton-y maps for the N-body simulations by pasting y profiles into mock sky maps at the locations of simulated halos. The y profile used for this purpose is the AGN feedback model (with $\Delta = 200$) from Table 1 of [22]. This approach to generating Compton-y maps misses contributions to y from halos below the resolution limit of the simulation. However, given that

175

Buzzard and MICE identify halos above $3 \times 10^{12} M_\odot/h$ and $10^{11} M_\odot/h$, respectively, Fig. 4.1 shows that for both simulations, we capture at least 95% of the contribution to $\langle bP_e \rangle$. Since the statistical errors on the simulation measurements are significantly larger than 5%, any missing contribution to $\langle bP_e \rangle$ is not important for this work. Note that since MICE uses only FoF masses, it is not strictly correct to apply the [22] profile to these halo mass estimates. However, this inconsistency should not impact our validation tests described below.

4.4   Analysis

4.4.1   Measuring the galaxy-y cross-correlation and galaxy-galaxy clustering

Our estimator for the galaxy-y cross-correlation for galaxies in a single redshift bin and in the angular bin labeled by θ_α is

$$\hat{\xi}^{yg}(\theta_\alpha) = \frac{1}{N_D} \sum_{ij}^{N_D} y_m f(\theta_{ij}) - \frac{1}{N_R} \sum_{i_R j}^{N_R} y_m f(\theta_{i_R j}), \tag{4.4.1}$$

where i (i_R) labels a galaxy (random point), m labels a map pixel, θ_{im} is the angle between point i and map pixel m, and f is an indicator function such that $f(\theta) = 1$ if θ is in the bin θ_α and $f(\theta) = 0$ otherwise. The total number of galaxies and random points are N_D and N_R, respectively. By subtracting the cross-correlation of random points with y, we can undo the effects of chance correlations between the mask and the underlying y field.

176

We measure the galaxy-galaxy correlation using the standard [178] estimator. Because we use the same catalogs, redshift bins, and angular bins as in [100], our measurements of clustering of the redMaGiC galaxies are identical to those in [100]. For both the galaxy-y and galaxy-galaxy correlations, we compute the estimators using TreeCorr [163].

We measure the galaxy-y cross-correlation in 20 radial bins from 1 Mpc/h to 40 Mpc/h. We measure galaxy-galaxy clustering in 20 angular bins from 2.5 arcmin to 250 arcmin which is the binning used in [100]. However, as described below in §4.4.5, we do not include all measured scales when fitting these correlation functions, since the model is not expected to be valid at all scales. Our angular scale cut choices are validated in §4.4.6.

4.4.2 Covariance Estimation

Jointly fitting the measurements of the galaxy-y and galaxy-galaxy correlations requires an estimate of the joint covariance between these two observables. For this purpose, we use a hybrid covariance matrix estimate built from a combination of jackknife and theoretical estimates. We validate the covariance estimation in §4.4.6.

For the covariance block describing only the galaxy clustering measurements, we use the theoretical halo-model based covariance described in [173]. This covariance has been extensively validated as part of the [89] analysis.

For the block describing the galaxy-y covariance and for the cross-term blocks between galaxy-y and galaxy clustering, we use jackknife estimates of the covariance. The use of a jackknife is well motivated because several noise sources in the $\hat{y}$ map are difficult to estimate. These include noise from CIB and galactic dust. Since the jackknife method uses the data itself to determine the covariance, it naturally captures these noise sources.

The jackknife method for estimating the covariance of correlation functions on the sky is described in [223]. To construct jackknife patches on the sky, we use the KMeans algorithm[3]. We find that 800 jackknife patches is sufficient for robust covariance estimation. This means that each jackknife patch is approximately 85 arcmin across, which is approximately 1.5 times larger than our maximum measured scale for each redshift bin.

Our jackknife estimates of the cross-covariance between the galaxy-clustering and galaxy-y measurements are noisy. When applying the jackknife covariance estimation to simulations (see §4.4.6), we find that this cross-covariance is largest when it is between two of the same redshift bins, as expected. For the simulated measurements, zeroing cross-covariance between clustering and galaxy-y measurements of *different* redshift bins has no impact on the inferred $\langle bP_e \rangle$. To reduce the impact of noise in our covariance estimates, we therefore set these blocks to zero in our data estimate of the covariance. The final covariance estimate is

[3]https://github.com/esheldon/kmeans_radec

shown in Fig. C.2.

4.4.3 y map estimation

4.4.4 Overview

The y signal on the sky can be estimated as a linear combination of multi-frequency maps. The constrained internal linear combination (CILC) method chooses weights in the linear combination that:

(a) impose the constraint that the estimator has unit response to a component with the frequency dependence of y,

(b) impose a constraint that the estimator has null response to some other component with known frequency dependence,

(c) minimize the variance of the estimator subject to the constraints from (a) and (b). Below, we will consider several different analysis variations that attempt to null different components (or none at all).

Note that the more components that are "nulled," the larger the variance of the resultant estimator, since imposing the nulling condition effectively reduces the number of degrees of freedom that can be used to minimize the variance.

When forming the estimated y map with the CILC, the multi-frequency maps themselves must be decomposed into some set of basis functions, such as pixels or spherical harmonics. In this analysis, we use maps decomposed using the

needlet frame on the sphere [83, 133, 200]. The *Planck* estimate of y generated using CILC methods in the needlet frame goes under the name Needlet Internal Linear Combination (NILC) and is described in [10]. We will use both the *Planck* NILC map and also construct our own versions for the purposes of testing biases due to contamination by the CIB and other astrophysical foregrounds. A brief description of the analysis choices and methodology is given in §4.4.4.1; details are provided in Appendix C.1.

4.4.4.1 Attempting to mitigate CIB bias in the y map

The *Planck* NILC $\hat{y}$ map [10] enforces null response to components on the sky with the same frequency dependence as the CMB. This choice is well motivated, since the CMB constitutes the dominant noise source over the frequency range that has significant signal-to-noise for the estimation of y. We will refer to this choice as `unit-y-null-cmb`. We will also consider a variation that does not explicitly null any components, which we refer to as `unit-y`.

In the end, however, we only care about the cross-correlation of $\hat{y}$ with galaxies. The CMB correlates only very minimally with galaxies (due, for instance, to the integrated Sachs-Wolfe effect), and so should not result in a bias to the estimated galaxy-y cross-correlation functions. Since the CILC imposes a minimum variance condition on $\hat{y}$, explicitly nulling the CMB is not necessary for our purposes. Attempting to null the CIB, on the other hand, is well motivated

to prevent potential biases in the $\langle bP_e \rangle$ estimation; we call this method `unit-y-null-cib`. To null the CIB, one must adopt some reasonable choice for its frequency dependence. Unfortunately, the frequency dependence of the CIB signal is uncertain, and furthermore, may vary with redshift, angular scale, or position on the sky.

We determine the frequency scaling of the CIB in the Sehgal simulations and the *Websky* mocks by cross-correlating the mock halos with the mock CIB maps. To approximate the `redMaGiC` selection, we correlate halos in the mass range $2 \times 10^{13} M_\odot/h < M < 3 \times 10^{13} M_\odot/h$ and redshift range $0.45 < z < 0.6$ with the simulated CIB maps. We then measure the frequency scaling of these correlations at 100 arcmin, near the regime of interest for our $\langle bP_e \rangle$ constraints. We compare this fiducial CIB frequency dependence to *Planck* [242] and Sehgal simulations in Fig. 4.3. The *Planck* points are derived from the rms fluctuations of the CIB anisotropy spectrum over the range $200 < \ell < 2000$. We note these measurements are consistent with the frequency scaling of the mean of the CIB field, as described in [242].

Fig. 4.3 shows that the frequency dependence of the CIB in both the simulations and the *Planck* data are consistent at roughly the 10% level over the frequency range relevant to this analysis. Larger deviations are observed at 545 and 857 GHz, but these channels are not used in the y map reconstruction (see below). We also show the redshift dependence of the frequency scaling by cross-

181

correlating with halos in different redshift bins, finding some variation. As mass of halos hosting the redMaGiC galaxies is not completely certain, we also test the dependence of the CIB frequency scaling on the mass of halo used for cross-correlation.

The CIB intensity rises quickly at the higher frequency channels of *Planck*. In order to reduce potential CIB contamination of the y maps, we do not use the 545 or 857 GHz channels in our y map reconstruction. This choice differs from that made by [10], where both the 545 and 857 GHz channels were employed. We see that variations in halo selection criteria impact the frequency dependence of CIB by less than 20% for frequency channels below 545 GHz. We have found that this choice makes the reconstructed y maps less sensitive to the details of the CIB modelling, with only a minor degradation in signal-to-noise.

Finally, when analyzing the Sehgal mocks, we employ a large scale contiguous apodized mask that covers 10% of the sky (near the galactic plane) in all the temperature maps to minimize the biases that might result from bright pixels in galactic plane. To minimize similar issues due to bright radio sources, we apply a point source mask that covers radio galaxies in the top decile. This mask is similar to the point source mask provided by the *Planck* collaboration that we use in the analysis of data. Since this is a highly non-contiguous mask, we inpaint masked pixels in the temperature maps.
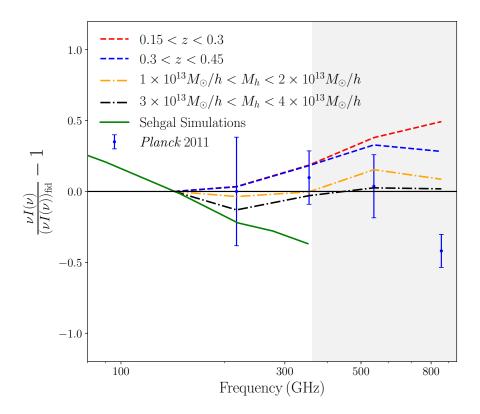
Figure 4.3: Frequency scaling of the halo-CIB correlation in the *Websky* mocks for different halo selections in redshift (dashed) and mass (dot-dashed). Measurements are shown relative to the fiducial CIB model, as described in the text. We also show the frequency scaling of the CIB in the Sehgal simulations (green solid curve), and the measurements from [239] (blue points with errorbars). For frequencies less than 545 GHz (i.e. the frequency range used in this analysis, corresponding to the unshaded region in this plot), departures from our fiducial CIB model are less than 20%, and are consistent with the *Planck* measurements.

4.4.4.2 Validation of y estimation with mock skys

We apply our NILC pipeline to the simulated skies described in §4.3.3, making the three nulling condition choices described above. We correlate the resultant y maps with a sample of halos that approximate the `redMaGiC` selection, with $2 \times 10^{13} M_\odot/h < M_h < 3 \times 10^{13} M_\odot/h$. The correlation results for the Sehgal simulation with halos in the redshift range $0.15 < z < 0.3$ are shown in Fig. 4.4. In general, all three methods yield roughly consistent results that are also in good agreement with the true correlation signal.

The CIB model of the Sehgal simulations is not complete in the sense that it does not capture CIB contributions from halos below the mass limit of the simulation. The CIB frequency model assumed in the Sehgal simulations is also somewhat out of date, and does not match current *Planck* observations. For these reasons, we additionally use the *Websky* mocks for testing potential CIB biases. The *Websky* mocks employ a model for CIB contributions from halos below the mass limit of the simulation, and also shows better agreement with recent *Planck* constraints on the CIB frequency dependence. However, because the *Websky* mocks do not include radio sources or galactic dust, we primarily rely on the Sehgal simulations for validation. We discuss tests using the *Websky* mocks in §C.2.
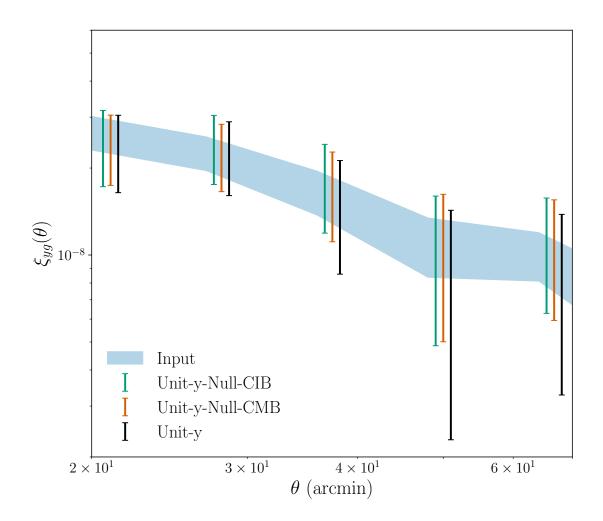
Figure 4.4: Galaxy-y cross-correlation measurements with reconstructed y maps from the Sehgal simulations. We show results for the halo bin with $2 \times 10^{13} M_\odot/h < M_h < 3 \times 10^{13} M_\odot/h$ and $0.15 < z < 0.3$. The results for other redshift bins are similar. We find that our y reconstruction methods are sufficient to recover an essentially unbiased estimate of the halo-y cross-correlation over the scales of interest.
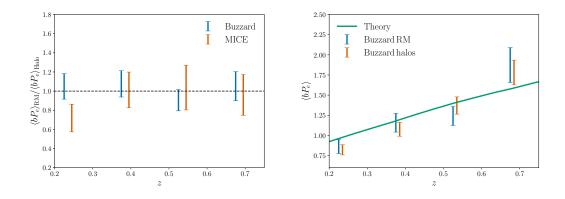
Figure 4.5: Left panel shows the ratio of $\langle bP_e \rangle$ inferred in simulations from measurements with redMaGiC galaxies to that inferred from halos. For both the Buzzard (blue) and MICE (orange) simulations, the redMaGiC galaxies and halos lead to consistent determinations of $\langle bP_e \rangle$. This supports the notion that the measurements are sufficiently far in the two-halo regime that the inference of $\langle bP_e \rangle$ is independent of the halo-galaxy connection. Right panel shows the measurements of $\langle bP_e \rangle$ in the Buzzard simulation compared to the theoretical prediction.

4.4.5 Model fitting

Our measurements of the galaxy-y and galaxy-galaxy correlations in different redshift bins can be concatenated to form a single data vector

$$\vec{d} = \left(d_1^{gg}, d_1^{gy}, d_2^{gg}, d_2^{gy}, \ldots, d_4^{gg}, d_4^{gy} \right), \tag{4.4.2}$$

where d_i^{gg} and d_i^{gy} are the clustering and galaxy-y correlations measurements in the ith redshift bin, respectively. We consider a Gaussian likelihood for the data:

$$\mathcal{L}(\vec{d} \,|\, \vec{\theta}) = -\frac{1}{2} \left(\vec{d} - \vec{m}(\vec{\theta}) \right)^T \mathbf{C}^{-1} \left(\vec{d} - \vec{m}(\vec{\theta}) \right), \tag{4.4.3}$$

where $\mathbf{C}$ is the covariance matrix described in §4.4.2, $\vec{\theta}$ represents the model parameters (galaxy bias, b_i, and bias-weighted pressure, $\langle bP_e \rangle_i$ for redshift bin i) for all redshift bins, and $\vec{m}$ represent the model vector calculated as described in §4.2. We adopt flat priors on all of the parameters, and sample the posterior using Monte Carlo Markov Chain methods as implemented in the code emcee [111].

We restrict our fits to the galaxy-galaxy correlation functions to scales $R >$ 8 Mpc/h. This restriction is imposed to ensure that the measurements are in the two-halo dominated regime, as discussed in §4.2, and is consistent with the scale cut choices motivated in [173] and [194].

The determination of appropriate scale cuts for the galaxy-y cross-correlation is somewhat more involved. As described in Appendix 4.4.3, the Compton-y map used in this analysis is smoothed with a beam of FWHM of 10 arcmin. The

beam has the effect of pushing power from small to large scales, and therefore shifts the location of the one-to-two-halo transition. For the highest redshift redMaGiC bins, this shift can be significant and hence we have to increase our scale cuts as we go to higher redshift bins. For the bins detailed in §4.3.1, we ensure that we only include the scale cuts that are approximately twice the beam size away for any given redshift bin in our analysis. This results in minimum scale cuts for each of the four redshift bins at 4, 6, 8 and 10 Mpc/h. For the maximum scale cut, we make sure that for each redshift bin, the size of an individual jackknife patch is approximately 1.5 times the maximum scale cut for that particular bin. To obtain a sufficiently low-noise estimate of the covariance matrix from the jackknifing procedure, we need of order 800 jackknife patches. These considerations yield maximum scale cuts for each of the 4 bins of 11, 17, 25 and 30 Mpc/h.

4.4.6 Validation of model assumptions and pipeline

We apply our analysis pipeline to the simulated data by correlating the mock y maps with both the simulated redMaGiC and halo catalogs. In the two-halo regime, both the redMaGiC galaxies and the halos should lead to consistent estimates of $\langle bP_e \rangle$. The left panel of Fig. 4.5 shows the ratio of these two measurements for both the Buzzard and MICE simulations. Indeed, we find that the redMaGiC and halo measurements are consistent in both simulations, a strong
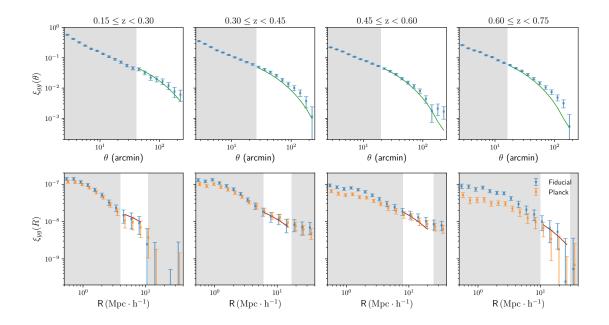
Figure 4.6: Measurements of the galaxy auto-correlation (*top row*) and Compton-y galaxy cross-correlation (*bottom row*) at different redshift bins corresponding to four redshift bins used in the analysis. Solid line is the best-fit to the fiducial model of Compton-y which is generated after removing 545GHz and 857GHz frequency channels from the analysis. Only data in the unshaded regions are used for fitting. These scale cut choices are validated in §4.4.6
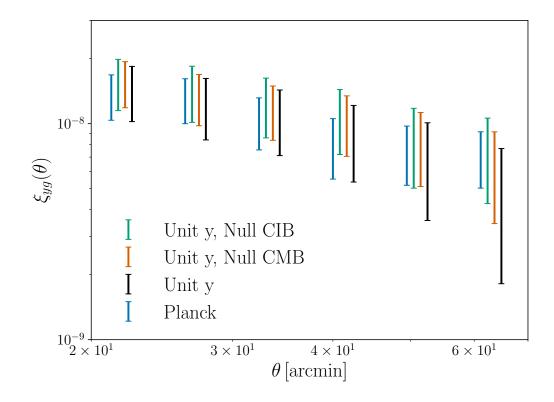
Figure 4.7: The galaxy-y cross-correlation function over the scales of interest when the component separation method used to estimate y is varied. We show the correlation measurements for the highest signal to noise redshift bin, $0.45 < z < 0.6$, but results for the other redshift bins are similar. We find that the estimated correlation function does not vary significantly when the y estimation choices are varied. Together with our validation with simulations, this constitutes strong evidence that our correlation measurements are not significantly biased by astrophysical contaminants in the estimated y.

test of our modeling assumptions and methodology.

We can also compare the recovered values of $\langle bP_e \rangle$ from the simulations to the value computed from the Eq. 4.2.15. Since we know the true cosmological and profile parameters used to generate the simulated y map, the measurement in simulations should match the theory calculation, provided our assumptions and methodology are correct. The right panel of Fig. 4.5 shows this comparison (using both halos and `redMaGiC` galaxies) for the `Buzzard` simulation. We find that the inferred values of $\langle bP_e \rangle$ are consistent with the theoretical expectation, providing a validation of our modeling, methodology, and scale cut choices. Note that we do not perform this test with the `MICE` simulation, since as discussed in §4.3.4, `MICE` uses FoF halo masses, while the [22] profile used to generate the simulated y maps requires spherical overdensity masses.

4.5   Results

4.5.1   Galaxy-y cross-correlation measurements

Our measurements of galaxy clustering (top) and the galaxy-y correlation (bottom) using DES and *Planck* data are shown in Fig. 4.6. We show the galaxy-y measurements with both our fiducial $\hat{y}$ map and the *Planck y* map in Fig. 4.6. We obtain significant detections of galaxy-y cross-correlation in all four redshift bins. Across all radial scales, the galaxy-y cross-correlation is detected at a sig-
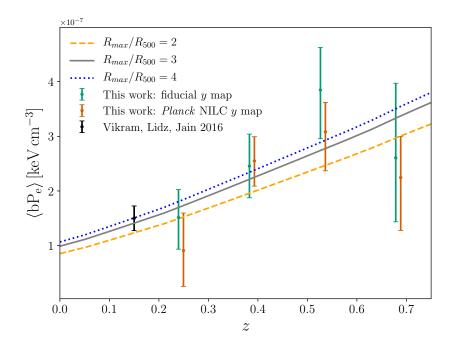
Figure 4.8: Constraints on the redshift evolution of the bias weighted pressure of the Universe (Eq. 4.2.15). We compare the datapoints obtained from this work with [314] and theory curves corresponding to shock heating model as described in [22]. For theory curves, all models are evaluated for $\Delta = 500$ and for various choices of R_{max}/R_{Δ}.

.
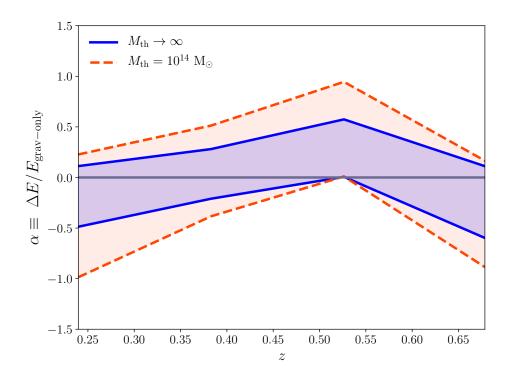
Figure 4.9: Constraints on the thermal energy of the gas as a function of red-shift. The parameter, α, defined in Eq. 4.2.28, measures the fractional departure of the gas thermal energy from the predictions of a model that only includes gravitational energy. Large α means that some process must have contributed extra thermal energy to the gas, while negative α means that the gas must have cooled. In our model, the addition (or deficit of) thermal energy impacts all halos below a threshold mass, M_{th}. We show the results for $M_{\text{th}} \to \infty$ (region between blue solid curves) and for $M_{\text{th}} = 10^{14} M_\odot$ (region between orange-red dashed curves). The $\langle bP_e \rangle$ measurements presented in this work are sensitive to halos with $10^{13} \lesssim M \lesssim 10^{15} M_\odot$, as shown in Fig. 4.1.

nificance of 12.3, 12.9, 12.2 and 8.4σ for four redshift bins in order of increasing redshift. We restrict our model fits to the scales outside of the shaded regions to ensure that we remain in the two-halo regime where our modeling approximations are valid, as discussed in §4.4. The restrictions at large scales ensure that our jackknife estimate of the covariance is accurate; this cut leads to only a small degradation in signal-to-noise.

In order to assess potential biases in our measurements of the galaxy-y cross-correlation, we repeat these measurements using the `unit-y-null-cib` and `unit-y` variations. In the absence of a correlated contaminant in the estimated y maps, different variations on the fiducial component separation choices should not lead to significant changes in the recovered mean galaxy-y cross-correlation. On the other hand, significant changes in the measured cross-correlation functions for varying component separation choices would be indicative of potential biases. Note, though, that different component separation choices can lead to significant changes in the uncertainties on the estimates of the galaxy-y cross-correlation, even in the absence of any contaminant.

The impact of changing the component separation choices on the galaxy-y cross-correlation measurements is shown in Fig. 4.7. The results are shown only for the third redshift bin of `redMaGiC` galaxies, since this has highest signal-to-noise. The results obtained for the other redshift bins are similar. We find that the different y estimation procedures yield statistically consistent measurements

194

of the galaxy-y cross-correlation over the range of scales used in this analysis. These measurements are also consistent with the cross-correlations performed with the *Planck y* map over the same range. The insensitivity of the galaxy-y cross-correlations to the component separation choices suggests that are our measurements are not biased by astrophysical contaminants.

However, as seen in Fig. 4.6, there is a trend with increasing redshift for the *Planck* measurements at small scales to be lower in amplitude than the measurements with our fiducial y map. The main difference between our fiducial y map and the *Planck* map is that we do not use the 545 and 857 GHz channels in our y reconstruction, as described in §4.4.4.1. It is difficult to determine precisely the cause of the small scale discrepancy between the two y map estimates seen in Fig. 4.6. It appears broadly consistent with contamination due to CIB, which would be expected to increase at higher redshift. We note that [10] also found evidence for CIB bias in the tSZ angular power spectrum at small scales. We note, however, that the amount and direction of this CIB bias in the y map obtained from NILC pipeline is sensitive to the frequency channels used, and that we consider here bias in galaxy-y cross-correlation rather than the y angular power spectrum considered in [10]. We emphasize, though, that over the range of scales fitted in this analysis, the estimates of the galaxy-y correlations are consistent between the different y maps.

4.5.2 Constraints on bias-weighted pressure

The quantity $\langle bP_e \rangle$, defined in Eq. 4.2.15 represents the halo bias weighted thermal energy of the gas at redshift z. Fig. 4.8 shows our constraints on this quantity as a function of redshift for two different y maps: our fiducial unit-y-null-cmb map and the *Planck* NILC y map. The measurements with the two y maps appear consistent, although precisely assessing the statistical consistency is complicated by the fact that the maps are highly correlated. We find significant detections of $\langle bP_e \rangle$ in all redshift bins considered. The multidimensional constraints on the model parameters are shown in Fig. C.3.

The black point in Fig. 4.8 shows the constraint on $\langle bP_e \rangle$ from the analysis of [314] using data from SDSS and *Planck*. The [314] point is at significantly lower redshift than the samples considered here ($z \sim 0.15$ as opposed to $0.2 \lesssim z \lesssim 0.75$). The small errorbars on the [314] measurements result from the large area of SDSS, roughly 10,000 sq. deg. Our analysis with DES Y1 data uses roughly 1300 sq. deg, although the galaxy density of the DES Y1 measurements is significantly higher than the group catalog considered by [314].

4.5.3 Constraints on feedback models

The quantity $\langle bP_e \rangle$ depends on the cosmological parameters and on the pressure profiles of gas in halos. Given the current uncertainty on the cosmological parameters from e.g. [243], and the large model uncertainties on the gas profiles

(especially at large radii), we focus on how $\langle bP_e \rangle$ can be used to constrain gas physics in this analysis. Fig. 4.1 shows that $\langle bP_e \rangle$ is sensitive primarily to halos with masses between 10^{13} and $10^{15} \, M_\odot$, with sensitivity to lower mass halos at high redshift. Because $\langle bP_e \rangle$ effectively measures the total thermal energy in halos, it is particularly sensitive to the thermodynamics of gas in halo outskirts, where the volume is large. As seen in [23], it is precisely the large-radius, high-redshift regime probed in this analysis for which the predictions of different feedback models are significantly different.

The curves in Fig. 4.8 show several predictions for the redshift evolution of $\langle bP_e \rangle$ for the 'shock heating' model of [22] and [23]. In this model, the baryons are shock heated during infall into the cluster potential, and subsequently thermalize (with no AGN feedback or radiative cooling).

We show several model predictions in Fig. 4.8, corresponding to different maximum radii for the halo gas profile. In our fiducial analysis, we compute $\langle bP_e \rangle$ by integrating the pressure profile to $3R_{500}$. Similarly, the curve with $R_{\max}/R_{500} = a$ corresponds to integrating the profile to aR_{500}. The data is consistent with shock heating models for $a = 2$, $a = 3$ and $a = 4$ with χ^2/d.o.f. of 2.9/4, 2.11/4 and 2.26/4, respectively.

For our fiducial shock heating model with $R_{\max} = 3R_{500}$, we find χ^2 per degree of freedom (d.o.f.), χ^2/d.o.f. = 2.11/4 for the cross-correlation measurements with the unit-y-null-cmb map, and $\chi^2/\nu = 3.99/4$ for the cross-correlation

with the *Planck* map. In both cases, the data are statistically consistent with the shock heating model from [22].

As described in §4.2.3, the quantity $\langle bP_e \rangle$ is sensitive to the (bias weighted) total thermal energy in the halo gas. We can use the measured $\langle P_e \rangle$ to constrain any sources of energy beyond that associated with gravitational collapse, such as could be generated by feedback. The additional energy model is described in §4.2.3, and parameterizes any additional energy contributions for halos with mass $M < M_{\text{th}}$ as a fractional excess, $\alpha(M)$, beyond that predicted by the shock heating model from [23], which only includes gravitational energy.

The constraints on $\alpha(z)$ are shown in Fig. 4.9. In the limit that the threshold mass is very large ($M_{\text{th}} \to \infty$, blue solid curve), we find that any mechanisms that change the thermal energy of the gas must not increase (or decrease) the thermal energy beyond about 30% of the total gravitational energy over the redshift range $0.15 < z < 0.75$. Note that this constraint applies to any thermal energy in the halos at that redshift. If, for instance, significant energy injection occurred at higher redshift and the gas was not able to cool by redshift z, this injected energy would still contribute to our measurement.

The red dashed curve in Fig. 4.9 shows the impact of restricting the additional energy contributions to halos with $M < M_{\text{th}} = 10^{14} M_\odot$. The limit in this case is necessarily weaker since fewer halos contribute additional thermal energy. We find that over the redshift range probed and for halos with $M < 10^{14} M_\odot$,

feedback (or other processes) must not contribute an amount of thermal energy greater than about 60% of the halo gravitational energy (or reduce the thermal energy below about 60% of the gravitational energy). This constraint demonstrates part of the power of the $\langle bP_e \rangle$ constraints: we obtain constraints on additional energy input into low mass halos, even without explicitly probing the one-halo regime.

The implications of this constraint for feedback models depends, among other things, on how black holes populate their host halos and a careful comparison with simulations of AGN feedback is warranted. However, a rough estimate may nevertheless be helpful. A plausible estimate of the energy added by black hole feedback is $E_{\text{feed}} = \epsilon_r \eta M_{\text{BH}} c^2$, where ϵ_r is the radiative efficiency and η is the fraction of the radiated energy which couples (here thermally) to the surrounding gas. Assuming $\epsilon_r = 0.1$ and $\eta = 0.05$ [92], a black hole of mass $10^9 M_\odot$ adds $E_{\text{feed}} = 9 \times 10^{60}$ ergs to the gas. This is comparable to the thermal energy resulting from gravitational collapse (i.e. in the shock heating model) of a halo of mass $M_h = 10^{13} M_\odot$, and 40% of that of a $M_h = 10^{14} M_\odot$ halo. This suggests that our constraints — limiting the extra thermal energy to about 60% of the gravitational energy for halos with $M < M_h = 10^{14} M_\odot$ — are reaching an interesting regime, and there are prospects to improve on them in the future.

It is also interesting to quantify the fraction of the total (i.e integrated over all redshifts) Compton-y parameter accounted for in our measurements, which

span roughly $z \sim 0.15$ to $z \sim 0.75$. Assuming the [22] shock heating pressure profile and $R_{\mathrm{max}} = 3R_{500}$, the total average Compton-y parameter is $\langle y \rangle = 2.9 \times 10^{-6}$, while the contribution from the redshifts of the redMaGiC sample, $0.15 \lesssim z \lesssim 0.75$ is $\langle y(0.15 \leq z \leq 0.75) \rangle = 6.7 \times 10^{-7}$. In some sense, our measurement thererefore accounts for 23% of the total Compton-y parameter (compared to only 2.5% by the analysis of [314]).

One caveat to the above statements is that our analysis necessarily misses any unclustered contribution to the thermal energy. Such a component would not be picked up in the galaxy-y cross-correlation. Furthermore, we have not accounted for the possibility of overlapping halos in our halo model calculation. If there is significant overlap of the pressure profiles, then we could be double counting some of hot gas.

4.6   Conclusions

We have measured the cross-correlation of DES-identified galaxies with maps of the Compton-y parameter generated from *Planck* data. We detect significant cross-correlation in four redshift bins out to $z \sim 0.75$. Using these measurements and measurements of galaxy clustering with the same galaxy sample, we constrain the redshift evolution of the bias-weighted thermal energy of the Universe, which we call $\langle bP_e \rangle$. Our measurement of $\langle bP_e \rangle$ extends the previous measurement of this quantity from [314] from $z \sim 0.15$ to $z \sim 0.75$. High redshifts are of

particular interest given the large uncertainties in both the modeling and data in this regime.

Several features make $\langle bP_e \rangle$ an interesting probe of gas physics. First, it can be measured robustly even without a complete understanding of the galaxy-halo connection, as demonstrated in this analysis. Second, $\langle bP_e \rangle$ is expected to be a sensitive probe of feedback models for several reasons. First, unlike pressure profile measurements around massive clusters ($M \gtrsim$ few $\times 10^{14} M_\odot$) (typically studied using x-ray measurements), the $\langle bP_e \rangle$ measurements probe mass scales down to $M \sim 10^{13} M_\odot/h$, and lower masses at high redshifts, as seen in Fig. 4.1. It is precisely the low-mass halos for which feedback is expected to have a large impact. Additionally, $\langle bP_e \rangle$ is sensitive to the outer pressure profiles ($R \gtrsim R_{\rm vir}$), as shown in Fig. 4.8. As shown in [23], various feedback prescriptions can make very different predictions in the outer halo regime. Finally, $\langle bP_e \rangle$ probes the *total* thermal energy in halos. Consequently, any process which changes the gas pressure profile, but does not inject or remove energy from the gas will not impact $\langle bP_e \rangle$. For instance, our measurements would not be sensitive to feedback processes that only move gas around without injecting any additional energy. If one is interested in separating changes to the thermal energy from changes in the bulk distribution of gas, then $\langle bP_e \rangle$ is a powerful tool to this end.

As shown in Fig. 4.8, our measurements are consistent with the shock heating model from [23], with small variations depending on the extent of the pro-

file. We use the $\langle bP_e \rangle$ measurements to constrain departures from the purely gravitational shock heating model, with the results shown in Fig. 4.9. Our measurements constrain such departures at roughly the 20-60% level.

The measurements presented here use data from only the first year of DES observations, covering roughly 25% of the full survey area of DES. We also employ several conservative data cuts: (1) the highest redshift bin ($0.75 < z < 0.9$) is removed owing to low numbers of galaxies and greater potential for CIB contamination, (2) we restrict the measurements to only the two-halo regime, (3) we remove the largest angular scales due to the limitations of our jackknife covariance estimation. With future improvements in data and methodology, these restrictions can be removed, enabling the full signal-to-noise of the measurements to be exploited.

We also note that in the present analysis, we have assumed a fixed cosmological model. This is reasonable given the uncertainties in our measurements and the precision of existing cosmological constraints. However with future observations, it may be necessary to include uncertainty in cosmological parameters.

Current and future CMB observations will also enable higher signal-to-noise and higher resolution measurements of Compton-y. Ground based CMB experiments like the South Pole Telescope [54] and the Atacama Cosmology Telescope [294] have achieved significantly lower noise levels than *Planck* over significant fractions of the sky. Ongoing CMB experiments like Advanced ACT-

Pol [140], SPT-3G [29], the Simons Observatory [6] and CMB Stage-4 [1] will yield very high signal-to-noise maps of y. One challenge facing current and future ground based experiments, though, is potentially greater contamination of Compton-y maps by foregrounds, owing to the narrower frequency coverage of these experiments.

The large apertures of ground based CMB experiments enables measurement of y at significantly higher resolution than with *Planck*. Because the analysis presented here was restricted to the two-halo regime, it is not necessarily the case that higher resolution measurements will dramatically extend the range of scales that can be exploited. Some improvement is expected, though, especially for high-redshift galaxies, for which the beam pushes into the two-halo regime. Future analyses with ground-based y maps will gain significantly from using data in the one-halo regime.

Chapter 5

Baryonic feedback constraints using weak lensing & tSZ correlations

The text in this chapter is based on the submitted manuscript [230]:

S. Pandey, M. Gatti, E. Baxter, J. C. Hill, X. Fang, C. Doux, G. Giannini, M. Raveri, J. DeRose, H. Huang, E. Moser, N. Battaglia, et al. 2021, Submitted to PRD,

Abstract

Hot, ionized gas leaves an imprint on the cosmic microwave background via the thermal Sunyaev Zel'dovich (tSZ) effect. The cross-correlation of gravitational lensing (which traces the projected mass) with the tSZ effect (which traces the projected gas pressure) is a powerful probe of the thermal state of ionized baryons throughout the Universe, and is sensitive to effects such as baryonic feedback. In Gatti et al. 2021 [123], we present tomographic measurements and validation tests of the cross-correlation between galaxy shear measurements from the first three years of observations of the Dark Energy Survey, and tSZ measurements from a combination of Atacama Cosmology Telescope and *Planck* observations. In this work, we use the same measurements to constrain models for the pressure profiles of halos across a wide range of halo mass and redshift. We find evidence for reduced pressure in low mass halos, consistent with predictions for the effects of feedback from active galactic nuclei. We infer the hydrostatic mass bias ($B \equiv M_{500c}/M_{SZ}$) from our measurements, finding $B = 1.8 \pm 0.1$ when adopting the *Planck*-preferred cosmological parameters. We additionally find that our measurements are consistent with a non-zero redshift evolution of B, with the correct sign and sufficient magnitude to explain the mass bias necessary to reconcile cluster count measurements with the *Planck*-preferred cosmology. Our analysis introduces a model for the impact of intrinsic alignments (IA) of galaxy shapes on the shear-tSZ correlation. We show that IA can have a significant impact on these correlations at current noise levels.

5.1 Introduction

The distribution and energetics of baryons within dark matter halos are significantly impacted by astrophysical feedback processes. In particular, large-scale winds driven by the supernova and active galactic nuclei (AGN) are expected to reduce the ability of gas in halos to form stars, and are therefore important ingredients in our understanding of galaxy formation [28]. At large halo mass, feedback from AGN is expected to dominate over other feedback mechanisms. Indeed, AGN feedback is sufficiently powerful that it modifies the total matter power spectrum at wavenumbers $k \gtrsim 0.1\,h/\mathrm{Mpc}$ [310]. Unfortunately, because feedback effects span a wide dynamical range — from sub-parsec scales to the scales of galaxy clusters — they are difficult to model and simulate. As a result, attempts to extract cosmological information from the matter power spectrum at small scales (e.g., with weak lensing surveys) are often limited by our ignorance of feedback [156]. Therefore, tighter observational constraints on feedback are of prime importance for our understanding of both galaxy formation and cosmology.

Because feedback changes the thermal energy and distribution of the baryons, it can change the pressure of ionized gas within halos, resulting in an observable signature in the thermal Sunyaev-Zel'dovich (tSZ) effect. The tSZ results from inverse Compton scattering of CMB photons with hot electrons, and the amplitude of the effect — typically expressed in terms of the Compton y parameter —

is directly sensitive to a line-of-sight integral of the ionized gas pressure [293]. However, because the tSZ effect is sensitive to the pressure of all ionized gas along the line of sight to the last scattering surface, it is difficult to use the tSZ by itself to probe the halo mass or redshift dependence of the halo gas pressure.

By *cross-correlating* y maps obtained from CMB observations with tracers of large scale structure observed at low redshift, contributions to y from particular subsets of halos can be isolated. Such cross-correlations therefore enable measurement of the evolution of the pressure of ionized gas over cosmic time [61, 145, 227, 228, 315].

The impact of feedback on halo pressure profiles is a function of halo mass and redshift. At large halo mass, the energy released by feedback is small compared to the gravitational potential energy of the halo, so the impact of feedback is generally less pronounced; at low halo mass, the reverse is true. For low-mass halos, feedback can push out a significant amount of gas from the halo, resulting in reduced pressure relative to expectations from self-similar models [184]. Feedback is also expected to generate significant non-thermal pressure support in low-mass halos, lowering the temperature needed to maintain equilibrium. Redshift evolution of the pressure profiles of halos is expected for several reasons, including evolving non-thermal pressure support and the fact that at fixed halo mass, halos at high redshift have deeper potential wells, making it more difficult for feedback to expel gas [184].

Here we consider the cross-correlation of the gravitational shearing of galaxy shapes with maps of the tSZ effect. As we show below (and as was pointed out previously by [24, 154, 225]), this correlation is predominantly sensitive to the pressure profiles of halos with masses $M_{200c} \sim 10^{14} M_\odot$ and $z \lesssim 1$.[1] One of the appealing features of the lensing-tSZ correlation is that — unlike the galaxy-tSZ correlation — it can be modeled without needing to understand the galaxy-halo connection. Several recent studies have measured the lensing-tSZ correlation [?, ?, ?, ?, 225].

In this work and in a companion paper (citepaper1, hereafter paper I), we present measurements and analysis of the correlation between lensing shear measurements from Year 3 observations of the Dark Energy Survey (DES) and tSZ measurements from the Atacama Cosmology Telescope (ACT) and *Planck*. DES is a six-year optical and near-infrared galaxy survey of 5000 sq. deg. of the southern sky.

ACT is a submillimeter telescope located in the Atacama desert that is currently performing the Advanced ACT survey. We use the data collected from its ACTPol receiver during 2014 and 2015. We detect the correlation between lensing and the tSZ at 21σ statistical significance, the highest signal to noise measurement of this correlation to date.

---

[1] We use $M_{\Delta c}$ to represent the mass enclosed in a sphere centered on the halo with radius chosen such that the mean enclosed density is $\Delta \rho_{\mathrm{crit}}(z)$, where $\rho_{\mathrm{crit}}(z)$ is the critical density of the Universe at the redshift of the halo.

A companion paper, paper I, presents the cross-correlation measurements, subjecting them to various systematic tests, and presents a comparison of the measurements to predictions from hydrodynamical simulations. Here, we focus on fitting the measurements with parameterized models to explore how the halo pressure profiles vary as a function of halo mass and redshift. We present constraints on the parameters of these models and on the inferred relationship between halo mass and the integrated tSZ signal. Our constraints exhibit a departure from the expectations of self-similar models at low halo mass ($M \lesssim 10^{14} M_\odot$), consistent with expectations from the impact of feedback from AGN. We translate our measurements into constraints on the so-called mass bias parameter, finding a preference for its evolution with redshift. Such redshift evolution helps to explain the mass bias values needed to reconcile cluster abundance measurements with the cosmological model preferred by *Planck* [243]. Additionally, we show that the impact of intrinsic alignments of galaxy shapes on the shear-tSZ correlation — an effect that has been ignored in previous analyses — can be significant, especially at low redshift.

The paper is organized as follows. In §5.2 we describe the shear-tSZ correlation measurements and the various models we use to fit these; in §5.3 we describe our methodology for fitting the data, including choices of parameter priors; we present our results in §5.4 and conclude in §5.5.

5.2 Measurements and Modeling

5.2.1 Measurements of the shear-y correlations

We analyze the cross-correlation between measurements of galaxy shear from DES Y3 observations [125, 278] and Compton-y maps generated by ACT [196] and *Planck* [9]. The details of the measurement process and tests of robustness to various systematics are described in detail in paper I. We summarize below the key aspects of the data and measurements relevant to the present analysis.

We use the shear catalog of the DES Y3 data as presented in [125]. The shape catalog primarily uses the `metacalibration` algorithm and additionally incorporates improvements in the PSF estimates [164] and improved astrometric methods [278]. However, this pipeline does not capture the object blending effects and shear-dependent detection biases; hence image simulations are used to calibrate this bias as detailed in [195]. This catalog consists of approximately 100 million galaxies with effective number density of $n_{\mathrm{eff}} = 5.6$ galaxies per arcmin^2 and an effective shape noise of $\sigma_{\mathrm{e}} = 0.26$.

The source galaxy sample is divided into four tomographic bins with redshift edges of the bins equal to [0.0, 0.358, 0.631, 0.872, 2.0]. The description of the tomographic bins of source samples and the methodology for calibrating their photometric redshift distributions are summarized in [219]. The redshift calibration methodology involves the use of self-organizing maps (SOMPZ) [219] which

leverage additional photometric bands in the DES deep-field observations [137] and the BALROG simulation software of [102] to characterize a mapping between color space and redshifts. The clustering redshift method is also used to provide additional redshift information in [124]. That work uses the information in the cross-correlation of the source galaxy sample with the spectroscopic data from Baryon Acoustic Oscillation Survey (BOSS) and its extension (eBOSS). Using a combination of SOMPZ and clustering redshifts, candidate source redshift distributions are drawn and provide us with the mean redshift distribution of the source galaxies and uncertainty in this distribution.

We use two y maps in this analysis, one generated from a combination of ACT and *Planck* data (described in [196]) and one using *Planck* data alone. For simplicity, we refer to these as the ACT and *Planck* y-maps, respectively. We construct the *Planck* Compton-y map using all the publicly available 2015 *Planck* High Frequency Instrument (HFI) and Low Frequency Instrument (LFI) frequency maps below 800 GHz [235, 241]. We use the map generated by the constrained Needlet Internal Linear Combination (NILC) algorithm [83, 255], which estimates the minimum variance Compton-y map as a linear combination of the temperature maps while imposing a unit-response to the frequency dependence of Compton-y and a null-response to the frequency dependence of Cosmic Infrared Background (CIB). The measurements and analysis of the cross-correlations of NILC y map with other large scale structure (LSS) tracers, as studied here,

largely removes the leakage of foreground to the measurements. The details of the implementation of this algorithm to obtain CIB de-projected y-maps used in this work are presented in Appendix A of [228].

The ACT y-map covers only the D56 region, amounting to 456 square degrees of overlap with the DES shear catalog, while the *Planck* y-map covers the full sky. Owing to the higher resolution and sensitivity of the ACT y map, we only use the *Planck* y-map over the region of the sky covered by DES, but not covered by the ACT map.

We measure two-point correlations between the galaxy shears and Compton y as a function of the angular separation of the two points being correlated. When measuring the correlations, we consider only the component of the spin-2 shear field orthogonal to the line connecting the two points being correlated, i.e., the tangential shear γ_t. The y-γ_t correlation, which we represent with $\xi_{\gamma_t,y}(\theta)$, is expected to contain all of the physical signal while being robust to additive systematics in the shear field. An added advantage of this quantity is that it can be computed using the shear field directly, without constructing a lensing convergence map from the shear catalog.

The final tomographic measurements of $\xi_{\gamma_t y}$ using both the *Planck* and ACT Compton-y maps are shown in Fig. 5.1. The correlation is detected at 21σ across all bins. The shaded regions correspond to angular scales that are not included in our fits (note that they are different for the *Planck* and ACT Compton-y map

correlations). These scales are excluded in order to reduce the biases from the non-linear intrinsic alignment of source galaxies and other effects at small scales that we do not include in our model (see further discussion in §5.3).

5.2.2 Halo model for the shear-y correlations

Owing to decreasing signal-to-noise at very large angular scales and possible large-scale systematics, we restrict our analysis to scales below 250 arcminutes. For simplicity, then, we adopt a flat sky approximation. In this case, the two-point angular correlation, $\xi_{\gamma_t y}(\theta)$, between galaxy shears in tomographic bin i, and Compton-y can be related to the angular cross-power spectrum, $C_{\kappa y}(\ell)$, between the lensing convergence, κ^i, and Compton-y via:

$$\xi^{ij}_{\gamma_t y}(\theta) = \int \frac{d\ell\,\ell}{2\pi} J_2(\ell\theta) C^{ij}_{\kappa y}(\ell), \tag{5.2.1}$$

where J_2 is the second-order Bessel function. Here, j labels the y map (i.e. either *Planck* or ACT), and i labels the redshift bin of the galaxy lensing measurements.

We model $C^{ij}_{\kappa y}(\ell)$ using a halo-model framework. We will initially keep our discussion quite general, as the same modeling framework can be used (with small adjustments) to describe all of the cross-spectra needed to build our final model. We use A and B to denote two tracers of the large scale structure, for instance, lensing and Compton-y.

In the halo model [69], the cross-power between A and B can be written as the sum of a one-halo term and a two-halo term. The one-halo term is given by
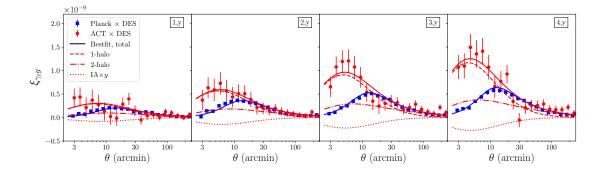
Figure 5.1: Measurements of our observable, $\xi_{y\gamma_t}$, using the DES Y3 shear catalog split into four tomographic bins and Compton-y map from Planck and ACT (see paper I for details). The shaded regions denote our scale cuts and are excluded in this analysis as they receive contributions from the cosmic infrared background and higher-order intrinsic alignment than our fiducial model. The light shaded region corresponds to the scale cuts for the *Planck*×DES, and the dark region corresponds to the ACT×DES datavectors, respectively. We show the total best-fit using solid lines for both the datavectors as well using the model detailed in §5.2. This total best-fit is decomposed into 1-halo, 2-halo, and intrinsic alignment (IA) correlations that are depicted using dashed, dot-dashed and dotted lines respectively for ACT×DES datavector. Note that the *Planck* and the ACT Compton-y maps have different beam sizes which impact the measurements in the small scales and we forward model the impact of beam in our theory model.

an integral over redshift (z) and halo mass (M):

$$C_{AB;1h}^{ij}(\ell) = \int_{z_{min}}^{z_{max}} dz \frac{dV}{dzd\Omega} \int_{M_{min}}^{M_{max}} dM \frac{dn}{dM} \bar{u}_A^i(\ell,M,z) \, \bar{u}_B^j(\ell,M,z), \qquad (5.2.2)$$

where dV is the cosmological volume element, $d\Omega$ is the solid angle constructed by that element and dn/dM is the halo mass function which we model using the [301] fitting function. In the following sub-sections we will describe the modeling of the multipole-space kernels, $\bar{u}_A^i(\ell,M,z)$ and $\bar{u}_B^j(\ell,M,z)$ of various LSS tracers. In particular we describe in detail the modeling of the lensing profile (through the convergence field, κ) and intrinsic alignment (I) for any tomographic bin i as well as Compton-y. We find that using $M_{min} = 10^{10} M_\odot/h$, $M_{max} = 10^{17} M_\odot/h$, $z_{min} = 10^{-2}$ and $z_{max} = 3.0$ ensure that the above integrals are converged.

The two-halo term is given by:

$$C_{AB;2h}^{ij}(\ell) = \int_{z_{min}}^{z_{max}} dz \frac{dV}{dzd\Omega} b_A^i(\ell,z) \, b_B^j(\ell,z) \, P_{lin}(k,z), \qquad (5.2.3)$$

where $P_{lin}(k,z)$ is the linear matter power spectrum and $k = (\ell + 1/2)/\chi$. The terms $b_A^i(\ell,z)$ and $b_B^j(\ell,z)$ are the effective linear bias parameters describing the clustering of tracers A and B respectively. In our case, there are three tracers of interest: lensing, y, and intrinsic alignments. We describe our models for these tracers in more detail below.

5.2.3 Pressure profile models

The multipole-space kernel of Compton-y is related to the pressure profile of hot electrons (P_e) as follows:

$$\bar{u}_y^j(\ell, M, z) = b^j(\ell) \frac{4\pi r_{200c}}{l_{200c}^2} \frac{\sigma_T}{m_e c^2} \int_{x_{min}}^{x_{max}} dx \, x^2 \, P_e(x|M, z)$$

$$\times \frac{\sin(\ell x/l_{200c})}{\ell x/l_{200c}}, \quad (5.2.4)$$

where $x = r/r_{200c}$, r is the radial distance; $l_{200c} = D_A/r_{200c}$, D_A is the angular diameter distance to redshift z and r_{200c} denotes the radius of the sphere having total enclosed mean density equal to 200 times the *critical* density of the universe [169]. The term $b^j(\ell) = \exp[-\ell(\ell+1)\sigma_j^2/2]$ captures the beam of experiment j. Here $\sigma_j = \theta_j^{FWHM}/\sqrt{8\ln 2}$ and we have $\theta_1^{FWHM} = 10$ arcmin for *Planck* and $\theta_2^{FWHM} = 1.6$ arcmin for ACT Compton-y maps.[2] We choose $x_{min} = 10^{-3}$ and $x_{max} = 4$, which ensures that the above integral captures the contribution to the pressure from the extended profile of hot gas. We have verified that our conclusions remain unchanged when lowering the value of x_{max}. We have also verified that inclusion of the pixel window function of Compton-y maps has negligible impact on the theory predictions as the scales analyzed to obtain our results here are significantly larger compared to the pixel size of the maps.

---

[2]Note that the full ACT beams, including variations with observing seasons season and telescope arrays have been taken into account when creating the Compton-y map as described in [196], and only the final y-map is reconvolved with a simple Gaussian beam.

The effective tSZ bias b_y^j is given by:

$$b_y^j(\ell,z) = \int_{M_{\min}}^{M_{\max}} dM \, \frac{dn}{dM} \bar{u}_y^j(\ell,M,z) b_{\lin}(M,z), \qquad (5.2.5)$$

where $b_{\lin}$ is the linear bias of halos with mass M at redshift z which we model using the [304] fitting function.

One of the aims of this analysis is to constrain the pressure profiles of halos as a function of mass and redshift. We consider several possible pressure profile models: one based on citealiasBattaglia:2012, a modified version of this profile that allows for additional freedom to capture the impact of feedback in low-mass halos, and the model from [16]. We describe each of these models in more detail below.

Battaglia et al. 2012 profile model: For a fully ionized gas, the total electron pressure P_e^{B12} that contributes to the Compton-y signal is related to total thermal pressure $(P_{\mathrm{th}}^{\mathrm{B12}})$ as:

$$P_e^{\mathrm{B12}} = \left[\frac{4-2Y}{8-5Y} \right] P_{\mathrm{th}}^{\mathrm{B12}}, \qquad (5.2.6)$$

where Y is the primordial helium fraction that we fix to $Y = 0.24$. The total thermal pressure profile in citealiasBattaglia:2012 is parametrized by a generalized NFW form:

$$P_{\mathrm{th}}^{\mathrm{B12}}(x|M,z) = P_\Delta \tilde{P}_0 \left(\frac{x}{\tilde{x}_c} \right)^{\tilde{\gamma}} \left[1 + (x/\tilde{x}_c)^{\tilde{\lambda}} \right]^{-\tilde{\beta}}, \qquad (5.2.7)$$

where

$$P_\Delta = \frac{G \Delta M_\Delta \rho_c(z) \Omega_b}{2 R_\Delta \Omega_m}, \qquad (5.2.8)$$

for any spherical overdensity, Δ, relative to the critical density, ρ_c, and we will use $\Delta = 200$. Following citealiasBattaglia:2012, we fix $\tilde{\lambda} = 1.0$ and $\tilde{\gamma} = -0.3$. For each of the parameters $\tilde{P}_0$, $\tilde{x}_c$ and $\tilde{\beta}$, citealiasBattaglia:2012 adopts a scaling relation with mass and redshift. This scaling relation is given by the following form (shown here for the parameter $\tilde{P}_0$):

$$\tilde{P}_0(M_{200}, z) = P_0 \left(\frac{M_{200c}}{M_*} \right)^{\alpha_{\mathrm{m}}} (1+z)^{\alpha_z}, \tag{5.2.9}$$

where P_0 is the amplitude of the pressure profile at $M_{200c} = M_* \equiv 10^{14} M_{\odot}/h$ and $z = 0$, and α_{m} and α_z describe the scaling of the parameter $\tilde{P}_0$ with mass and redshift, respectively. Similar equations can be written down for the parameters $\tilde{x}_c$ and $\tilde{\beta}$ (with their respective mass and redshift power-law indices). We have experimented with changing the value of the break mass M_*, but find that our results are not very sensitive to this choice. The pressure profile parameters that are not varied are fixed to the values from Table 1 of citealiasBattaglia:2012.

Break model: The $\kappa - y$ cross-correlations receive contributions from a very wide range of halo masses (as shown in Fig. 5.2 and discussed in §5.2.6). At low halo mass, the pressure profiles of halos may depart from the citealiasBattaglia:2012 form as a result of, for example, baryonic feedback. We introduce additional freedom into our model to allow for this possibility using the formal-

218

ism described in [227]. We consider a modified version of the P_e^{B12} profile:

$$P_e^{\mathrm{B12,break}}(r|M,z) = \begin{cases} P_e^{\mathrm{B12}}(r|M,z), & M \geq M_{\mathrm{break}} \\[2ex] P_e^{\mathrm{B12}}(r|M,z)\left(\frac{M}{M_{\mathrm{break}}}\right)^{\alpha_{\mathrm{m}}^{\mathrm{break}}}, & M < M_{\mathrm{break}} \end{cases}$$

$$(5.2.10)$$

where we choose $M_{\mathrm{break}} = 2 \times 10^{14} M_{\odot}/h$ and we will treat the power-law index $\alpha_{\mathrm{m}}^{\mathrm{break}}$ as a free parameter. The location of the break is motivated by the results of simulations [184], which show a break in the self-similar scaling of integrated y with mass at roughly this mass value.

Arnaud et al. profile model: We also test the [16] profile (denoted with A10), which is another universal profile form where its parameters have been calibrated using X-ray and tSZ observations of clusters. We note that the parameter values obtained by [16] are from an analysis of high mass and low redshift clusters. The shear-y correlation will be sensitive to somewhat different halos. Another crucial assumption adopted in the model of [16] is that the clusters are in hydrostatic equilibrium (HSE), allowing for an estimate of HSE mass. However, significant non-thermal pressure support would violate this assumption. Hence, the HSE mass can be different from the true mass of the halos. The relation between these two can by parameterized by a mass bias parameter B.

The [16] profile is:

$$P_e^{\mathrm{A10}}(x|M,z) = 1.65(h/0.7)^2 \mathrm{eVcm}^{-3}$$

$$\times E^{8/3}(z)\left[\frac{M_{500c}^{\mathrm{SZ}}}{3 \times 10^{14}(0.7/h)M_\odot}\right]^{2/3+\alpha_p^{\mathrm{A10}}} p^{\mathrm{A10}}(x), \quad (5.2.11)$$

where $E(z) = H(z)/H_0$ and the generalized NFW profile $p^{\mathrm{A10}}(x)$ is given by:

$$p^{\mathrm{A10}}(x) = \frac{P_0^{\mathrm{A10}}(0.7/h)^{3/2}}{(c_{500}^{\mathrm{A10}}x)^{\gamma^{\mathrm{A10}}}\left[1 + (c_{500}^{\mathrm{A10}}x)^{\alpha^{\mathrm{A10}}}\right]^{(\beta^{\mathrm{A10}}-\gamma^{\mathrm{A10}})/\alpha^{\mathrm{A10}}}} \quad (5.2.12)$$

We adopt the best-fit values obtained from the analysis of the stacked pressure profile of *Planck* tSZ clusters, $P^{\mathrm{A10}} = 6.41$, $c_{500}^{\mathrm{A10}} = 1.81$, $\alpha^{\mathrm{A10}} = 1.33$, $\beta^{\mathrm{A10}} = 4.13$ and $\gamma^{\mathrm{A10}} = 0.31$ [7]. We also fix the parameter $\alpha_p^{\mathrm{A10}} = 0.12$ as obtained by [16] in their X-ray sample analysis. The mass obtained from the mass-pressure relation in Eq. 5.2.11 is related to the true mass of halos by the mass bias parameter, B. We consider a model with a constant mass bias parameter, where the true cluster mass M_{500c} is related to the tSZ mass used in Eq. 5.2.11 by $M_{500c}^{\mathrm{SZ}} = M_{500c}/B$ and r_{200c} in Eq.5.2.4 is replaced by $r_{200c}^{\mathrm{SZ}} = r_{200c}/(B^{1/3})$. We refer to this model as P_e^{A10c}. We also test another model, P_e^{A10z}, where the mass bias evolves with redshift as:

$$B(z) = B(1 + z)^{\rho_B} \quad (5.2.13)$$

We treat B and ρ_B as free parameters in this model.

5.2.4 Lensing model

The effective multipole-space kernel of convergence can be related to the dark-matter kernel (u_{m}) as:

$$\bar{u}_{\kappa}^{i}(\ell, M, z) = \frac{W_{\kappa}^{i}(z)}{\chi^2} u_{\mathrm{m}}(k, M),\qquad(5.2.14)$$

where $k = (\ell + 1/2)/\chi$, χ is the comoving distance to redshift z and $W_{\kappa}^{i}(z)$ is the lensing efficiency which is given by:

$$W_{\kappa}^{i}(z) = \frac{3H_0^2\Omega_m}{2c^2} \frac{\chi}{a(\chi)} \int_{\chi}^{\infty} d\chi' n_{\kappa}^{i}(z(\chi')) \frac{dz}{d\chi'} \frac{\chi' - \chi}{\chi'}.\qquad(5.2.15)$$

Here n_{κ}^{i} is the normalized redshift distribution of the source galaxies corresponding to the tomographic bin i (see [123]).

In order to model the matter multipole-space kernel we use the modeling framework similar to the one described in [209], which is written as:

$$u_{\mathrm{m}}(k, M) = \sqrt{[1 - \mathrm{e}^{-(k/k_*)^2}]} \frac{1}{\bar{\rho}} M\, W(\nu^{\eta_{\mathrm{hm}}} k, M),\qquad(5.2.16)$$

where, $\nu = \delta_{\mathrm{sc}}/\sigma(M)$ is the peak height, δ_{sc} is the collapse threshold calculated from linear-theory and $\sigma(M)$ is the standard-deviation of the linear density field filtered on scale containing mass M. The exponential factor inside the square root, depending on k_*, damps the one-halo term to prevent one-halo power from rising above linear at the largest scales (c.f., [211]). The parameter η_{hm} bloats the halo profiles, and we describe $W(k, M)$ below.

The halo window function, $W(k, M)$, has an analytical form for an NFW profile depending upon the halo concentration c [69]:

$$W(k, M)\psi(c) = [\text{Ci}(k_\text{s}(1 + c)) - \text{Ci}(k_\text{s})] \cos(k_\text{s})$$
$$+ [\text{Si}(k_\text{s}(1 + c)) - \text{Si}(k_\text{s})] \sin(k_\text{s}) - \frac{\sin(ck_\text{s})}{k_\text{s}(1 + c)}, \quad (5.2.17)$$

where $\psi(c) = \ln(1 + c) - c/(1 + c)$, $\text{Si}(x)$ and $\text{Ci}(x)$ are the sine and cosine integrals, $k_\text{s} = kr_\text{v}/c$ and r_v is the halo virial radius. The halo concentration is calculated by following the prescriptions of [49] using:

$$c(M, z) = A_\text{hm} \frac{1 + z_\text{f}}{1 + z}, \quad (5.2.18)$$

where A_hm is a free parameter. The formation redshift, z_f, is then calculated using via [249]:

$$\frac{g(z_\text{f})}{g(z)} \sigma(\zeta M, z) = \delta_c, \quad (5.2.19)$$

where we fix $\zeta = 0.01$ [49, 209] and $g(z)$ is the growth function. We numerically invert the equation (5.2.19) to find z_f for a fixed M. Following the prescription of [209], if $z_\text{f} < z$, then we set $c = A_\text{hm}$.

For the two-halo term,

$$b_\kappa^i(\ell, z) = \frac{W_\kappa^i(z)}{\chi^2} \sqrt{\left[1 - f \tanh^2\left(k\sigma_\text{v}/\sqrt{f}\right)\right]}, \quad (5.2.20)$$

where $k = (\ell + 1/2)/\chi$ and we fix $f = 0.188 \times \sigma_8^{4.29}(z)$ [209]. The parameter σ_v denoting the 1D displacement standard deviation of the matter particles in linear theory is calculated via

$$\sigma_\text{v}^2 = \frac{1}{3} \int_0^\infty \frac{P_\text{lin}(k)}{2\pi^2} \, \text{d}k. \quad (5.2.21)$$

5.2.5 Intrinsic Alignment Model

The gravitational interaction of galaxies with the underlying dark matter field leads to their coherent alignment, also known as intrinsic alignments (IA) (see [308] for a recent review). Since the alignments of galaxy shapes can be related to the underlying tidal field, intrinsic alignments can be described using perturbation theory [45, 152] or halo model [112, 272] frameworks. However, the detailed mechanism of IA depends on galaxy samples, their redshifts, host halo masses, and environments. The detailed modeling of IA, especially in one-halo and one-to-two halo transition regime, is an area of active study using data and simulations [126, 144, 166, 167, 198, 224, 265, 266, 283]. In this study, we model the effects of IA on our observable using the well studied non-linear alignment model (NLA) [45]. This model is an effective two-halo model of IA and can be used to model the one-to-two halo transition scale and larger scales. We determine the scales over which this model is robust by comparing it to a halo model of IA as described below. We expect the halo model to be a better description of the small-scale intrinsic alignments, but it is computationally intensive to evaluate, and the specific analysis choices await future studies. Therefore, we determine the scales over which the NLA model of IA is a good approximation using the procedure described below.

In the halo model framework, the multipole space profile of intrinsic align-

ment is modeled as:

$$\bar{u}_I^i(\ell, M, z) = f_s(z)\frac{n_\kappa^i}{\chi^2}\frac{dz}{d\chi}\frac{N_s(z, M)}{\bar{n}_s(z)}|\gamma_s^I(k, z, M)|, \tag{5.2.22}$$

where $f_s(z)$ is the satellite fraction, $N_s(z, M)$ is the number of satellite galaxies in halo of mass M at redshift z, $\bar{n}_s(z) = \int dM \frac{dn}{dM} N_s(z, M)$ is the number density of the satellite galaxies, and $|\gamma_s^I(k, z, M)|$ is the density weighted ellipticity of the satellite galaxies. We assume that we are dominated by blue galaxies in our source galaxy sample [265] and we model the satellite fraction, $f_s(z)$ as (see Fig. A1 of [112]):

$$f_s(z) = \begin{cases} 0.25 - 0.2z, & z < 1.0 \\ \\ 0.05, & z > 1.0 \end{cases}$$

We model the number of satellite galaxies as:

$$N_s(z, M) = \frac{1}{2}\left[1 + \text{erf}\left(\frac{\log M - \log M_{\min}}{\sigma_{\log M}}\right)\right] \times \left(\frac{M_h}{M_1}\right)^{\alpha_g} \tag{5.2.23}$$

where we fix $\log M_{\min} = 11.57$, $\sigma_{\log M} = 0.17$, $\log M_1 = 12.75$ and $\alpha_g = 0.99$. For modeling $|\gamma_s^I(k, z, M)|$, we use Eq.16 of [112]. However, in order to be conservative compared to the results of [112] (to account for differences between the DES galaxies and their galaxy samples and modeling uncertainties), we use a large value of the amplitude of one-halo IA term $a_{1h} = 0.003$.

The effective bias for the two-halo term is given by:

$$b_I^i(\ell, z) = A(z)\frac{n_\kappa^i}{\chi^2}\frac{dz}{d\chi}, \tag{5.2.24}$$

224

where the IA amplitude is modeled using a power-law scaling as:

$$A(z) = -A_{\mathrm{IA}} \left(\frac{1+z}{1+z_0} \right)^{\eta_{\mathrm{IA}}} \frac{C_1 \rho_{\mathrm{m},0}}{D(z)},$$

(5.2.25)

and we set $z_0 = 0.62$ and $C_1 = 5 \times 10^{-14} M_\odot^{-1} h^{-2} \mathrm{Mpc}^3$ [47].

We model the one-halo correlations between Compton-y and IA similar to Eq. 5.2.2 with $A = \mathrm{I}$ and $B = y$. The two-halo term is modeled similar to Eq. 5.2.3, but in order to describe the correlations on smaller non-linear scales, we use the non-linear matter power-spectrum ($P_{\mathrm{NL}}(k,z)$) obtained from the HALOFIT fitting function. This model is hence similar to the non-linear alignment model (NLA) as used previously in the calculation of the lensing cross-correlations:

$$C_{\mathrm{I}y;\mathrm{NLA}}^{ij}(\ell) = \int_{z_{\mathrm{min}}}^{z_{\mathrm{max}}} dz \frac{dV}{dz d\Omega} b_{\mathrm{I}}^i(\ell,z)\, b_y^j(\ell,z)\, P_{\mathrm{NL}}(k,z).$$

(5.2.26)

In order to mitigate systematic biases originating from complex inter-halo dynamics that might violate our assumptions described above, we use NLA as our fiducial intrinsic alignment model. We determine the scales that can be well described with this model through simulated analysis as described in §5.3. We compare theory $\xi_{\gamma_t y}$ datavectors with no IA contributions, full halo model IA, $\xi_{\gamma_t y;\mathrm{HM}}^{ij}$, and NLA model IA, $\xi_{\gamma_t y;\mathrm{NLA}}^{ij}$ (see §5.3.1 for details). Note that in order to model halo exclusion and avoid double counting of non-linear information, when predicting $\xi_{\gamma_t y;\mathrm{HM}}^{ij}$ we truncate the two-halo contribution with a window function $f^{\mathrm{2h-trunc}} = \exp\left[-(k/k_{\mathrm{2h}})^2 \right]$, where $k_{\mathrm{2h}} = 6h/\mathrm{Mpc}$ [112].

5.2.6 Final model for the shear-y correlations

The total model for the lensing-y correlation is given by Eq. 5.2.1, where $C^i_{\kappa y;\text{model}}(\ell)$ is given by:

$$C^{ij}_{\kappa y;\text{model}}(\ell) = C^i_{\kappa y;1h}(\ell) + C^{ij}_{\kappa y;2h}(\ell) + C^{ij}_{Iy;\text{NLA}}(\ell) \qquad (5.2.27)$$

We model the photometric uncertainity in our source redshift distribution $n^i_\kappa(z)$ using the shift parameters (Δz^i_κ) which modify the source redshift distributions as [172]:

$$n^i_\kappa(z) \rightarrow n^i_\kappa(z - \Delta z^i_\kappa) \qquad (5.2.28)$$

We model the multiplicative shear calibration using:

$$\xi^{ij}_{\gamma_t y}(\theta) \rightarrow (1 + m^i)\, \xi^{ij}_{\gamma_t y}(\theta) \qquad (5.2.29)$$

We treat the four shift parameters Δz^i_κ and four m^i as free parameters and marginalize over them with Gaussian priors (see Table 5.1).

In Fig. 5.2 we show the sensitivity of the measured correlations to halo mass and redshift. We use the *break model* to model the pressure profile and the parameter values of the full model (along with reference equations) are detailed in Table 5.1. We plot results for several θ values. Due to the 10 arcmin smoothing applied to the *Planck* y-map, cross-correlations between this map and DES are dominated by contribution from halos with $M_{200c} > 10^{14} M_\odot/h$. The significantly smaller beam of the ACT y-map (roughly 1.6 arcmin) means that cross-correlations between the ACT y-map and DES probe much lower halo masses

and higher redshifts.

Model	Parameter	Fiducial, Prior	Equation
	Intrinsic Alignment		
	A_{IA}	$0.5, \mathcal{U}[-0.3, 1.5]$	Eq. 5.2.25
	η_{IA}	$0.0, \mathcal{U}[-3.0, 4.0]$	Eq. 5.2.25
	Dark Matter Profile		
	A_{hm}	$2.32, \mathcal{U}[0.1, 5.0]$	Eq. 5.2.18
	η_{hm}	$0.76, \mathcal{U}[0.1, 1.0]$	Eq. 5.2.16
	Shear Calibration		
Common Parameters	m^1	$0.0, \mathcal{G}[-0.0063, 0.0091]$	Eq. 5.2.29
	m^2	$0.0, \mathcal{G}[-0.0198, 0.0078]$	Eq. 5.2.29
	m^3	$0.0, \mathcal{G}[-0.0241, 0.0076]$	Eq. 5.2.29
	m^4	$0.0, \mathcal{G}[-0.0369, 0.0076]$	Eq. 5.2.29
	Source photo-z		
	Δz_κ^1	$0.0, \mathcal{G}[0.0, 0.018]$	Eq. 5.2.28
	Δz_κ^2	$0.0, \mathcal{G}[0.0, 0.015]$	Eq. 5.2.28
	Δz_κ^3	$0.0, \mathcal{G}[0.0, 0.011]$	Eq. 5.2.28
	Δz_κ^4	$0.0, \mathcal{G}[0.0, 0.017]$	Eq. 5.2.28
	Pressure Profile		
Break Model $P_e \equiv P_e^{\mathrm{B12,break}}$	P_0	$18.1, \mathcal{U}[2.0, 40.0]$	Eq. 5.2.9
	β	$4.35, \mathcal{U}[2.0, 8.0]$	Eq. 5.2.9

	α_z	$0.758, \mathcal{U}[-6.0, 6.0]$	Eq. 5.2.9
	$\alpha_{\mathrm{m}}^{\mathrm{break}}$	$0.0, \mathcal{U}[-2.0, 2.0]$	Eq. 5.2.10
	Mass Bias		
Arnaud10 Model 1 $P_e \equiv P_e^{\mathrm{A10c}}$	B	$1.4, \mathcal{U}[0.9, 2.8]$	Eq. 5.2.11
	Mass Bias Redshift Evolution		
Arnaud10 Model 2 $P_e \equiv P_e^{\mathrm{A10z}}$	B	$1.4, \mathcal{U}[0.9, 2.8]$	Eq. 5.2.13
	ρ_B	$0.0, \mathcal{U}[-3.0, 3.0]$	Eq. 5.2.13

Table 5.1: The parameters varied in different models, their prior range used ($\mathcal{U}[X, Y] \equiv$ Uniform prior between X and Y; $\mathcal{G}[\mu, \sigma] \equiv$ Gaussian prior with mean μ and standard-deviation σ) in this analysis and the equations in the text where the parameter is primarily used.

5.2.7 Covariance model

We measure the cross-correlations of the DES shears with the ACT y-map and the *Planck* y-map. We leave a buffer region of approximately 6 degrees between the two y-maps to minimize covariance between the two measurements and ignore

covariance between these two measurements below. However, we do need to model the covariance between different angular and redshift bins.

We model the covariance, $\mathbb{C}$, of the shear and Compton-y cross-spectra as a sum of Gaussian ($\mathbb{C}^{\mathrm{G}}$) and non-Gaussian ($\mathbb{C}^{\mathrm{NG}}$) terms. The multipole-space Gaussian covariance is given by [155]:

$$
\mathbb{C}^{\mathrm{G}}(C_{\kappa,y}^{i,j}(\ell_1), C_{\kappa,y}^{l,j}(\ell_2)) = \frac{\delta_{\ell_1 \ell_2}}{f_{\mathrm{sky}}^{(j)}(2\ell_1 + 1)\Delta\ell_1}
$$
$$
\left[\hat{C}_{\kappa\kappa}^{il}(\ell_1)\hat{C}_{yy}^{jj}(\ell_2) + \hat{C}_{\kappa y}^{ij}(\ell_1)\hat{C}_{\kappa y}^{lj}(\ell_2) \right]. \quad (5.2.30)
$$

Here, $\delta_{\ell_1 \ell_2}$ is the Kronecker delta, $f_{\mathrm{sky}}^{(1)} = 0.083$ for *Planck*$\times$DES and $f_{\mathrm{sky}}^{(2)} = 0.0095$ for ACT$\times$DES are the effective sky coverage fractions; $\Delta\ell_1$ is the size of the multipole bin, and $\hat{C}_\ell$ is the total cross-spectrum between any pair of fields including the noise contribution: $\hat{C}_\ell = C_\ell + N_\ell$, where N_ℓ is the noise power spectrum of the field. For the lensing convergence, we assume

$$
N_{\kappa\kappa}^i(\ell) = \frac{\sigma_{e,i}^2}{n_{\mathrm{eff}}^i}, \quad (5.2.31)
$$

where $\sigma_{e,i}^2$ is the ellipticity dispersion and n_{eff}^i is the effective number density of source galaxies, both in the ith source galaxy bin. For the y field, we replace $\hat{C}_{yy}$ with the measured Compton-y auto-power spectrum, which captures all the contributions from astrophysical and systematic sources of noise. We use the `NaMaster` [11] algorithm to estimate this auto-power spectrum of both *Planck* and ACT Compton-y maps after accounting for their respective masks.

The non-Gaussian part can be written as

$$\mathbb{C}^{\mathrm{NG}}(C^{i,j}_{\kappa,y}(\ell_1), C^{l,j}_{\kappa,y}(\ell_2)) = \frac{1}{4\pi f^{(j)}_{\mathrm{sky}}} \mathbb{T}^{\mathrm{i,j;l,j}}_{\kappa y;\kappa y}(\ell_1\ell_2), \tag{5.2.32}$$

where we model only the 1-halo part of the trispectrum $\mathbb{T}$ as that is expected to be dominant for the large halo masses that we are sensitive to [66]. This term is modeled as:

$$\mathbb{T}^{\mathrm{i,j;l,j}}_{\kappa y;\kappa y}(\ell_1\ell_2) = \int dz \frac{dV}{dz d\Omega} dM \frac{dn}{dM} \bar{u}^i_\kappa(\ell_1)\bar{u}^j_y(\ell_1)\bar{u}^l_\kappa(\ell_2)\bar{u}^j_y(\ell_2). \tag{5.2.33}$$

Finally, we convert the multipole-space estimates of covariance to angular space using:

$$\mathbb{C}(\xi^{ij}_{\gamma_t y}(\theta_1), \xi^{lj}_{\gamma_t y}(\theta_2)) =$$

$$\frac{1}{4\pi^2} \int \frac{d\ell_1}{\ell_1} \int \frac{d\ell_2}{\ell_2} \ell^2_1 \ell^2_2 J_2(\ell_1\theta_1)J_2(\ell_2\theta_2)$$

$$\times \left[\mathbb{C}^{\mathrm{G}}(C^{i,j}_{\kappa,y}(\ell_1), C^{l,j}_{\kappa,y}(\ell_2)) + \mathbb{C}^{\mathrm{NG}}(C^{i,j}_{\kappa,y}(\ell_1), C^{l,j}_{\kappa,y}(\ell_2)) \right] \tag{5.2.34}$$

To evaluate these integrals, we use the fast-Fourier transform technique as detailed in [107]. We estimate our fiducial covariance matrix at *Planck* cosmology and fiducial parameter values as described in Table 5.1. The correlation matrix corresponding to our fiducial covariance is presented in Appendix D.1. We refer the reader to paper I for details on validation of the covariance using simulations and jackknife procedure (this validated covariance is used in the data analysis of both papers).

As described in [226] using the Compton-y auto-power spectrum, the trispectrum term (see Eq. 5.2.32, also referred to as connected non-Gaussian term, cNG)

is the dominant contributor to the non-Gaussian covariance in Compton-y correlations. The super-sample covariance makes a subdominant contribution in the presence of cNG due to large Poisson number fluctuations of massive clusters, and hence we ignore its contribution in this analysis (see [226] for details).

5.3   Data analysis

We do not expect our model to capture all physical effects over all angular scales. For instance, we expect our fiducial intrinsic alignment model to break down at small scales due to complex non-linear processes impacting the tidal field and alignment of satellite galaxies. Even though we can remove the mean CIB contamination in our Compton-y map using our constrained NILC methodology described in §5.2.1, we expect other complex small-scale systematics like the variations in the CIB spectral energy distribution (SED) across the sky to contaminate our estimated y-maps. We prevent these effects from biasing our results by excluding those angular scales that are most impacted.

5.3.1   Impact of intrinsic alignments

A comparison of our shear-y models with the halo model of IA ($\xi_{\gamma_t y;\mathrm{HM}}$), our fiducial NLA model ($\xi_{\gamma_t y;\mathrm{NLA}}$), and without any IA contribution is shown in Fig. 5.3. We also show the estimated errorbars for *Planck*×DES and ACT×DES in the figure, demonstrating our sensitivity to the IA model. Especially for the first

two tomographic bins, we see that the impact of IA can be significant relative to our errorbars. Note that we use the value of $A_{IA} = 0.5$ for the NLA model which is the mean of marginalized constraints obtained from DES-Y1 joint analysis of galaxy clustering and weak lensing [3]. Apparently, shear-y correlations have now reached the sensitivity where the impact of IA should be included for an unbiased analysis; previous analyses of the shear-y correlation have ignored the impact of IA.

In order to mitigate the biases originating from the high-order intrinsic alignment process, we estimate the scales where our fiducial NLA model is a good approximation to a more complex halo model of IA (as described in §5.2.5). We use the halo model framework as described in [112], but we expect the specific parameter values of the model to be uncertain due to differences in the colors and environment of the source galaxies as well as due to the impact of baryonic physics, which was not modeled in their simulation-based study. Therefore, being conservative, we choose the values of the parameters describing the one-halo IA profile as three times the constraints in [112]. The predicted theory curve with this configuration is shown using blue color in Fig. 5.3.

We restrict our fits to those angular scales for which the difference between our fiducial IA model and the halo-model model is small relative to our uncertainties. In particular, we set a threshold total $\Delta\chi^2 = 1$ between NLA and halo-model simulated theory curves, and require that no single redshift bin contribute

more than $1/N_{\text{bins}}$ to the total $\Delta\chi^2$, where N_{bins} is the number of redshift bins in the analysis measured for both ACT and *Planck* (i.e. $N_{\text{bins}} = 8$). For each tomographic cross-correlation $\xi^i_{\gamma_t y_j;\text{NLA}}$, we find the minimum angular separation that satisfies our χ^2 requirement and exclude data points at smaller separations. In calculating this $\Delta\chi^2$ per bin, $\mathbb{C}_{ij}$ is the covariance matrix corresponding to that specific tomographic bin and scales greater θ^{ij}_{sc}.

5.3.2 Impact of CIB

We also find that scales below 20 arcmin in the correlations between the last tomographic bin of DES shear catalog and *Planck* y-map are impacted by the leakage of CIB. Additionally, we also remove the scales below 7 arcmin for all the tomographic bins of *Planck* $\times$ DES, due to the impact of the non-trivial structure of the DES Y3 mask in the *Planck* footprint on the small scales covariance between *Planck*$\times$DES (see paper I for details on the impact of CIB and covariance validation). Note that, as the *Planck* Compton-y map has a beam of 10 arcmin, the smaller scales are heavily correlated, and we do not lose any appreciable signal-to-noise (see Fig. D.1). After the scale cuts, we are left with $N_{\text{data}} = 123$ points in our final datavector.

5.3.3 Bayesian analysis

We perform our analysis at fixed cosmology, but explore the impact of using a different cosmological parameter choice on our results. Our baseline analysis uses the best-fit flat ΛCDM model from [243], with $\Omega_{\mathrm{m}} = 0.315$, $\sigma_8 = 0.811$, $H_0 = 67.4$, $\Omega_{\mathrm{b}} = 0.0486$ and $n_{\mathrm{s}} = 0.965$. We test the impact of changing the cosmological parameters Ω_m and σ_8, which are the parameters Compton-y correlations are most sensitive to [146, 169]. To that end we use DES Year 1 constraints obtained from the joint analysis of galaxy clustering and lensing, $\Omega_{\mathrm{m}} = 0.264$ and $\sigma_8 = 0.807$ [3].

We list the set of parameters we vary in Table 5.1 along with the priors used. We use wide uninformative uniform priors on all the parameters except shear calibration and source photo-z shift parameters. We refer the reader to [219] and [195] for details on the estimation of priors on the shear calibration and source photo-z shift parameters.

We assume the likelihood to be a multivariate Gaussian:

$$\ln \mathcal{L}(\mathcal{D}|\Theta) = -\frac{1}{2}\left[\vec{\mathcal{D}} - \vec{\mathcal{T}}(\Theta)\right]^{\mathrm{T}} \mathbb{C}^{-1}\left[\vec{\mathcal{D}} - \vec{\mathcal{T}}(\Theta)\right]. \tag{5.3.1}$$

Here $\vec{\mathcal{D}}$ is the measured $\xi_{\gamma_t y}$ correlation datavector, with length N_{data}, $\vec{\mathcal{T}}$ is the theoretical prediction for the cross-correlation at the parameter values given by Θ, and $\mathbb{C}^{-1}$ is the inverse covariance matrix.

We use Polychord [134] to draw samples from the posterior:

$$\mathcal{P}(\Theta|\mathcal{D}) \propto \mathcal{L}(\mathcal{D}|\Theta)\mathrm{P}(\Theta) \qquad (5.3.2)$$

where $\mathrm{P}(\Theta)$ are the priors on the parameters of our model. We use 128 live-points as the settings of the Polychord sampler and set the length of the slice sampling chain to produce a new sample as 30. Convergence is declared when the total posterior mass inside the live points is 0.01 of the total calculated evidence. We note that the common parameters in Table 5.1 and the likelihood sampler settings are same between paper I and this paper.

5.4 Results

We now present the results of our analysis for the pressure profile models introduced in §5.2.3: the *break model* and the [16] model. We first analyze our measurements using the *break model*, obtaining the parameter constraints of this generalized NFW model, inferring physical observables from these constraints and comparing them with previous studies. Lastly, we present the constraints on the hydrostatic mass bias parameter using the [16] model and compare with previous studies.

5.4.1 *Break model*

5.4.1.1 Parameter constraints

In Fig. 5.4 we show the residuals of our fit to the data using the *break model* as described in §5.2.3. We also show the one-halo and two-halo contributions to the total best-fit curve. Note that the contribution from the one-halo term extends out to large angular scales. This behavior is because the lensing-y correlation is sensitive to massive halos, and that γ_t is a non-local quantity, with γ_t at a scale θ sensitive to the correlation function at scales below θ. Also note that for the first two tomographic bins, the sum of the one-halo and two-halo contributions is more than the total best-fit curve; this is a consequence of intrinsic alignments in our best-fit model, which acts to suppress the correlation functions.

Our best fit yields a total $\chi^2 = 150.2$ with $N_{\mathrm{data}} = 123$ data points, which corresponds to a probability-to-exceed (PTE) of 0.033 after accounting for the number of constrained model variables. In order to estimate the total constrained parameters, we compare the parameter constraints to the prior as described in [252].[3] The somewhat high value of χ^2 appears to be driven at least partly by the large-scale measurements of the shear-y correlation with ACT. Excluding scales above 100 arcmins for these measurements yields a PTE of 0.1. As the D56 region that the ACT Compton-y map covers is near the galactic plane, there could be additional sources of noise that are not modeled in our fiducial

---

[3]We use the publicly available `tensiometer` code at https://tensiometer.readthedocs.io/

covariance. We also note that in the residuals shown in Fig. 5.4, we see some evidence for departures from the model near the one-to-two halo transition regime. We find slight preference for higher pressure at the transition scales, which is particularly evident in top panels for *Planck*×DES. Our model for the shear-y correlation ignores the impact of shocks, which have recently been shown to impact the outskirts of stacked y profiles of galaxy clusters [26], and could therefore impact the shear-y correlation measurements in the one-to-two halo regime. Additionally, the assumption used in this study that the linear halo bias model describes the 2-halo correlations can be broken near the transition regime due to non-linear effects of gravity. However, given that the PTE found in our fiducial analysis is not very low, we do not pursue these possibilities further and leave them to a future study.

In Fig. 5.5 we show the constraints on the pressure profile parameters of the *break model*. The full constraints for this model at both *Planck* and DES-Y1 cosmologies on all the parameters (other than shear calibration and photo-z shift parameters, as they are prior dominated) are shown in Fig. D.2 in Appendix D.2. We find the constraints from analyzing the *Planck*-only and ACT correlations to be consistent. The correlations with the *Planck*-only map have a higher total signal to noise owing to the larger area. Note, though, from Fig. 5.1 that the smaller beam size of ACT equates to higher sensitivity to low mass and high-redshift halos.

Our results exhibit a strong degeneracy between P_0 and β, making the marginalized posterior on P_0 very weak and the marginalized posterior on β somewhat sensitive to our P_0 prior. The redshift evolution parameter, α_z, and the power-law index below the break mass, α_m^{break}, are weakly constrained when using both the ACT and *Planck* maps. The dashed line in Fig. 5.5 indicates the parameter values corresponding to the [22] model.

5.4.1.2   Inferred redshift and mass dependence of the pressure profiles

We can translate the model posterior from our fits to the shear-y correlation into constraints on the relation between the integrated halo y signal and halo mass. In Fig. 5.6 we show the $\tilde{Y}_{500} - M_{500}$ relationship inferred from the *break model* fits, where $\tilde{Y}_{500}$ is given by:

$$\tilde{Y}_{500}(M,z) = \frac{D_A^2(z)}{(500\text{Mpc})^2 E^{2/3}(z)} \frac{\sigma_T}{m_e c^2} \int_0^{R_{500c}} dr\, 4\pi r^2 \frac{P_e(r|M,z)}{D_A^2(z)}, \tag{5.4.1}$$

where $E(z)$ is the dimensionless Hubble parameter. In order to obtain the blue-shaded band in Fig. 5.6, we estimate the $\tilde{Y}_{500}-M_{500}$ relationship for 2000 samples from the posterior of the *break model* and estimate the 68% credible interval from the resulting curves.

We compare the inferred $\tilde{Y}_{500} - M_{500}$ relationship from data to the predictions from various hydro-dynamical simulations incorporating different feedback mechanisms. The OWLS REF and OWLS AGN curves correspond to the cosmo-OverWhelmingly Large Simulation (cosmo-OWLS) simulations [183,205].

OWLS REF includes the prescriptions for radiative cooling and supernovae feedback while OWLS AGN additionally includes the feedback from active AGN. The Battaglia 12 curve is derived from the [22] model. This model also incorporates prescriptions for feedback mechanisms from supernovae and AGN feedback, but because it was calibrated at cluster-scale halo masses, we do not expect these effects to be captured correctly at low halo mass. We find that at higher masses, our inferred constraints agree with all three predicted pressure profile models. However, we find evidence for a decline in $\tilde{Y}_{500}$ for halos with mass $M < 10^{14} M_\odot/h$ compared to predictions from [22] and the OWLS REF simulations. We find that our constraints are in better agreement with OWLS AGN simulations. Note that [145] also found similar results using the cross-correlation of galaxies with y.

We also predict the evolution of the bias weighted average pressure of the universe ($\langle bP_e \rangle$) from our *Break Model* constraints using:

$$\langle bP_e \rangle(z) = (1+z)^3 \int_0^\infty \frac{dn}{dM} b(M,z) E_T(M,z) dM, \qquad (5.4.2)$$

where the total thermal energy of halo of mass M at redshift z is given by:

$$E_T(M,z) = \int_0^\infty dr\, 4\pi r^2 P_e(r,M,z). \qquad (5.4.3)$$

Here $P_e(r,M,z)$ are predicted using the samples from the posterior using Eq. 5.2.10. The inferred constraints on $\langle bP_e \rangle$ following above methodology is shown in the blue band in Fig. 5.7. We compare our predictions to the previous studies that

estimated $\langle bP_e \rangle$ by analyzing cross-correlations between Compton-y and cluster catalogs [315] or galaxy catalogs [61, 170, 228] . We find a good agreement in our inference and previous studies at lower redshift with a mild deviation at higher redshift. Note that at higher redshifts ($z > 0.7$), $\langle bP_e \rangle$ receives a contribution from lower-mass halos (see Fig. 1 of [228]) that our analysis is less sensitive to. We also note that our inference assumes the validity of the halo model to even small mass halos, and hence this methodology will miss the contribution in the filaments between large clusters. These caveats can qualitatively explain the mild deviation between our inference and previous measurements at high redshift.

Next, we propagate our parameter constraints to the auto-power spectra of Compton-y. The inferred constraints are shown using the blue band in Fig. 5.8. We compare these predictions to the measurements from the Compton-y maps from *Planck* [9] at larger scales. At smaller scales, we compare our inferences with estimates from ACT [62] and the South Pole Telescope (SPT) Collaboration [253] obtained from analyzing CMB data. We find that our inferences using the *break model* is consistent with all the measurements. We also show the prediction from the [22] model. While this simulation curve provides a good fit to the *Planck* measurements, it over-predicts the auto-power spectrum at high multipoles that are dominated by high-redshift and low-mass halos. This figure highlights that inferences made using imminent higher significance measurements of the shear-y cross-correlations, particularly in the small scales from ACT and

SPT, will be crucial in establishing the consistency of the probe with Compton-y auto-correlations and comparisons with simulations.

We now use our inferred model constraints to generate constraints on the pressure profiles of halos as a function of mass and redshift. In Fig. 5.9 we show our constraints on the total thermal energy of hot gas inside r_{200c}:

$$E_{200c}(M,z) = 4\pi \int_0^{r_{200c}} dr\, r^2 P_e(r,M,z),$$ (5.4.4)

with similar predictions using the [22] model (labeled E_{200c}^{B12}). We find good agreement between our inferences and the simulation prediction for higher masses and lower redshift halos. However we see a clear departure from simulation predictions in lower mass halos. We find our inferences on the ratio $E_{200c}/E_{200c}^{\mathrm{B12}}$ are discrepant from unity in the mass range $10^{13} < M_{200c}(M_\odot/h) < 2\times 10^{14}$ at 3.0σ, 4.0σ and 5.4σ for $z = 0.1, 0.2$ and 0.4 respectively (see the left panel of Fig. 5.9). Similar conclusions were reached when extrapolating the tSZ analysis around Sloan Digital Sky Survey (SDSS) galaxy samples to smaller radii (see [12, 268]). However note that our sensitivity to the host halo masses and redshifts of the relevant SDSS galaxies used by [12] is small. Moreover, they report excess pressure compared to the predictions from the [22] model outside of the virial radius of the halos. This behavior can occur due to ejection of hot gas from inside the halos due to feedback processes, which can lower the pressure inside the halos while raising it outside the virial radius.

5.4.2   Mass bias constraints

As described in § 5.2.3, estimating the pressure profile of hot gas in halos gives a handle on its mass estimation. This is typically done using the [16] profile (see Eq. 5.2.11), assuming the hot gas exists in hydro-static equilibrium. However, several physical processes (e.g., the flow of gases in filaments) can violate this assumption and bias the mass calibration. This bias is captured using a mass bias parameter B and is typically studied in cluster mass scale halos. As the shear-y cross-correlation is sensitive to these high-mass, cluster-scale halos (see Fig. 5.2), we can infer the hydro-static mass bias from our measurements and compare them with previous studies. Calibrating cluster masses is difficult, and some recent methodologies have lead to mild tension with the ΛCDM cosmology obtained from primary CMB power spectra analysis from the *Planck* Collaboration [5, 9, 39, 71, 138, 240, 333]. This uncertainty in cluster mass calibration is the leading systematic in obtaining cosmology from cluster counts (see e.g. [153, 206, 212, 218, 317]). The tSZ cross-correlation analysis studied here can provide an independent handle on this calibration.

In Fig. 5.10, at *Planck* cosmology and with a model assuming a redshift independent mass bias parameter, we obtain marginalized constraints of $B = 1.8^{+0.1}_{-0.1}$, which translates to large $b_{\mathrm{HSE}} = (B-1)/B = 0.4^{+0.03}_{-0.04}$. In Fig. 5.11, we compare our constraints obtained using shear-y cross-correlations ($\langle \gamma_t y \rangle$) with previous studies based on the combinations of various observables, like cluster abundance

(N_c), Compton-y auto-power spectra ($\langle yy \rangle$), Compton-y bispectra ($\langle yyy \rangle$), shear-2pt auto-correlations ($\gamma_t \gamma_t$) and cross-correlations between galaxy overdensity and Compton-y ($\langle gy \rangle$).

We find that our constraints on a redshift-independent mass-bias for the *Planck* cosmology is consistent with previous analysis using tSZ cluster abundances and Compton-y power spectra [9, 41, 42, 240]. The cluster abundance and Compton-y power spectra are largely sensitive to high mass halos which occupy lower redshifts. While we do expect a non-zero mass bias due to non-thermal pressure support of hot gas in halos, this mass bias value is large compared to the predictions from hydrodynamical simulations [34] as well as analytical calculations [281] (typically preferring $b_{\mathrm{HSE}} \in [0.1, 0.2]$). Alternatively, this inconsistency can also be cast into the σ_8 parameter due to degeneracy between B and σ_8. Several low-redshift probes prefer a lower value of σ_8 compared to the constraints from primary CMB anisotropy analysis by *Planck* [3, 17, 143]. Hence lowering the value of preferred σ_8 can result in a lower value of the mass bias parameter. A previous study by [333] based on weak lensing based mass calibration, sensitive to lower redshifts, has reported a lower value of the mass bias as well as a lower value of $\sigma_8 = 0.76^{+0.04}_{-0.04}$ (see their paper for caveats about priors on Compton-y scaling relations). Similarly other studies using weak lensing based mass calibration and richness-based mass calibrations have also reported a preference for lower mass bias [149, 150, 153, 212, 317]. For exam-

ple, in a recent analysis detailing updated ACT cluster catalog, [150] estimated $b_{\mathrm{HSE}} = 0.31^{+0.07}_{-0.07}$ for clusters lying in the DES footprint with measured richness and using richness-mass relation as described in [206].[4] In a study by [158], jointly analyzing Compton-y auto power spectra, bispectra and cluster abundances has also reported a lower value of mass bias and $\sigma_8 = 0.79^{+0.02}_{-0.02}$ which is still in mild tension with hydrodynamical and analytical estimates on B. In Fig. 5.10 we also find a lower value of redshift independent B when using DES-Y1 cosmological parameters which prefers a lower value of σ_8 and Ω_{m} (see §5.3.3). This sensitivity of the mass bias parameter to cosmological parameters demands a study jointly constraining cosmological parameters and pressure profiles of halos. Note that the mass bias cannot be jointly constrained with cosmological parameters from our observable ($\langle \gamma_t y \rangle$) alone due to a large degeneracy between σ_8 and B. We defer the joint analysis of our observable with other observables, like shear-2pt auto-correlations to a future study.

As our source galaxy sample is divided into multiple redshift bins, we can probe the change in mass bias parameter with redshift using our tomographic datavector. While allowing for this redshift evolution, we obtain $B = 1.5^{+0.3}_{-0.3}$ at $z = 0$, which translates to $b_{\mathrm{HSE}} = 0.34^{+0.1}_{-0.2}$ for the *Planck* cosmology. With this model, the power-law index of the evolution of mass bias with redshift is found

---

[4]Note that this updated value of b_{HSE} is obtained from ACT DR5 catalog documentation detailed in https://lambda.gsfc.nasa.gov/product/act/actpol_dr5_szcluster_catalog_info.cfm and differs slightly from the value published in [150].

to be $\rho_B = 0.8^{+0.8}_{-1.0}$. This model makes the mass bias estimate at low redshift consistent with the estimates from previous studies using analytical calculation and simulations mentioned above as well as from cross-correlation analysis with other LSS tracers [61,170] and direct observations of clusters [97,286]. However, a previous study by [148], analyzing cross-correlations between CMB lensing and Compton-y, was sensitive to even higher redshift but reported a mass bias consistent with unity. Note that [148] used a slightly different cosmology for their analysis and probed the redshifts that are more impacted by the CIB contamination and its appropriate mitigation strategy. Similarly, an earlier analysis by [192] used shear-y correlations and obtained a lower mass bias value, but they also used a slightly different cosmology and ignored the impact of CIB which we find to be significant (see paper I). We also note that the galaxy cross-correlation analysis of [61, 170] and $q_{\mathrm{cut}} = 6$ analysis of [259] are sensitive to lower mass halos compared to our peak sensitivity (see Fig. 5.2). We defer a detailed analysis of the evolution of mass bias parameter with halo masses to a future study (c.f. [21]). Although the model of redshift evolution of mass bias awaits future data to obtain more precise constraints, this analysis shows how a redshift evolution of sign and magnitude found here can resolve apparent tensions in the inference of this quantity from different probes.

5.5 Discussion

This is the second paper in a series of two on the analysis of the cross-correlation between gravitational lensing shears from DES Y3 data and Compton-y measurements from ACT and *Planck*. The total signal-to-noise of these measurements is approximately 21, the highest significance measurement of the shear-y correlation to date. The companion paper [123] presented the measurements and systematic tests, and analyzed how well the data fit the feedback predictions from hydrodynamical simulations. In this paper, we take an alternate approach, varying the parameters describing the pressure profiles of halos in our fits to the data.

The shear-y correlation is sensitive to the pressure profiles across a wide range of halo mass and redshift. Our particular measurements are most sensitive to the pressure within halos with masses of few $\times 10^{13} M_{\odot} \lesssim M \lesssim 2 \times 10^{15} M_{\odot}$ and redshifts $z \lesssim 0.8$, as seen in Fig. 5.2. We fit the measured shear-y correlation to constrain the redshift and halo mass-dependence of the pressure profiles of dark matter halos. Our fits are performed at fixed cosmological parameters, but we present results using both the best-fit *Planck* and best-fit DES-Y1 parameters. Our main results do not depend on this choice, although our quantitative conclusions are somewhat sensitive to the assumed cosmological model.

Our main findings are as follows:

- The shear-y correlation measurements are fit reasonably well by a halo

model based on the pressure profile of [22], but which introduces additional freedom in the mass-dependence of the pressure profile for low-mass ($M < 10^{14} M_\odot$) halos (Fig. 5.4)

- Our model fits prefer lower amplitude pressure profiles at low halo mass (Fig. 5.6 and Fig. 5.9) and weakly prefer stronger redshift evolution than predicted by the [22] model

- Our inference of the amplitude of the pressure profiles of low-mass halos is consistent with predictions from hydrodynamical simulations that include the impact of AGN feedback (Fig. 5.6)

- Our findings are generally consistent with measurements of the galaxy-y correlation from [145] and [228], and constraints on the y autospectrum from SPT and ACT.

- We infer the hydrostatic mass bias from our analysis, finding that its value can change if redshift evolution is allowed (see Fig. 5.10), which can also resolve the apparent tension between this quantity obtained from different probes (see Fig. 5.11).

- We model the impact of intrinsic alignments on our analysis, finding it to have a small but non-negligible impact. Previous analyses have ignored this effect.

The shear-y correlation provides a powerful probe of the thermal energy distribution throughout the Universe. This probe also bridges the gap in the halo-mass sensitivity of galaxy-y correlations and Compton-y auto-correlations. Our measurements suggest that the thermal energy in low-mass halos ($M < 10^{14} M_\odot$) is suppressed relative to predictions that ignore the impact of AGN feedback. These findings will be crucial in estimating the impact of baryonic physics on cosmological analyses using the cosmic shear data from ongoing and future photometric surveys. We also expect inclusion of kinematic SZ (kSZ) effect and its cross-correlations with tracers of the large scale structure to provide complementary constraints on the physics of feedback (see [12, 268]). We leave a joint analysis of tSZ and kSZ effects and its cross-correlations with the shear field to a future study.

Our findings suggest that we will be able to answer important and outstanding questions related to the physics of hot gas and its cosmological implications using the lower noise Compton-y maps covering a larger area from ongoing and future CMB experiments. The imminent release of Compton-y maps from ongoing high resolution surveys like ACT and SPT, as well as future experiments like Simons Observatory[5] and CMB-S4[6] would significantly decrease the statistical uncertainty in small scales which are sensitive to smaller mass and higher redshift halos, and are therefore more sensitive to the feedback mechanisms. More-

---

[5]https://simonsobservatory.org/
[6]https://cmb-s4.org/

248

over, availability of deeper and lower noise shear catalogs from DES in coming years as well as larger scale surveys like the Euclid Space Telescope,[7] the Dark Energy Spectroscopic Instrument,[8] the Nancy G. Roman Space Telescope,[9] and the Vera C. Rubin Observatory Legacy Survey of Space and Time[10] will result in a qualitative improvement in the shear-y correlation as a probe, advancing our understanding of feedback physics.

---

[7] https://www.euclid-ec.org
[8] https://www.desi.lbl.gov
[9] https://roman.gsfc.nasa.gov
[10] https://www.lsst.org
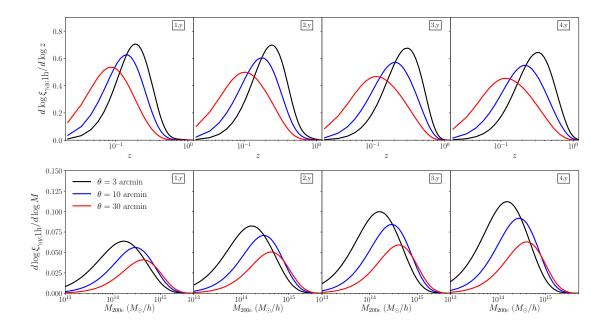
Figure 5.2: Sensitivity of the one-halo contribution to the shear-y correlation, $\xi_{\gamma_t y}$. We show the logarithmic derivative of the correlation with respect to halo redshift (top) and halo mass (bottom). Note that no Compton-y map beam smoothing is applied when producing these curves. The different columns represent the different redshift bins of the shear sample. To obtain this plot, we use the *break model* of pressure profile (as described in §5.2.3) and the parameter values of the full model are given in Table 5.1.
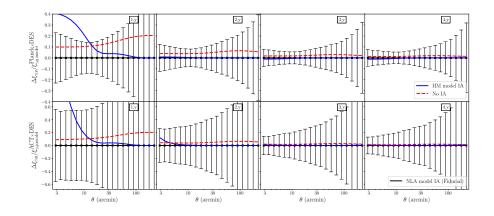
Figure 5.3: Differences between the predicted shear-y correlation ($\xi_{\gamma_t y}$) for different models of intrinsic alignment (IA), see § 5.2.5 for details. The quantity $\Delta\xi_{\gamma_t y}$ is the difference relative to our fiducial model (NLA), and we normalize all curves by this model. Note that due to the different beam sizes of the *Planck* (top row) and ACT (bottom row) y-maps, the models for these two datasets are different. The error-bars indicate the uncertainty on the model using the angular binning applied in the data analysis. We see that in some cases, the difference between the models that include IA and the model without IA can approach a significant fraction of the uncertainty on the measurements. The gray regions indicate the scale cuts used in our analysis (see § 5.3 for details). While determining these scale cuts, we impose the criteria that the difference in χ^2 between the predictions from the two IA models is less than 1/8 (where χ^2 is computed using the covariance used to analyze the data). This ensures that the total difference in χ^2 across all bins is less than one. We restrict our analysis to scales larger than this threshold to minimize the impact of uncertainty in the IA model on our analysis.

251
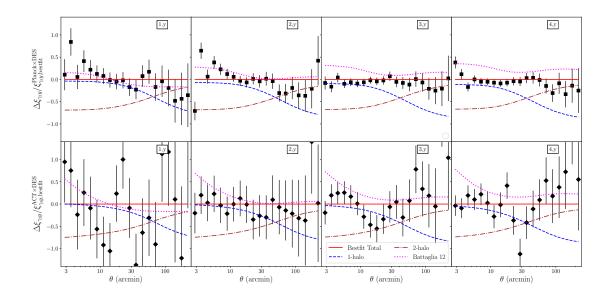
Figure 5.4: Residuals of the best-fit to the *Planck* × DES (top) and ACT × DES (bottom) shear-*y* correlation measurements, using the *break model* of pressure profile (see §5.2.3). Different columns represent the different redshift bins of the lensed source galaxy sample. We show the contributions to the total best-fit from 1-halo and 2-halo terms using blue dashed and brown dot-dashed curves (see Eq. 5.2.27). We also compare with the predictions for shear-*y* correlations when using preferred values of the pressure profile parameters from [22] fitting function with magenta dotted line.
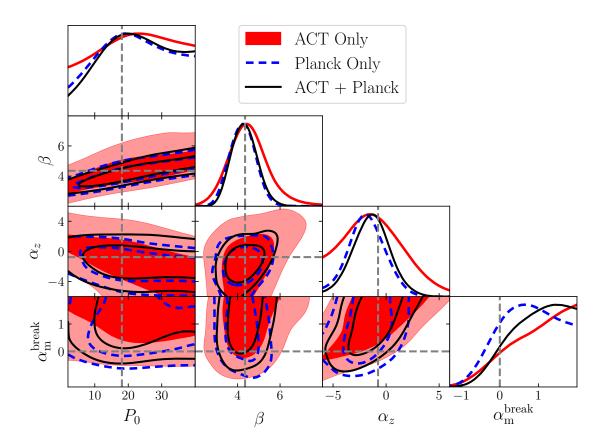
Figure 5.5: Constraints on the pressure profile parameters from the *break model* when using the Compton-*y* map from ACT only, *Planck* only and both. The gray dashed lines indicate the preferred values of the parameters from [22] fitting function.
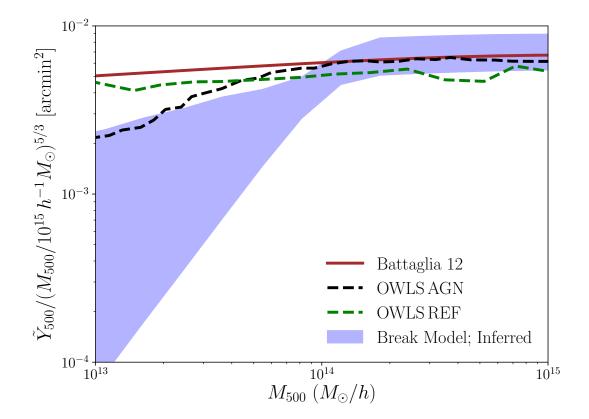
Figure 5.6: Inferred 68% credible interval (blue shaded region) on the $\tilde{Y}_{500} - M_{500}$ relation at $z = 0.25$ using the *break model*. We compare predictions from various hydrodynamical simulations (curves). We find our inferences to be consistent with all the hydrodynamical simulations at high mass, but we find a departure for lower mass halos where AGN feedback has its greater impact.
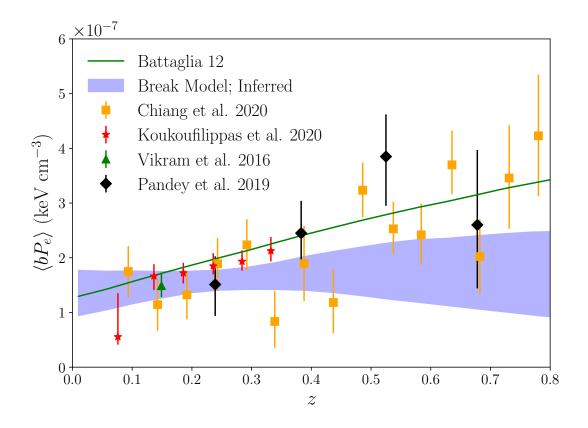
Figure 5.7: Inferred 68% credible interval (blue shaded region) on the bias weighted pressure of the universe ($\langle bP_e \rangle$) from our pressure profile constraints, assuming the *break model*. We compare this inference to previous studies where constraints are obtained from cross-correlations between galaxy/halo catalogs with Compton-y maps.
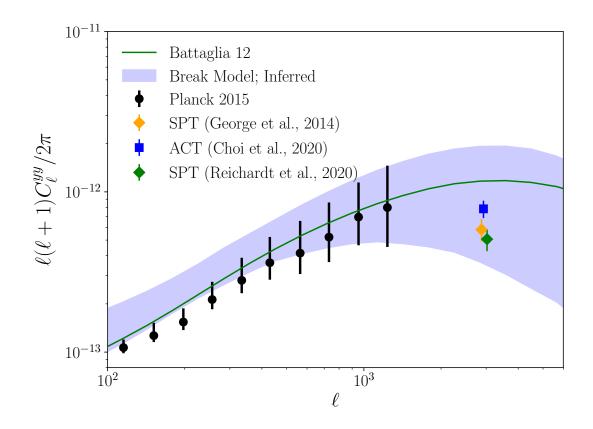
Figure 5.8: Inferred 68% credible interval (blue shaded region) on the auto-power spectra of Compton-*y* when adopting the *break model*. We compare this inference with measurements from the *Planck*, ACT and SPT Collaborations, finding a good agreement across all scales. Our measurement is also consistent with expectations from the model of [22] (green curve).
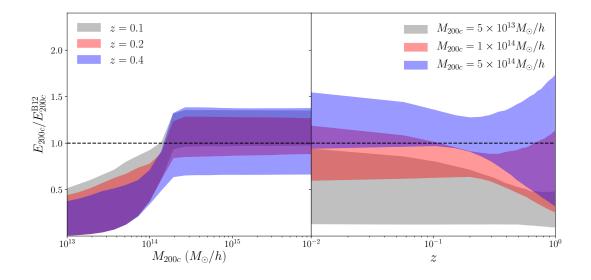
Figure 5.9: Constraints on the total thermal energy within r_{200c} (see Eq. 5.4.4) of hot gas in halos inferred from the *break model* analysis. We compare our constraints to the simulation-based predictions of [22], finding good agreement at high halo mass but differences at low mass.
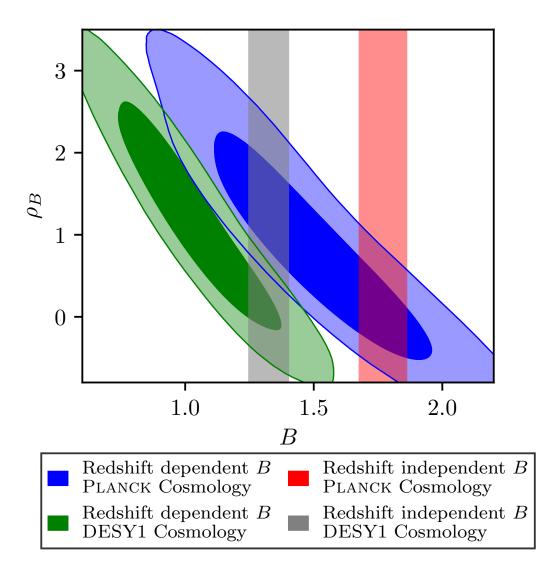
Figure 5.10: Constraints on the mass bias and its redshift evolution using shear-y cross-correlations. The red and gray vertical bands show the constraints on a constant mass bias parameter using the P_e^{A10c} model at the *Planck*-preferred and the DES-preferred cosmologies respectively. The blue and green contours corresponds to the P_e^{A10z} model (see Eq.5.2.11) with mass bias evolving with redshift as $B(z) = B(1 + z)^{\rho_B}$ at the *Planck*-preferred and the DES-preferred cosmologies respectively.
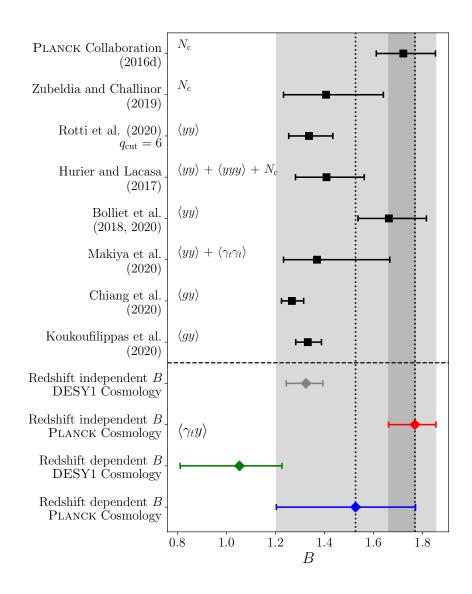
Figure 5.11: Comparison of constraints on mass bias from this work and previous studies. The dashed black line and gray-bands correspond to the marginalized mean and uncertainty on the mass bias parameter obtained using both the redshift-independent and redshift-dependent mass bias models at the *Planck*-preferred cosmology.

Chapter 6

Outlook

In this thesis, we developed novel models to analyze the cross-correlations between various tracers of the LSS. Complex and poorly understood astrophysics impacts our ability to constrain cosmological and astrophysical models from the LSS. Two major sources of systematic errors tackled in this thesis are galaxy biasing (non-linear mapping between dark matter and galaxies) and baryonic feedback (impact of supernovae or active galactic nuclei, AGN, on LSS):

- In Chapter 2 we describe and validate a hybrid galaxy biasing model aimed at analyzing the correlations between galaxy positions and weak gravitational lensing from photometric surveys. Using the 3D configuration space correlations between galaxies and matter, we show that a two-parameter hybrid perturbation theory model can describe correlation statistics from current datasets.

- In Chapter 3 we apply this model to recent data from the Dark Energy Survey. We find that this model leads to a 20% gain in the cosmological constraining power (compared to the linear bias model) by analyzing the information from small scales. We also find a tantalizing signature of an unresolved color-dependent photometric issue in the DES data, impacting the cosmological inferences from the color-selected red galaxy sample. We fix this issue by changing the selection criteria of red galaxies.

- In Chapter 4 we carry out high significance measurements of the correlations between galaxies and pressure of hot gas in the Universe (as traced by the thermal Sunyaev-Zel'dovich, tSZ effect). We use the large-scale measurements of these correlations to infer the tomographic evolution of the average thermal energy of the Universe, finding it to be consistent with predictions from the hydrodynamical simulations.

- In Chapter 5 we use the to-date highest significance measurements of the correlations between weak gravitational lensing and tSZ effect, where in addition to *Planck*, we use the high-resolution tSZ map from the ACT telescope as well. This correlation probes the pressure profile in the deep 1-halo regime of lower mass halos, and we find a significant detection of lower pressure inside lower mass halos. This points towards increased baryonic feedback, pushing the hot gas out of the lower mass halos that have lower gravitational potential well.

The results obtained in this thesis will be useful in pushing the cosmological analysis from the current and next-generation LSS surveys to the non-linear regime of small scales. Furthermore, the theoretical models and covariance methodology would enable joint multi-probe analysis of multiple tracers of the LSS. For example, a joint analysis of all the 2pt correlations constructed out of weak lensing, galaxy positions, and SZ effects can self-calibrate and result in robust constraints on cosmological parameters while correctly marginalizing over the unknown astrophysical parameters. Moreover, the models developed in this thesis can be extended to describe the correlations beyond the 2pt statistics. For instance, a hybrid perturbation theory framework can be used to analyze the small-scale correlations in 3pt statistics between galaxies and weak gravitational lensing maps from LSS and CMB surveys. Such a study would be very timely to design the analysis choices of multiple upcoming survey telescopes in this decade.

Appendix A

Appendix for Chapter 2

A.1 Covariance of the data-vectors

The measurements of the correlation functions ξ_{gg} and ξ_{gm} are highly correlated in the configuration space due to the mixing of modes. However, since the correlation function ξ_{mm} is also impacted by similar mode-mixing, analyzing the ratio of the correlation functions ξ_{gg}/ξ_{mm} and ξ_{gm}/ξ_{mm} makes the covariance more diagonal. In the Fig. A.1 we compare the correlation matrix for ξ_{gg} and ξ_{gg}/ξ_{mm} for the third tomographic bin for 20 radial bins ranging from 0.8-50 Mpc/h. We clearly see that analyzing the ratio gives us much better behaved correlation matrix.

We generate the *fiducial* jackknife covariance from 300 patches distributed over the simulation footprint. As the total area populated by both our galaxy

sample is equal to one octant of the sky, changing the number of jackknife patches, changes the size of each patch. In Fig.A.2, we compare the signal to noise estimate when using a different number of patches. We see that the diagonal elements of the covariance are robust to changes in the number of patches. We have also compared the changes in best-fit curves when using the covariance matrix generated using a different number of patches. We get consistent reduced χ^2 and best-fit curves for $z > 0.3$. However, we find that we can not get a robust covariance for the tomographic bin corresponding to $z < 0.3$ without sacrificing large scale information (which is required to constrain the linear bias parameter). For this reason, we only analyze the tomographic bins satisfying $z > 0.3$ and find that with 300 patches, we can get a robust estimate of jackknife covariance.

A.2   Results with fitting ξ_{gg} and ξ_{gm} directly

As mentioned in the main text, we consider the ratios, ξ_{gg}/ξ_{mm} and ξ_{gm}/ξ_{mm}, as our data-vector. This ratio is more sensitive to the galaxy-matter connection than the correlation functions ξ_{gg} and ξ_{gm} themselves. However, when we try to fit directly the correlation functions, ξ_{gg} and ξ_{gm}, our conclusions do not change. The residuals of the ξ_{gg} and ξ_{gm} using our *fiducial* model are shown in Fig. A.3 for the third tomographic bin. We compare the residuals obtained when directly fitting the correlation functions ξ_{gg}, ξ_{gm} with the results shown in the main text obtained when fitting the ratios of the correlation functions, $\xi_{gg}/\xi_{mm}, \xi_{gm}/\xi_{mm}$.
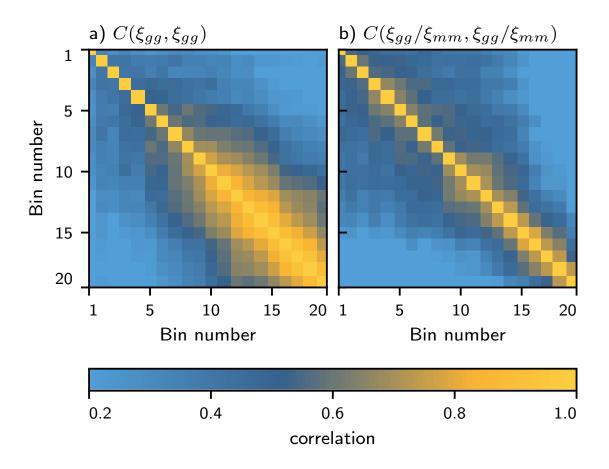
Figure A.1: The correlation matrix for the two-point galaxy correlation function ξ_{gg} and the ratio ξ_{gg}/ξ_{mm} for the second tomographic bin. Both correlation matrices are estimated using 300 jackknife patches. We see that the covariance is more diagonal for the ratio.
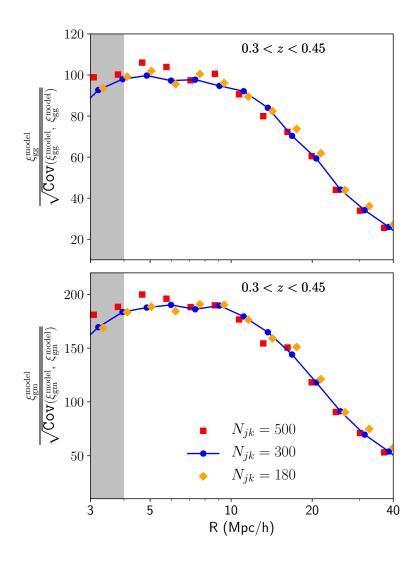
Figure A.2: The comparison of errorbars (and signal to noise) estimated using the jackknife procedure, for a different number of patches. We show the comparison for the smallest tomographic bin used in our analysis since that is most susceptible to the sizes of the jackknife patches. Also, since the covariance matrix of the correlation function ratios has small cross-bin covariance (see Fig. A.1), we only compare the diagonal value. The blue points (and solid) curve corresponds to our *fiducial* choice of 300 as the number of jackknife patches used for covariance estimation.

We find that our residuals are consistent with zero above the scales of 4Mpc/h for both data-vectors.

A.3   Analyzing the 2D correlation function at fixed cosmology

As described in the section §2.2.5 and Fig. 2.9, we convert the 3D statistics to the projected statistics. However, we can also fit our perturbation theory models directly to the measured projected statistics. Therefore, in this appendix, we fit our *fiducial* model to the projected statistics $w(\theta)$ and γ_t in the four lens and source tomographic bins. We refer the readers to [194] for the details about the estimation of the projected statistics and the tomographic redshift distribution of our bins.

The residuals of this model are shown in Fig. A.4 when using scales above 4Mpc/h. For the observable γ_t, we show the results for only the fourth source bin and all four lens tomographic bin (since this has the highest signal to noise). The fit has a reduced χ^2 of 0.88. There are some points in the residuals that are inconsistent with zero; however, as there is a significant correlation between different radial bins, they do not impact the χ^2 of the fit. The measured relation between b_2 and b_1 from this model is shown in Fig. A.5. We also compare this relationship with the one inferred from the 3D measurements and find them
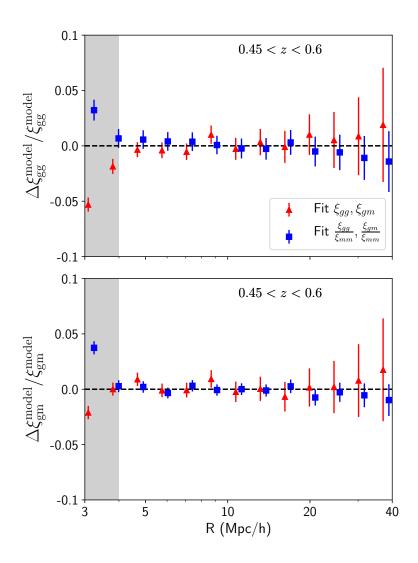
Figure A.3: Comparing the residuals when fitting the measured correlation functions ξ_{gg}, ξ_{gm} directly and when fitting the ratio $\xi_{gg}/\xi_{mm}, \xi_{gm}/\xi_{mm}$ for the second tomographic bin. We use our *fiducial* model as our theory model in both cases. We find the fits are consistent.

consistent.

Hence, when fitting the measured projected correlation functions directly, we also get a reduced χ^2 consistent with one. These results motivate us to model the correlations on the scales down to $4\,\mathrm{Mpc}/h$ in the DES Y3 cosmological analysis. To determine the scale cuts for DES analysis with non-linear bias model, we will study the cosmological parameter biases in a future study with the range of scale cut choices motivated by this study.
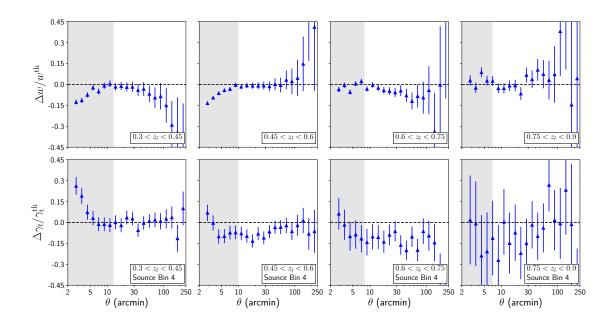
Figure A.4: Residual from joint fits to the measurements of the 2D statistics, in four tomographic lens and source bins (see [194] for source $n(z)$), using our *fiducial* model. The top row show the residuals for $w(\theta)$, and the bottom row for γ_t, with the source redshift distribution taken as the fourth bin in the DES Y1 analysis. We use a scale cut of 4Mpc/h here and only fit the data-points outside the grey region. The reduced χ^2 including all the datapoints (total degrees of freedom=342) above the scale cut is 0.88.
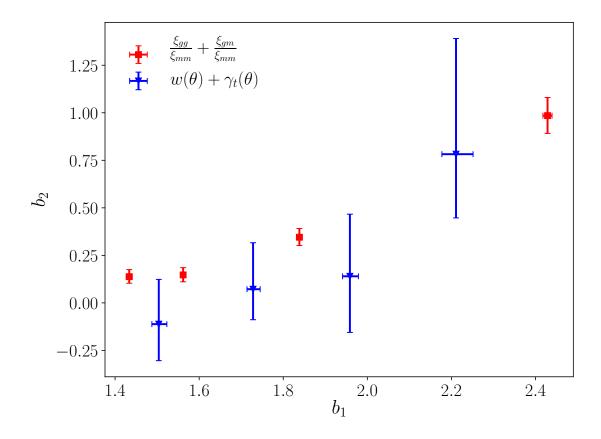
Figure A.5: The relation between the marginalized non-linear and linear bias parameters for four tomographic bins estimated from fitting $w(\theta)$ and γ_t. We also compare these values to the ones estimated from the 3D correlation functions and find consistent $b_2 - b_1$ relation.

Appendix B

Appendix for Chapter 3

B.1 Point mass marginalization

The point mass parameter (B) can also be expressed as residual mass bias, $B = \delta M/\pi$ where δM is approximately related to the difference between the model and true estimate of halo mass below the scales of our model validity (r_{min}). More accurately, δM_{halo} can be expressed in terms of galaxy-matter correlation as:

$$\delta M = \int_0^{r_{min}} dr_p (2\pi r_p) \int_{-\infty}^{\infty} d\Pi \, \Delta\xi_{gm}\left(\sqrt{r_p^2 + \Pi^2}, z\right), \qquad (B.1.1)$$

where $\Delta\xi_{gm} = \xi_{gm}^{true} - \xi_{gm}^{model}$.

In Fig. B.1 we compare the constraining power of 2×2pt and 3×2pt *simulated* analysis at our *fiducial* scale cuts for different point mass parameter settings. We generate a noiseless theory baseline datavector using the linear bias model and the *fiducial* parameter values given in Table 3.1. In the blue and red filled

contours, instead of analytically marginalizing over the point mass parameters, we explicitly sample them when analyzing 2×2pt and 3×2pt datavectors respectively. To test the impact of point mass marginalization on the constraining power, we also show the constraints obtained after fixing the PM parameters to their fiducial value of zero using unfilled contours. The black and green unfilled contours show the constraints using 2×2pt and 3×2pt datavectors respectively. We see that although point mass marginalization has a significant impact on the constraining power of the 2×2pt analysis, it has a small impact on the 3×2pt analysis. The main reason is that, due to extra constraints from cosmic shear, we break the degeneracy between PM parameters and cosmological parameters, and hence uncertainty in PM parameters do not dilute our cosmology constraints.

As PM marginalization degrades the constraining power of 2×2pt significantly, it might be desirable to implement an informative prior on the PM parameters. However, motivating an astrophysical prior on the PM parameters is not possible for our scale cuts as the majority of residual mass constraints are contributed from the 2-halo regime, as shown in Fig. B.2. For simplicity, we assume all our galaxies occupy the center of $2.5 \times 10^{13} M_{\odot}/h$ mass halos. The input "truth" curve in black solid line uses ξ_{gm} that is generated using the Navarro-Frenk-White profile [220] in the 1-halo regime ($r < 0.5$ Mpc/h) and one–loop PT in the 2-halo regime ($r > 0.5$ Mpc/h). Given this input halo mass, the halo model framework predicts the effective large scale linear bias value [68]. The dashed

273

blue curve is generated using a linear bias model, using a linear bias value that is 1σ lower from this predicted value. Here σ is the uncertainity obtained from 2×2pt marginalized constraints on the galaxy bias for first tomographic bin. The area between the two curves below some scale is equal to total δM as calculated using Eq. B.1.1.

We show the contribution to δM separately for the 1-halo region (below the red dashed line) and 2-halo regimes (up to the scales of 6Mpc/h, which are our scale cuts for $\gamma_t(\theta)$). We find that the 2-halo regime contributes significantly more than the 1-halo region and the resulting δM value is significantly more than the input halo mass of $2.5\times10^{13}M_\odot/h$. An informative prior would amount to understanding the galaxy-matter correlation and its dependence on cosmology and galaxy bias model from all scales below our scale cuts. Therefore we choose an uninformative wide prior on the point mass parameters.

The baseline model parameterization assumes the point mass parameter to be constant within each tomographic bin. We test this assumption implicitly in the suite of Buzzard simulations. The datavector measured in N-body Buzzard simulation will capture the effects of evolving point-mass parameters due to the evolution of the galaxy-matter correlation within a lens tomographic bin. As we have validated that our scale cuts pass our threshold criteria of bias in cosmological parameters being less than 0.3σ, we can conclude that the effect of point mass parameter evolution is small. Here we also test this effect explicitly by
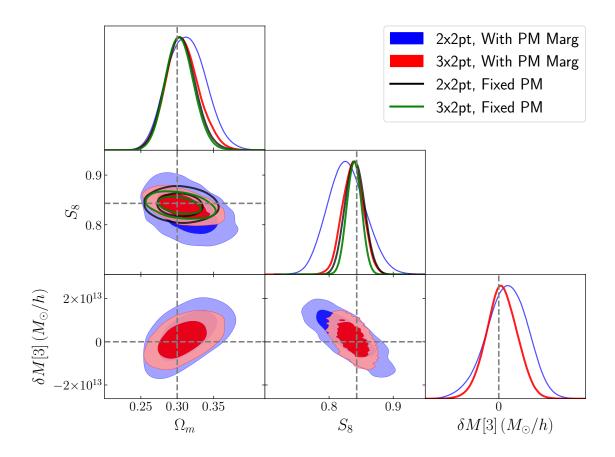
Figure B.1: Effect of point mass marginalization on the constraining power of 2×2pt and 3×2pt. We see that the constraining power of 2×2pt degrades significantly with point mass marginalization, while for 3×2pt the change is minimal. Including the shear-shear correlation breaks the degeneracy between point-mass (we show PM for third bin, $M_{\text{halo}}[3]$) and S_8, leading to smaller sensitivity of cosmology constraints on point mass constraints.
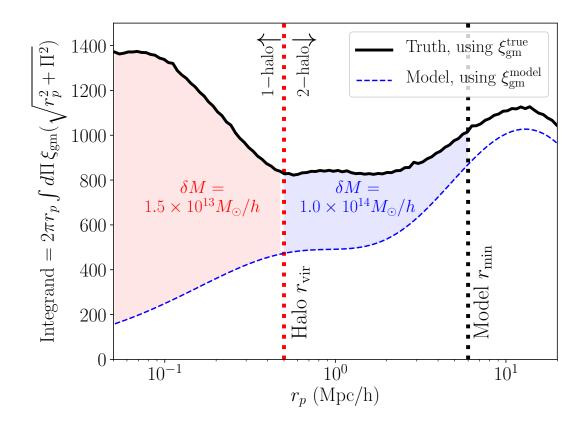
Figure B.2: We show the contribution to the residual mass shown in Eq. B.1.1 from different radial regimes. We find a significant contribution from 2-halo regime and therefore we cannot motivate an astrophysical informative prior on the PM parameters, without putting an informative prior on cosmology as well.

generating a simulated galaxy matter correlation function using the halo model. We assume a constant HOD of the redMaGiC galaxies but include the evolution of halo mass function and halo bias to predict the evolution of the galaxy-matter correlation function. The contribution to the PM parameter due to this evolution in each tomographic bin is given by Eq. B.1.1. In Fig. B.3, we show this contribution to each redshift bin by the black solid line. We compare this bias with the expected level of uncertainty in the PM parameters by plotting the marginalized constraints on these parameters as shown in Fig. B.1 for 2×2pt analyses. We see that the uncertainty in PM parameters is significantly greater than the expected bias.

B.2   Datavector residuals

We show the comparison between our measurements and best-fit theory datavector in Fig. B.4. We show the residuals between data and best-fit theory model from both the *fiducial* model as well as with $X_{\mathrm{lens}} = 0.87$ model . Using the *fiducial* linear bias model scale cuts of (8,6) Mpc/h (that leaves 302 datapoints in total), we find a minimum χ^2 of 347.2 and 351.1 for the *fiducial* model and $X_{\mathrm{lens}} = 0.87$ model respectively.
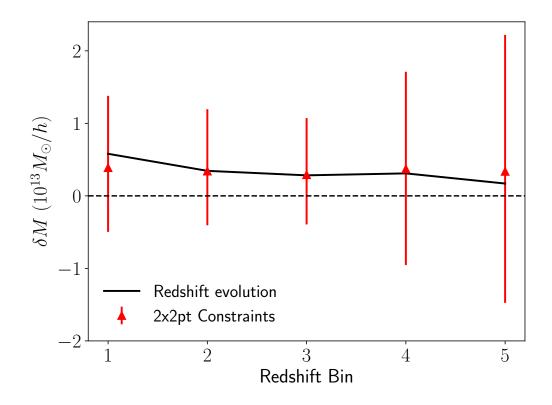
Figure B.3: We show the effect of the evolution of galaxy matter correlation functions on the PM parameters for each tomographic bin in the black line. The red errorbars show the expected errorbars on PM parameters for 2×2pt as shown in Fig. B.1. The blue errorbars are the constraints from 3×2pt.
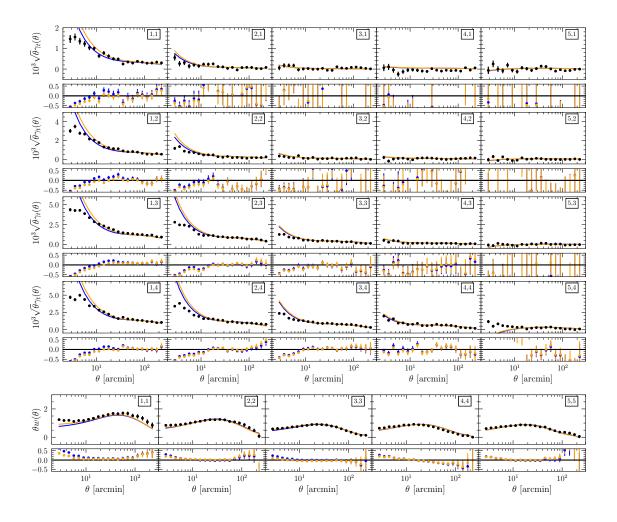
Figure B.4: The measurements of $w(\theta)$ and $\gamma_t(\theta)$ with redMaGiC sample are shown with black dots. We show the best fit using the *fiducial Linear bias* model in blue and model with $X_{lens} = 0.87$ in orange.
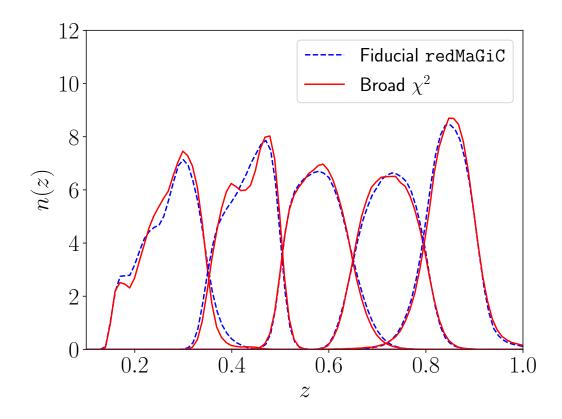
Figure B.5: We compare the redshift distribution of the fiducial `redMaGiC` sample with the broad-χ^2 `redMaGiC` sample.

B.3 Broad-χ^2 sample

As detailed in the main text, we generate a new galaxy sample by relaxing the selection criteria and selecting galaxies with goodness-of-fit $\chi^2_{\rm RM} = 8$ to the red-MaGiC template. This new sample is constructed to reduce the sensitivity of any color-dependent photometric issue that might be present in the fiducial red-MaGiC sample and causing $X_{\rm lens} < 1$. After analyzing the 2×2pt datavector, we do find that this sample prefers $X_{\rm lens} = 1$ and results in S_8 consistent with the Maglim galaxy sample.

In Fig. B.5, we show the comparison of the lens number densities for the five tomographic bins. We perform the calibration of these redshift distributions using cross-correlations with BOSS/eBOSS data using the same methods described in [59]. The lens photo-z prior that we use are shown in Table. B.1. After down-sampling the full catalog by a factor of 2, the number density (in the units of arcmin^{-2}) for this sample are $\langle n_{\rm g} \rangle = 0.027, 0.04, 0.07, 0.03, 0.03$ for the five tomographic bins. We generate a non-Gaussian covariance corresponding to these number densities. To mitigate the bias caused by wrong parameter values input to theory covariance calculations, we recalculate the covariance matrix using the best-fit parameters of an initial 2×2pt analysis and show the cosmological constraints corresponding to this new covariance.

Using the best-fit parameter values obtained with the linear bias model, we show the residuals in Fig. B.6. We find a best-fit χ^2 of 353 for 302 datapoints,

and both the $w(\theta)$ and γ_t measurements are fit well with a linear bias, ΛCDM model. In Fig. B.7 we show the parameters constraints and compare them to the ones obtained with the fiducial redMaGiC sample.

Parameter	Prior
Δz_g^1	$\mathcal{G}[0.0088, 0.0029]$
σz_g^1	$\mathcal{G}[1.015, 0.035]$
Δz_g^2	$\mathcal{G}[-0.0033, 0.0022]$
σz_g^2	$\mathcal{G}[0.991, 0.028]$
Δz_g^3	$\mathcal{G}[0.0076, 0.0029]$
σz_g^3	$\mathcal{G}[1.096, 0.029]$
Δz_g^4	$\mathcal{G}[0.0015, 0.0042]$
σz_g^4	$\mathcal{G}[1.104, 0.045]$
Δz_g^5	$\mathcal{G}[-0.0058, 0.0061]$
σz_g^5	$\mathcal{G}[1.193, 0.056]$

Table B.1: The lens photo-z shift and stretch parameters varied in the analysis using the broad-χ^2 sample and their prior range used ($\mathcal{G}[\mu, \sigma] \equiv$ Gaussian prior with mean μ and standard-deviation σ).
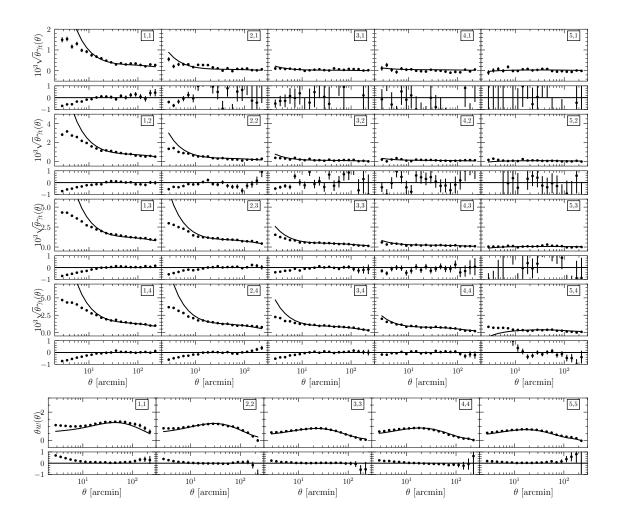
Figure B.6: The measurements of $w(\theta)$ and $\gamma_{\mathrm{t}}(\theta)$ with the broad-χ^2 `redMaGiC` sample are shown with black dots. We show the best fit model in black.
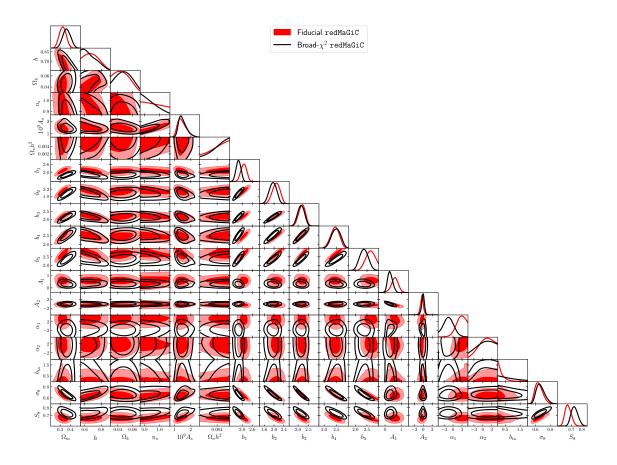
Figure B.7: Comparison of parameter constraints using fiducial and broad-χ^2 redMaGiC for all the parameters sampled in the analysis without a tight gaussian prior. We also show the derived parameters σ_8 and S_8.
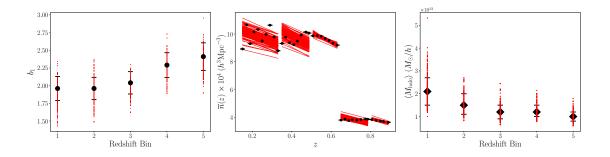
Figure B.8: This figure shows the marginalized constraints on the large-scale bias of redMaGiC sample for the five tomographic bins on the left panel. The black dots denote the mean, and the error bars correspond to 68% credible interval. Using these constraints and co-moving number density (middle panel), we infer the constraints on mean halo mass, as shown in the right panel for five tomographic bins. The red line and dots correspond to MCMC samples. We use the *Linear bias* model with $X_{\mathrm{lens}} = 0.87$.

B.4   Halo mass inference

In this section we detail the methodology to infer the host halo mass of our red-MaGiC lens galaxy sample from the constraints on galaxy bias parameters and number density. We use the halo model framework to make this prediction and parameterize the number of galaxies in a halo of mass M in tomographic bin j as $N_{\rm g}^j(M) = N_{\rm cen}^j(M) + N_{\rm sat}^j(M)$ where $N_{\rm cen}^j$ is the number of central galaxies and $N_{\rm sat}^j$ is the number of satellite galaxies. We parameterize these two components as:

$$N_{\rm cen}^j = \frac{f_{\rm cen}^j}{2}\left[1 + {\rm erf}\left(\frac{\log M - (\log M_{\rm min})^j}{(\sigma_{\log M})^j}\right)\right] \tag{B.4.1}$$

$$N_{\rm sat}^j = \frac{1}{2}\left[1 + {\rm erf}\left(\frac{\log M - (\log M_{\rm min})^j}{(\sigma_{\log M})^j}\right)\right] \times \left(\frac{M_{\rm h}}{M_1^j}\right)^{\alpha^j}. \tag{B.4.2}$$

Here we have five free parameters, $f_{\rm cen}^j$, $(\log M_{\rm min})^j$, $(\sigma_{\log M})^j$, M_1^j and α^j, that we marginalize over. We can predict the comoving number density $(\overline{n}(z)^j)$ and galaxy bias for a given tomographic bin j, b_1^j, from galaxy HOD as follows:

$$\overline{n}^j(z) = \int_0^\infty dM \frac{dn}{dM} N_{\rm g}^j(M)$$

$$b_1^j = \int dz \frac{n_g^j(z)}{\overline{n}^j(z)} \int_0^\infty dM \frac{dn}{dM} N_{\rm g}^j(M) b_1^{\rm halo}(M, z)$$

$$\tag{B.4.3}$$

We use the [302] halo mass function (dn/dM) and the [305] relation for linear halo bias $(b_1^{\rm halo}(M, z))$.

Therefore, Eqs. B.4.3 allow us to predict the number density and galaxy bias

values. We then sample these HOD parameters to fit the datavector $\vec{\mathcal{D}}_H =$
$\bar{n}^j(z_1)...\bar{n}^j(z_n), b_1^j, b_2^j]$ of length d where $\bar{n}^j(z_1)...\bar{n}^j(z_n)$ are the $n = d - 2$ observed comoving number density of redMaGiC galaxies as shown in middle panel of Fig.B.8 and b_1^j and b_2^j are the marginalized mean bias values obtained at our *fiducial* scale cut. For a given set of HOD parameters (Θ_H), the theoretical prediction is given by $\mathcal{T}_H$ and we write our log-likelihood as:

$$\ln \mathcal{L}(\vec{\mathcal{D}}_H | \Theta) = -\frac{1}{2}\left[(\vec{\mathcal{D}}_H - \vec{\mathcal{T}}_H(\Theta_H)) \mathcal{C}_H^{-1} (\vec{\mathcal{D}}_H - \vec{\mathcal{T}}_H(\Theta_H))^{\mathrm{T}} \right.$$
$$\left. - \ln(|\mathcal{C}_H|) \right] \quad \text{(B.4.4)}$$

In order to account for variation of HOD within a tomographic bin that contributes to the variation on $\bar{n}^j(z)$ within each tomographic bin as seen in Fig.B.8, we implement an analytical marginalization scheme. We change the covariance of our datavector $\mathcal{C}_H$ as :

$$\mathcal{C}_H \rightarrow \mathcal{C}_H + \alpha_c \mathcal{I}_D \quad \text{(B.4.5)}$$

where $\mathcal{I}_D$ is a diagonal matrix of dimension $d \times d$ whose diagonal elements equal to 1 from index 1 to d-1, and equal to 0 otherwise. We sample over the parameter α_c, treating it as a free parameter.

Appendix C

Appendix for Chapter 4

C.1 NILC pipeline

In this appendix we elaborate on the y map reconstruction pipeline. We follow the pipeline exactly as used in *Planck* y map reconstruction with the freedom of changing the frequency dependence of the component that gets unit response as well as the number of components that get null response. The basic steps in the reconstruction are as follows:

1. In the simulations, create the temperature maps by adding various relevant component `Healpix` maps of simulations at a given value of NSIDE. In the analysis using the *Websky* mocks and Sehgal simulations, we add the components described in §4.3.3 with NSIDE of 1024 and in common units of μK_{CMB}. In data we are given the temperature maps which we convert to

common NSIDE of 1024 and to units of μK_{CMB} using the factors given in table 6 of [237]

$$T_v(\theta) = a_v y(\theta) + b_v^{(1)} C(\theta) + b_v^{(2)} S(\theta) + n_v(\theta), \qquad (C.1.1)$$

where $T_v(\theta)$ is the temperature map at a given frequency v at θ position in sky, $y(\theta)$ is the Compton-y map with a_v frequency scaling, $C(\theta)$ is the CIB map (here we have assumed that it scales as $b_v^{(1)}$ across whole sky which may not be correct), $S(\theta)$ is the lensed CMB map and it scales as $b_v^{(2)}$ and $n_v(\theta)$ denotes all other components combined. For data, we download the publicly available temperature maps from the *Planck* collaboration [1]. We also apply the relevant masks as described in the main text on these temperature maps before further processing .

2. Smooth all the temperature maps $(T_v \rightarrow T_{v,s})$ with a Gaussian beam of FWHM = 10 arcmin. We choose this beam size as the Compton-y map by *Planck* Collaboration is also created with temperature maps smoothed with 10 arcmin beam.

$$T_{v,s} = \mathcal{F}^{-1}(B(\ell) \times \mathcal{F}(T_v)), \qquad (C.1.2)$$

where $T_{v,s}$ are the smoothed temperature maps of frequency v with gaussian window of given FWHM ($B(\ell)$). Here $\mathcal{F}$ denotes taking spherical har-

---

[1] pla.esac.esa.int/

monic transform to convert `Healpix` maps to ℓ, m space and $\mathcal{F}^{-1}$ takes the inverse fourier transform and converts back to map space.

3. Construct and save the spherical Fourier components, $T_{f,\nu}^{\ell,m}$ for each of above smoothed temperature maps (f in the subscript denote the fourier space quantity).

4. Use the 10 needlet band window functions ($h^i(\ell)$) provided by *Planck* Collaboration. These bands have the property that sum of square of all the bands is equal to 1 for all ℓ. For each band, filter each frequency map with the corresponding window function.

$$\hat{T}_{\nu}^i = \mathcal{F}^{-1}(h^i(\ell) \times T_{f,\nu}^{\ell,m}) \tag{C.1.3}$$

5. Calculate the weights for each frequency and needlet band corresponding to the input constraints for generating y map. We always give unit response to Compton-y, that means we always have $\sum_\nu w_\nu a_\nu = 1$ for each needlet band i. Now, we experiment with either nulling one of the CIB signal and the CMB signal (nulling both would degrade our signal to noise) or not nulling any component. These weights are given by:

$$\vec{w} = \frac{(\vec{b}^{(i),T}\mathbf{R}^{-1}\vec{b}^{(i)})(\mathbf{R}^{-1}\vec{a}) - (\vec{b}^{(i),T}\mathbf{R}^{-1}\vec{a})(\mathbf{R}^{-1}\vec{b}^{(i)})}{(\vec{a}^T\mathbf{R}^{-1}\vec{a})(\vec{b}^{(i),T}\mathbf{R}^{-1}\vec{b}^{(i)}) - (\vec{a}^T\mathbf{R}^{-1}\vec{b}^{(i)})^2}, \tag{C.1.4}$$

where i can be 1 or 2 corresponding to the case of `unit-y-null-cib` and `unit-y-null-cmb` respectively. Here $\mathbf{R}$ is the covariance caluclated in a

smaller patch of sky that is determined by the maximum ℓ of each needlet band, number of frequencies and ilc-bias that we choose [82, 83, 254, 256]. We choose an ilc bias (b_{ilc}) value of 0.1%. This means that we need to calculate covariance using approximately ($\frac{N_\nu^i - 1}{b_{\mathrm{ilc}}}$) pixels for any needlet band i, which uses N_ν^i channels for Compton-y estimation in any needlet band i.

6. For each needlet band, i, multiply the weights obtained for each frequency with the needlet window filtered temperature maps. Now, sum all the resultant maps to get the final map for the given needlet band i.

7. Now multiply the final map obtained for each band in previous step with the corresponding needlet window function and sum the resultant maps for all the bands. This gives us the estimated Compton-y map for given sets of conditions and parameters.

C.2   Validation of y estimation on *Websky* mocks

As described in the text, the Sehgal CIB model is somewhat out of date, and is not expected to perfectly capture dependence of the CIB on frequency, redshift, and halo mass. Consequently, we also test our y estimation pipelines using the *Websky* mocks.

We reconstruct Compton-y maps from the *Websky* mocks using the temperature maps corresponding to the frequencies less than 545GHz, as in our analysis

of data. We cross-correlate the reconstructed maps with halos in the mass range $2 \times 10^{13} M_\odot/h < M_h < 3 \times 10^{13} M_\odot/h$. The result of this cross-correlation for the redshift bin $0.45 < z < 0.6$ is shown in Fig. C.1. We see that Compton-y maps obtained from various choices of reconstruction methods, as detailed in §4.4.4.1, result in halo-y correlations that agree with each other as well as with the correlations with the true y map. We find similar results for other redshift bins. As noted in the main text, since we do not have simulated radio galaxies for the *Websky* mocks, we rely mostly on the Sehgal simulations for validating our y analysis choices.

C.3   Covariance and Multidimensional Parameter constraints

We show the estimated covariance and correlation matrices for the measurements in Fig. C.2. As described in §4.4.2, we use a jackknife resampling approach to estimating the blocks of the covariance matrix involving the galaxy-y cross-correlation. For the block involving only galaxy-galaxy clustering, we use the theoretical covariance estimate from [173]. We also set to zero the cross redshift-bin covariance for the blocks corresponding to cross-covariance between galaxy-galaxy and galaxy-y.

The multidimensional parameter constraints on the galaxy bias and $\langle bP_e \rangle$ pa-
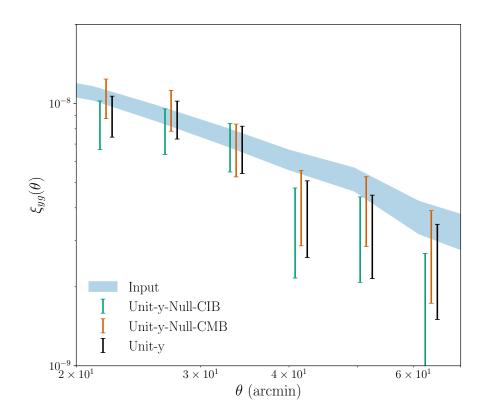
Figure C.1: Cross-correlation of reconstructed Compton-y with the halos in *Web-sky* mocks for various reconstruction methods. We correlate halos satisfying $0.3 < z < 0.45$ and $2 \times 10^{13} M_\odot/h < M_h < 3 \times 10^{13} M_\odot/h$. The points labelled 'input' correspond to the true halo-y cross-correlation in the absence of any contamination. The other points show the results of applying component separation to simulated sky maps that include the CIB signal. In all cases, we use frequencies 100, 143, 217 and 343 GHz. We find that the choice of unit-y, null-CMB leads to no significant bias in the inferred halo-y cross-correlation.

rameters are shown in Fig. C.3 resulting from the MCMC analysis. The MCMC is well converged, and there are no strong degeneracies between the parameters.
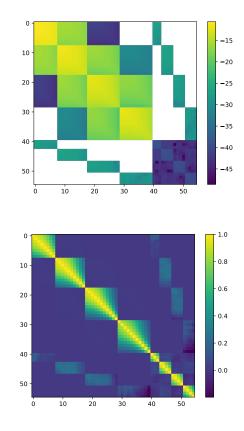
Figure C.2: Top panel shows the log of the absolute value of the final covariance matrix. Bottom panel shows the corresponding cross-correlation matrix
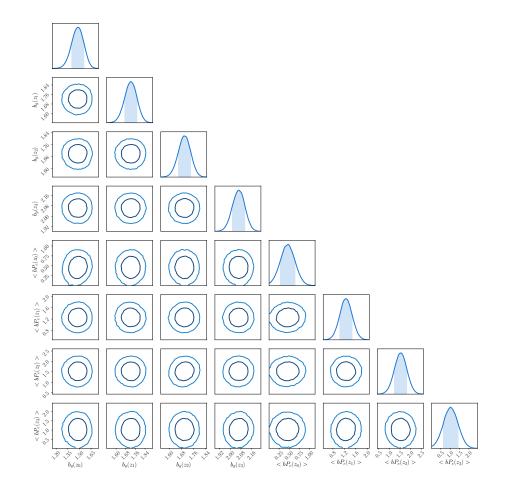
Figure C.3: Multi-dimensional parameter constraints from the model fits to data.

First four parameters are galaxy bias for each of the four redshift bin used in this

analysis and next four are bias weighted pressure corresponding to same bins

Appendix D

Appendix for Chapter 5

D.1 Covariance matrix

Our full model of theory covariance, including the Gaussian and non-Gaussian terms is shown is Eq. 5.2.34. In paper I we validated the Gaussian part of our total covariance using simulations. We have also compared it to the jackknife covariance estimate which partly captures the non-Gaussian contribution to the total covariance. Our total covariance includes the contribution from poisson fluctuations of large clusters.

In Fig. D.1 we show the part of the correlation matrix using fourth source tomographic bin. It clearly shows that due to large beam, the small scale angular bins corresponding to $\theta < 10 \mathrm{arcmin}$ are more correlated in the $Planck \times \mathrm{DES}$ part of the matrix compared to $\mathrm{ACT} \times \mathrm{DES}$.
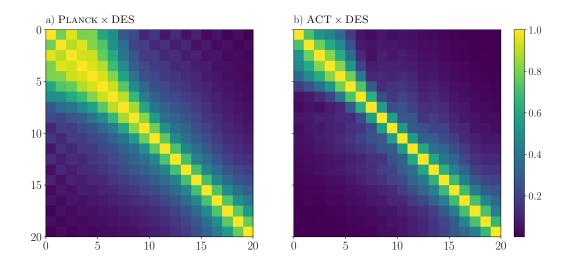
Figure D.1: Correlation matrix of $\xi_{\gamma_t y}$ using the fourth source bin and the two Compton-y maps, binned into 20 radial bins from 2.5 to 250 arcmin.

D.2 Impact of assumed cosmological model on parameter constraints

We repeat our analysis adopting the best-fit cosmological parameters from [243] and from the DES Year 1 analysis of [3]. The full posteriors for these two analyses are shown in Fig. D.2. We find that our results are largely insensitive to the choice of cosmological model.
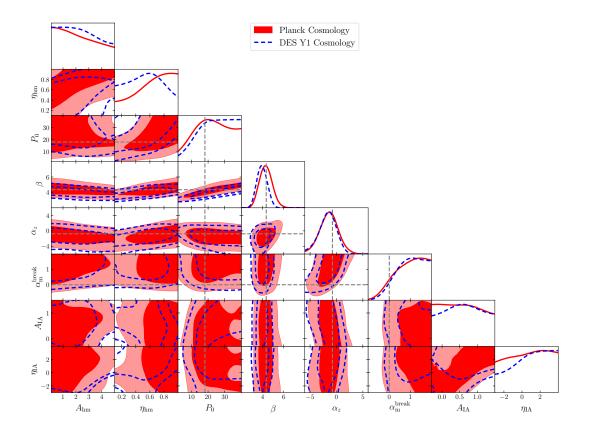
Figure D.2: Constraints on the pressure profile parameters from the *break* model assuming two different cosmological models.

Bibliography

[1] K. N. Abazajian, P. Adshead, Z. Ahmed, S. W. Allen, D. Alonso, K. S. Arnold, C. Baccigalupi, J. G. Bartlett, N. Battaglia, B. A. Benson, C. A. Bischoff, J. Borrill, V. Buza, E. Calabrese, R. Caldwell, J. E. Carlstrom, C. L. Chang, T. M. Crawford, F.-Y. Cyr-Racine, F. De Bernardis, T. de Haan, S. di Serego Alighieri, J. Dunkley, C. Dvorkin, J. Errard, G. Fabbian, S. Feeney, S. Ferraro, J. P. Filippini, R. Flauger, G. M. Fuller, V. Gluscevic, D. Green, D. Grin, E. Grohs, J. W. Henning, J. C. Hill, R. Hlozek, G. Holder, W. Holzapfel, W. Hu, K. M. Huffenberger, R. Keskitalo, L. Knox, A. Kosowsky, J. Kovac, E. D. Kovetz, C.-L. Kuo, A. Kusaka, M. Le Jeune, A. T. Lee, M. Lilley, M. Loverde, M. S. Madhavacheril, A. Mantz, D. J. E. Marsh, J. McMahon, P. D. Meerburg, J. Meyers, A. D. Miller, J. B. Munoz, H. N. Nguyen, M. D. Niemack, M. Peloso, J. Peloton, L. Pogosian, C. Pryke, M. Raveri, C. L. Reichardt, G. Rocha, A. Rotti, E. Schaan, M. M. Schmittfull, D. Scott, N. Sehgal, S. Shandera, B. D. Sherwin, T. L. Smith, L. Sorbo, G. D. Starkman, K. T. Story, A. van Engelen, J. D. Vieira, S. Wat-

son, N. Whitehorn, and W. L. Kimmy Wu. CMB-S4 Science Book, First Edition. *ArXiv e-prints*, Oct. 2016.

[2] T. Abbott, F. Abdalla, A. Alarcon, J. AleksiÄ, S. Allam, S. Allen, A. Amara, J. Annis, J. Asorey, S. Avila, and et al. Dark energy survey year 1 results: Cosmological constraints from galaxy clustering and weak lensing. *Physical Review D*, 98(4), Aug 2018.

[3] T. Abbott, F. Abdalla, A. Alarcon, J. AleksiÄ, S. Allam, S. Allen, A. Amara, J. Annis, J. Asorey, S. Avila, and et al. Dark energy survey year 1 results: Cosmological constraints from galaxy clustering and weak lensing. , 98(4), Aug 2018.

[4] T. Abbott, M. Aguena, A. Alarcon, S. Allam, S. Allen, J. Annis, S. Avila, D. Bacon, K. Bechtol, A. Bermeo, and et al. Dark energy survey year 1 results: Cosmological constraints from cluster abundances and weak lensing. *Physical Review D*, 102(2), Jul 2020.

[5] T. Abbott, M. Aguena, A. Alarcon, S. Allam, S. Allen, J. Annis, S. Avila, D. Bacon, K. Bechtol, A. Bermeo, and et al. Dark energy survey year 1 results: Cosmological constraints from cluster abundances and weak lensing. , 102(2), Jul 2020.

[6] P. Ade, J. Aguirre, Z. Ahmed, S. Aiola, A. Ali, D. Alonso, M. A. Alvarez, K. Arnold, P. Ashton, J. Austermann, H. Awan, C. Baccigalupi,

T. Baildon, D. Barron, N. Battaglia, R. Battye, E. Baxter, A. Bazarko, J. A. Beall, R. Bean, D. Beck, S. Beckman, B. Beringue, F. Bianchini, S. Boada, D. Boettger, J. R. Bond, J. Borrill, M. L. Brown, S. M. Bruno, S. Bryan, E. Calabrese, V. Calafut, P. Calisse, J. Carron, A. Challinor, G. Chesmore, Y. Chinone, J. Chluba, H.-M. S. Cho, S. Choi, G. Coppi, N. F. Cothard, K. Coughlin, D. Crichton, K. D. Crowley, K. T. Crowley, A. Cukierman, J. M. D'Ewart, R. Dünner, T. de Haan, M. Devlin, S. Dicker, J. Didier, M. Dobbs, B. Dober, C. J. Duell, S. Duff, A. Duivenvoorden, J. Dunkley, J. Dusatko, J. Errard, G. Fabbian, S. Feeney, S. Ferraro, P. Fluxà, K. Freese, J. C. Frisch, A. Frolov, G. Fuller, B. Fuzia, N. Galitzki, P. A. Gallardo, J. Tomas Galvez Ghersi, J. Gao, E. Gawiser, M. Gerbino, V. Gluscevic, N. Goeckner-Wald, J. Golec, S. Gordon, M. Gralla, D. Green, A. Grigorian, J. Groh, C. Groppi, Y. Guan, J. E. Gudmundsson, D. Han, P. Hargrave, M. Hasegawa, M. Hasselfield, M. Hattori, V. Haynes, M. Hazumi, Y. He, E. Healy, S. W. Henderson, C. Hervias-Caimapo, C. A. Hill, J. C. Hill, G. Hilton, M. Hilton, A. D. Hincks, G. Hinshaw, R. Hložek, S. Ho, S.-P. P. Ho, L. Howe, Z. Huang, J. Hubmayr, K. Huffenberger, J. P. Hughes, A. Ijjas, M. Ikape, K. Irwin, A. H. Jaffe, B. Jain, O. Jeong, D. Kaneko, E. D. Karpel, N. Katayama, B. Keating, S. S. Kernasovskiy, R. Keskitalo, T. Kisner, K. Kiuchi, J. Klein, K. Knowles, B. Koopman, A. Kosowsky, N. Krachmalnicoff, S. E. Kuenstner, C.-L. Kuo, A. Kusaka, J. Lashner, A. Lee, E. Lee, D. Leon,

J. S. Y. Leung, A. Lewis, Y. Li, Z. Li, M. Limon, E. Linder, C. Lopez-Caraballo, T. Louis, L. Lowry, M. Lungu, M. Madhavacheril, D. Mak, F. Maldonado, H. Mani, B. Mates, F. Matsuda, L. Maurin, P. Mauskopf, A. May, N. McCallum, C. McKenney, J. McMahon, P. D. Meerburg, J. Meyers, A. Miller, M. Mirmelstein, K. Moodley, M. Munchmeyer, C. Munson, S. Naess, F. Nati, M. Navaroli, L. Newburgh, H. N. Nguyen, M. Niemack, H. Nishino, J. Orlowski-Scherer, L. Page, B. Partridge, J. Peloton, F. Perrotta, L. Piccirillo, G. Pisano, D. Poletti, R. Puddu, G. Puglisi, C. Raum, C. L. Reichardt, M. Remazeilles, Y. Rephaeli, D. Riechers, F. Rojas, A. Roy, S. Sadeh, Y. Sakurai, M. Salatino, M. Sathyanarayana Rao, E. Schaan, M. Schmittfull, N. Sehgal, J. Seibert, U. Seljak, B. Sherwin, M. Shimon, C. Sierra, J. Sievers, P. Sikhosana, M. Silva-Feaver, S. M. Simon, A. Sinclair, P. Siritanasak, K. Smith, S. R. Smith, D. Spergel, S. T. Staggs, G. Stein, J. R. Stevens, R. Stompor, A. Suzuki, O. Tajima, S. Takakura, G. Teply, D. B. Thomas, B. Thorne, R. Thornton, H. Trac, C. Tsai, C. Tucker, J. Ullom, S. Vagnozzi, A. van Engelen, J. Van Lanen, D. D. Van Winkle, E. M. Vavagiakis, C. Vergès, M. Vissers, K. Wagoner, S. Walker, J. Ward, B. Westbrook, N. Whitehorn, J. Williams, J. Williams, E. J. Wollack, Z. Xu, B. Yu, C. Yu, F. Zago, H. Zhang, N. Zhu, and The Simons Observatory collaboration. The Simons Observatory: science goals and forecasts. *Journal of Cosmology and Astro-Particle Physics*, 2019:056, Feb 2019.

[7] P. A. R. Ade, N. Aghanim, M. Arnaud, M. Ashdown, F. Atrio-Barandela, J. Aumont, C. Baccigalupi, A. Balbi, A. J. Banday, and et al. Planckintermediate results. , 550:A131, Feb 2013.

[8] N. Aghanim, Y. Akrami, M. Ashdown, J. Aumont, C. Baccigalupi, M. Ballardini, A. J. Banday, R. B. Barreiro, N. Bartolo, and et al. Planck 2018 results. *Astronomy & Astrophysics*, 641:A6, Sep 2020.

[9] N. Aghanim, M. Arnaud, M. Ashdown, J. Aumont, C. Baccigalupi, A. J. Banday, R. B. Barreiro, J. G. Bartlett, N. Bartolo, and et al. Planck2015 results. , 594:A22, Sep 2016.

[10] P. C. N. Aghanim, M. Arnaud, M. Ashdown, J. Aumont, C. Baccigalupi, A. J. Banday, and R. B. Barreiro. Planck 2015 results XXII . A map of the thermal Sunyaev-Zeldovich effect. *arXiv: 1502.01596v1 [astro-ph.CO]*, page 25, 2015.

[11] D. Alonso, J. Sanchez, and A. Slosar. A unified pseudo-câ framework. , 484(3):4127â4151, Jan 2019.

[12] S. Amodeo, N. Battaglia, E. Schaan, S. Ferraro, E. Moser, S. Aiola, J. E. Austermann, J. A. Beall, R. Bean, D. T. Becker, R. J. Bond, E. Calabrese, V. Calafut, S. K. Choi, E. V. Denison, M. Devlin, S. M. Duff, A. J. Duivenvoorden, J. Dunkley, R. Dünner, P. A. Gallardo, K. R. Hall, D. Han, J. C. Hill, G. C. Hilton, M. Hilton, R. Hložek, J. Hubmayr, K. M. Huffen-

berger, J. P. Hughes, B. J. Koopman, A. MacInnis, J. McMahon, M. S. Madhavacheril, K. Moodley, T. Mroczkowski, S. Naess, F. Nati, L. B. Newburgh, M. D. Niemack, L. A. Page, B. Partridge, A. Schillaci, N. Sehgal, C. Sifón, D. N. Spergel, S. Staggs, E. R. Storer, J. N. Ullom, L. R. Vale, A. van Engelen, J. Van Lanen, E. M. Vavagiakis, E. J. Wollack, and Z. Xu. Atacama Cosmology Telescope: Modeling the gas thermodynamics in BOSS CMASS galaxies from kinematic and thermal Sunyaev-Zel'dovich measurements. , 103(6):063514, Mar. 2021.

[13] S. Amodeo, N. Battaglia, E. Schaan, S. Ferraro, E. Moser, S. Aiola, J. E. Austermann, J. A. Beall, R. Bean, D. T. Becker, and et al. Atacama cosmology telescope: Modeling the gas thermodynamics in boss cmass galaxies from kinematic and thermal sunyaev-zelâdovich measurements. *Physical Review D*, 103(6), Mar 2021.

[14] A. Amon et al. Dark Energy Survey Year 3 Results: . *To be submitted to PRD*, 2021.

[15] R. Angulo, M. Fasiello, L. Senatore, and Z. Vlah. On the statistics of biased tracers in the effective field theory of large scale structures. *Journal of Cosmology and Astroparticle Physics*, 2015(09):029â029, Sep 2015.

[16] M. Arnaud, G. W. Pratt, R. Piffaretti, H. Böhringer, J. H. Croston, and E. Pointecouteau. The universal galaxy cluster pressure profile from a

representative sample of nearby systems (REXCESS) and the Y_{SZ} - M_{500} relation. , 517:A92, July 2010.

[17] M. Asgari, C.-A. Lin, B. Joachimi, B. Giblin, C. Heymans, H. Hildebrandt, A. Kannawadi, B. Stölzner, T. Tröster, J. L. van den Busch, and et al. Kids-1000 cosmology: Cosmic shear constraints and comparison between two point statistics. *Astronomy & Astrophysics*, 645:A104, Jan 2021.

[18] T. Baldauf, L. Mercolli, and M. Zaldarriaga. Effective field theory of large scale structure at two loops: The apparent scale dependence of the speed of sound. , 92(12):123007, Dec. 2015.

[19] T. Baldauf, U. c. v. Seljak, V. Desjacques, and P. McDonald. Evidence for quadratic tidal tensor bias from the halo bispectrum. *Phys. Rev. D*, 86:083540, Oct 2012.

[20] T. Baldauf, R. E. Smith, U. Seljak, and R. Mandelbaum. Algorithm for the direct reconstruction of the dark matter correlation function from weak lensing and galaxy clustering. *Physical Review D*, 81(6), Mar 2010.

[21] D. J. Barnes, M. Vogelsberger, F. A. Pearce, A.-R. Pop, R. Kannan, K. Cao, S. T. Kay, and L. Hernquist. Characterizing hydrostatic mass bias with mock-x. , May 2021.

[22] N. Battaglia, J. R. Bond, C. Pfrommer, and J. L. Sievers. On the Cluster Physics of Sunyaev-Zel'dovich and X-Ray Surveys. II. Deconstructing the Thermal SZ Power Spectrum. , 758:75, Oct. 2012.

[23] N. Battaglia, J. R. Bond, C. Pfrommer, J. L. Sievers, and D. Sijacki. Simulations of the Sunyaev-Zel'dovich Power Spectrum with Active Galactic Nucleus Feedback. , 725:91–99, Dec. 2010.

[24] N. Battaglia, J. C. Hill, and N. Murray. Deconstructing Thermal Sunyaev-Zel'dovich - Gravitational Lensing Cross-correlations: Implications for the Intracluster Medium. , 812(2):154, Oct 2015.

[25] D. Baumann, A. Nicolis, L. Senatore, and M. Zaldarriaga. Cosmological non-linearities as an effective fluid. , 2012(7):051, July 2012.

[26] E. J. Baxter, S. Adhikari, J. Vega-Ferrero, W. Cui, C. Chang, B. Jain, and A. Knebe. Shocks in the Stacked Sunyaev-Zel'dovich Profiles of Clusters I: Analysis with the Three Hundred Simulations. *arXiv e-prints*, page arXiv:2101.04179, Jan. 2021.

[27] M. R. Becker. CALCLENS: weak lensing simulations for large-area sky surveys and second-order effects in cosmic shear power spectra. , 435(1):115–132, October 2013.

[28] A. J. Benson. Galaxy formation theory. , 495(2-3):33–86, Oct. 2010.

[29] B. A. Benson, P. A. R. Ade, Z. Ahmed, S. W. Allen, K. Arnold, J. E. Auster-
mann, A. N. Bender, L. E. Bleem, J. E. Carlstrom, C. L. Chang, H. M. Cho,
J. F. Cliche, T. M. Crawford, A. Cukierman, T. de Haan, M. A. Dobbs,
D. Dutcher, W. Everett, A. Gilbert, N. W. Halverson, D. Hanson, N. L.
Harrington, K. Hattori, J. W. Henning, G. C. Hilton, G. P. Holder, W. L.
Holzapfel, K. D. Irwin, R. Keisler, L. Knox, D. Kubik, C. L. Kuo, A. T. Lee,
E. M. Leitch, D. Li, M. McDonald, S. S. Meyer, J. Montgomery, M. My-
ers, T. Natoli, H. Nguyen, V. Novosad, S. Padin, Z. Pan, J. Pearson, C. Re-
ichardt, J. E. Ruhl, B. R. Saliwanchik, G. Simard, G. Smecher, J. T. Sayre,
E. Shirokoff, A. A. Stark, K. Story, A. Suzuki, K. L. Thompson, C. Tucker,
K. Vanderlinde, J. D. Vieira, A. Vikhlinin, G. Wang, V. Yefremenko, and
K. W. Yoon. SPT-3G: a next-generation cosmic microwave background po-
larization experiment on the South Pole telescope. In *Millimeter, Submil-
limeter, and Far-Infrared Detectors and Instrumentation for Astronomy VII*,
volume 9153 of , page 91531P, July 2014.

[30] A. A. Berlind and D. H. Weinberg. The halo occupation distribution:
Toward an empirical determination of the relation between galaxies and
mass. *The Astrophysical Journal*, 575(2):587â616, Aug 2002.

[31] A. A. Berlind and D. H. Weinberg. The Halo Occupation Distribution:
Toward an Empirical Determination of the Relation between Galaxies and
Mass. , 575(2):587–616, Aug 2002.

[32] F. Bernardeau, S. Colombi, E. Gaztanaga, and R. Scoccimarro. Large scale structure of the universe and cosmological perturbation theory. *Phys. Rept.*, 367:1–248, 2002.

[33] F. Beutler, H.-J. Seo, S. Saito, C.-H. Chuang, A. J. Cuesta, D. J. Eisenstein, H. Gil-MarÃn, J. N. Grieb, N. Hand, F.-S. Kitaura, and et al. The clustering of galaxies in the completed sdss-iii baryon oscillation spectroscopic survey: anisotropic galaxy clustering in fourier space. *Monthly Notices of the Royal Astronomical Society*, 466(2):2242â2260, Dec 2016.

[34] V. Biffi, S. Borgani, G. Murante, E. Rasia, S. Planelles, G. L. Granato, C. Ragone-Figueroa, A. M. Beck, M. Gaspari, and K. Dolag. On the Nature of Hydrostatic Equilibrium in Galaxy Clusters. , 827(2):112, Aug. 2016.

[35] S. Bird, M. Viel, and M. G. Haehnelt. Massive neutrinos and the non-linear matter power spectrum. , 420(3):2551–2561, Mar. 2012.

[36] C. Blake, S. Brough, M. Colless, C. Contreras, W. Couch, S. Croom, T. Davis, M. J. Drinkwater, K. Forster, D. Gilbank, and et al. The wigglez dark energy survey: the growth rate of cosmic structure since redshift z=0.9. *Monthly Notices of the Royal Astronomical Society*, 415(3):2876â2891, Jun 2011.

[37] J. Blazek, Z. Vlah, and U. Seljak. Tidal alignment of galaxies. *Journal of Cosmology and Astroparticle Physics*, 2015(08):015â015, Aug 2015.

[38] J. A. Blazek, N. MacCrann, M. Troxel, and X. Fang. Beyond linear galaxy alignments. *Physical Review D*, 100(10), Nov 2019.

[39] S. Bocquet, J. P. Dietrich, T. Schrabback, L. E. Bleem, M. Klein, S. W. Allen, D. E. Applegate, M. L. N. Ashby, M. Bautz, M. Bayliss, and et al. Cluster cosmology constraints from the 2500 deg2 spt-sz survey: Inclusion of weak gravitational lensing data from magellan and the hubble space telescope. , 878(1):55, Jun 2019.

[40] H. Böhringer and N. Werner. X-ray spectroscopy of galaxy clusters: studying astrophysical processes in the largest celestial laboratories. , 18:127–196, Feb. 2010.

[41] B. Bolliet, T. Brinckmann, J. Chluba, and J. Lesgourgues. Including massive neutrinos in thermal sunyaev zeldovich power spectrum and cluster counts analyses. , 497(2):1332â1347, Jul 2020.

[42] B. Bolliet, B. Comis, E. Komatsu, and J. F. MacÃas-PÃ©rez. Dark energy constraints from the thermal sunyaevâzeldovich power spectrum. , 477(4):4957â4967, Mar 2018.

[43] F. R. Bouchet, S. Colombi, E. Hivon, and R. Juszkiewicz. Perturbative Lagrangian approach to gravitational instability. , 296:575, Apr 1995.

[44] S. Bridle and L. King. Dark energy constraints from cosmic shear power spectra: impact of intrinsic alignments on photometric redshift requirements. *New Journal of Physics*, 9(12):444, Dec. 2007.

[45] S. Bridle and L. King. Dark energy constraints from cosmic shear power spectra: impact of intrinsic alignments on photometric redshift requirements. *New Journal of Physics*, 9(12):444, Dec. 2007.

[46] S. L. Bridle, R. Crittenden, A. Melchiorri, M. P. Hobson, R. Kneissl, and A. N. Lasenby. Analytic marginalization over cmb calibration and beam uncertainty. *Monthly Notices of the Royal Astronomical Society*, 335(4):1193â1200, Oct 2002.

[47] M. L. Brown, A. N. Taylor, N. C. Hambly, and S. Dye. Measurement of intrinsic alignments in galaxy ellipticities. , 333(3):501–509, July 2002.

[48] G. Bruzual and S. Charlot. Stellar population synthesis at the resolution of 2003. , 344:1000–1028, Oct. 2003.

[49] J. S. Bullock, T. S. Kolatt, Y. Sigad, R. S. Somerville, A. V. Kravtsov, A. A. Klypin, J. R. Primack, and A. Dekel. Profiles of dark haloes: evolution, scatter and environment. , 321(3):559â575, Mar 2001.

[50] M. Cacciato, O. Lahav, F. C. van den Bosch, H. Hoekstra, and A. Dekel. On combining galaxy clustering and weak lensing to unveil galaxy bias-

ing via the halo model. *Monthly Notices of the Royal Astronomical Society*, 426(1):566â587, Sep 2012.

[51] M. Cacciato, F. C. van den Bosch, S. More, R. Li, H. J. Mo, and X. Yang. Galaxy clustering and galaxy-galaxy lensing: a promising union to constrain cosmological parameters. *Monthly Notices of the Royal Astronomical Society*, 394(2):929â946, Apr 2009.

[52] M. Cacciato, F. C. van den Bosch, S. More, H. Mo, and X. Yang. Cosmological constraints from a combination of galaxy clustering and lensing â iii. application to sdss data. *Monthly Notices of the Royal Astronomical Society*, 430(2):767â786, Feb 2013.

[53] J. Carlson, B. Reid, and M. White. Convolution Lagrangian perturbation theory for biased tracers. , 429(2):1674–1685, Feb 2013.

[54] J. E. Carlstrom, P. A. R. Ade, K. A. Aird, B. A. Benson, L. E. Bleem, S. Busetti, C. L. Chang, E. Chauvin, H.-M. Cho, T. M. Crawford, A. T. Crites, M. A. Dobbs, N. W. Halverson, S. Heimsath, W. L. Holzapfel, J. D. Hrubes, M. Joy, R. Keisler, T. M. Lanting, A. T. Lee, E. M. Leitch, J. Leong, W. Lu, M. Lueker, D. Luong-Van, J. J. McMahon, J. Mehl, S. S. Meyer, J. J. Mohr, T. E. Montroy, S. Padin, T. Plagge, C. Pryke, J. E. Ruhl, K. K. Schaffer, D. Schwan, E. Shirokoff, H. G. Spieler, Z. Staniszewski, A. A. Stark, C. Tucker, K. Vanderlinde, J. D. Vieira, and R. Williamson. The 10 meter

south pole telescope. *Publications of the Astronomical Society of the Pacific*, 123(903):568, 2011.

[55] J. E. Carlstrom, G. P. Holder, and E. D. Reese. Cosmology with the Sunyaev-Zel'dovich Effect. *Annual Review of Astronomy and Astrophysics*, 40:643–680, Jan. 2002.

[56] J. J. M. Carrasco, M. P. Hertzberg, and L. Senatore. The Effective Field Theory of Cosmological Large Scale Structures. *JHEP*, 09:082, 2012.

[57] J. Carretero, F. J. Castander, E. Gaztanaga, M. Crocce, and P. Fosalba. An algorithm to build mock galaxy catalogues using MICE simulations. , 447:646–670, Feb. 2015.

[58] R. Cawthon, C. Davis, M. Gatti, P. Vielzeuf, J. Elvin-Poole, E. Rozo, J. Frieman, E. S. Rykoff, A. Alarcon, G. M. Bernstein, C. Bonnett, A. Carnero Rosell, F. J. Castander, C. Chang, L. N. da Costa, J. De Vicente, J. DeRose, A. Drlica-Wagner, E. Gaztanaga, T. Giannantonio, D. Gruen, J. Gschwend, W. G. Hartley, B. Hoyle, H. Lin, M. A. G. Maia, R. Miquel, R. L. C. Ogando, M. M. Rau, A. Roodman, A. J. Ross, I. Sevilla-Noarbe, M. A. Troxel, R. H. Wechsler, T. M. C. Abbott, F. B. Abdalla, S. Allam, J. Annis, S. Avila, M. Banerji, K. Bechtol, R. A. Bernstein, E. Bertin, D. Brooks, D. L. Burke, M. Carrasco Kind, J. Carretero, C. E. Cunha, C. B. D'Andrea, D. L. DePoy, S. Desai, H. T. Diehl, P. Doel, T. F. Eifler, A. E. Evrard, B. Flaugher,

P. Fosalba, J. García-Bellido, D. W. Gerdes, R. A. Gruendl, G. Gutierrez, D. Hollowood, K. Honscheid, D. J. James, T. Jeltema, E. Krause, K. Kuehn, S. Kuhlmann, N. Kuropatkin, O. Lahav, M. Lima, J. L. Marshall, P. Martini, F. Menanteau, C. J. Miller, A. A. Plazas, E. Sanchez, V. Scarpine, R. Schindler, M. Schubnell, E. Sheldon, M. Smith, R. C. Smith, M. Soares-Santos, F. Sobreira, E. Suchyta, M. E. C. Swanson, G. Tarle, D. Thomas, D. L. Tucker, A. R. Walker, and DES Collaboration. Dark Energy Survey Year 1 Results: calibration of redMaGiC redshift distributions in DES and SDSS from cross-correlations. , 481:2427–2443, Dec. 2018.

[59] R. Cawthon et al. Dark Energy Survey Year 3 Results: Calibration of Lens Sample Redshift Distributions using Clustering Redshifts with BOSS/eBOSS. *Submitted to MNRAS*, 12 2020.

[60] K. C. Chan, R. Scoccimarro, and R. K. Sheth. Gravity and large-scale non-local bias. *Phys. Rev. D*, 85:083509, Apr 2012.

[61] Y.-K. Chiang, R. Makiya, E. Komatsu, and B. Ménard. The Thermal and Gravitational Energy Densities in the Large-scale Structure of the Universe. , 910(1):32, Mar. 2021.

[62] S. K. Choi, M. Hasselfield, S.-P. P. Ho, B. Koopman, M. Lungu, M. H. Abitbol, G. E. Addison, P. A. R. Ade, S. Aiola, D. Alonso, M. Amiri, S. Amodeo, E. Angile, J. E. Austermann, T. Baildon, N. Battaglia, J. A. Beall, R. Bean,

D. T. Becker, J. R. Bond, S. M. Bruno, E. Calabrese, V. Calafut, L. E. Campusano, F. Carrero, G. E. Chesmore, H.-m. Cho, S. E. Clark, N. F. Cothard, D. Crichton, K. T. Crowley, O. Darwish, R. Datta, E. V. Denison, M. J. Devlin, C. J. Duell, S. M. Duff, A. J. Duivenvoorden, J. Dunkley, R. Dünner, T. Essinger-Hileman, M. Fankhanel, S. Ferraro, A. E. Fox, B. Fuzia, P. A. Gallardo, V. Gluscevic, J. E. Golec, E. Grace, M. Gralla, Y. Guan, K. Hall, M. Halpern, D. Han, P. Hargrave, S. Henderson, B. Hensley, J. C. Hill, G. C. Hilton, M. Hilton, A. D. Hincks, R. Hložek, J. Hubmayr, K. M. Huffenberger, J. P. Hughes, L. Infante, K. Irwin, R. Jackson, J. Klein, K. Knowles, A. Kosowsky, V. Lakey, D. Li, Y. Li, Z. Li, M. Lokken, T. Louis, A. MacInnis, M. Madhavacheril, F. Maldonado, M. Mallaby-Kay, D. Marsden, L. Maurin, J. McMahon, F. Menanteau, K. Moodley, T. Morton, S. Naess, T. Namikawa, F. Nati, L. Newburgh, J. P. Nibarger, A. Nicola, M. D. Niemack, M. R. Nolta, J. Orlowski-Sherer, L. A. Page, C. G. Pappas, B. Partridge, P. Phakathi, H. Prince, R. Puddu, F. J. Qu, J. Rivera, N. Robertson, F. Rojas, M. Salatino, E. Schaan, A. Schillaci, B. L. Schmitt, N. Sehgal, B. D. Sherwin, C. Sierra, J. Sievers, C. Sifon, P. Sikhosana, S. Simon, D. N. Spergel, S. T. Staggs, J. Stevens, E. Storer, D. D. Sunder, E. R. Switzer, B. Thorne, R. Thornton, H. Trac, J. Treu, C. Tucker, L. R. Vale, A. Van Engelen, J. Van Lanen, E. M. Vavagiakis, K. Wagoner, Y. Wang, J. T. Ward, E. J. Wollack, Z. Xu, F. Zago, and N. Zhu. The Atacama Cosmology Telescope: a measurement

of the Cosmic Microwave Background power spectra at 98 and 150 GHz. , 2020(12):045, Dec. 2020.

[63] A. Chudaykin and M. M. Ivanov. Measuring neutrino masses with large-scale structure: Euclid forecast with controlled theoretical error. *Journal of Cosmology and Astroparticle Physics*, 2019(11):034â034, Nov 2019.

[64] J. Clampitt, C. SÃ¡nchez, J. Kwan, E. Krause, N. MacCrann, Y. Park, M. A. Troxel, B. Jain, E. Rozo, E. S. Rykoff, and et al. Galaxyâgalaxy lensing in the dark energy survey science verification data. *Monthly Notices of the Royal Astronomical Society*, 465(4):4204â4218, Nov 2016.

[65] P. Coles. Galaxy formation with a local bias. , 262(4):1065–1075, June 1993.

[66] A. Cooray. Non-gaussian aspects of thermal and kinetic sunyaev-zelâdovich effects. , 64(6), Aug 2001.

[67] A. Cooray and R. Sheth. Halo models of large scale structure. , 372(1):1–129, Dec 2002.

[68] A. Cooray and R. Sheth. Halo models of large scale structure. *Physics Reports*, 372(1):1â129, Dec 2002.

[69] A. Cooray and R. Sheth. Halo models of large scale structure. , 372:1–129, Dec. 2002.

315

[70] J. P. Cordero, I. Harrison, et al. Dark Energy Survey Year 3 Results: Marginalisation over redshiftdistribution uncertainties using ranking of discrete realisations. *To be submitted to MNRAS*, 2021.

[71] M. Costanzi, E. Rozo, M. Simet, Y. Zhang, A. E. Evrard, A. Mantz, E. S. Rykoff, T. Jeltema, D. Gruen, S. Allen, and et al. Methods for cluster cosmology and application to the sdss in preparation for des year 1 release. , 488(4):4779â4800, Jul 2019.

[72] J. Coupon, S. Arnouts, L. van Waerbeke, T. Moutard, O. Ilbert, E. van Uitert, T. Erben, B. Garilli, L. Guzzo, C. Heymans, and et al. The galaxyâhalo connection from a joint lensing, clustering and abundance analysis in the cfhtlens/vipers field. *Monthly Notices of the Royal Astronomical Society*, 449(2):1352â1379, Mar 2015.

[73] M. Crocce, F. J. Castander, E. Gaztanaga, P. Fosalba, and J. Carretero. The mice grand challenge lightcone simulation â ii. halo and galaxy catalogues. *Monthly Notices of the Royal Astronomical Society*, 453(2):1513â1530, Aug 2015.

[74] M. Crocce, F. J. Castander, E. Gaztanaga, P. Fosalba, and J. Carretero. The MICE Grand Challenge lightcone simulation - II. Halo and galaxy catalogues. , 453:1513–1530, Oct. 2015.

[75] M. Crocce, S. Pueblas, and R. Scoccimarro. 2LPTIC: 2nd-order Lagrangian Perturbation Theory Initial Conditions, Jan. 2012.

[76] M. Crocce and R. Scoccimarro. Renormalized cosmological perturbation theory. , 73(6):063519, Mar 2006.

[77] G. D'Amico, J. Gleyzes, N. Kokron, D. Markovic, L. Senatore, P. Zhang, F. Beutler, and H. Gil-Marín. The Cosmological Analysis of the SDSS/BOSS data from the Effective Field Theory of Large-Scale Structure. *arXiv e-prints*, page arXiv:1909.05271, Sep 2019.

[78] Dark Energy Survey Collaboration, T. Abbott, F. B. Abdalla, J. Aleksić, S. Allam, A. Amara, D. Bacon, E. Balbinot, M. Banerji, K. Bechtol, A. Benoit-Lévy, G. M. Bernstein, E. Bertin, J. Blazek, C. Bonnett, S. Bridle, D. Brooks, R. J. Brunner, E. Buckley-Geer, D. L. Burke, G. B. Caminha, D. Capozzi, J. Carlsen, A. Carnero-Rosell, M. Carollo, M. Carrasco-Kind, J. Carretero, F. J. Castander, L. Clerkin, T. Collett, C. Conselice, M. Crocce, C. E. Cunha, C. B. D'Andrea, L. N. da Costa, T. M. Davis, S. Desai, H. T. Diehl, J. P. Dietrich, S. Dodelson, P. Doel, A. Drlica-Wagner, J. Estrada, J. Etherington, A. E. Evrard, J. Fabbri, D. A. Finley, B. Flaugher, R. J. Foley, P. Fosalba, J. Frieman, J. García-Bellido, E. Gaztanaga, D. W. Gerdes, T. Giannantonio, D. A. Goldstein, D. Gruen, R. A. Gruendl, P. Guarnieri, G. Gutierrez, W. Hartley, K. Honscheid, B. Jain, D. J. James, T. Jeltema,

S. Jouvel, R. Kessler, A. King, D. Kirk, R. Kron, K. Kuehn, N. Kuropatkin, O. Lahav, T. S. Li, M. Lima, H. Lin, M. A. G. Maia, M. Makler, M. Manera, C. Maraston, J. L. Marshall, P. Martini, R. G. McMahon, P. Melchior, A. Merson, C. J. Miller, R. Miquel, J. J. Mohr, X. Morice-Atkinson, K. Naidoo, E. Neilsen, R. C. Nichol, B. Nord, R. Ogando, F. Ostrovski, A. Palmese, A. Papadopoulos, H. V. Peiris, J. Peoples, W. J. Percival, A. A. Plazas, S. L. Reed, A. Refregier, A. K. Romer, A. Roodman, A. Ross, E. Rozo, E. S. Rykoff, I. Sadeh, M. Sako, C. Sánchez, E. Sanchez, B. Santiago, V. Scarpine, M. Schubnell, I. Sevilla-Noarbe, E. Sheldon, M. Smith, R. C. Smith, M. Soares-Santos, F. Sobreira, M. Soumagnac, E. Suchyta, M. Sullivan, M. Swanson, G. Tarle, J. Thaler, D. Thomas, R. C. Thomas, D. Tucker, J. D. Vieira, V. Vikram, A. R. Walker, R. H. Wechsler, J. Weller, W. Wester, L. Whiteway, H. Wilcox, B. Yanny, Y. Zhang, and J. Zuntz. The Dark Energy Survey: more than dark energy - an overview. , 460:1270–1299, Aug. 2016.

[79] L. F. de la Bella, D. Regan, D. Seery, and D. Parkinson. Impact of bias and redshift-space modelling for the halo power spectrum: Testing the effective field theory of large-scale structure, 2018.

[80] J. De Vicente, E. Sánchez, and I. Sevilla-Noarbe. DNF - Galaxy photometric redshift by Directional Neighbourhood Fitting. , 459(3):3078–3088, Jul 2016.

[81] A. Dekel and O. Lahav. Stochastic nonlinear galaxy biasing. *The Astro-physical Journal*, 520(1):24â34, Jul 1999.

[82] J. Delabrouille, J. F. Cardoso, M. L. Jeune, M. Betoule, G. Fay, and F. Guilloux. A full sky , low foreground , high resolution CMB map from WMAP. 2014.

[83] J. Delabrouille, J.-F. Cardoso, M. Le Jeune, M. Betoule, G. Fay, and F. Guilloux. A full sky, low foreground, high resolution CMB map from WMAP. , 493:835–857, Jan. 2009.

[84] J. DeRose, M. R. Becker, and R. H. Wechsler. Modeling Redshift-Space Clustering with Abundance Matching. *arXiv e-prints*, page arXiv:2105.12104, May 2021.

[85] J. DeRose et al. Dark Energy Survey Year 3 Results: Validating 3×2-point Modeling and Analysis Choices using Cosmological Simulations. *To be submitted to MNRAS*, 2021.

[86] J. DeRose, R. H. Wechsler, M. R. Becker, M. T. Busha, E. S. Rykoff, N. Mac-Crann, B. Erickson, A. E. Evrard, A. Kravtsov, D. Gruen, S. Allam, S. Avila, S. Bridle, D. Brooks, E. Buckley-Geer, A. Carnero Rosell, M. Carrasco Kind, J. Carretero, F. J. Castander, R. Cawthon, M. Crocce, L. N. da Costa, C. Davis, J. De Vicente, J. P. Dietrich, P. Doel, A. Drlica-Wagner, P. Fosalba, J. Frieman, J. Garcia-Bellido, G. Gutierrez, W. G. Hartley, D. L.

Hollowood, B. Hoyle, D. J. James, E. Krause, K. Kuehn, N. Kuropatkin, M. Lima, M. A. G. Maia, F. Menanteau, C. J. Miller, R. Miquel, R. L. C. Ogando, A. Plazas Malagón, A. K. Romer, E. Sanchez, R. Schindler, S. Serrano, I. Sevilla-Noarbe, M. Smith, E. Suchyta, M. E. C. Swanson, G. Tarle, and V. Vikram. The Buzzard Flock: Dark Energy Survey Synthetic Sky Catalogs. *arXiv e-prints*, page arXiv:1901.02401, Jan. 2019.

[87] J. DeRose, R. H. Wechsler, M. R. Becker, M. T. Busha, E. S. Rykoff, N. Mac-Crann, B. Erickson, A. E. Evrard, A. Kravtsov, D. Gruen, S. Allam, S. Avila, S. Bridle, D. Brooks, E. Buckley-Geer, A. Carnero Rosell, M. Carrasco Kind, J. Carretero, F. J. Castander, R. Cawthon, M. Crocce, L. N. da Costa, C. Davis, J. De Vicente, J. P. Dietrich, P. Doel, A. Drlica-Wagner, P. Fosalba, J. Frieman, J. Garcia-Bellido, G. Gutierrez, W. G. Hartley, D. L. Hollowood, B. Hoyle, D. J. James, E. Krause, K. Kuehn, N. Kuropatkin, M. Lima, M. A. G. Maia, F. Menanteau, C. J. Miller, R. Miquel, R. L. C. Ogand o, A. Plazas Malagón, A. K. Romer, E. Sanchez, R. Schindler, S. Serrano, I. Sevilla-Noarbe, M. Smith, E. Suchyta, M. E. C. Swanson, G. Tarle, and V. Vikram. The Buzzard Flock: Dark Energy Survey Synthetic Sky Catalogs. *arXiv e-prints*, page arXiv:1901.02401, Jan 2019.

[88] DES Collaboration. Dark Energy Survey Year 3 Results: Cosmological Constraints from Galaxy Clustering and Weak Lensing. *To be submitted to PRD*, 2021.

[89] DES Collaboration, T. M. C. Abbott, F. B. Abdalla, A. Alarcon, J. Alek-
     sić, S. Allam, S. Allen, A. Amara, J. Annis, J. Asorey, S. Avila, D. Bacon,
     E. Balbinot, M. Banerji, N. Banik, W. Barkhouse, M. Baumer, E. Baxter,
     K. Bechtol, M. R. Becker, A. Benoit-Lévy, B. A. Benson, G. M. Bernstein,
     E. Bertin, J. Blazek, S. L. Bridle, D. Brooks, D. Brout, E. Buckley-Geer, D. L.
     Burke, M. T. Busha, D. Capozzi, A. Carnero Rosell, M. Carrasco Kind,
     J. Carretero, F. J. Castander, R. Cawthon, C. Chang, N. Chen, M. Chil-
     dress, A. Choi, C. Conselice, R. Crittenden, M. Crocce, C. E. Cunha, C. B.
     D'Andrea, L. N. da Costa, R. Das, T. M. Davis, C. Davis, J. De Vicente,
     D. L. DePoy, J. DeRose, S. Desai, H. T. Diehl, J. P. Dietrich, S. Dodelson,
     P. Doel, A. Drlica-Wagner, T. F. Eifler, A. E. Elliott, F. Elsner, J. Elvin-
     Poole, J. Estrada, A. E. Evrard, Y. Fang, E. Fernandez, A. Ferté, D. A.
     Finley, B. Flaugher, P. Fosalba, O. Friedrich, J. Frieman, J. García-Bellido,
     M. Garcia-Fernandez, M. Gatti, E. Gaztanaga, D. W. Gerdes, T. Giannan-
     tonio, M. S. S. Gill, K. Glazebrook, D. A. Goldstein, D. Gruen, R. A. Gru-
     endl, J. Gschwend, G. Gutierrez, S. Hamilton, W. G. Hartley, S. R. Hinton,
     K. Honscheid, B. Hoyle, D. Huterer, B. Jain, D. J. James, M. Jarvis, T. Jel-
     tema, M. D. Johnson, M. W. G. Johnson, T. Kacprzak, S. Kent, A. G. Kim,
     A. King, D. Kirk, N. Kokron, A. Kovacs, E. Krause, C. Krawiec, A. Kremin,
     K. Kuehn, S. Kuhlmann, N. Kuropatkin, F. Lacasa, O. Lahav, T. S. Li,
     A. R. Liddle, C. Lidman, M. Lima, H. Lin, N. MacCrann, M. A. G. Maia,

M. Makler, M. Manera, M. March, J. L. Marshall, P. Martini, R. G. McMahon, P. Melchior, F. Menanteau, R. Miquel, V. Miranda, D. Mudd, J. Muir, A. Möller, E. Neilsen, R. C. Nichol, B. Nord, P. Nugent, R. L. C. Ogando, A. Palmese, J. Peacock, H. V. Peiris, J. Peoples, W. J. Percival, D. Petravick, A. A. Plazas, A. Porredon, J. Prat, A. Pujol, M. M. Rau, A. Refregier, P. M. Ricker, N. Roe, R. P. Rollins, A. K. Romer, A. Roodman, R. Rosenfeld, A. J. Ross, E. Rozo, E. S. Rykoff, M. Sako, A. I. Salvador, S. Samuroff, C. Sánchez, E. Sanchez, B. Santiago, V. Scarpine, R. Schindler, D. Scolnic, L. F. Secco, S. Serrano, I. Sevilla-Noarbe, E. Sheldon, R. C. Smith, M. Smith, J. Smith, M. Soares-Santos, F. Sobreira, E. Suchyta, G. Tarle, D. Thomas, M. A. Troxel, D. L. Tucker, B. E. Tucker, S. A. Uddin, T. N. Varga, P. Vielzeuf, V. Vikram, A. K. Vivas, A. R. Walker, M. Wang, R. H. Wechsler, J. Weller, W. Wester, R. C. Wolf, B. Yanny, F. Yuan, A. Zenteno, B. Zhang, Y. Zhang, and J. Zuntz. Dark Energy Survey Year 1 Results: Cosmological Constraints from Galaxy Clustering and Weak Lensing. *ArXiv e-prints*, Aug. 2017.

[90] DES Collaboration et al. *in preparation*, 2022.

[91] V. Desjacques, D. Jeong, and F. Schmidt. Large-scale galaxy bias. *Physics Reports*, 733:1â193, Feb 2018.

[92] T. Di Matteo, V. Springel, and L. Hernquist. Energy input from quasars

regulates the growth and activity of black holes and their host galaxies. ,
433:604–607, Feb. 2005.

[93] B. Diemer, S. More, and A. V. Kravtsov. The pseudo-evolution of halo
mass. *The Astrophysical Journal*, 766(1):25, Mar 2013.

[94] S. Dodelson. *Modern Cosmology*. 2003.

[95] S. Dodelson. *Gravitational Lensing*. 2017.

[96] A. Dvornik, H. Hoekstra, K. Kuijken, P. Schneider, A. Amon, R. Nakajima,
M. Viola, A. Choi, T. Erben, D. J. Farrow, and et al. Unveiling galaxy bias
via the halo model, kids, and gama. *Monthly Notices of the Royal Astronom-
ical Society*, 479(1):1240â1259, Jun 2018.

[97] D. Eckert, V. Ghirardini, S. Ettori, E. Rasia, V. Biffi, E. Pointecouteau,
M. Rossetti, S. Molendi, F. Vazza, F. Gastaldello, M. Gaspari, S. De Grandi,
S. Ghizzardi, H. Bourdin, C. Tchernin, and M. Roncarelli. Non-thermal
pressure support in X-COP galaxy clusters. , 621:A40, Jan. 2019.

[98] A. Eggemeier, R. Scoccimarro, M. Crocce, A. Pezzotta, and A. G. SÃ¡nchez.
Testing one-loop galaxy bias – i. power spectrum, 2020.

[99] A. Eggemeier, R. Scoccimarro, and R. E. Smith. Bias loop corrections to the
galaxy bispectrum. *Physical Review D*, 99(12), Jun 2019.

[100] J. Elvin-Poole, M. Crocce, A. J. Ross, T. Giannantonio, E. Rozo, E. S. Rykoff, S. Avila, N. Banik, J. Blazek, S. L. Bridle, R. Cawthon, A. Drlica-Wagner, O. Friedrich, N. Kokron, E. Krause, N. MacCrann, J. Prat, C. Sánchez, L. F. Secco, I. Sevilla-Noarbe, M. A. Troxel, T. M. C. Abbott, F. B. Abdalla, S. Allam, J. Annis, J. Asorey, K. Bechtol, M. R. Becker, A. Benoit-Lévy, G. M. Bernstein, E. Bertin, D. Brooks, E. Buckley-Geer, D. L. Burke, A. Carnero Rosell, D. Carollo, M. Carrasco Kind, J. Carretero, F. J. Castander, C. E. Cunha, C. B. D'Andrea, L. N. da Costa, T. M. Davis, C. Davis, S. Desai, H. T. Diehl, J. P. Dietrich, S. Dodelson, P. Doel, T. F. Eifler, A. E. Evrard, E. Fernandez, B. Flaugher, P. Fosalba, J. Frieman, J. García-Bellido, E. Gaztanaga, D. W. Gerdes, K. Glazebrook, D. Gruen, R. A. Gruendl, J. Gschwend, G. Gutierrez, W. G. Hartley, S. R. Hinton, K. Honscheid, J. K. Hoormann, B. Jain, D. J. James, M. Jarvis, T. Jeltema, M. W. G. Johnson, M. D. Johnson, A. King, K. Kuehn, S. Kuhlmann, N. Kuropatkin, O. Lahav, G. Lewis, T. S. Li, C. Lidman, M. Lima, H. Lin, E. Macaulay, M. March, J. L. Marshall, P. Martini, P. Melchior, F. Menanteau, R. Miquel, J. J. Mohr, A. Möller, R. C. Nichol, B. Nord, C. R. O'Neill, W. J. Percival, D. Petravick, A. A. Plazas, A. K. Romer, M. Sako, E. Sanchez, V. Scarpine, R. Schindler, M. Schubnell, E. Sheldon, M. Smith, R. C. Smith, M. Soares-Santos, F. Sobreira, N. E. Sommer, E. Suchyta, M. E. C. Swanson, G. Tarle, D. Thomas, B. E. Tucker, D. L. Tucker, S. A. Uddin, V. Vikram, A. R. Walker, R. H.

Wechsler, J. Weller, W. Wester, R. C. Wolf, F. Yuan, B. Zhang, J. Zuntz, and DES Collaboration. Dark Energy Survey year 1 results: Galaxy clustering for combined probes. , 98:042006, Aug. 2018.

[101] J. Elvin-Poole, N. MacCrann, et al. Dark Energy Survey Year 3 Results: Measurement, modelling and cosmological impact of magnification in galaxy clustering and galaxy-galaxy lensing. *To be submitted to MNRAS*, 2021.

[102] S. Everett et al. Dark Energy Survey Year 3 Results: Measuring the Survey Transfer Function with Balrog. *Submitted to ApJS*, 12 2020.

[103] S. Everett, B. Yanny, N. Kuropatkin, E. M. Huff, Y. Zhang, J. Myles, A. Masegian, J. Elvin-Poole, S. Allam, G. M. Bernstein, I. Sevilla-Noarbe, M. Splettstoesser, E. Sheldon, M. Jarvis, A. Amon, I. Harrison, A. Choi, W. G. Hartley, A. Alarcon, C. Sãnchez, D. Gruen, K. Eckert, J. Prat, M. Tabbutt, V. Busti, M. R. Becker, N. MacCrann, H. T. Diehl, D. L. Tucker, E. Bertin, T. Jeltema, A. Drlica-Wagner, R. A. Gruendl, K. Bechtol, A. C. Rosell, T. M. C. Abbott, M. Aguena, J. Annis, D. Bacon, S. Bhargava, D. Brooks, D. L. Burke, M. C. Kind, J. Carretero, F. J. Castander, C. Conselice, M. Costanzi, L. N. da Costa, M. E. S. Pereira, J. D. Vicente, J. DeRose, S. Desai, T. F. Eifler, A. E. Evrard, I. Ferrero, P. Fosalba, J. Frieman, J. GarcÃa-Bellido, E. Gaztanaga, D. W. Gerdes, G. Gutierrez, S. R.

Hinton, D. L. Hollowood, K. Honscheid, D. Huterer, D. J. James, S. Kent, E. Krause, K. Kuehn, O. Lahav, M. Lima, H. Lin, M. A. G. Maia, J. L. Marshall, P. Melchior, F. Menanteau, R. Miquel, J. J. Mohr, R. Morgan, J. Muir, R. L. C. Ogando, A. Palmese, F. Paz-Chinchon, A. A. Plazas, M. Rodriguez-Monroy, A. K. Romer, A. Roodman, E. Sanchez, V. Scarpine, S. Serrano, M. Smith, M. Soares-Santos, E. Suchyta, M. E. C. Swanson, G. Tarle, C. To, M. A. Troxel, T. N. Varga, J. Weller, and R. D. Wilkinson. Dark energy survey year 3 results: Measuring the survey transfer function with balrog, 2020.

[104] A. E. Evrard. Formation and evolution of X-ray clusters - A hydrodynamic simulation of the intracluster medium. , 363:349–366, Nov. 1990.

[105] X. Fang, J. A. Blazek, J. E. McEwen, and C. M. Hirata. FAST-PT II : an algorithm to calculate convolution integrals of general tensor quantities in cosmological perturbation theory. *JCAP*, 2016.

[106] X. Fang, T. Eifler, and E. Krause. 2D-FFTLog: Efficient computation of real space covariance matrices for galaxy clustering and weak lensing. *arXiv e-prints*, page arXiv:2004.04833, Apr. 2020.

[107] X. Fang, T. Eifler, and E. Krause. 2d-fftlog: efficient computation of real-space covariance matrices for galaxy clustering and weak lensing. , 497(3):2699â2714, Jun 2020.

[108] X. Fang, E. Krause, T. Eifler, and N. MacCrann. Beyond Limber: efficient computation of angular power spectra for galaxy clustering and weak lensing. , 2020(5):010, May 2020.

[109] B. Flaugher, H. T. Diehl, K. Honscheid, T. M. C. Abbott, O. Alvarez, R. Angstadt, J. T. Annis, M. Antonik, O. Ballester, L. Beaufore, G. M. Bernstein, R. A. Bernstein, B. Bigelow, M. Bonati, D. Boprie, D. Brooks, E. J. Buckley-Geer, J. Campa, L. Cardiel-Sas, F. J. Castander, J. Castilla, H. Cease, J. M. Cela-Ruiz, S. Chappa, E. Chi, C. Cooper, L. N. da Costa, E. Dede, G. Derylo, D. L. DePoy, J. de Vicente, P. Doel, A. Drlica-Wagner, J. Eiting, A. E. Elliott, J. Emes, J. Estrada, A. F. Neto, D. A. Finley, R. Flores, J. Frieman, D. Gerdes, M. D. Gladders, B. Gregory, G. R. Gutierrez, J. Hao, S. E. Holland, S. Holm, D. Huffman, C. Jackson, D. J. James, M. Jonas, A. Karcher, I. Karliner, S. Kent, R. Kessler, M. Kozlovsky, R. G. Kron, D. Kubik, K. Kuehn, S. Kuhlmann, K. Kuk, O. Lahav, A. Lathrop, J. Lee, M. E. Levi, P. Lewis, T. S. Li, I. Mandrichenko, J. L. Marshall, G. Martinez, K. W. Merritt, R. Miquel, F. Muatoz, E. H. Neilsen, R. C. Nichol, B. Nord, R. Ogando, J. Olsen, N. Palaio, K. Patton, J. Peoples, A. A. Plazas, J. Rauch, K. Reil, J.-P. Rheault, N. A. Roe, H. Rogers, A. Roodman, E. Sanchez, V. Scarpine, R. H. Schindler, R. Schmidt, R. Schmitt, M. Schubnell, K. Schultz, P. Schurter, L. Scott, S. Serrano, T. M. Shaw, R. C. Smith, M. Soares-Santos, A. Stefanik, W. Stuermer, E. Suchyta, A. Sypniewski,

G. Tarle, J. Thaler, R. Tighe, C. Tran, D. Tucker, A. R. Walker, G. Wang, M. Watson, C. Weaverdyck, W. Wester, R. Woods, B. Yanny, and T. D. Collaboration. The dark energy camera. *The Astronomical Journal*, 150(5):150, 2015.

[110] B. Flaugher, H. T. Diehl, K. Honscheid, T. M. C. Abbott, O. Alvarez, R. Angstadt, J. T. Annis, M. Antonik, O. Ballester, L. Beaufore, and et al. The dark energy camera. *The Astronomical Journal*, 150(5):150, Oct 2015.

[111] D. Foreman-Mackey, D. W. Hogg, D. Lang, and J. Goodman. emcee: The MCMC Hammer. *Publications of the Astronomical Society of the Pacific*, 125:306, Mar. 2013.

[112] M. C. Fortuna, H. Hoekstra, B. Joachimi, H. Johnston, N. E. Chisari, C. Georgiou, and C. Mahony. The halo model as a versatile tool to predict intrinsic alignments. , 501(2):2983–3002, Feb. 2021.

[113] P. Fosalba, M. Crocce, E. Gaztanaga, and F. J. Castand er. The MICE grand challenge lightcone simulation - I. Dark matter clustering. , 448(4):2987–3000, Apr 2015.

[114] P. Fosalba, M. Crocce, E. Gaztanaga, and F. J. Castander. The mice grand challenge lightcone simulation â i. dark matter clustering. *Monthly Notices of the Royal Astronomical Society*, 448(4):2987â3000, Mar 2015.

[115] P. Fosalba, M. Crocce, E. Gaztanaga, and F. J. Castander. The MICE grand challenge lightcone simulation - I. Dark matter clustering. , 448:2987–3000, Apr. 2015.

[116] P. Fosalba, E. Gaztanaga, F. J. Castander, and M. Crocce. The mice grand challenge light-cone simulation â iii. galaxy lensing mocks from all-sky lensing maps. *Monthly Notices of the Royal Astronomical Society*, 447(2):1319â1332, Dec 2014.

[117] P. Fosalba, E. Gaztanaga, F. J. Castander, and M. Crocce. The MICE Grand Challenge light-cone simulation - III. Galaxy lensing mocks from all-sky lensing maps. , 447:1319–1332, Feb. 2015.

[118] O. Friedrich et al. Dark Energy Survey Year 3 Results: Covariance Modelling and its Impact on Parameter Estimation and Quality of Fit. *Submitted to MNRAS*, 12 2020.

[119] O. Friedrich, S. Seitz, T. F. Eifler, and D. Gruen. Performance of internal Covariance Estimators for Cosmic Shear Correlation Functions. *Mon. Not. Roy. Astron. Soc.*, 456(3):2662–2680, 2016.

[120] Friedrich, O. et al. Sept. prep.

[121] J. N. Fry. The Evolution of Bias. , 461:L65, Apr. 1996.

[122] J. N. Fry and E. Gaztanaga. Biasing and Hierarchical Statistics in Large-Scale Structure. , 413:447, Aug. 1993.

[123] M. Gatti et al. Cross-correlation of DES Y3 lensing and ACT/Planck thermal Sunyaev Zelâdovich Effect I: Measurements, systematics tests, and feedback model constraints. *in preparation*, 2021.

[124] M. Gatti, G. Giannini, et al. Dark Energy Survey Year 3 Results: Clustering Redshifts – Calibration of the Weak Lensing Source Redshift Distributions with redMaGiC and BOSS/eBOSS. *Submitted to MNRAS*, 12 2020.

[125] M. Gatti, E. Sheldon, et al. Dark Energy Survey Year 3 Results: Weak Lensing Shape Catalogue. , 504(3):4312–4336, 2021.

[126] C. Georgiou, N. E. Chisari, M. C. Fortuna, H. Hoekstra, K. Kuijken, B. Joachimi, M. Vakili, M. Bilicki, A. Dvornik, T. Erben, and et al. Gama+kids: Alignment of galaxies in galaxy groups and its dependence on galaxy scale. , 628:A31, Jul 2019.

[127] G. Giannini et al. Dark Energy Survey Year 3 Results: Phenotypic redshift calibration for the DES Y3 Maglim lens galaxies. *To be submitted to PRD*, 2021.

[128] H. Gil-MarÃn, W. J. Percival, L. Verde, J. R. Brownstein, C.-H. Chuang, F.-S. Kitaura, S. A. RodrÃguez-Torres, and M. D. Olmstead. The clustering of

galaxies in the sdss-iii baryon oscillation spectroscopic survey: Rsd measurement from the power spectrum and bispectrum of the dr12 boss galaxies. *Monthly Notices of the Royal Astronomical Society*, 465(2):1757â1788, Oct 2016.

[129] W. D. Goldberger and I. Z. Rothstein. Effective field theory of gravity for extended objects. , 73(10):104029, May 2006.

[130] M. H. Goroff, B. Grinstein, S. J. Rey, and M. B. Wise. Coupling of modes of cosmological mass density fluctuations. , 311:6–14, Dec 1986.

[131] J. P. Greco, J. C. Hill, D. N. Spergel, and N. Battaglia. The Stacked Thermal Sunyaev-Zel'dovich Signal of Locally Brightest Galaxies in Planck Full Mission Data: Evidence for Galaxy Feedback? , 808:151, Aug. 2015.

[132] J. N. Grieb, A. G. SÃ¡nchez, S. Salazar-Albornoz, R. Scoccimarro, M. Crocce, C. Dalla Vecchia, F. Montesano, H. Gil-MarÃn, A. J. Ross, F. Beutler, and et al. The clustering of galaxies in the completed sdss-iii baryon oscillation spectroscopic survey: Cosmological implications of the fourier space wedges of the final sample. *Monthly Notices of the Royal Astronomical Society*, page stw3384, Jan 2017.

[133] F. Guilloux, G. Fay, and J.-F. Cardoso. Practical wavelet design on the sphere. *arXiv e-prints*, page arXiv:0706.2598, June 2007.

[134] W. J. Handley, M. P. Hobson, and A. N. Lasenby. polychord: nested sampling for cosmology. , 450:L61–L65, June 2015.

[135] Q. Hang, S. Alam, J. A. Peacock, and Y.-C. Cai. Galaxy clustering in the desi legacy survey and its imprint on the cmb. *Monthly Notices of the Royal Astronomical Society*, 501(1):1481â1498, Dec 2020.

[136] J. Hartlap, P. Simon, and P. Schneider. Why your model parameter confidences might be too optimistic. unbiased estimation of the inverse covariance matrix. *Astronomy & Astrophysics*, 464(1):399â404, Dec 2006.

[137] W. G. Hartley, A. Choi, et al. Dark Energy Survey Year 3 Results: Deep Field Optical + Near-Infrared Images and Catalogue. *Submitted to MNRAS*, 12 2020.

[138] M. Hasselfield, M. Hilton, T. A. Marriage, G. E. Addison, L. F. Barrientos, N. Battaglia, E. S. Battistelli, J. R. Bond, D. Crichton, S. Das, and et al. The atacama cosmology telescope: Sunyaev-zelâdovich selected galaxy clusters at 148 ghz from three seasons of data. , 2013(07):008â008, Jul 2013.

[139] A. F. Heavens, S. Matarrese, and L. Verde. The non-linear redshift-space power spectrum of galaxies. , 301(3):797–808, Dec. 1998.

[140] S. W. Henderson, R. Allison, J. Austermann, T. Baildon, N. Battaglia, J. A. Beall, D. Becker, F. De Bernardis, J. R. Bond, E. Calabrese, S. K. Choi,

K. P. Coughlin, K. T. Crowley, R. Datta, M. J. Devlin, S. M. Duff, J. Dunkley, R. Dünner, A. van Engelen, P. A. Gallardo, E. Grace, M. Hasselfield, F. Hills, G. C. Hilton, A. D. Hincks, R. Hložek, S. P. Ho, J. Hubmayr, K. Huffenberger, J. P. Hughes, K. D. Irwin, B. J. Koopman, A. B. Kosowsky, D. Li, J. McMahon, C. Munson, F. Nati, L. Newburgh, M. D. Niemack, P. Niraula, L. A. Page, C. G. Pappas, M. Salatino, A. Schillaci, B. L. Schmitt, N. Sehgal, B. D. Sherwin, J. L. Sievers, S. M. Simon, D. N. Spergel, S. T. Staggs, J. R. Stevens, R. Thornton, J. Van Lanen, E. M. Vavagiakis, J. T. Ward, and E. J. Wollack. Advanced ACTPol Cryogenic Detector Arrays and Readout. *Journal of Low Temperature Physics*, 184:772–779, Aug. 2016.

[141] C. Heymans, E. Grocutt, A. Heavens, M. Kilbinger, T. D. Kitching, F. Simpson, J. Benjamin, T. Erben, H. Hildebrandt, H. Hoekstra, Y. Mellier, L. Miller, L. Van Waerbeke, M. L. Brown, J. Coupon, L. Fu, J. Harnois-Déraps, M. J. Hudson, K. Kuijken, B. Rowe, T. Schrabback, E. Semboloni, S. Vafaei, and M. Velander. CFHTLenS tomographic weak lensing cosmological parameter constraints: Mitigating the impact of intrinsic galaxy alignments. , 432(3):2433–2453, July 2013.

[142] C. Heymans, T. Tröster, M. Asgari, C. Blake, H. Hildebrandt, B. Joachimi, K. Kuijken, C.-A. Lin, A. G. Sánchez, J. L. van den Busch, and et al. Kids-1000 cosmology: Multi-probe weak gravitational lensing and spectro-

scopic galaxy clustering constraints. *Astronomy & Astrophysics*, 646:A140, Feb 2021.

[143] C. Hikage, M. Oguri, T. Hamana, S. More, R. Mandelbaum, M. Takada, F. KÃ¶hlinger, H. Miyatake, A. J. Nishizawa, H. Aihara, and et al. Cosmology from cosmic shear power spectra with subaru hyper suprime-cam first-year data. *Publications of the Astronomical Society of Japan*, 71(2), Mar 2019.

[144] S. Hilbert, D. Xu, P. Schneider, V. Springel, M. Vogelsberger, and L. Hernquist. Intrinsic alignments of galaxies in the illustris simulation. , 468(1):790â823, Feb 2017.

[145] J. C. Hill, E. J. Baxter, A. Lidz, J. P. Greco, and B. Jain. Two-halo term in stacked thermal Sunyaev-Zel'dovich measurements: Implications for self-similarity. , 97(8):083501, Apr. 2018.

[146] J. C. Hill and E. Pajer. Cosmology from the thermal Sunyaev-Zel'dovich power spectrum: Primordial non-Gaussianity and massive neutrinos. , 88(6):063526, Sept. 2013.

[147] J. C. Hill and D. N. Spergel. Detection of Thermal SZ – CMB Lensing Cross-Correlation in Planck Nominal Mission Data. *Journal of Cosmology and Astroparticle Physics*, 2014(02):030–030, 2013.

[148] J. C. Hill and D. N. Spergel. Detection of thermal sz-cmb lensing cross-correlation in planck nominal mission data. , 2014(02):030â030, Feb 2014.

[149] M. Hilton, M. Hasselfield, C. SifÃ³n, N. Battaglia, S. Aiola, V. Bharadwaj, J. R. Bond, S. K. C Thetwo−seasonactpolsunyaevzeldovicheffectselectedclustercatalog. TheAstrophysicalJo 20, Mar2018.

[150] M. Hilton, C. SifÃ³n, S. Naess, M. Madhavacheril, M. Oguri, E. Rozo, E. Rykoff, T. M. C.A Acatalogof > 4000sunyaevzeldovichgalaxyclusters. TheAstrophysicalJournalSupplemen 3, Feb2021.

[151] C. M. Hirata and U. Seljak. Intrinsic alignment-lensing interference as a contaminant of cosmic shear. , 70(6):063526, Sept. 2004.

[152] C. M. Hirata and U. Seljak. Intrinsic alignment-lensing interference as a contaminant of cosmic shear. , 70(6):063526, Sept. 2004.

[153] H. Hoekstra, R. Herbonnet, A. Muzzin, A. Babul, A. Mahdavi, M. Viola, and M. Cacciato. The canadian cluster comparison project: detailed study of systematics and updated weak lensing massesâ. , 449(1):685â714, Mar 2015.

[154] A. Hojjati, I. G. McCarthy, J. Harnois-Deraps, Y.-Z. Ma, L. V. Waerbeke, G. Hinshaw, and A. M. L. Brun. Dissecting the thermal sunyaev-zeldovich-gravitational lensing cross-correlation with hydrodynamical simulations. , 2015(10):047â047, Oct 2015.

[155] W. Hu and B. Jain. Joint galaxy-lensing observables and the dark energy. , 70(4), Aug 2004.

[156] H.-J. Huang, T. Eifler, R. Mandelbaum, and S. Dodelson. Modelling baryonic physics in future weak lensing surveys. , 488(2):1652–1678, Sep 2019.

[157] E. Huff and R. Mandelbaum. Metacalibration: Direct self-calibration of biases in shear measurement, 2017.

[158] G. Hurier and F. Lacasa. Combined analysis of galaxy cluster number count, thermal sunyaev-zelâdovich power spectrum, and bispectrum. , 604:A71, Aug 2017.

[159] D. Huterer and M. S. Turner. Probing dark energy: Methods and strategies. *Physical Review D*, 64(12), Nov 2001.

[160] M. M. Ivanov, M. Simonović, and M. Zaldarriaga. Cosmological Parameters and Neutrino Masses from the Final Planck and Full-Shape BOSS Data. *arXiv e-prints*, page arXiv:1912.08208, Dec 2019.

[161] B. Jain and E. Bertschinger. Second-Order Power Spectrum and Nonlinear Evolution at High Redshift. , 431:495, Aug 1994.

[162] M. Jarvis, G. Bernstein, and B. Jain. The skewness of the aperture mass statistic. , 352(1):338–352, July 2004.

[163] M. Jarvis, G. Bernstein, and B. Jain. The skewness of the aperture mass statistic. , 352:338–352, July 2004.

[164] M. Jarvis et al. Dark Energy Survey year 3 results: point spread function modelling. , 501(1):1282–1299, 2021.

[165] B. Joachimi, C.-A. Lin, M. Asgari, T. TrÃ¶ster, C. Heymans, H. Hilde-brandt, F. KÃ¶hlinger, A. G. SÃ¡nchez, A. H. Wright, M. Bilicki, and et al. Kids-1000 methodology: Modelling and inference for joint weak gravitational lensing and spectroscopic galaxy clustering analysis. *Astronomy & Astrophysics*, 646:A129, Feb 2021.

[166] B. Joachimi, R. Mandelbaum, F. B. Abdalla, and S. L. Bridle. Constraints on intrinsic alignment contamination of weak lensing surveys using the megaz-lrg sample. , 527:A26, Jan 2011.

[167] H. Johnston, C. Georgiou, B. Joachimi, H. Hoekstra, N. E. Chisari, D. Farrow, M. C. Fortuna, C. Heymans, S. Joudaki, K. Kuijken, and et al. Kids+gama: Intrinsic alignment model constraints for current and future weak lensing cosmology. , 624:A30, Apr 2019.

[168] E. Kitanidis and M. White. Cross-correlation of planck cmb lensing with desi-like lrgs. *Monthly Notices of the Royal Astronomical Society*, 501(4):6181â6198, Dec 2020.

[169] E. Komatsu and U. Seljak. The sunyaev-zelâdovich angular power spectrum as a probe of cosmological parameters. , 336(4):1256â1270, Nov 2002.

[170] N. Koukoufilippas, D. Alonso, M. Bilicki, and J. A. Peacock. Tomographic measurement of the intergalactic gas pressure through galaxy-tSZ cross-correlations. , 491(4):5464–5480, Feb. 2020.

[171] E. Krause and T. Eifler. cosmolike â cosmological likelihood analyses for photometric galaxy surveys. *Mon. Not. Roy. Astron. Soc.*, 470(2):2100–2112, 2017.

[172] E. Krause and T. Eifler. cosmolike â cosmological likelihood analyses for photometric galaxy surveys. *Monthly Notices of the Royal Astronomical Society*, 470(2):2100â2112, May 2017.

[173] E. Krause, T. F. Eifler, J. Zuntz, O. Friedrich, M. A. Troxel, S. Dodelson, J. Blazek, L. F. Secco, N. MacCrann, E. Baxter, C. Chang, N. Chen, M. Crocce, J. DeRose, A. Ferte, N. Kokron, F. Lacasa, V. Miranda, Y. Omori, A. Porredon, R. Rosenfeld, S. Samuroff, M. Wang, R. H. Wechsler, T. M. C. Abbott, F. B. Abdalla, S. Allam, J. Annis, K. Bechtol, A. Benoit-Levy, G. M. Bernstein, D. Brooks, D. L. Burke, D. Capozzi, M. Carrasco Kind, J. Carretero, C. B. D'Andrea, L. N. da Costa, C. Davis, D. L. DePoy, S. Desai, H. T. Diehl, J. P. Dietrich, A. E. Evrard, B. Flaugher, P. Fosalba, J. Frie-

man, J. Garcia-Bellido, E. Gaztanaga, T. Giannantonio, D. Gruen, R. A. Gruendl, J. Gschwend, G. Gutierrez, K. Honscheid, D. J. James, T. Jeltema, K. Kuehn, S. Kuhlmann, O. Lahav, M. Lima, M. A. G. Maia, M. March, J. L. Marshall, P. Martini, F. Menanteau, R. Miquel, R. C. Nichol, A. A. Plazas, A. K. Romer, E. S. Rykoff, E. Sanchez, V. Scarpine, R. Schindler, M. Schubnell, I. Sevilla-Noarbe, M. Smith, M. Soares-Santos, F. Sobreira, E. Suchyta, M. E. C. Swanson, G. Tarle, D. L. Tucker, V. Vikram, A. R. Walker, and J. Weller. Dark Energy Survey Year 1 Results: Multi-Probe Methodology and Simulated Likelihood Analyses. *arXiv e-prints*, page arXiv:1706.09359, June 2017.

[174] E. Krause, T. F. Eifler, J. Zuntz, O. Friedrich, M. A. Troxel, S. Dodelson, J. Blazek, L. F. Secco, N. MacCrann, E. Baxter, C. Chang, N. Chen, M. Crocce, J. DeRose, A. Ferte, N. Kokron, F. Lacasa, V. Miranda, Y. Omori, A. Porredon, R. Rosenfeld, S. Samuroff, M. Wang, R. H. Wechsler, T. M. C. Abbott, F. B. Abdalla, S. Allam, J. Annis, K. Bechtol, A. Benoit-Levy, G. M. Bernstein, D. Brooks, D. L. Burke, D. Capozzi, M. Carrasco Kind, J. Carretero, C. B. D'Andrea, L. N. da Costa, C. Davis, D. L. DePoy, S. Desai, H. T. Diehl, J. P. Dietrich, A. E. Evrard, B. Flaugher, P. Fosalba, J. Frieman, J. Garcia-Bellido, E. Gaztanaga, T. Giannantonio, D. Gruen, R. A. Gruendl, J. Gschwend, G. Gutierrez, K. Honscheid, D. J. James, T. Jeltema, K. Kuehn, S. Kuhlmann, O. Lahav, M. Lima, M. A. G. Maia, M. March, J. L.

Marshall, P. Martini, F. Menanteau, R. Miquel, R. C. Nichol, A. A. Plazas, A. K. Romer, E. S. Rykoff, E. Sanchez, V. Scarpine, R. Schindler, M. Schubnell, I. Sevilla-Noarbe, M. Smith, M. Soares-Santos, F. Sobreira, E. Suchyta, M. E. C. Swanson, G. Tarle, D. L. Tucker, V. Vikram, A. R. Walker, and J. Weller. Dark Energy Survey Year 1 Results: Multi-Probe Methodology and Simulated Likelihood Analyses. *ArXiv e-prints*, June 2017.

[175] E. Krause et al. Dark Energy Survey Year 3 Results: Multi-probe modeling validation. *To be submitted to PRD*, 2021.

[176] A. Krolewski, S. Ferraro, and M. White. Cosmological constraints from unwise and planck cmb lensing tomography, 2021.

[177] J. Kwan, C. SÃ¡nchez, J. Clampitt, J. Blazek, M. Crocce, B. Jain, J. Zuntz, A. Amara, M. R. Becker, G. M. Bernstein, and et al. Cosmology from large-scale galaxy clustering and galaxyâgalaxy lensing with dark energy survey science verification data. *Monthly Notices of the Royal Astronomical Society*, 464(4):4045â4062, Oct 2016.

[178] S. D. Landy and A. S. Szalay. Bias and variance of angular correlation functions. , 412:64–71, July 1993.

[179] S. D. Landy and A. S. Szalay. Bias and Variance of Angular Correlation Functions. , 412:64, July 1993.

[180] J. U. Lange, A. Leauthaud, S. Singh, H. Guo, R. Zhou, T. L. Smith, and F.-Y. Cyr-Racine. On the halo-mass and radial scale dependence of the lensing is low effect. *Monthly Notices of the Royal Astronomical Society*, 502(2):2074â2086, Jan 2021.

[181] A. M. C. Le Brun, I. G. McCarthy, and J.-B. Melin. Testing sun-yaevâzel'dovich measurements of the hot gas content of dark matter haloes using synthetic skies. *Monthly Notices of the Royal Astronomical Society*, 451(4):3868–3881, 2015.

[182] A. M. C. Le Brun, I. G. McCarthy, J. Schaye, and T. J. Ponman. Towards a realistic population of simulated galaxy groups and clusters. *Monthly Notices of the Royal Astronomical Society*, 441(2):1270â1290, May 2014.

[183] A. M. C. Le Brun, I. G. McCarthy, J. Schaye, and T. J. Ponman. Towards a realistic population of simulated galaxy groups and clusters. , 441:1270–1290, June 2014.

[184] A. M. C. Le Brun, I. G. McCarthy, J. Schaye, and T. J. Ponman. The scatter and evolution of the global hot gas properties of simulated galaxy cluster populations. , 466(4):4442–4469, Apr. 2017.

[185] A. Leauthaud, S. Saito, S. Hilbert, A. Barreira, S. More, M. White, S. Alam, P. Behroozi, K. Bundy, J. Coupon, and et al. Lensing is low: cosmology,

galaxy formation or new physics? *Monthly Notices of the Royal Astronomical Society*, 467(3):3024â3047, Feb 2017.

[186] M. Lemos, P. Raveri et al. Assessing tension metrics with Dark Energy Survey and Planck data. *Submitted to MNRAS*, 12 2020.

[187] P. Lemos et al. Dark Energy Survey Year 3 Results: . *To be submitted to MNRAS*, 2021.

[188] D. N. Limber. The Analysis of Counts of the Extragalactic Nebulae in Terms of a Fluctuating Density Field. , 117:134, Jan. 1953.

[189] D. N. Limber. The Analysis of Counts of the Extragalactic Nebulae in Terms of a Fluctuating Density Field. , 117:134, Jan. 1953.

[190] M. LoVerde and N. Afshordi. Extended Limber Approximation. *Phys. Rev. D*, 78:123506, 2008.

[191] M. Loverde and N. Afshordi. Extended Limber approximation. , 78(12):123506, Dec. 2008.

[192] Y.-Z. Ma, L. V. Waerbeke, G. Hinshaw, A. Hojjati, D. Scott, and J. Zuntz. Probing the diffuse baryon distribution with the lensing-tsz cross-correlation. , 2015(09):046â046, Sep 2015.

[193] N. MacCrann, J. Blazek, B. Jain, and E. Krause. Controlling and leveraging small-scale information in tomographic galaxyâgalaxy lensing. *Mon. Not. Roy. Astron. Soc.*, 491(4):5498–5509, 2020.

[194] N. MacCrann, J. DeRose, R. H. Wechsler, J. Blazek, E. Gaztanaga, M. Crocce, E. S. Rykoff, M. R. Becker, B. Jain, E. Krause, T. F. Eifler, D. Gruen, J. Zuntz, M. A. Troxel, J. Elvin-Poole, J. Prat, M. Wang, S. Dodelson, A. Kravtsov, P. Fosalba, M. T. Busha, A. E. Evrard, D. Huterer, T. M. C. Abbott, F. B. Abdalla, S. Allam, J. Annis, S. Avila, G. M. Bernstein, D. Brooks, E. Buckley-Geer, D. L. Burke, A. Carnero Rosell, M. Carrasco Kind, J. Carretero, F. J. Castander, R. Cawthon, C. E. Cunha, C. B. D'Andrea, L. N. da Costa, C. Davis, J. De Vicente, H. T. Diehl, P. Doel, J. Frieman, J. García-Bellido, D. W. Gerdes, R. A. Gruendl, G. Gutierrez, W. G. Hartley, D. Hollowood, K. Honscheid, B. Hoyle, D. J. James, T. Jeltema, D. Kirk, K. Kuehn, N. Kuropatkin, M. Lima, M. A. G. Maia, J. L. Marshall, F. Menanteau, R. Miquel, A. A. Plazas, A. Roodman, E. Sanchez, V. Scarpine, M. Schubnell, I. Sevilla-Noarbe, M. Smith, R. C. Smith, M. Soares-Santos, F. Sobreira, E. Suchyta, M. E. C. Swanson, G. Tarle, D. Thomas, A. R. Walker, and J. Weller. DES Y1 Results: validating cosmological parameter estimation using simulated Dark Energy Surveys. , 480:4614–4635, Nov. 2018.

[195] N. MacCrann et al. DES Y3 results: Blending shear and redshift biases in

image simulations. *Submitted to MNRAS*, 12 2020.

[196] M. S. Madhavacheril, J. C. Hill, S. Næss, G. E. Addison, S. Aiola, T. Baildon, N. Battaglia, R. Bean, J. R. Bond, E. Calabrese, V. Calafut, S. K. Choi, O. Darwish, R. Datta, M. J. Devlin, J. Dunkley, R. Dünner, S. Ferraro, P. A. Gallardo, V. Gluscevic, M. Halpern, D. Han, M. Hasselfield, M. Hilton, A. D. Hincks, R. Hložek, S.-P. P. Ho, K. M. Huffenberger, J. P. Hughes, B. J. Koopman, A. Kosowsky, M. Lokken, T. Louis, M. Lungu, A. MacInnis, L. Maurin, J. J. McMahon, K. Moodley, F. Nati, M. D. Niemack, L. A. Page, B. Partridge, N. Robertson, N. Sehgal, E. Schaan, A. Schillaci, B. D. Sherwin, C. Sifón, S. M. Simon, D. N. Spergel, S. T. Staggs, E. R. Storer, A. van Engelen, E. M. Vavagiakis, E. J. Wollack, and Z. Xu. Atacama Cosmology Telescope: Component-separated maps of CMB temperature and the thermal Sunyaev-Zel'dovich effect. , 102(2):023534, July 2020.

[197] R. Makiya, S. Ando, and E. Komatsu. Joint analysis of the thermal Sunyaev-Zeldovich effect and 2MASS galaxies: probing gas physics in the local Universe and beyond. , 480:3928–3941, Nov 2018.

[198] R. Mandelbaum, C. M. Hirata, M. Ishak, U. Seljak, and J. Brinkmann. Detection of large-scale intrinsic ellipticity–density correlation from the sloan digital sky survey and implications for weak lensing surveys. , 367(2):611â626, Apr 2006.

[199] R. Mandelbaum, A. Slosar, T. Baldauf, U. Seljak, C. M. Hirata, R. Naka-jima, R. Reyes, and R. E. Smith. Cosmological parameter constraints from galaxyâgalaxy lensing and galaxy clustering with the sdss dr7. *Monthly Notices of the Royal Astronomical Society*, 432(2):1544â1575, Apr 2013.

[200] D. Marinucci, D. Pietrobon, A. Balbi, P. Baldi, P. Cabella, G. Kerkyachar-ian, P. Natoli, D. Picard, and N. Vittorio. Spherical needlets for cosmic microwave background data analysis. , 383:539–545, Jan. 2008.

[201] F. A. MarÃn, C. Blake, G. B. Poole, C. K. McBride, S. Brough, M. Col-less, C. Contreras, W. Couch, D. J. Croton, S. Croom, and et al. The wig-glez dark energy survey: constraining galaxy bias and cosmic growth with three-point correlation functions. *Monthly Notices of the Royal Astronomi-cal Society*, 432(4):2654â2668, May 2013.

[202] T. Matsubara. Stochasticity of bias and nonlocality of galaxy formation: Linear scales. *The Astrophysical Journal*, 525(2):543â553, Nov 1999.

[203] T. Matsubara. Resumming cosmological perturbations via the La-grangian picture: One-loop results in real space and in redshift space. , 77(6):063530, Mar 2008.

[204] T. Matsubara. Integrated Perturbation Theory and One-loop Power Spectra of Biased Tracers. 2013.

[205] I. G. McCarthy, A. M. C. Le Brun, J. Schaye, and G. P. Holder. The thermal Sunyaev-Zel'dovich effect power spectrum in light of Planck. , 440:3645–3657, June 2014.

[206] T. McClintock, T. Varga, D. Gruen, E. Rozo, E. Rykoff, T. Shin, P. Melchior, J. DeRose, S. Seitz, J. Dietrich, and et al. Dark energy survey year 1 results: weak lensing mass calibration of redmapper galaxy clusters. , 482(1):1352â1378, Oct 2018.

[207] P. McDonald and A. Roy. Clustering of dark matter tracers: generalizing bias for the coming era of precision LSS. *Journal of Cosmology and Astroparticle Physics*, 2009(08):020–020, 2009.

[208] J. E. McEwen, X. Fang, C. M. Hirata, and J. A. Blazek. FAST-PT: a novel algorithm to calculate convolution integrals in cosmological perturbation theory. 2016.

[209] A. Mead, J. Peacock, C. Heymans, S. Joudaki, and A. Heavens. An accurate halo model for fitting non-linear cosmological power spectra and baryonic feedback models. , 454(2):1958–1975, 2015.

[210] A. J. Mead, S. Brieden, T. Tröster, and C. Heymans. HMCODE-2020: improved modelling of non-linear cosmological power spectra with baryonic feedback. , 502(1):1401–1422, Mar. 2021.

[211] A. J. Mead, S. Brieden, T. Tröster, and C. Heymans. hmcode-2020: improved modelling of non-linear cosmological power spectra with baryonic feedback. , 502(1):1401â1422, Jan 2021.

[212] H. Miyatake, N. Battaglia, M. Hilton, E. Medezinski, A. J. Nishizawa, S. More, S. Aiola, N. Bahcall, J. R. Bond, E. Calabrese, and et al. Weaklensing mass calibration of actpol sunyaevâzelâdovich clusters with the hyper suprime-cam survey. , 875(1):63, Apr 2019.

[213] C. Modi, E. Castorina, and U. Seljak. Halo bias in lagrangian space: estimators and theoretical predictions. *Monthly Notices of the Royal Astronomical Society*, 472(4):3959â3970, Aug 2017.

[214] S. More, H. Miyatake, R. Mandelbaum, M. Takada, D. N. Spergel, J. R. Brownstein, and D. P. Schneider. The weak lensing signal and the clustering of boss galaxies. ii. astrophysical and cosmological constraints. *The Astrophysical Journal*, 806(1):2, Jun 2015.

[215] E. Morganson, R. A. Gruendl, F. Menanteau, M. Carrasco Kind, Y. C. Chen, G. Daues, A. Drlica-Wagner, D. N. Friedel, M. Gower, M. W. G. Johnson, M. D. Johnson, R. Kessler, F. Paz-Chinchón, D. Petravick, C. Pond, B. Yanny, S. Allam, R. Armstrong, W. Barkhouse, K. Bechtol, A. Benoit-Lévy, G. M. Bernstein, E. Bertin, E. Buckley-Geer, R. Covarrubias, S. Desai, H. T. Diehl, D. A. Goldstein, D. Gruen, T. S. Li, H. Lin, J. Marriner,

347

J. J. Mohr, E. Neilsen, C. C. Ngeow, K. Paech, E. S. Rykoff, M. Sako, I. Sevilla-Noarbe, E. Sheldon, F. Sobreira, D. L. Tucker, W. Wester, and DES Collaboration. The Dark Energy Survey Image Processing Pipeline. , 130(989):074501, July 2018.

[216] E. Morganson, R. A. Gruendl, F. Menanteau, M. C. Kind, Y.-C. Chen, G. Daues, A. Drlica-Wagner, D. N. Friedel, M. Gower, M. W. G. Johnson, and et al. The dark energy survey image processing pipeline. *Publications of the Astronomical Society of the Pacific*, 130(989):074501, May 2018.

[217] J. Muir et al. Blinding multiprobe cosmological experiments. , 494(3):4454–4470, 2020.

[218] R. Murata, T. Nishimichi, M. Takada, H. Miyatake, M. Shirasaki, S. More, R. Takahashi, and K. Osato. Constraints on the massârichness relation from the abundance and weak lensing of sdss clusters. , 854(2):120, Feb 2018.

[219] J. Myles, A. Alarcon, et al. Dark Energy Survey Year 3 Results: Redshift Calibration of the Weak Lensing Source Galaxies. *Submitted to MNRAS*, 12 2020.

[220] J. F. Navarro, C. S. Frenk, and S. D. M. White. The structure of cold dark matter halos. *The Astrophysical Journal*, 462:563, May 1996.

[221] J. A. Nelder and R. Mead. A Simplex Method for Function Minimization. *The Computer Journal*, 7(4):308–313, 01 1965.

[222] P. Norberg, C. M. Baugh, E. Gaztanaga, and D. J. Croton. Statistical Analysis of Galaxy Surveys - I. Robust error estimation for 2-point clustering statistics. *Mon. Not. Roy. Astron. Soc.*, 396:19, 2009.

[223] P. Norberg, C. M. Baugh, E. Gaztanaga, and D. J. Croton. Statistical analysis of galaxy surveys - I. Robust error estimation for two-point clustering statistics. , 396:19–38, June 2009.

[224] T. Okumura and Y. P. Jing. The gravitational shear-intrinsic ellipticity correlation functions of luminous red galaxies in observation and in the Îcdm model. , 694(1):L83âL86, Mar 2009.

[225] K. Osato, S. Flender, D. Nagai, M. Shirasaki, and N. Yoshida. Investigating cluster astrophysics and cosmology with cross-correlation of the thermal Sunyaev-Zel'dovich effect and weak lensing. , 475(1):532–542, Mar. 2018.

[226] K. Osato and M. Takada. Super sample covariance of the thermal Sunyaev-Zel'dovich effect. , 103(6):063501, Mar. 2021.

[227] S. Pandey, E. J. Baxter, and J. C. Hill. Constraining the properties of gaseous halos via cross-correlations of upcoming galaxy surveys and thermal Sunyaev-Zel'dovich maps. , 101(4):043525, Feb. 2020.

[228] S. Pandey, E. J. Baxter, Z. Xu, J. Orlowski-Scherer, N. Zhu, A. Lidz, J. Aguirre, J. DeRose, M. Devlin, J. C. Hill, B. Jain, R. K. Sheth, S. Avila, E. Bertin, D. Brooks, E. Buckley-Geer, A. Carnero Rosell, M. Carrasco Kind, J. Carretero, F. J. Castander, R. Cawthon, L. N. da Costa, J. De Vicente, S. Desai, H. T. Diehl, J. P. Dietrich, P. Doel, A. E. Evrard, B. Flaugher, P. Fosalba, J. Frieman, J. García-Bellido, D. W. Gerdes, T. Giannantonio, R. A. Gruendl, J. Gschwend, W. G. Hartley, D. L. Hollowood, D. J. James, E. Krause, K. Kuehn, N. Kuropatkin, M. A. G. Maia, J. L. Marshall, P. Melchior, F. Menanteau, R. Miquel, A. A. Plazas, A. Roodman, E. Sanchez, S. Serrano, I. Sevilla-Noarbe, M. Smith, M. Soares-Santos, F. Sobreira, E. Suchyta, M. E. C. Swanson, G. Tarle, and R. H. Wechsler. Constraints on the redshift evolution of astrophysical feedback with Sunyaev-Zeldovich effect cross-correlations. *arXiv e-prints*, page arXiv:1904.13347, Apr 2019.

[229] S. Pandey et al. Dark Energy Survey Year 3 Results: Constraints on cosmological parameters and galaxy bias models from galaxy clustering and galaxy-galaxy lensing. *Submitted to PRD*, 2021.

[230] S. Pandey, M. Gatti, E. Baxter, J. C. Hill, X. Fang, C. Doux, G. Giannini, M. Raveri, J. DeRose, H. Huang, E. Moser, N. Battaglia, A. Alarcon, A. Amon, M. Becker, A. Campos, C. Chang, R. Chen, A. Choi, K. Eckert, J. Elvin-Poole, S. Everett, A. Ferte, I. Harrison, N. Maccrann, J. Mccullough, J. Myles, A. Navarro Alsina, J. Prat, R. P. Rollins, C. Sanchez,

350

T. Shin, M. Troxel, I. Tutusaus, B. Yin, M. Aguena, S. Allam, F. Andrade-Oliveira, G. M. Bernstein, E. Bertin, B. Bolliet, J. R. Bond, D. Brooks, E. Calabrese, A. Carnero Rosell, M. Carrasco Kind, J. Carretero, R. Cawthon, M. Costanzi, M. Crocce, L. N. da Costa, M. E. S. Pereira, J. De Vicente, S. Desai, H. T. Diehl, J. P. Dietrich, P. Doel, J. Dunkley, S. Everett, A. E. Evrard, S. Ferraro, I. Ferrero, B. Flaugher, P. Fosalba, J. Garcia-Bellido, E. Gaztanaga, D. W. Gerdes, T. Giannantonio, D. Gruen, R. A. Gruendl, J. Gschwend, G. Gutierrez, K. Herner, A. D. Hincks, S. R. Hinton, D. L. Hollowood, K. Honscheid, J. P. Hughes, D. Huterer, B. Jain, D. J. James, T. Jeltema, E. Krause, K. Kuehn, O. Lahav, M. Lima, M. Lokken, M. S. Madhavacheril, M. A. G. Maia, J. J. Mcmahon, P. Melchior, F. Menanteau, R. Miquel, J. J. Mohr, K. Moodley, R. Morgan, F. Nati, M. D. Niemack, L. Page, A. Palmese, F. Paz-Chinchon, A. Pieres, A. A. Plazas Malagon, M. Rodriguez-Monroy, A. K. Romer, E. Sanchez, V. Scarpine, E. Schaan, S. Serrano, I. Sevilla-Noarbe, E. Sheldon, B. D. Sherwin, C. Sifon, M. Smith, M. Soares-Santos, D. Spergel, E. Suchyta, M. E. C. Swanson, G. Tarle, D. Thomas, C. To, T. N. Varga, J. Weller, E. J. Wollack, and Z. Xu. Cross-correlation of DES Y3 lensing and ACT/*Planck* thermal Sunyaev Zel'dovich Effect II: Modeling and constraints on halo pressure profiles. *arXiv e-prints*, page arXiv:2108.01601, Aug. 2021.

[231] S. Pandey, E. Krause, B. Jain, N. MacCrann, J. Blazek, M. Crocce, J. DeRose,

X. Fang, I. Ferrero, O. Friedrich, and et al. Perturbation theory for modeling galaxy bias: Validation with simulations of the dark energy survey. *Physical Review D*, 102(12), Dec 2020.

[232] A. Perko, L. Senatore, E. Jennings, and R. H. Wechsler. Biased tracers in redshift space in the eft of large-scale structure, 2016.

[233] S. Perlmutter, G. Aldering, G. Goldhaber, R. A. Knop, P. Nugent, P. G. Castro, S. Deustua, S. Fabbro, A. Goobar, D. E. Groom, I. M. Hook, A. G. Kim, M. Y. Kim, J. C. Lee, N. J. Nunes, R. Pain, C. R. Pennypacker, R. Quimby, C. Lidman, R. S. Ellis, M. Irwin, R. G. McMahon, P. Ruiz-Lapuente, N. Walton, B. Schaefer, B. J. Boyle, A. V. Filippenko, T. Matheson, A. S. Fruchter, N. Panagia, H. J. M. Newberg, W. J. Couch, and T. S. C. Project. Measurements of Ω and Λ from 42 High-Redshift Supernovae. , 517(2):565–586, June 1999.

[234] O. H. Philcox, M. M. Ivanov, M. SimonoviÄ, and M. Zaldarriaga. Combining full-shape and bao analyses of galaxy power spectra: a 1.6cmb-independent constraint on h0. *Journal of Cosmology and Astroparticle Physics*, 2020(05):032â032, May 2020.

[235] Planck Collaboration, R. Adam, P. A. R. Ade, N. Aghanim, M. Arnaud, M. Ashdown, J. Aumont, C. Baccigalupi, A. J. Banday, R. B. Barreiro, and

et al. Planck 2015 results. VIII. High Frequency Instrument data processing: Calibration and maps. , 594:A8, Sept. 2016.

[236] Planck Collaboration, P. A. R. Ade, N. Aghanim, F. Argüeso, C. Armitage-Caplan, M. Arnaud, M. Ashdown, F. Atrio-Barandela, J. Aumont, C. Baccigalupi, and et al. Planck 2013 results. XXVIII. The Planck Catalogue of Compact Sources. , 571:A28, Nov. 2014.

[237] Planck Collaboration, P. A. R. Ade, N. Aghanim, C. Armitage-Caplan, M. Arnaud, M. Ashdown, F. Atrio-Barandela, J. Aumont, C. Baccigalupi, A. J. Banday, and et al. Planck 2013 results. IX. HFI spectral response. , 571:A9, Nov. 2014.

[238] Planck Collaboration, P. A. R. Ade, N. Aghanim, M. Arnaud, M. Ashdown, F. Atrio-Barandela, J. Aumont, C. Baccigalupi, A. Balbi, A. J. Banday, R. B. Barreiro, R. Barrena, J. G. Bartlett, E. Battaner, K. Benabed, J. P. Bernard, M. Bersanelli, I. Bikmaev, J. J. Bock, H. Böhringer, A. Bonaldi, J. R. Bond, J. Borrill, F. R. Bouchet, H. Bourdin, R. Burenin, C. Burigana, R. C. Butler, P. Cabella, A. Chamballu, R. R. Chary, L. Y. Chiang, G. Chon, P. R. Christensen, D. L. Clements, S. Colafrancesco, S. Colombi, L. P. L. Colombo, B. Comis, A. Coulais, B. P. Crill, F. Cuttaia, A. Da Silva, H. Dahle, R. J. Davis, P. de Bernardis, G. de Gasperis, A. de Rosa, G. de Zotti, J. Delabrouille, J. Démoclès, J. M. Diego, H. Dole,

S. Donzelli, O. Doré, M. Douspis, X. Dupac, G. Efstathiou, T. A. Enßlin, F. Finelli, I. Flores-Cacho, O. Forni, M. Frailis, E. Franceschi, M. Frommert, S. Galeotta, K. Ganga, R. T. Génova-Santos, M. Giard, Y. Giraud-Héraud, J. González-Nuevo, K. M. Górski, A. Gregorio, A. Gruppuso, F. K. Hansen, D. Harrison, C. Hernández- Monteagudo, D. Herranz, S. R. Hildebrandt, E. Hivon, M. Hobson, W. A. Holmes, A. Hornstrup, W. Hovest, K. M. Huffenberger, G. Hurier, T. R. Jaffe, A. H. Jaffe, W. C. Jones, M. Juvela, E. Keihänen, R. Keskitalo, I. Khamitov, T. S. Kisner, R. Kneissl, J. Knoche, M. Kunz, H. Kurki-Suonio, A. Lähteenmäki, J. M. Lamarre, A. Lasenby, C. R. Lawrence, M. Le Jeune, R. Leonardi, P. B. Lilje, M. Linden-Vørnle, M. López- Caniego, P. M. Lubin, G. Luzzi, J. F. Macías-Pérez, C. J. Mac-Tavish, B. Maffei, D. Maino, N. Mandolesi, M. Maris, F. Marleau, D. J. Marshall, E. Martínez- González, S. Masi, M. Massardi, S. Matarrese, P. Mazzotta, S. Mei, A. Melchiorri, J. B. Melin, L. Mendes, A. Mennella, S. Mitra, M. A. Miville-Deschênes, A. Moneti, L. Montier, G. Morgante, D. Mortlock, D. Munshi, J. A. Murphy, P. Naselsky, F. Nati, P. Natoli, H. U. Nørgaard-Nielsen, F. Noviello, D. Novikov, I. Novikov, S. Osborne, C. A. Oxborrow, F. Pajot, D. Paoletti, L. Perotto, F. Perrotta, F. Piacentini, M. Piat, E. Pierpaoli, R. Piffaretti, S. Plaszczynski, E. Pointecouteau, G. Polenta, L. Popa, T. Poutanen, G. W. Pratt, S. Prunet, J. L. Puget, J. P. Rachen, R. Rebolo, M. Reinecke, M. Remazeilles, C. Renault, S. Ricciardi, I. Ris-

354

torcelli, G. Rocha, M. Roman, C. Rosset, M. Rossetti, J. A. Rubiño-Martín, B. Rusholme, M. Sandri, G. Savini, D. Scott, L. Spencer, J. L. Starck, V. Stolyarov, R. Sudiwala, R. Sunyaev, D. Sutton, A. S. Suur-Uski, J. F. Sygnet, J. A. Tauber, L. Terenzi, L. Toffolatti, M. Tomasi, M. Tristram, L. Valenziano, B. Van Tent, P. Vielva, F. Villa, N. Vittorio, L. A. Wade, B. D. Wandelt, W. Wang, N. Welikala, J. Weller, S. D. M. White, M. White, D. Yvon, A. Zacchei, and A. Zonca. Planck intermediate results. XI. The gas content of dark matter halos: the Sunyaev-Zeldovich-stellar mass relation for locally brightest galaxies. , 557:A52, Sept. 2013.

[239] Planck Collaboration, P. A. R. Ade, N. Aghanim, M. Arnaud, M. Ashdown, J. Aumont, C. Baccigalupi, M. Baker, A. Balbi, A. J. Banday, and et al. Planck early results. I. The Planck mission. , 536:A1, Dec. 2011.

[240] Planck Collaboration, P. A. R. Ade, N. Aghanim, M. Arnaud, M. Ashdown, J. Aumont, C. Baccigalupi, A. J. Banday, R. B. Barreiro, J. G. Bartlett, and et al. Planck 2015 results. XXIV. Cosmology from Sunyaev-Zeldovich cluster counts. , 594:A24, Sept. 2016.

[241] Planck Collaboration, P. A. R. Ade, N. Aghanim, M. Ashdown, J. Aumont, C. Baccigalupi, A. J. Banday, R. B. Barreiro, N. Bartolo, E. Battaner, K. Benabed, A. Benoît, A. Benoit-Lévy, J.-P. Bernard, M. Bersanelli, P. Bielewicz, A. Bonaldi, L. Bonavera, J. R. Bond, J. Borrill, F. R. Bouchet,

M. Bucher, C. Burigana, R. C. Butler, E. Calabrese, J.-F. Cardoso, A. Catalano, A. Chamballu, R.-R. Chary, P. R. Christensen, S. Colombi, L. P. L. Colombo, B. P. Crill, A. Curto, F. Cuttaia, L. Danese, R. D. Davies, R. J. Davis, P. de Bernardis, A. de Rosa, G. de Zotti, J. Delabrouille, C. Dickinson, J. M. Diego, H. Dole, S. Donzelli, O. Doré, M. Douspis, A. Ducout, X. Dupac, G. Efstathiou, F. Elsner, T. A. Enßlin, H. K. Eriksen, J. Fergusson, F. Finelli, O. Forni, M. Frailis, E. Franceschi, A. Frejsel, S. Galeotta, S. Galli, K. Ganga, M. Giard, Y. Giraud-Héraud, E. Gjerløw, J. González-Nuevo, K. M. Górski, S. Gratton, A. Gregorio, A. Gruppuso, F. K. Hansen, D. Hanson, D. L. Harrison, S. Henrot-Versillé, D. Herranz, S. R. Hildebrandt, E. Hivon, M. Hobson, W. A. Holmes, A. Hornstrup, W. Hovest, K. M. Huffenberger, G. Hurier, A. H. Jaffe, T. R. Jaffe, M. Juvela, E. Keihänen, R. Keskitalo, K. Kiiveri, T. S. Kisner, J. Knoche, M. Kunz, H. Kurki-Suonio, A. Lähteenmäki, J.-M. Lamarre, A. Lasenby, M. Lattanzi, C. R. Lawrence, J. P. Leahy, R. Leonardi, J. Lesgourgues, F. Levrier, M. Liguori, P. B. Lilje, M. Linden-Vørnle, V. Lindholm, M. López-Caniego, P. M. Lubin, J. F. Macías-Pérez, G. Maggio, D. Maino, N. Mandolesi, A. Mangilli, P. G. Martin, E. Martínez-González, S. Masi, S. Matarrese, P. Mazzotta, P. McGehee, P. R. Meinhold, A. Melchiorri, L. Mendes, A. Mennella, M. Migliaccio, S. Mitra, L. Montier, G. Morgante, D. Mortlock, A. Moss, D. Munshi, J. A. Murphy, P. Naselsky, F. Nati, P. Natoli, C. B. Netterfield, H. U.

356

Nørgaard-Nielsen, D. Novikov, I. Novikov, F. Paci, L. Pagano, D. Paoletti, B. Partridge, F. Pasian, G. Patanchon, T. J. Pearson, O. Perdereau, L. Perotto, F. Perrotta, V. Pettorino, E. Pierpaoli, D. Pietrobon, E. Pointecouteau, G. Polenta, G. W. Pratt, G. Prézeau, S. Prunet, J.-L. Puget, J. P. Rachen, R. Rebolo, M. Reinecke, M. Remazeilles, A. Renzi, G. Rocha, C. Rosset, M. Rossetti, G. Roudier, J. A. Rubiño-Martín, B. Rusholme, M. Sandri, D. Santos, M. Savelainen, D. Scott, M. D. Seiffert, E. P. S. Shellard, L. D. Spencer, V. Stolyarov, R. Stompor, D. Sutton, A.-S. Suur-Uski, J.-F. Sygnet, J. A. Tauber, L. Terenzi, L. Toffolatti, M. Tomasi, M. Tristram, M. Tucci, J. Tuovinen, L. Valenziano, J. Valiviita, B. Van Tent, T. Vassallo, P. Vielva, F. Villa, L. A. Wade, B. D. Wandelt, R. Watson, I. K. Wehus, D. Yvon, A. Zacchei, and A. Zonca. Planck 2015 results. VI. LFI mapmaking. , 594:A6, Sept. 2016.

[242] Planck Collaboration, Ade, P. A. R., Aghanim, N., Arnaud, M., Ashdown, M., Aumont, J., Baccigalupi, C., Balbi, A., Banday, A. J., Barreiro, R. B., Bartlett, J. G., Battaner, E., Benabed, K., Benoît, A., Bernard, J.-P., Bersanelli, M., Bhatia, R., Blagrave, K., Bock, J. J., Bonaldi, A., Bonavera, L., Bond, J. R., Borrill, J., Bouchet, F. R., Bucher, M., Burigana, C., Cabella, P., Cardoso, J.-F., Catalano, A., Cayón, L., Challinor, A., Chamballu, A., Chiang, L.-Y, Chiang, C., Christensen, P. R., Clements, D. L., Colombi, S., Couchot, F., Coulais, A., Crill, B. P., Cuttaia, F., Danese, L., Davies, R. D.,

Davis, R. J., de Bernardis, P., de Gasperis, G., de Rosa, A., de Zotti, G., Delabrouille, J., Delouis, J.-M., Désert, F.-X., Dole, H., Donzelli, S., Doré, O., Dörl, U., Douspis, M., Dupac, X., Efstathiou, G., Enßlin, T. A., Eriksen, H. K., Finelli, F., Forni, O., Fosalba, P., Frailis, M., Franceschi, E., Galeotta, S., Ganga, K., Giard, M., Giardino, G., Giraud-Héraud, Y., González-Nuevo, J., Górski, K. M., Grain, J., Gratton, S., Gregorio, A., Gruppuso, A., Hansen, F. K., Harrison, D., Helou, G., Henrot-Versillé, S., Herranz, D., Hildebrandt, S. R., Hivon, E., Hobson, M., Holmes, W. A., Hovest, W., Hoyland, R. J., Huffenberger, K. M., Jaffe, A. H., Jones, W. C., Juvela, M., Keihänen, E., Keskitalo, R., Kisner, T. S., Kneissl, R., Knox, L., Kurki-Suonio, H., Lagache, G., Lamarre, J.-M., Lasenby, A., Laureijs, R. J., Lawrence, C. R., Leach, S., Leonardi, R., Leroy, C., Lilje, P. B., Linden-Vørnle, M., Lockman, F. J., López-Caniego, M., Lubin, P. M., Macías-Pérez, J. F., MacTavish, C. J., Maffei, B., Maino, D., Mandolesi, N., Mann, R., Maris, M., Martin, P., Martínez-González, E., Masi, S., Matarrese, S., Matthai, F., Mazzotta, P., Melchiorri, A., Mendes, L., Mennella, A., Mitra, S., Miville-Deschênes, M.-A., Moneti, A., Montier, L., Morgante, G., Mortlock, D., Munshi, D., Murphy, A., Naselsky, P., Natoli, P., Netterfield, C. B., Nørgaard-Nielsen, H. U., Novikov, D., Novikov, I., O´Dwyer, I. J., Oliver, S., Osborne, S., Pajot, F., Pasian, F., Patanchon, G., Perdereau, O., Perotto, L., Perrotta, F., Piacentini, F., Piat, M., Pinheiro Gonçalves, D., Plaszczynski, S., Pointecouteau,

E., Polenta, G., Ponthieu, N., Poutanen, T., Prézeau, G., Prunet, S., Puget, J.-L., Rachen, J. P., Reach, W. T., Reinecke, M., Remazeilles, M., Renault, C., Ricciardi, S., Riller, T., Ristorcelli, I., Rocha, G., Rosset, C., Rowan-Robinson, M., Rubiño-Martín, J. A., Rusholme, B., Sandri, M., Santos, D., Savini, G., Scott, D., Seiffert, M. D., Shellard, P., Smoot, G. F., Starck, J.-L., Stivoli, F., Stolyarov, V., Stompor, R., Sudiwala, R., Sunyaev, R., Sygnet, J.-F., Tauber, J. A., Terenzi, L., Toffolatti, L., Tomasi, M., Torre, J.-P., Tristram, M., Tuovinen, J., Umana, G., Valenziano, L., Vielva, P., Villa, F., Vittorio, N., Wade, L. A., Wandelt, B. D., White, M., Yvon, D., Zacchei, A., and Zonca, A. Planck early results. xviii. the power spectrum of cosmic infrared background anisotropies. *A&A*, 536:A18, 2011.

[243] Planck Collaboration, N. Aghanim, Y. Akrami, M. Ashdown, J. Aumont, C. Baccigalupi, M. Ballardini, A. J. Banday, R. B. Barreiro, N. Bartolo, S. Basak, R. Battye, K. Benabed, J. P. Bernard, M. Bersanelli, P. Bielewicz, J. J. Bock, J. R. Bond, J. Borrill, F. R. Bouchet, F. Boulanger, M. Bucher, C. Burigana, R. C. Butler, E. Calabrese, J. F. Cardoso, J. Carron, A. Challinor, H. C. Chiang, J. Chluba, L. P. L. Colombo, C. Combet, D. Contreras, B. P. Crill, F. Cuttaia, P. de Bernardis, G. de Zotti, J. Delabrouille, J. M. Delouis, E. Di Valentino, J. M. Diego, O. Doré, M. Douspis, A. Ducout, X. Dupac, S. Dusini, G. Efstathiou, F. Elsner, T. A. Enßlin, H. K. Eriksen, Y. Fantaye, M. Farhang, J. Fergusson, R. Fernandez-Cobos, F. Finelli,

F. Forastieri, M. Frailis, E. Franceschi, A. Frolov, S. Galeotta, S. Galli, K. Ganga, R. T. Génova-Santos, M. Gerbino, T. Ghosh, J. González-Nuevo, K. M. Górski, S. Gratton, A. Gruppuso, J. E. Gudmundsson, J. Hamann, W. Handley, D. Herranz, E. Hivon, Z. Huang, A. H. Jaffe, W. C. Jones, A. Karakci, E. Keihänen, R. Keskitalo, K. Kiiveri, J. Kim, T. S. Kisner, L. Knox, N. Krachmalnicoff, M. Kunz, H. Kurki-Suonio, G. Lagache, J. M. Lamarre, A. Lasenby, M. Lattanzi, C. R. Lawrence, M. Le Jeune, P. Lemos, J. Lesgourgues, F. Levrier, A. Lewis, M. Liguori, P. B. Lilje, M. Lilley, V. Lindholm, M. López-Caniego, P. M. Lubin, Y. Z. Ma, J. F. Macías-Pérez, G. Maggio, D. Maino, N. Mandolesi, A. Mangilli, A. Marcos-Caballero, M. Maris, P. G. Martin, M. Martinelli, E. Martínez- González, S. Matar-rese, N. Mauri, J. D. McEwen, P. R. Meinhold, A. Melchiorri, A. Men-nella, M. Migliaccio, M. Millea, S. Mitra, M. A. Miville-Deschênes, D. Moli-nari, L. Montier, G. Morgante, A. Moss, P. Natoli, H. U. Nørgaard-Nielsen, L. Pagano, D. Paoletti, B. Partridge, G. Patanchon, H. V. Peiris, F. Perrotta, V. Pettorino, F. Piacentini, L. Polastri, G. Polenta, J. L. Puget, J. P. Rachen, M. Reinecke, M. Remazeilles, A. Renzi, G. Rocha, C. Rosset, G. Roudier, J. A. Rubiño-Martín, B. Ruiz-Granados, L. Salvati, M. Sandri, M. Save-lainen, D. Scott, E. P. S. Shellard, C. Sirignano, G. Sirri, L. D. Spencer, R. Sunyaev, A. S. Suur-Uski, J. A. Tauber, D. Tavagnacco, M. Tenti, L. Tof-folatti, M. Tomasi, T. Trombetti, L. Valenziano, J. Valiviita, B. Van Tent,

L. Vibert, P. Vielva, F. Villa, N. Vittorio, B. D. Wandelt, I. K. Wehus, M. White, S. D. M. White, A. Zacchei, and A. Zonca. Planck 2018 results. VI. Cosmological parameters. *arXiv e-prints*, page arXiv:1807.06209, July 2018.

[244] A. Porredon et al. Dark Energy Survey Year 3 Results: Cosmological Constraints from Galaxy Clustering and Galaxy-Galaxy Lensing using an Optimized Lens Sample. *To be submitted to PRD*, 2021.

[245] A. Porredon et al. Dark Energy Survey Year 3 results: Optimizing the lens sample in a combined galaxy clustering and galaxy-galaxy lensing analysis. *Phys. Rev. D*, 103(4):043503, 2021.

[246] Porredon, A. et al. Sept. prep.

[247] J. Prat et al. Dark Energy Survey Year 3 Results: High-precision measurement and modeling of galaxy-galaxy lensing. *To be submitted to PRD*, 2021.

[248] J. Prat, C. Sánchez, Y. Fang, D. Gruen, J. Elvin-Poole, N. Kokron, L. Secco, B. Jain, R. Miquel, N. MacCrann, and et al. Dark energy survey year 1 results: Galaxy-galaxy lensing. *Physical Review D*, 98(4), Aug 2018.

[249] W. H. Press and P. Schechter. Formation of Galaxies and Clusters of Galaxies by Self-Similar Gravitational Condensation. , 187:425–438, Feb. 1974.

[250] M. H. Qenouille. NOTES ON BIAS IN ESTIMATION. *Biometrika*, 43(3-4):353–360, 12 1956.

[251] B. Ratra and M. S. Vogeley. The beginning and evolution of the universe. *Publications of the Astronomical Society of the Pacific*, 120(865):235â265, Mar 2008.

[252] M. Raveri and W. Hu. Concordance and discordance in cosmology. , 99(4), Feb 2019.

[253] C. L. Reichardt, S. Patil, P. A. R. Ade, A. J. Anderson, J. E. Austermann, J. S. Avva, E. Baxter, J. A. Beall, A. N. Bender, B. A. Benson, F. Bianchini, L. E. Bleem, J. E. Carlstrom, C. L. Chang, P. Chaubal, H. C. Chiang, T. L. Chou, R. Citron, C. C. Moran, T. M. Crawford, A. T. Crites, T. de Haan, M. A. Dobbs, W. Everett, J. Gallicchio, E. M. George, A. Gilbert, N. Gupta, N. W. Halverson, N. Harrington, J. W. Henning, G. C. Hilton, G. P. Holder, W. L. Holzapfel, J. D. Hrubes, N. Huang, J. Hubmayr, K. D. Irwin, L. Knox, A. T. Lee, D. Li, A. Lowitz, D. Luong-Van, J. J. McMahon, J. Mehl, S. S. Meyer, M. Millea, L. M. Mocanu, J. J. Mohr, J. Montgomery, A. Nadolski, T. Natoli, J. P. Nibarger, G. Noble, V. Novosad, Y. Omori, S. Padin, C. Pryke, J. E. Ruhl, B. R. Saliwanchik, J. T. Sayre, K. K. Schaffer, E. Shirokoff, C. Sievers, G. Smecher, H. G. Spieler, Z. Staniszewski, A. A. Stark, C. Tucker, K. Vanderlinde, T. Veach, J. D. Vieira, G. Wang, N. Whitehorn, R. Williamson,

W. L. K. Wu, and V. Yefremenko. An Improved Measurement of the Secondary Cosmic Microwave Background Anisotropies from the SPT-SZ + SPTpol Surveys. , 908(2):199, Feb. 2021.

[254] M. Remazeilles, P. C. N. Aghanim, and M. Douspis. Reconstruction of high-resolution Sunyaev-Zeldovich maps from heterogeneous data sets using needlets. *Monthly Notices of the Royal Astronomical Society*, 430(1):370–385, 2013.

[255] M. Remazeilles, J. Delabrouille, and J.-F. Cardoso. Cmb and sz effect separation with constrained internal linear combinations. , 410(4):2481â2487, Nov 2010.

[256] M. Remazeilles, J. Delabrouille, and J. F. Cardoso. CMB and SZ effect separation with constrained Internal Linear Combinations. *Monthly Notices of the Royal Astronomical Society*, 410(4):2481–2487, 2011.

[257] A. G. Riess, A. V. Filippenko, P. Challis, A. Clocchiatti, A. Diercks, P. M. Garnavich, R. L. Gilliland, C. J. Hogan, S. Jha, R. P. Kirshner, B. Leibundgut, M. M. Phillips, D. Reiss, B. P. Schmidt, R. A. Schommer, R. C. Smith, J. Spyromilio, C. Stubbs, N. B. Suntzeff, and J. Tonry. Observational evidence from supernovae for an accelerating universe and a cosmological constant. *The Astronomical Journal*, 116(3):1009â1038, Sep 1998.

[258] M. Rodríguez-Monroy et al. Dark Energy Survey Year 3 Results: Galaxy clustering and systematics treatment for lens galaxy samples. *To be submitted to MNRAS*, 2021.

[259] A. Rotti, B. Bolliet, J. Chluba, and M. Remazeilles. Removing the giants and learning from the crowd: A new SZ power spectrum method and revised Compton y-map analysis. , 503(4):5310–5328, June 2021.

[260] E. Rozo, E. S. Rykoff, A. Abate, C. Bonnett, M. Crocce, C. Davis, B. Hoyle, B. Leistedt, H. V. Peiris, R. H. Wechsler, T. Abbott, F. B. Abdalla, M. Banerji, A. H. Bauer, A. Benoit-Lévy, G. M. Bernstein, E. Bertin, D. Brooks, E. Buckley-Geer, D. L. Burke, D. Capozzi, A. C. Rosell, D. Carollo, M. C. Kind, J. Carretero, F. J. Castander, M. J. Childress, C. E. Cunha, C. B. D'Andrea, T. Davis, D. L. DePoy, S. Desai, H. T. Diehl, J. P. Dietrich, P. Doel, T. F. Eifler, A. E. Evrard, A. F. Neto, B. Flaugher, P. Fosalba, J. Frieman, E. Gaztanaga, D. W. Gerdes, K. Glazebrook, D. Gruen, R. A. Gruendl, K. Honscheid, D. J. James, M. Jarvis, A. G. Kim, K. Kuehn, N. Kuropatkin, O. Lahav, C. Lidman, M. Lima, M. A. G. Maia, M. March, P. Martini, P. Melchior, C. J. Miller, R. Miquel, J. J. Mohr, R. C. Nichol, B. Nord, C. R. O'Neill, R. Ogando, A. A. Plazas, A. K. Romer, A. Roodman, M. Sako, E. Sanchez, B. Santiago, M. Schubnell, I. Sevilla-Noarbe, R. C. Smith, M. Soares-Santos, F. Sobreira, E. Suchyta, M. E. C. Swanson, J. Thaler, D. Thomas, S. Uddin, V. Vikram, A. R. Walker, W. Wester, Y. Zhang, and L. N. da Costa. red-

magic: selecting luminous red galaxies from the des science verification data. *Monthly Notices of the Royal Astronomical Society*, 461(2):1431–1450, 2016.

[261] E. Rozo, E. S. Rykoff, A. Abate, C. Bonnett, M. Crocce, C. Davis, B. Hoyle, B. Leistedt, H. V. Peiris, R. H. Wechsler, and et al. redmagic: selecting luminous red galaxies from the des science verification data. *Monthly Notices of the Royal Astronomical Society*, 461(2):1431â1450, May 2016.

[262] D. H. Rudd, A. R. Zentner, and A. V. Kravtsov. Effects of Baryons and Dissipation on the Matter Power Spectrum. , 672:19–32, Jan. 2008.

[263] S. Saito, T. Baldauf, Z. Vlah, U. Seljak, T. Okumura, and P. McDonald. Understanding higher-order nonlocal halo bias at large scales by combining the power spectrum with the bispectrum. *Physical Review D - Particles, Fields, Gravitation and Cosmology*, 90(12):1–29, 2014.

[264] S. Samuroff, J. Blazek, M. A. Troxel, N. MacCrann, E. Krause, C. D. Leonard, J. Prat, D. Gruen, S. Dodelson, T. F. Eifler, and et al. Dark energy survey year 1 results: constraints on intrinsic alignments and their colour dependence from galaxy clustering and weak lensing. *Monthly Notices of the Royal Astronomical Society*, 489(4):5453â5482, Aug 2019.

[265] S. Samuroff, J. Blazek, M. A. Troxel, N. MacCrann, E. Krause, C. D. Leonard, J. Prat, D. Gruen, S. Dodelson, T. F. Eifler, M. Gatti, W. G. Hart-

ley, B. Hoyle, P. Larsen, J. Zuntz, T. M. C. Abbott, S. Allam, J. Annis, G. M. Bernstein, E. Bertin, S. L. Bridle, D. Brooks, A. Carnero Rosell, M. Carrasco Kind, J. Carretero, F. J. Castander, C. E. Cunha, L. N. da Costa, C. Davis, J. De Vicente, D. L. DePoy, S. Desai, H. T. Diehl, J. P. Dietrich, P. Doel, B. Flaugher, P. Fosalba, J. Frieman, J. García-Bellido, E. Gaztanaga, D. W. Gerdes, R. A. Gruendl, J. Gschwend, G. Gutierrez, D. L. Hollowood, K. Honscheid, D. J. James, K. Kuehn, N. Kuropatkin, M. Lima, M. A. G. Maia, M. March, J. L. Marshall, P. Martini, P. Melchior, F. Menanteau, C. J. Miller, R. Miquel, R. L. C. Ogando, A. A. Plazas, E. Sanchez, V. Scarpine, R. Schindler, M. Schubnell, S. Serrano, I. Sevilla-Noarbe, E. Sheldon, M. Smith, F. Sobreira, E. Suchyta, G. Tarle, D. Thomas, V. Vikram, and DES Collaboration. Dark Energy Survey Year 1 results: constraints on intrinsic alignments and their colour dependence from galaxy clustering and weak lensing. , 489(4):5453–5482, Nov. 2019.

[266] S. Samuroff, R. Mandelbaum, and J. Blazek. Advances in constraining intrinsic alignment models with hydrodynamic simulations, 2020.

[267] C. Sánchez, J. Prat, et al. Dark Energy Survey Year 3 Results: Exploiting small-scale information with lensing ratios. *To be submitted to PRD*, 2021.

[268] E. Schaan, S. Ferraro, S. Amodeo, N. Battaglia, S. Aiola, J. E. Austermann, J. A. Beall, R. Bean, D. T. Becker, R. J. Bond, and et al. Atacama cosmol-

ogy telescope: Combined kinematic and thermal sunyaev-zelâdovich mea-surements from boss cmass and lowz halos. , 103(6), Mar 2021.

[269] R. J. Scherrer and D. H. Weinberg. Constraints on the Effects of Locally Biased Galaxy Formation. , 504(2):607–611, Sept. 1998.

[270] S. J. Schmidt, B. Ménard, R. Scranton, C. B. Morrison, M. Rahman, and A. M. Hopkins. Inferring the redshift distribution of the cosmic infrared background. , 446:2696–2708, Jan 2015.

[271] M. Schmittfull, Z. Vlah, and P. McDonald. Fast large scale structure perturbation theory using one-dimensional fast Fourier transforms. , 93(10):103528, May 2016.

[272] M. D. Schneider and S. Bridle. A halo model for intrinsic alignments of galaxy ellipticities. , 402(4):2127–2139, Mar. 2010.

[273] L. F. Secco, S. Samuroff, et al. Dark Energy Survey Year 3 Results: Cosmology from Cosmic Shear and Robustness to Modeling Uncertainty. *To be submitted to PRD*, 2021.

[274] N. Sehgal, P. Bode, S. Das, C. Hernandez-Monteagudo, K. Huffenberger, Y.-T. Lin, J. P. Ostriker, and H. Trac. Simulations of the Microwave Sky. , 709:920–936, Feb. 2010.

[275] L. Senatore. Bias in the effective field theory of large scale structures. , 2015(11):007, Nov. 2015.

[276] I. Sevilla, R. Armstrong, E. Bertin, A. Carlson, G. Daues, S. Desai, M. Gower, R. Gruendl, W. Hanlon, M. Jarvis, R. Kessler, N. Kuropatkin, H. Lin, J. Marriner, J. Mohr, D. Petravick, E. Sheldon, M. E. C. Swanson, T. Tomashek, D. Tucker, Y. Yang, and B. Yanny. The Dark Energy Survey Data Management System. *arXiv e-prints*, page arXiv:1109.6741, Sept. 2011.

[277] Sevilla, N. et al. Sept. prep.

[278] I. Sevilla-Noarbe et al. Dark Energy Survey Year 3 Results: Photometric Data Set for Cosmology. *Submitted to ApJS*, 11 2020.

[279] E. S. Sheldon and E. M. Huff. Practical weak-lensing shear measurement with metacalibration. *The Astrophysical Journal*, 841(1):24, May 2017.

[280] Sheldon, E. et al. Sept. prep.

[281] X. Shi and E. Komatsu. Analytical model for non-thermal pressure in galaxy clusters. , 442(1):521–532, July 2014.

[282] M. Shirasaki. Impact of radio sources and cosmic infrared background on thermal Sunyaev-Zel'dovich - gravitational lensing cross-correlation. , 483:342–351, Feb 2019.

[283] S. Singh, R. Mandelbaum, and S. More. Intrinsic alignments of sdss-iii boss lowz sample galaxies. , 450(2):2195â2216, May 2015.

[284] S. Singh, R. Mandelbaum, U. Seljak, S. RodrÃguez-Torres, and A. Slosar. Cosmological constraints from galaxyâlensing cross-correlations using boss galaxies with sdss and cmb lensing. *Monthly Notices of the Royal Astronomical Society*, 491(1):51â68, Oct 2019.

[285] S. Singh, R. Mandelbaum, U. Seljak, A. Slosar, and J. Vazquez Gonzalez. Galaxyâgalaxy lensing estimators and their covariance properties. *Monthly Notices of the Royal Astronomical Society*, 471(4):3827â3844, Jul 2017.

[286] G. P. Smith, P. Mazzotta, N. Okabe, F. Ziparo, S. L. Mulroy, A. Babul, A. Finoguenov, I. G. McCarthy, M. Lieu, Y. M. Bahé, H. Bourdin, A. E. Evrard, T. Futamase, C. P. Haines, M. Jauzac, D. P. Marrone, R. Martino, P. E. May, J. E. Taylor, and K. Umetsu. LoCuSS: Testing hydrostatic equilibrium in galaxy clusters. , 456(1):L74–L78, Feb. 2016.

[287] V. Springel. The cosmological simulation code GADGET-2. , 364:1105–1134, Dec. 2005.

[288] V. Springel, S. D. M. White, A. Jenkins, C. S. Frenk, N. Yoshida, L. Gao, J. Navarro, R. Thacker, D. Croton, J. Helly, and et al. Simulations of

the formation, evolution and clustering of galaxies and quasars. *Nature*, 435(7042):629â636, Jun 2005.

[289] G. Stein, M. A. Alvarez, and J. R. Bond. The mass-Peak Patch algorithm for fast generation of deep all-sky dark matter halo catalogues and its N-body validation. , Nov. 2018.

[290] E. Suchyta, E. M. Huff, J. AleksiÄ, P. Melchior, S. Jouvel, N. MacCrann, A. J. Ross, M. Crocce, E. Gaztanaga, K. Honscheid, and et al. No galaxy left behind: accurate measurements with the faintest objects in the dark energy survey. *Monthly Notices of the Royal Astronomical Society*, 457(1):786â808, Jan 2016.

[291] R. A. Sunyaev and I. B. Zeldovich. Microwave background radiation as a probe of the contemporary structure and history of the universe. , 18:537–560, 1980.

[292] R. A. Sunyaev and Y. B. Zeldovich. The Observations of Relic Radiation as a Test of the Nature of X-Ray Radiation from the Clusters of Galaxies. *Comments on Astrophysics and Space Physics*, 4:173, Nov. 1972.

[293] R. A. Sunyaev and Y. B. Zeldovich. The Observations of Relic Radiation as a Test of the Nature of X-Ray Radiation from the Clusters of Galaxies. *Comments on Astrophysics and Space Physics*, 4:173, Nov. 1972.

[294] D. S. Swetz, P. A. R. Ade, M. Amiri, J. W. Appel, E. S. Battistelli, B. Burger, J. Chervenak, M. J. Devlin, S. R. Dicker, W. B. Doriese, R. Dünner, T. Essinger-Hileman, R. P. Fisher, J. W. Fowler, M. Halpern, M. Hasselfield, G. C. Hilton, A. D. Hincks, K. D. Irwin, N. Jarosik, M. Kaul, J. Klein, J. M. Lau, M. Limon, T. A. Marriage, D. Marsden, K. Martocci, P. Mauskopf, H. Moseley, C. B. Netterfield, M. D. Niemack, M. R. Nolta, L. A. Page, L. Parker, S. T. Staggs, O. Stryzak, E. R. Switzer, R. Thornton, C. Tucker, E. Wollack, and Y. Zhao. Overview of the Atacama Cosmology Telescope: Receiver, Instrumentation, and Telescope Systems. , 194:41, June 2011.

[295] A. G. SÃ¡nchez, R. Scoccimarro, M. Crocce, J. N. Grieb, S. Salazar-Albornoz, C. D. Vecchia, M. Lippich, F. Beutler, J. R. Brownstein, C.-H. Chuang, and et al. The clustering of galaxies in the completed sdss-iii baryon oscillation spectroscopic survey: Cosmological implications of the configuration-space clustering wedges. *Monthly Notices of the Royal Astronomical Society*, 464(2):1640â1658, Sep 2016.

[296] R. Takahashi, M. Sato, T. Nishimichi, A. Taruya, and M. Oguri. Revising the Halofit Model for the Nonlinear Matter Power Spectrum. *Astrophys. J.*, 761:152, 2012.

[297] H. Tanimura, G. Hinshaw, I. G. McCarthy, L. Van Waerbeke, N. Aghanim, Y.-Z. Ma, A. Mead, T. Tröster, A. Hojjati, and B. Moraes. Probing hot

gas around luminous red galaxies through the Sunyaev-Zel'dovich effect. *arXiv e-prints*, page arXiv:1903.06654, Mar 2019.

[298] A. Taruya and J. Soda. Stochastic biasing and the galaxyâmass density relation in the weakly nonlinear regime. *The Astrophysical Journal*, 522(1):46â58, Sep 1999.

[299] J. A. Tauber, N. Mandolesi, J.-L. Puget, T. Banos, M. Bersanelli, F. R. Bouchet, R. C. Butler, J. Charra, G. Crone, J. Dodsworth, and et al. Planck pre-launch status: The Planck mission. , 520:A1, Sept. 2010.

[300] J. Tinker, A. V. Kravtsov, A. Klypin, K. Abazajian, M. Warren, G. Yepes, S. Gottlöber, and D. E. Holz. Toward a Halo Mass Function for Precision Cosmology: The Limits of Universality. , 688(2):709–728, Dec 2008.

[301] J. Tinker, A. V. Kravtsov, A. Klypin, K. Abazajian, M. Warren, G. Yepes, S. Gottlöber, and D. E. Holz. Toward a Halo Mass Function for Precision Cosmology: The Limits of Universality. , 688:709–728, Dec. 2008.

[302] J. Tinker, A. V. Kravtsov, A. Klypin, K. Abazajian, M. Warren, G. Yepes, S. GottlÃ¶ber, and D. E. Holz. Toward a halo mass function for precision cosmology: The limits of universality. *The Astrophysical Journal*, 688(2):709â728, Dec 2008.

[303] J. L. Tinker, B. E. Robertson, A. V. Kravtsov, A. Klypin, M. S. Warren, G. Yepes, and S. Gottlöber. The Large-scale Bias of Dark Matter Halos: Numerical Calibration and Model Tests. , 724(2):878–886, Dec 2010.

[304] J. L. Tinker, B. E. Robertson, A. V. Kravtsov, A. Klypin, M. S. Warren, G. Yepes, and S. Gottlöber. The Large-scale Bias of Dark Matter Halos: Numerical Calibration and Model Tests. , 724:878–886, Dec. 2010.

[305] J. L. Tinker, B. E. Robertson, A. V. Kravtsov, A. Klypin, M. S. Warren, G. Yepes, and S. Gottlöber. The large-scale bias of dark matter halos: Numerical calibration and model tests. *The Astrophysical Journal*, 724(2):878â886, Nov 2010.

[306] C. To, E. Krause, E. Rozo, H. Wu, D. Gruen, R. Wechsler, T. Eifler, E. Rykoff, M. Costanzi, M. Becker, and et al. Dark energy survey year 1 results: Cosmological constraints from cluster abundances, weak lensing, and galaxy correlations. *Physical Review Letters*, 126(14), Apr 2021.

[307] M. Troxel, N. MacCrann, J. Zuntz, T. Eifler, E. Krause, S. Dodelson, D. Gruen, J. Blazek, O. Friedrich, S. Samuroff, and et al. Dark energy survey year 1 results: Cosmological constraints from cosmic shear. *Physical Review D*, 98(4), Aug 2018.

[308] M. A. Troxel and M. Ishak. The intrinsic alignment of galaxies and its impact on weak gravitational lensing in an era of precision cosmology. ,

558:1–59, Feb. 2015.

[309] J. Tukey. Bias and confidence in not quite large samples. *Ann. Math. Statist.*, 29:614, 1958.

[310] M. P. van Daalen, J. Schaye, C. M. Booth, and C. Dalla Vecchia. The effects of galaxy formation on the matter power spectrum: a challenge for precision cosmology. , 415:3649–3665, Aug. 2011.

[311] F. C. van den Bosch, S. More, M. Cacciato, H. Mo, and X. Yang. Cosmological constraints from a combination of galaxy clustering and lensing - I. Theoretical framework. , 430(2):725–746, Apr. 2013.

[312] F. C. van den Bosch, S. More, M. Cacciato, H. Mo, and X. Yang. Cosmological constraints from a combination of galaxy clustering and lensing â i. theoretical framework. *Monthly Notices of the Royal Astronomical Society*, 430(2):725â746, Feb 2013.

[313] L. Van Waerbeke, G. Hinshaw, and N. Murray. Detection of warm and diffuse baryons in large scale structure from the cross correlation of gravitational lensing and the thermal Sunyaev-Zeldovich effect. , 89:023508, Jan 2014.

[314] V. Vikram, A. Lidz, and B. Jain. A Measurement of the Galaxy Group-Thermal Sunyaev-Zel'dovich Effect Cross-Correlation Function. , 467:2315–2330, May 2017.

[315] V. Vikram, A. Lidz, and B. Jain. A Measurement of the Galaxy Group-Thermal Sunyaev-Zel'dovich Effect Cross-Correlation Function. , 467:2315–2330, May 2017.

[316] Z. Vlah, M. White, and A. Aviles. A Lagrangian effective field theory. , 2015(9):014, Sep 2015.

[317] A. von der Linden, A. Mantz, S. W. Allen, D. E. Applegate, P. L. Kelly, R. G. Morris, A. Wright, M. T. Allen, P. R. Burchat, D. L. Burke, and et al. Robust weak-lensing mass calibration of planck galaxy clusters. , 443(3):1973â1978, Jul 2014.

[318] Y. Wang. Figure of merit for dark energy constraints from current observational data. *Physical Review D*, 77(12), Jun 2008.

[319] R. H. Wechsler, J. DeRose, M. T. Busha, M. R. Becker, E. Rykoff, and A. Evrard. ADDGALS: Simulated Sky Catalogs for Wide Field Galaxy Surveys. *arXiv e-prints*, page arXiv:2105.12105, May 2021.

[320] K. F. Werner and C. Porciani. Renormalization of linear halo bias in n-body simulations. *Monthly Notices of the Royal Astronomical Society*, 492(2):1614â1633, Dec 2019.

[321] Weschler, r. et al. Sept. prep.

[322] B. D. Wibking, A. N. Salcedo, D. H. Weinberg, L. H. Garrison, D. Ferrer, J. Tinker, D. Eisenstein, M. Metchnik, and P. Pinto. Emulating galaxy clustering and galaxyâgalaxy lensing into the deeply non-linear regime: methodology, information, and forecasts. *Monthly Notices of the Royal Astronomical Society*, 484(1):989â1006, Aug 2018.

[323] B. D. Wibking, D. H. Weinberg, A. N. Salcedo, H.-Y. Wu, S. Singh, S. RodrÃguez-Torres, L. H. Garrison, and D. J. Eisenstein. Cosmology with galaxyâgalaxy lensing on non-perturbative scales: emulation method and application to boss lowz. *Monthly Notices of the Royal Astronomical Society*, 492(2):2872â2896, Dec 2019.

[324] C. M. Will. The confrontation between general relativity and experiment. *Living Reviews in Relativity*, 17(1), Jun 2014.

[325] X. Yang, H. J. Mo, F. C. van den Bosch, A. Pasquali, C. Li, and M. Barden. Galaxy Groups in the SDSS DR4. I. The Catalog and Basic Properties. , 671:153–170, Dec. 2007.

[326] S. Yuan, D. J. Eisenstein, and A. Leauthaud. Can assembly bias explain the lensing amplitude of the boss cmass sample in a planck cosmology? *Monthly Notices of the Royal Astronomical Society*, 493(4):5551â5564, Mar 2020.

[327] Zacharegkas, G. et al. Sept. prep.

[328] I. Zehavi, Z. Zheng, D. H. Weinberg, M. R. Blanton, N. A. Bahcall, A. A. Berlind, J. Brinkmann, J. A. Frieman, J. E. Gunn, R. H. Lupton, and et al. Galaxy clustering in the completed sdss redshift survey: The dependence on color and luminosity. *The Astrophysical Journal*, 736(1):59, Jul 2011.

[329] I. Zehavi, Z. Zheng, D. H. Weinberg, J. A. Frieman, A. A. Berlind, M. R. Blanton, R. Scoccimarro, R. K. Sheth, M. A. Strauss, I. Kayo, Y. Suto, M. Fukugita, O. Nakamura, N. A. Bahcall, J. Brinkmann, J. E. Gunn, G. S. Hennessy, Ž. Ivezić, G. R. Knapp, J. Loveday, A. Meiksin, D. J. Schlegel, D. P. Schneider, I. Szapudi, M. Tegmark, M. S. Vogeley, D. G. York, and SDSS Collaboration. The Luminosity and Color Dependence of the Galaxy Correlation Function. , 630:1–27, Sept. 2005.

[330] Z. Zheng, A. A. Berlind, D. H. Weinberg, A. J. Benson, C. M. Baugh, S. Cole, R. Davé, C. S. Frenk, N. Katz, and C. G. Lacey. Theoretical Models of the Halo Occupation Distribution: Separating Central and Satellite Galaxies. , 633(2):791–809, Nov 2005.

[331] Z. Zheng, A. A. Berlind, D. H. Weinberg, A. J. Benson, C. M. Baugh, S. Cole, R. Dave, C. S. Frenk, N. Katz, and C. G. Lacey. Theoretical models of the halo occupation distribution: Separating central and satellite galaxies. *The Astrophysical Journal*, 633(2):791â809, Nov 2005.

[332] Y. Zu. On the "lensing is low" of boss galaxies, 2020.

[333] I. Zubeldia and A. Challinor. Cosmological constraints from planck galaxy clusters with cmb lensing mass bias calibration. , 489(1):401â419, Aug 2019.

[334] J. Zuntz, M. Paterno, E. Jennings, D. Rudd, A. Manzotti, S. Dodelson, S. Bridle, S. Sehrish, and J. Kowalkowski. Cosmosis: Modular cosmological parameter estimation. *Astronomy and Computing*, 12:45â59, Sep 2015.